Progress in Materials Science 134 (2023) 101084

Contents lists available at ScienceDirect

Progress in Materials Science

journal homepage: www.elsevier.com/locate/pmatsci

The past, present and future of photonic glasses: A review in homage to the United Nations International Year of glass 2022

Wilfried Blanc [a], Yong Gyu Choi [b], Xianghua Zhang [c], Marcelo Nalin [d], Kathleen A. Richardson [e], Giancarlo C. Righini [f], Maurizio Ferrari [g], Animesh Jha [h], Jonathan Massera [i], Shibin Jiang [j], John Ballato [k,*], Laeticia Petit [l,*]

[a] Université Côte d'Azur, Institut de Physique de Nice, CNRS, Nice, France
[b] Department of Materials Science and Engineering, Korea Aerospace University, Goyang, Gyeonggi 10540, South Korea
[c] Laboratory of Glasses and Ceramics, Institute of Chemistry, UMR CNRS-Université de Rennes I, Campus de Beaulieu, 35042 Rennes, France
[d] Institute of Chemistry – São Paulo State University – UNESP, Araraquara, SP 14800-060, Brazil
[e] College of Optics and Photonics, CREOL, Department of Materials Science and Engineering, University of Central Florida, FL 32816, USA
[f] CNR-IFAC, MiPLab, Via Madonna del Piano 10, 50019 Sesto Fno, Firenze, Italy
[g] CNR-IFN, CSMFO Lab. via alla Cascata 56/C, Povo, 38123 Trento, Italy
[h] School of Chemical and Process Engineering, University of Leeds, Leeds LS2 9JT, UK
[i] Faculty of Medicine and Health Technology, Tampere University, Korkeakoulunkatu 3, 33720 Tampere, Finland
[j] AdValue Photonics Inc, 2700 E. Bilby Road, Tucson, AZ 85706, USA
[k] Department of Materials Science and Engineering, Clemson University, Clemson, SC 29634 USA
[l] Laboratory of Photonics, Tampere University, Korkeakoulunkatu 3, 33720 Tampere, Finland

ARTICLE INFO

Keywords:
Optical glass
Chalcogenide glass
Glass–ceramic
Hybrid
Composite
Fiber
Film
Waveguide

ABSTRACT

Since the invention and further development of lasers in the 1960s, photonics has grown into a field that permeates virtually every aspect of modern life. As photonics deals with the generation, transmission, modulation, amplification, conversion, and detection of light, glasses have played crucial and central roles in a multitude of applications given glasses' diverse range of compositions, properties, and forms. They are also low-cost materials, recyclable and generally easy to fabricate. In homage to the United Nations International Year of Glass 2022, this paper reviews the past, present, and future of photonic glasses.

1. Introduction

Glasses are defined as non-crystalline solids that exhibit a glass transition. This is distinct from crystals which exhibit long-range atomic periodicity and a well-defined melting point. Glasses can be prepared in a wide variety of sizes and forms (e.g., powders, bulk samples, thin films, and fibers) with excellent homogeneity and transparency. As opposed to crystals, the composition of the glasses can be tailored to achieve a range of properties that meet the needs of specific applications. As a direct consequence, glasses have been central to many of humankind's technological and societal advancements.

For centuries, one of the most significant impacts of glass has been in the field of art and architecture. The discovery of x-ray

* Corresponding authors.
E-mail addresses: a.jha@leeds.ac.uk (A. Jha), jballat@clemson.edu (J. Ballato), laeticia.petit@tuni.fi (L. Petit).

https://doi.org/10.1016/j.pmatsci.2023.101084
Received 31 March 2022; Received in revised form 26 December 2022; Accepted 24 January 2023
Available online 3 February 2023

diffraction, microscopic techniques, optical and light-guiding properties, and theory of glass formation in 20th century has led to a multitude of applications ranging from heat-resistant toughened kitchenware to lossless optical fibers and exceptionally large TV screens with optoelectronic displays. As the demand for glass production increased, the need for energy in production processes has remained a concern for commoditized products, namely container and flat glass products. In the 21st century, the flat glass used in the built environment absorbs UV, cuts down heat loss by reflecting IR inside the dwelling, and creates an ambience which feels natural. The recycling of glass has become an important part of energy saving in manufacturing, with further aims on increasing the functionality of the designed product. Increasing the strength of glass remains an important goal so that the product may be used many times by adopting the circular economy and digital identification approaches. To underline the importance of glass in everyday life, from technological, scientific and economic perspectives, 2022 was declared the International Year of Glass (IYOG2022) by the United Nations. The IYOG'2022 aims to spread the importance of the already identified 17 Sustainable Development Goals of UN, amongst which the following goals (SDGS: 7 (Clean Energy e.g. via PV), 9 (Industry and Innovation), 12 (Responsible Consumption and Production), 13 (Climate Change)) are highly relevant for functionalized glass products widely used in photonic devices which is main theme of this review.

The materials reviewed in this paper are limited to optical glasses as they have been especially important for modern life in an age of information and data. This review focuses especially on novel glasses developed from the classical optical glasses and their technological uses. Before discussing the latest progress in the development and applications of the most common photonic glasses (e.g., laser glasses, nonlinear optical glasses, photochromic/photosensitive glasses and magneto-optical glasses), the fundamentals of glass formation, fabrication, and characterization are first presented. Also reviewed are recent developments of glass optical waveguides. Finally, the authors' view on the future of photonic glasses is presented as new applications will emerge across various fields, such as environmental monitoring and medicine.

2. History of optical glasses

The history of terrestrial glass is in many ways the history of the Earth since the earliest glasses, known as obsidian, were made from volcanic activity. The first human-made glasses date back to at least 2600 BC in Mesopotamia [1]. The beginning of shaping glasses into vessels, for example, started as early as 1450 BCE in Egypt using a basic soda (Na_2O) – lime (CaO) – silica (SiO_2) composition. The first glasses were prepared using a mixture of sand (the source of silica), ground seashells (the source of lime) and hardwood ash (the source of soda). Glass blowing was developed only near the beginning of the Christian era. While the first flat glass was obtained during Roman times, the first glass windows only appeared in the 12th century. At this time, efforts were focused on the preparation and selection of better raw materials and that work led to the realization of glasses with improved optical quality, i.e., transparency. Some of the best examples of this progress are Bohemian "crystal," a potash-lime glass, in 1680 [2] and "flint" glass, a lead-silica composition, in 1674 [3]. The science of glassmaking was first described in the 18th-19th centuries with the publication of the atomic theory by John Dalton in 1808 [4], the beginning of the quantitative chemical analysis by Jöns Jacob Berzelius, also in 1808, and, importantly, with the publication of *The Atomic Arrangement in Glass* by W.H. Zachariasen in 1932, which remains amongst the most foundational works on glass science to the present day [5]. Because glasses of high optical quality were rare until the mid-19th century, crystals were mainly used. For example, the spectacle lenses, the first transmissive optical elements, were fabricated using natural crystals (mostly, colorless quartz, aka crystal rock) in the 13th century [6]. Therefore, efforts began to focus on the preparation of colorless and transparent glasses. Although glass-makers were able to fabricate colorless glasses in the 15th century, the first optical glasses useful for light-based instruments were not obtained until 100 years later. Galileo played an important role in glass science by devoting special attention to the fabrication of lenses and developing a telescope for observing ships further away than could be seen by the human eye [7]. The first optical glasses obtained using a melt-stirring process were those developed in 1805 by Pierre Louis Guinand [8] and Joseph Fraunhofer, who were the first to characterize their optical properties. Fraunhofer measured the absorption lines in the solar spectrum now known as the Fraunhofer lines. His work led to great improvement in the manufacturing of optical glasses. He also successfully built astronomical telescopes from high quality lenses with a diameter as large as 28 cm. The melting of glasses other than silicates started from 1830 by Michael Faraday who worked on a wide variety of glass compositions. However, commercial optical glasses were limited at the end of the 19th century and only few companies, such as *Chance and Brothers* in England and the *Glastechnisches Laboratorium Schott* in Germany, were manufacturing them [9]. At this time, glasses still possessed unpredictable optical quality. There was a need for commercial glasses with better quality and this need led to the successful collaboration between Carl Zeiss (an instrument maker), Ernst Abbe (a physicist), and Otto Schott (a chemist). Due their complementary theoretical and technical expertise, a large variety of new glasses were developed in a very short time [10] as Schott was able to melt glasses with high, precise, and reproductible optical quality. This partnership opened the door to the systematic glass development from the methods Schott developed to estimate selected glass properties based on its composition. Hereafter, great progress in the development of new glass types was achieved, one being, for example, heat-resistant borosilicate glasses used in streetlights at the end of the 19th century. Glasses became materials of interest, particularly after the discovery of the lanthanum-doped glasses in the 1930s, of new lead-borate glasses in the 1950s and, shortly thereafter, of the fluorophosphate glasses, all of which contributed to energize glass research. An out-growth of this rise in glass research was the discovery of glass-ceramics by Donald Stookey of *Corning Glass Works* in 1954 [11]. Stookey pioneered an understanding of nucleation and crystal growth processes in glasses and his work led to significant technologic advancements and commercial successes in astronomical mirrors and missile radomes, as well as cook-top panels and cookware. More recently, in the 1990s, the world of glass science, especially the industrial sector, was shaken due to the need for glasses free of lead and arsenic, which were shown to have negative health and environmental impacts. Another revolution in glass science occurred in mid-1950 s with the development of amorphous non oxygen–containing chalcogenide (ChG) glasses based on the

first reports by Schulz–Sellack in 1870 [12]. These glasses contain at least one of the chalcogen (Group VI) elements (S, Se, and / or Te, excluding O) and exhibited weaker bonding than oxides. In the 1950s, Frerichs was the first to investigate the transparency of ChG glasses [13]. One of the first uses of ChGs was in computer memories, due to switching effects first demonstrated in 1968 by Ovshinsky [14]. To prove the potential of ChGs, an early review on the progress in ChGs was published in 1977 [15]. Since then, based on ChGs and their unique properties (large linear refractive index and broad infrared transparency), a large number of new ChGs have been investigated by combining chalcogens and other elements [9]. Other non-oxide glasses, such as those based on a fluorine anion (e.g., fluoride glasses) have also been of great interest. This fluoride glass family is based on the discovery by Poulainet al. in the 1970s, that ZrF_4 is a glass-forming compound [16]. For the past few decades, global efforts have focused on the development of oxyfluoride glasses as their (molecular) structure and properties can be tailored through control of the oxygen to fluorine ratio [17]. Another important milestone in the history of glass relates to the invention of the first glass laser in 1961 [18], which drove the subsequent development of optical communication systems, including passive and active optical fibers [19]. After the "groundbreaking achievements concerning the transmission of light in fibers for optical communication" reported in 1966 by Kao [20], who was awarded the Nobel Prize in Physics in 2009 as a result, global efforts focused on the development of optical fibers with low-loss through novel fabrication methods to achieve intrinsically high purity glass preforms. In 1970, optical fibers with 20 dB/km at 632.8 nm were successfully drawn by *Corning* after successive technological developments [21] and losses were reduced to 0.20 dB/km at 1550 nm in 1979 [22]. The attenuation minimum in mass-produced single-mode fiber today is now below 0.17 dB/km. A history of optical fiber can be found in [23].

These are just few examples of selected milestones in the modern development of optical and photonic glasses. Readers are referred to [24–26] for additional details on the history of optical glasses and glass-ceramics. Glass science is one of the oldest research fields and has continuously evolved since at least 2600 BCE. Despite the great advancement in glass science over intervening millennia, glass scientists worldwide should continue to develop novel glasses with improved properties and/or new functionality, particularly with recent advances in nano-scale science, so that glass continues to meet technological and societal needs.

3. Glass formation, fabrication and characterization

The theory of glass formation and nucleation and growth process are introduced in this section. The most common techniques used for the glass preparation and analysis of glass properties are also discussed briefly. This section is intended for students and researchers who study optical glasses.

3.1. Theory of glass formation

Conventionally, to produce glass, powder raw materials of the respective components (e.g., SiO_2, CaO, Na_2O), with alkali or alkaline earth species most frequently obtained in the form of less expensive carbonates or nitrates, are mixed in the appropriate compositional ratios, and melted in a crucible at a high temperature. The melt is then rapidly quenched to prevent crystallization [27]. As shown in Fig. 1**a,** the melt is rapidly cooled to prevent crystallization during solidification (as defined by the decrease of viscoplastic

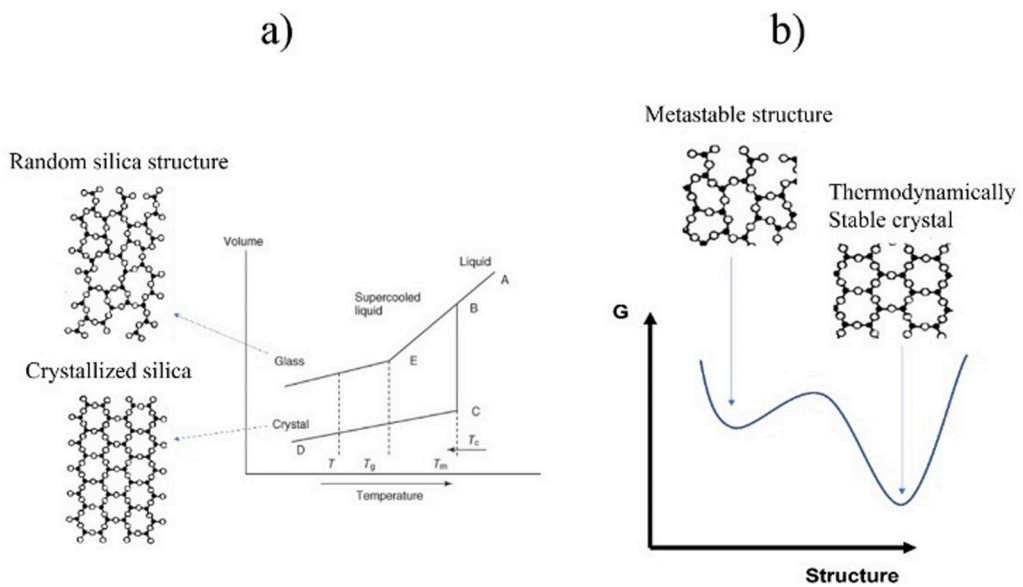

Fig. 1. (a) Volume change as a function of temperature during glass formation, along with the resulting structure for crystallized and amorphous SiO_2. (b) Energy, represented by free energy, G, for both the supercooled metastable structure and the thermodynamically stable crystal. (Modified from [28]).

relaxation over a measurable timescale) which takes place at the glass transition temperature, T_g. This leads to a material that does not exhibit structural long-range order, as well as to an increased volume and enthalpy when compared to the corresponding (i.e., compositionally equivalent) crystal. Accordingly, glass is metastable. However, below its glass transition temperature, the relaxation time for structural reorganization (or spatial displacement, i.e., flow) is so long as to make glass effectively a solid, despite its liquid-like structure.

The formation of silicate (SiO_2-based) glasses is often defined by Zachariesen's theory of glass formation [5]. This theory is also referred to as the crystallochemical theory and led to the well-known 3D continuous random network representation of (silicate) glass structure [29]. In brief, Zachariesen's theory postulates that (1) the interatomic forces and nature of the bonds, in the crystal and the glass, are similar, (2) glass, being metastable, is in a slightly higher energy state, as depicted in Fig. 1**b** and (3) the nearest neighbor coordination polyhedral are similar in the glass and the crystal [5]. Therefore, based on these postulates, the following rules apply to the formation of silicate glasses: (1) each oxygen atom is bonded to one or a maximum of two glass forming cations, (2) the coordination number of the glass forming cation is 3 or 4, (3) the oxygen coordination polyhedral share only corners, and (4) the polyhedral structural units form a 3D continuous random network in which each polyhedron shares at least 3 corners with its neighbors. However, this model only applies to silicate glasses, thus excluding metallic, fluoride, and chalcogenide glasses, for example. The model also fails to represent the formation of chain-like or polymeric glass structures such as found in metaphosphate glasses. More generally, glass formation can be represented as a kinetic model, thereby, any material can be made glassy, in theory, assuming that the critical cooling rate is exceeded. Dietzel and Wickert refer to this as "glassiness," that is, materials cooled at a sufficiently high rate such that crystals cannot form [30]. This idea was revisited by D. Turnbull who adopted a criterion of avoiding a crystal nucleation event during cooling [31]. However, those views lacked an ability to predict the critical cooling rate by which a melt must cool to yield a glass. To answer this critical question, D. R. Uhlmann reflected on the nucleation and growth of crystals upon cooling / heating [32]. Crystal nucleation and growth show both thermodynamic (temperature dependent) and kinetic (time dependent) dependencies. Here the idea was that melts can be vitrified if the cooling rate is fast enough to inhibit the nucleation of the crystals above a critical size. Such a concept, called transformation theory, is discussed in the next section [32–35].

3.2. Nucleation and growth theory

The theory of transformation kinetics relates the volume fraction crystallized, V_c/V, to the nucleation rate per unit volume, I_v, and the crystal growth rate, u, over the time period, t, based on the equation $\frac{V_c}{V} = 1 - exp\left(\left| -\int_0^t I_v\left(\int_t^t u d\tau\right)^3 dt'\right|\right)$. However, both I_v and u are functions of time at a given temperature. Indeed, if one calculates the nucleation and growth rates at a specific temperature, it is then possible to calculate the fractional crystallinity. It is important to note that if no nuclei are formed, crystallization is avoided and a glass results.

Nucleation processes: Nucleation can either be homogeneous or heterogeneous. Homogeneous nucleation refers to nuclei formed uniformly in the melt while heterogeneous nucleation occurs at an interface, such as an impurity or the crucible wall. Typical impurities are seeds or bubbles, to name just two. The nucleation mechanism is both kinetic and thermodynamic. The thermodynamic contribution relates to the free energy change associated with crystal formation, W*, whereas the kinetic contribution corresponds to the energy barrier required to initiate the formation of nuclei, $\triangle G_D$. The nucleation rate can be expressed as $I = A^{\left[-(W^* + \Delta G_D)/kT\right]}$ where I is the homogeneous nucleation rate, A is the pre-exponential factor, k is the Boltzmann constant, and T is absolute temperature.

The thermodynamic contribution in the nucleation process relates to the change in free energy to form a nucleus. As shown in Fig. 2**,** there are two distinct contributions to the nucleation.

One contribution is in favor of nucleation, i.e., the volume energy gain, and one that prevents nucleation, i.e., the surface energy barrier. Therefore, once the surface energy barrier is overcome, spontaneous nucleation can occur. As such, the free energy change can then be expressed as [37] $\Delta G = V\Delta G_v + A\sigma_{ls}$ where $\triangle G$ is the change in energy that leads to a phase transformation, $\triangle G_v$ is the Gibbs free energy difference between the liquid and the solid state, V and A are the volume and area of the crystals, respectively, and σ_{ls} is the

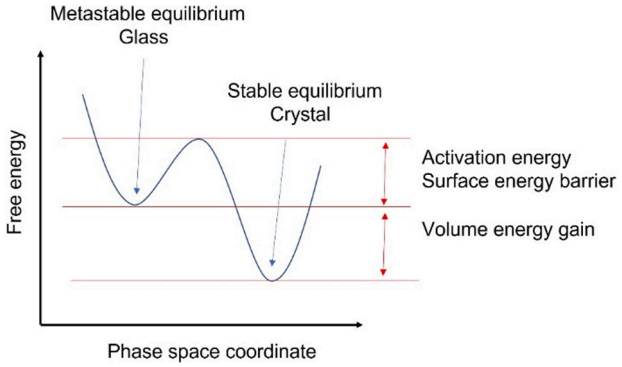

Fig. 2. Energy change from the metastable glass to the stable crystal (Modified from [36] with permission from Elsevier).

surface tension between the two phases. In the case of a spherical nucleus the equation can be expressed as $\Delta G = \frac{4\pi r^3}{3}\Delta G_v + 4\pi r^2 \sigma_{ls}$ where r is the radius of the nucleus.

As shown in Fig. 3, the sum of the volume energy gain and surface energy barrier, leads to a maximum. This maximum corresponds to the critical size a nucleus (or "embryo" as noted in Fig. 3) must have to remain stable and spontaneously grow. Indeed, a nucleus with $r \ll r^*$ will resorb into the melt and the crystallization process will be inhibited. If $r \gg r^*$, the volume energy gain becomes dominant and will favor nucleation and crystal growth. The minimum energy needed to form a nucleus with critical radius, r*, is expressed by $\Delta G^* = \frac{16\pi\sigma_{ls}^3}{3\Delta G_v^2}$.

The kinetic barrier to crystallization, $\triangle G_d$, is a function of (melt) viscosity and diffusion coefficient D and is expressed as $D = \frac{kT\lambda^2}{h}\exp\left(\frac{\Delta G_d}{kT}\right)$ where D is the diffusion coefficient, k is the Boltzmann constant, h is the Planck constant, λ is the atomic jump distance, and T is absolute temperature. The diffusion coefficient, D, can also be expressed as a function of viscosity, η, at a specific temperature, T, by the Stokes-Einstein equation [38], $D = \frac{kT}{3\pi\lambda\eta}$. Therefore, the steady state nucleation can be expressed as $I = \frac{Ah}{3\pi\lambda^3\eta} exp\left(-\frac{16\pi\sigma_{ls}}{3\Delta G_v kT}\right)$.

At temperatures close to or above the melting temperature, $\triangle G_v$ is small and therefore I is close to 0, thus no nuclei form. When the temperature decreases, $\triangle G_v$ increases, thus decreasing the value for r* and, consequently, increasing I. If the system remains at a temperature long enough to produce nuclei with size equal to or greater than r*, crystallization from the melt occurs [38]. This demonstrates the importance to know and control, for each glass composition, the critical cooling rate to inhibit nucleation. It is important to note that while steady nucleation in glass implies a linear dependence of the nucleation rate as a function of nucleation time, a transient nucleation time is often noticed as demonstrated by K. F. Kelton [39].

While the above-mentioned nucleation theory applies to homogeneous nucleation, one should keep in mind that any impurities such as bubbles, seeds, etc., can lead to heterogeneous crystallization. In such case, the interface between the seed and the liquid (melt) will govern the nucleation mechanism. The free energy needed for a heterogeneous nucleation is accepted to be the product of homogeneous nucleation and a function of the contact angle between the seed and the liquid ($\Delta G_{heterogeneous} = \Delta G_{homogeneous} \cdot f(\theta)$, where $f(\theta) is f(\theta) = \frac{1}{2} + \frac{3}{4}\cos\theta - \frac{1}{4}cos^3\theta$). The barrier energy needed for heterogeneous nucleation is then reduced by the presence of the foreign surface. The wetting angle determines the ease of nucleation while the critical radius of the nuclei remains unchanged. However, the volume can be significantly less for heterogeneous nucleation due to the wetting angle affecting the shape of the cluster [38].

Growth process: Once nuclei are formed, two distinct energy barriers must be overcome to subsequently grow the crystals, i.e., the thermodynamic barrier ($\triangle G_c$) and the kinetic barrier ($\triangle G_a$), also called the activation energy. Crystal growth occurs through the addition of atoms / molecules to an already formed (stable) nuclei at a rate that is a function of the thermodynamic and kinetic barrier energies. The equation related to crystal growth can be expressed as $U = a_0\nu\exp\left(-\frac{\Delta G_a}{kT}\right)\left[1 - \exp\left(-\frac{V\Delta G_c}{kT}\right)\right]$ where a_0 is the interatomic separation distance and ν the (atomic) jump frequency [40]. For an atom to migrate from the supercooled liquid to the interface of the (crystalline) nucleus, the activation energy, $\triangle G_a$, must be reached. Using the Stokes-Einstein equation, the growth rate, U, can be formulated as $U = \left(\frac{kT}{3\pi a_0^3\eta}\right)\left[1 - \exp\left(\frac{\Delta G_c}{kT}\right)\right]$ and can be represented as a function of temperature as in Fig. 4.

Upon cooling the melt, the formation of nuclei and, thus, crystals are unlikely to occur if the nucleation and growth curves do not overlap. However, one can re-heat the formed glass within the nucleation domain, to form a given number of nuclei. By increasing the temperature within the crystal growth domain, it is then possible to obtain a glassy matrix with controlled volume density of crystals. The controlled crystallization of a glass leads to the formation of a "glass–ceramic.".

Kirkpatrick in 1981, following the work of Johnson and Avrami, described the overall rate of crystallization based on several hypotheses: (1) both nucleation and growth occur simultaneously, (2) there is a uniform parent phase that does not contain any crystals and (3) the nucleation occurs randomly leading to a three-dimensional (3D) bulk crystallization (spherical crystal) [33–35,41]. The total extended volume of crystals that formed or could form in the melt from the start of crystallization to any time, t, can be expressed as $V_{ext} = \frac{4\pi}{3} V \int_{\tau=0}^{\tau=t} I_\tau \left(\int_\tau^t U_t dt\right)^3 d\tau$ where V is the total volume of the material and τ is the time. I and U are the nucleation and

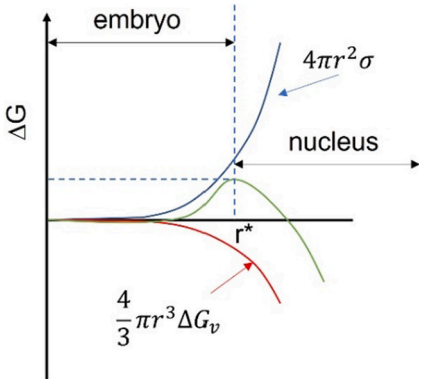

Fig. 3. Nucleation free energy ΔG as a function of the cluster radius r.

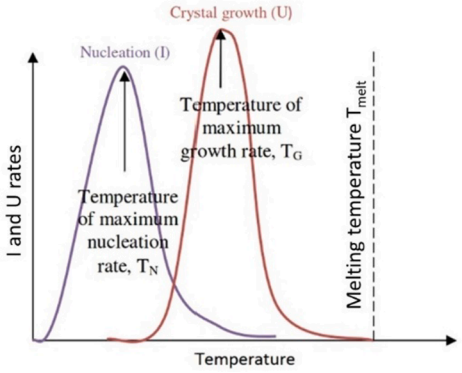

Fig. 4. Nucleation and growth rate as a function of temperature.

growth rates, respectively. This equation shows several limitations and leads to an overestimation of the true volume crystallized. Indeed, the assumptions neglect "phantom" nuclei and the phenomenon of crystal impingement. Phantom nuclei correspond to crystals that would form, in a specific location, if a crystal would not be already present. Crystal impingement relates to crystals that, upon growing, "touch," leading to a deceleration of their growth. A more general equation, given by $\varphi = 1 - \exp\left[-\frac{4\pi}{3} \int_{\tau=0}^{\tau=t} I_\tau \left(\int_\tau^t U_t dt \right)^3 d\tau \right]$, was therefore proposed to consider those two effects [41]. This expression takes into consideration any variation in nucleation and growth rates as a function of time. In the case of constant nucleation and growth rates, the above equation gives the classic Johnson-Mehl-Avrami (JMA) relationship [41], $\varphi = 1 - \exp\left[-\frac{\pi}{3} I U^3 t^4 \right]$. Although this equation was derived for 3D crystallization, Avrami explained that a more general equation could be used in order be applicable to crystallization occurring in the volume or at the surface and regardless of the shape of the crystals: $\varphi = 1 - \exp(- gIU^m t^n)$, where g is the crystal geometric factor, m and n are the Johnson-Mehl-Avrami exponents. The exponents m and n are typically integers or half integers that depend on the type of growth occurring in the material (surface crystallization versus 1D, 2D or 3D bulk crystallization). Typical value for n and the associated nucleation process are presented in Table 1.

Often this kinetic law equation is expressed as $\varphi = 1 - \exp(- (kt)^n)$, where k is the effective overall reaction rate and is often expressed using the Arrhenius temperature dependence as $k = k_0 \exp\left(-\frac{E}{RT} \right)$, where E is the overall activation energy for crystallization, k_0 is the initial reaction rate constant and R the gas constant.

Predicting nucleation and growth of crystals in glass remains challenging. Zanotto et al. studied in detail the fundamentals of glass crystallization, focusing, for example, on the correlation between glass structure and nucleation mechanism, the effect of liquid phase separation on crystal nucleation, the impact of surface crystallization on concurrent sintering or the diffusional processes controlling crystallization [42]. Crystallization mechanism has been studied in a wide variety of glassy matrices, such as silicate [43,44], tellurite [45], germanate [46], chalcogenide [47] or metallic glasses [48]. Crystallization of glasses, aside from improving the mechanical properties, can also improve the spectroscopic properties [49]. More details about the impact of crystallization on spectroscopic properties of glasses are discussed in **Section 4**.

Table 1
Value of n in kinetic law. Modified from [37].

Polymorphic changes, discontinuous precipitation, eutectoids reactions, interfaced control growth.	
Conditions	n value
Increasing nucleation rate	>4
Constant nucleation rate	4
Decreasing nucleation rate	3–4
Zero nucleation rate	3
Grain edge nucleation after saturation	3
Grain boundary nucleation after saturation	1
Diffusion controlled growth	
Conditions	**n value**
All shapes growing from small dimensions, increasing nucleation rate	>2.5
All shapes growing from small dimensions, constant nucleation rate	2.5
All shapes growing from small dimensions, deceasing nucleation rate	1.5–2.5
All shapes growing from small dimensions, zero nucleation rate	1.5
Growth of particles of appreciable initial volume	1–1.5
Needles and plates of finite long dimensions	1
Thickening of long needles (after complete impingement)	1
Thickening of large plate (after edge impingement)	0.5
Precipitations of dislocations	~0.5

3.3. Most common fabrication methods

Glasses have mainly been fabricated by melt-quench methods, though, more recently, chemical vapor deposition and sol–gel approaches have gained in importance.

The main feature of the melt (fusion) process is the large number of oxide and non-oxide compositions that can be suitably made. In this process, the raw materials are weighed according to a desired composition. A batch of suitable precursors, usually powders, in given component ratios, is meticulously mixed and, possibly, ground to obtain powders with uniform and small particle size. This batch is then melted using a crucible or combustion tube. The melt may be further mixed, after which the melt is cast on (or in) a mold whose temperature is often controlled to avoid cracking during the cooling. The resultant glass is often annealed using a thermal treatment at a temperature near the glass transition to relieve internal stresses that may arise due to differential cooling between, for example, the glass center and its surface. After annealing, the glass is slowly cooled to room temperature. The melting and annealing temperatures depend on the glass composition. For example, pure silica glass melts at ~1700 °C whereas some phosphate and chalcogenide glasses can be melted at temperatures below 950 °C. Non-oxide glasses require melting in an oxygen-free atmosphere to prevent oxidation, which can degrade selected properties. They can be melted under a reactive atmosphere (CCl_4 or SF_6), in a neutral atmosphere (Ar or N_2), or in vacuum, which is typical for the preparation of chalcogenide glasses. Chalcogenide glasses are commonly melted inside a silica tube.

The main issue with the melting process is the preparation of glasses with low concentrations of impurities, such as OH, Fe^{2+}, Fe^{3+}, Cu^{2+}, which can greatly affect transparency. Despite the use of high purity chemicals (99.999% pure or 5 N), purification of the glass batch is usually needed to prepare optical glass with low impurity content. A double distillation method using chlorides and metals has been reported to eliminate impurities such as carbon, oxygen and hydrogen [50]. Another source of impurities is from the crucible used for the melting, even when made of SiO_2, Au or Pt. For example, the melting of chalcogenide glasses in silica tube leads often to the inclusion of Si or SiO_2 particles in the glasses [51]. Hydroxyl, OH, groups can have detrimental impact on various glass properties, especially on the spectroscopic ones as discussed in the **Section 4**. Massera et al. showed a significant reduction in OH content by adding fluorine-based raw materials, such as NH_4F-HF in the batch and melting in O_2-rich atmosphere [52]. To reduce contamination in chalcogenide glasses, the atmosphere in the glove box has a low amount of both O_2 and H_2O (typically < 1 ppm) and the silica tubes are usually etched with HF to remove the surface impurities, washed with distilled water, and dried under vacuum.

Sol-gel methods have been shown to be reliable and low-cost approaches to synthesize multicomponent glasses with high purity, controlled stoichiometry, and chemical homogeneity, all at low-temperatures. A “sol” is defined as a dispersion of colloidal (nano) particles in a liquid whereas a “gel” is a rigid network with interconnected pores and polymeric chains [53]. The sol–gel principle is based on wet-chemical technique typically using organic precursors for gelation. In this process, the precursors are first mixed. Then, water is added for the hydrolysis of the precursors leading to formation of groups that interact to form an amorphous network via a polycondensation process. The hydrolysis and polycondensation can occur simultaneous. The interconnected network is formed due to the hydrolysis and polycondensation of organometallic and silica precursors. The formation of gels is then converted into glasses without melting. The main challenge of this technique is the drying step due to the fracture of the gels caused by the large degree of shrinkage, which creates stress. Sol-gel was first used to prepare silica and silicate glasses due to the moderate reactivity of silicone sources and great efforts were directed to the preparation of silica and silicate glasses and glass-ceramics with good optical transparency using this technique [54]. Since the beginning of the sol–gel technology in the late 1960s [55], many multicomponent glasses in other glass systems have been successfully prepared with sol–gel technique, such as borate and phosphate [56], fluoride [57,58], and chalcogenide glasses [59], just to cite few examples.

Finally, another relatively common alternative approach to prepare optical glasses is sintering compacted powders. The transparency of the resultant glass is governed not only by the shape, size, and size distribution of the glass particles comprising the compact, but also by the temperature, sintering time, pressure, atmosphere, heating and cooling rate, etc. The glass powder should be nanosized for the reduction in the processing temperature and / or time. As the sintering occurs at viscosities of $10^{9\text{-}12}$ Pa.s, transparent glass can only be obtained if the sintering temperature is lower than the crystallization temperature. The sintering atmosphere should be also properly chosen to obtain transparent glasses. Transparent silica glass was successfully obtained by powder sintering [60]. Hot pressing has been also used to prepare glasses and glass-ceramics. Heavy metal oxide (HMO) glasses, which often experience volatilization of constituents during melt processing that lead to compositional variation, have also been explored using hot pressing [61]. Recently, spark plasma sintering (SPS) has been employed to rapidly heat and compress the glassy powder compacts allowing the enhancement of the density (reduction in porosity) while using a reduced sintering temperature. As opposed to the hot-pressing technique, the heating rates used in SPS are very fast and the holding times very short. Over just a few years, transparent oxide, oxyfluoride and chalcogenides glasses and glass-ceramics (GCs) have been successfully prepared using this sintering method [62–65]. Further information about the latest development of SPS to develop optical glass-ceramics can be found in [66].

3.4. Characterization methods

This section highlights some of the common measurements used to characterize glasses.

As it is discussed in more detail elsewhere in this review, glass-ceramics are of great interest for photonic applications. As noted, glass-ceramics are usually prepared by crystallizing a glass. The crystallization needs to be controlled and so the glass transition (T_g) and crystallization (T_p) temperatures are crucial parameters to determine. The temperature difference ($\triangle T$) between the onset of crystallization (T_x) and T_g can be used to determine the suitability of a given glass composition for various hot-forming applications in which the glass needs to be heat-treated above its glass transition temperature to flow. A $\triangle T$ of ~100 K generally suggests that the

glass is a sufficiently good glass former and can then be a candidate for hot-forming as no crystallization is expected to occur during the hot-forming process, such as fiber drawing for example. Differential Scanning Calorimetry (DSC) or Differential Thermal Analysis (DTA) can be used to provide the thermal properties of a glass. These instruments can be used to investigate the thermodynamics and kinetics of crystal nucleation and growth and also to calculate the nucleation rate.

As optical glasses need to be shaped into various forms (e.g., lens, fiber, film, etc), their resistance to shear deformation or, as more commonly stated, their viscosity, needs to be measured. Viscosity is given in units of Poise (P), Pa.s, or $N.s.m^{-2}$. As the viscosity is temperature dependent and varies over >12 orders of magnitude from the practical melting point to the strain point, different instruments are required to measure the viscosity over a wide temperature range (Table 2**)**.

The viscosity curve can provide useful information such as the working point, which corresponds to a viscosity of 10^3 Pa-s and is the temperature where the molten glass can be formed / manipulated. In other words, the viscosity is low enough for some shear processing (e.g., pressing, blowing, etc.) but high enough to retain some shape after shear is removed. The softening point, which is the temperature at which glass will deform under its own weight, corresponds to a viscosity of $10^{6.6}$ Pa-s. Fiber drawing is normally performed near the softening point. Glass manufacturers are interested in the annealing point, corresponding to a viscosity of $\sim 10^{12}$ Pa.s, which is temperature at which the stress can be substantially relieved in a few minutes. The curvature of the viscosity/temperature plot provides useful information about the glass' short-range order. It determines if a glass is "strong" or "fragile." A fragile glass would exhibit a larger degree of curvature in this representation (Fig. 5).

Strong glasses have a higher degree of short-range order with covalent bonds gradually dissociating with increasing temperature whereas fragile glasses possess less defined short-range order with ionic bonds disintegrating rapidly with increasing temperature. Silica glass is one of the least fragile glasses whereas borate and halide glasses are among the most fragile glasses due to their low connectivity network. Germanate, tellurite and phosphate glasses have viscosities and fragilities between those of silica and boric oxide.

Another parameter related to thermal properties is the coefficient of thermal expansion (CTE) of a glass. The CTE is the rate of change in volume with temperature and it should be determined especially when fabricating lenses or core-clad fibers to avoid cracking or stress-optic effects during processing. With few exceptions, the thermal expansion of a glass increases with increasing temperature. Silica glass has a low CTE (6.7×10^{-7}/K) compared to that of phosphate and chalcogenide glasses which range from 7 to 13×10^{-6}/K and 12–22.5×10^{-6}/K, respectively. CTE is typically determined using a push-rod dilatometer. The thermal expansion curve allows the determination of the glass transformation temperature which corresponds to the onset of viscoelastic behavior and of the dilatometric softening temperature which corresponds to the deformation of the glass as the rod sinks into it.

For most photonic applications, the glass should be sufficiently transparent over a given spectral range. Transmittance is measured using a spectrometer often from ultraviolet (UV) to infrared (IR). Absorptions in the UV and visible ranges are often a result of electronic transitions and the optical band gap is due to transition of a valence electron of a network anion to an excited state. Absorptions in the IR region typically are related to impurities such as dissolved gases, bound hydrogen species or vibrational / multiphonon interactions. Absorption bands in the visible can result from the 3d states of transition metal ions or 4f levels of rare earth (lanthanide) ions, as well as metal or semiconductor colloidal particles or optical defects induced by solarization or radiation (see **Section 6**). Changes in the glass composition and so in the structure, changes the transmission properties (Fig. 6).

The refractive index, defined as the ratio of the velocity of light in a vacuum to that in the glass, is typically measured using a refractometer. The refractive index is related to the electron density or polarizability of the ions comprising the constituent compounds. Low refractive indices are expected from glasses composed of low atomic number compounds. Under radiation with intense laser beam, the refractive index, n, can change proportionally to the intensity of the beam, I, through the Kerr Effect, which is expressed as $n = n_0 + n_2 I$, where n_0 is the linear refractive index and n_2 is the nonlinear refractive index. The nonlinear index, n_2, of silica glass is small ($\sim 3 \times 10^{-16}$ cm^2 W^{-1}) whereas chalcogenide glasses have large n_2 (even $>5 \times 10^{-14}$ cm^2 W^{-1}) [69]. The nonlinear properties of glasses are further discussed in **Section 5**. While silica glass has a linear index, n_0, of ~1.458, the use of lead or bismuth, for example, can lead to glasses with indices as high at 2.5, whereas the addition of fluorine can be used to reduce the refractive index [70].

Raman and Fourier-transform infrared (FTIR) spectroscopies have been intensively used to investigate the molecular groups and bonding types in glass. Energy is absorbed exciting the bonds in a molecule to a higher vibrational state. Each molecule produces a different spectrum, akin to a chemical fingerprint. For a vibrational motion to be IR active, the dipole moment of the molecule must change whereas for a transition to be Raman active, there must be a change in polarizability of the molecule. Another difference between FTIR and Raman is their limit of detection: concentration of the species as small as 0.1% can be detected using FTIR whereas the concentration of the species needs to be approximately 1% or greater when using Raman spectroscopy. Consequently, FTIR spectroscopy has been used to detect impurities in optical glass such as OH groups with a typical broad absorption band in the 2000–4000 cm^{-1} range. Readers are referred to the recent reviews on the use of FTIR and Raman spectroscopies to analyze glasses [71,72]. Nuclear magnetic resonance (NMR) is another common technique used to investigate the structure of glass as it is element-

Table 2
Most common methods to measure the glass viscosity.

Range	Method	Viscosity Values (Pa.s)
Melting	Rotation	$< 10^4$
	Falling sphere	$< 10^6$
Softening and annealing	Parallel plate	10^5 to 10^9
	Beam-bending	10^7 to 10^{12}

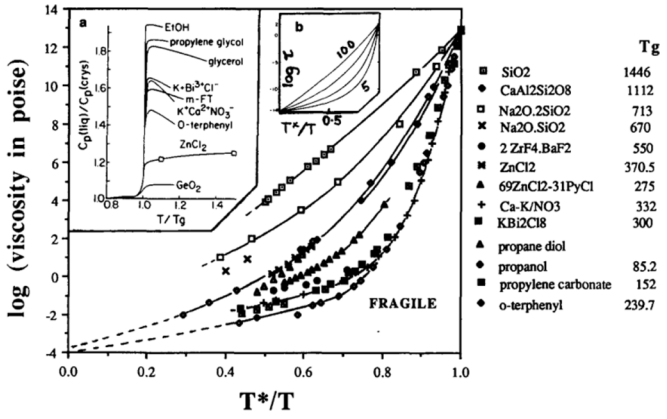

Fig. 5. Viscosity as a function of scaled temperature (T*/T), (T* being the temperature at which the shear viscosity reaches 10^{12} Pa.s), illustrating Angell's strong fragile classification. (Reproduced from Ref. [67] with permission from Elsevier).

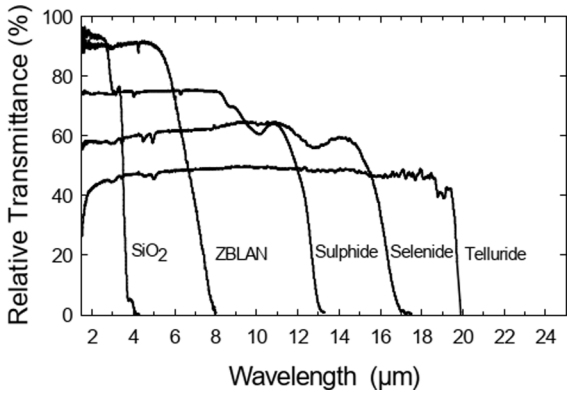

Fig. 6. Transmission spectra for several glasses (thickness of about 2–3 mm) (Reproduced from Ref. [68] under the terms of the Open Access Publishing Agreement).

specific. In this technique, the atomic nuclei in a strong constant magnetic field produce an electromagnetic signal when perturbed by a weak magnetic oscillator field. NMR provides information about short to medium-range order; the network modifier cation-oxygen distances and coordination numbers (short-range order), network former connectivity and network modifier distance distributions (intermediate-range order), and ring-size statistics (medium-range order). A review of the benefits and challenges of using NMR to analyze glasses can be found in [73].

X-ray diffraction (XRD) analysis has been commonly used to confirm the production of amorphous materials or the presence of crystals in glass-ceramics for example. Using XRD, all issues related to the crystal structure of solids, including lattice constants and atomic arrangement, identification of unknown materials, orientation of single crystals, preferred orientation of polycrystals, defects, stresses, etc. can be investigated. The interaction of the incident rays with the sample produces constructive interference when conditions satisfy Bragg's Law, $n\lambda = 2d\sin\theta$, where d is the spacing between atomic planes in the crystalline phase, n is the diffraction order and λ is the X-ray wavelength. This law allows one to characterize the formation and structure of the crystalline phases precipitating in glass during thermal or radiation treatments. The crystallite size, t, can then be estimated using the Scherrer's equation, $t = K\lambda/\beta\cos\theta$, where K is a dimensionless shape factor, with a value close to 0.9, and β is the full width at half maximum of the X-ray diffraction peak in radians.

Scanning electron microscopy (SEM), coupled with image analysis techniques, has played an important role in the development of glasses and glass-ceramics as it can provide morphology and compositional information on bulk, fiber, film, etc., and powder samples as well as the distribution of crystals in glass-ceramics, for example. When coupled with Energy Dispersive X-ray Spectroscopy (EDS), it can be used for composition analysis. As a complementary tool to image the sample with higher resolution, a transmission electron microscope (TEM) can be used. The high resolution is obtained using localized electron beam due to small de Broglie wavelength of the electron. Example of SEM and TEM images of crystals and metallic nanoparticles in glasses are presented in the **Section 4**.

As glasses typically are brittle, it is also important to measure their mechanical properties, the most common ones being the fracture strength, elastic modulus, and hardness. The fracture strength of a glass is given by the force that must be applied to overcome the maximum restorative force and describes the resistance of the glass to the propagation of flaw. The fracture strength can be measured using linear elastic fracture mechanics (LEFM) method. The elastic modulus is determined using a bending test, from the slope and

maximum stress values of the load versus displacement graph. It is typically from 10 to 200 GPa for glasses, arising from the changes in the distance between the atoms induced by the applied force. The hardness of glasses is usually defined in terms of either the scratch hardness using the Mohs scale, or indentation hardness using a Vickers indenter. The Vickers hardness of oxide glasses is between 2 and 8 MPa, silicate glasses being harder than borate, germanate, phosphate glasses whereas the chalcogenide glasses are soft glasses [74].

In summary, the thermal, physical, optical, structural, and mechanical properties of a glass should be measured systematically as they are strongly dependent on the glass composition. They serve as a basis for comparison, selection, and quality assurance of glass-based materials.

4. Luminescent glasses

The rare-earth (RE) ions comprise the fifteen lanthanoid elements of the periodic table, plus scandium and yttrium. The lanthanides are mostly used for their luminescent properties, except promethium because it does not have a stable form naturally, as well as scandium and yttrium due to their lack of luminescent properties. The RE electronic configuration is $[Xe]4f^n5d^16s^2$, where [Xe] is the electronic configuration for Xenon and *n is* the number of electrons in the f shell, varying from 0 (La) to 14 (Lu). The atomic number of the lanthanide elements range from 57 (Lanthanum) to 71 (Lutetium), along with Scandium (Sc, Z = 21) and Yttrium (Y, Z = 39). During ionization to form the typically stable trivalent form, 2 electrons of the 6 s shell and one electron of the 4f shell are removed leading to partially filled 4f shell, whose electrons are electrostatically shielded by the outer-lying $5s^2$ and $5p^6$ electrons. A few of the RE ions can be found in or converted to divalent and tetravalent oxidation states, for example (Eu^{2+}, Yb^{2+} and Sm^{2+}) and (Ce^{4+}, Pr^{4+} and Tb^{4+}), respectively [75]. Because of their favorable energy level structure, RE ions can be used to produce emission across much of the visible region and into the NIR, depending on the RE (Table 3).

4.1. Principle

This section provides a brief overview of RE ions' electronic structure and the processes involved in electron transitions between energy levels. In-depth descriptions of RE optical properties can be found in references [76,77].

4.1.1. Energy levels diagram

Light emissions from RE ions originate from intra-configurational ($4f^n \rightarrow 4f^n$) or inter-configurational ($4f^{n-1}5d^1 \rightarrow 4f^n$) electronic transitions leading to spectral band coverage from the ultraviolet (UV) to the infrared (IR), depending on the rare earth, the specific transition, and the host material. For example, UV light emission is obtained from Ce^{3+} doped fluorides due to the $4f^05d^1 \rightarrow 4f^1$

Table 3
Common emissions from rare earth (RE) species.

Rare-earth ions	Transition and corresponding emission	Rare-earth ions	Transition and corresponding emission
Ce^{3+}	5d → 4f – 338 nm & 662 nm	Tb^{3+}	$^5D_3 \rightarrow {}^7F_5$ – 415 nm $^5D_3 \rightarrow {}^7F_4$ – 440 nm $^5D_3 \rightarrow {}^7F_3$ – 460 nm $^5D_4 \rightarrow {}^7F_6$ – 488 nm $^5D_4 \rightarrow {}^7F_5$ – 545 nm $^5D_4 \rightarrow {}^7F_4$ – 585 nm $^5D_4 \rightarrow {}^7F_3$ – 620 nm
Pr^{3+}	$^1S_0 \rightarrow {}^1I_6$ – 420 nm $^3P_0 \rightarrow {}^3H_4$ – 515 nm $^1D_2 \rightarrow {}^3H_4$ – 630 nm $^3P_0 \rightarrow {}^3F_2$ – 670 nm $^3P_0 \rightarrow {}^3F_4$ – 770 nm $^1G_4 \rightarrow {}^3H_5$ – 1300 nm $^1D_2 \rightarrow {}^1G_4$ – 1470 nm $^3F_{4,3} \rightarrow {}^3H_4$ – 1600 nm	Dy^{3+}	$^4F_{9/2} \rightarrow {}^6H_{15/2}$ – 490 nm $^4F_{9/2} \rightarrow {}^6H_{13/2}$ – 575 nm $^4F_{9/2} \rightarrow {}^6H_{11/2}$ – 665 nm
Nd^{3+}	$^4D_{3/2} \rightarrow {}^4I_{13/2}$ – 395 nm $^2P_{3/2} \rightarrow {}^4I_{15/2}$ – 470 nm $^4F_{3/2} \rightarrow {}^4I_{9/2}$ – 900 nm $^4F_{3/2} \rightarrow {}^4I_{11/2}$ – 1060 nm $^4F_{3/2} \rightarrow {}^4I_{13/2}$ – 1345 nm	Ho^{3+}	$^5F_3 \rightarrow {}^5I_8$ – 490 nm $^5S_2$, $^5F_4 \rightarrow {}^5I_8$ – 550 nm $^5F_3 \rightarrow {}^5I_8$; $^5F_3 \rightarrow {}^5I_7$ – 660 nm
Sm^{3+}	$^4G_{5/2} \rightarrow {}^6H_{5/2}$ – 565 nm $^4G_{5/2} \rightarrow {}^6H_{7/2}$ – 600 nm $^4G_{5/2} \rightarrow {}^6H_{9/2}$ – 650 nm $^4G_{5/2} \rightarrow {}^6H_{11/2}$ – 705 nm	Er^{3+}	$^4H_{11/2} \rightarrow {}^4I_{15/2}$ – 530 nm $^4S_{3/2} \rightarrow {}^4I_{15/2}$ – 550 nm $^4F_{9/2} \rightarrow {}^4I_{15/2}$ – 670 nm $^4S_{3/2} \rightarrow {}^4I_{13/2}$ – 850 nm $^4I_{13/2} \rightarrow {}^4I_{15/2}$ – 1540 nm
Eu^{3+}	$^5D_0 \rightarrow {}^7F_0$ – 580 nm $^5D_0 \rightarrow {}^7F_1$ – 590 nm $^5D_0 \rightarrow {}^7F_2$ – 615 nm $^5D_0 \rightarrow {}^7F_3$ – 650 nm $^5D_0 \rightarrow {}^7F_4$ – 700 nm	Tm^{3+}	$^1G_4 \rightarrow {}^3H_6$ – 480 nm $^1G_4 \rightarrow {}^3F_4$ – 650 nm $^1H_4 \rightarrow {}^3H_6$ – 800 nm
Gd^{3+}	$^6P_{7/2} \rightarrow {}^8S_{7/2}$ – 310 nm	Yb^{3+}	$^5F_{5/2} \rightarrow {}^5F_{7/2}$ – 1020 nm

transition [78], whereas the same transition leads to red emission when emitting from Ce^{3+} doped nitrides [79]. The line shape and the linewidth of the corresponding spectral emission may vary significantly. The 4*f* wave functions lie within the closed $5s^25p^6$ xenon shell. Due to screening, the electrons of the 4*f* shell have weak interaction with the host. The energy level scheme with the splitting induced by the different interactions is shown in Fig. 7.

The Hamiltonian of the RE ions in bulk material can then be described as [76] $H = H_0 + H_{el} + H_{SO} + H_{CF}$ where (1) H_0 describes the interaction between the nucleus and the electron together with the electron kinetic energy, (2) H_{el} considers the electrostatic interaction (repulsion) between electrons. The 4*f* configuration becomes decomposed in states labelled ^{2S+1}L where *S* and *L* are the sum vectors for the spin and the orbital quantum numbers respectively, for the 4*f* layer electrons, (3) H_{SO} is related to the spin–orbit interaction, leading to $^{2S+1}L_J$ multiplets, where *J* is the total angular momentum, i.e., the vectoral sum of *L* and *S* (Russell-Saunders or *LS* coupling). The host influence is weak, leading the *J* multiplets to split into Stark components, typically separated by 10–100 cm^{-1} (in comparison, SO states are separated by 1000–10,000 cm^{-1}). The degeneracy strongly depends on the site symmetry. The position of the Stark levels depends on the covalent nature of the RE-host interaction (i.e., partial distribution of the RE electron density on the surrounding atoms, similar to that of oxygen atoms in oxide materials). However, this effect, known as the **nephelauxetic effect**, is more pronounced for the 5*d* electrons because there is no screening from the closed $5s^25p^6$ shell, contrary to what occurs with electrons in the 4*f* shell, and (4) H_{CF} represents the interaction between the RE ions and the host. In the case of 4f-4f transitions, $H_{CF} < H_{SO}$ due to the screening of the 4f electrons by the 5s and 5p electrons. In the case of 5d-4f transitions, $H_{SO} < H_{CF}$.

4.1.2. Dipole transitions

Two types of dipole transition can occur between two electronic states: electric and magnetic dipole transitions. Except for a few specific transitions, such as $^4I_{13/2} \rightarrow {}^4I_{15/2}$ for Er^{3+}, the magnetic dipole transitions are several orders of magnitude weaker than electric dipole transitions and will not be covered in this section [80].

The line strength, $S_{a,b}$, of a transition between states *a* and *b* is given by $S_{a,b} = \sum_{i,j}\left|\langle b_j|D|a_i\rangle^2\right|$, where *D* is the electric dipole interaction operator and i,j, are the designations for the respective initial and final transition levels. Although the electric dipole transitions are forbidden due to the selection rules (no transitions between states of same parity), these transitions are allowed as the crystal field combines ("admixes") *5d* states (of opposite parity) with the *4f* states. The oscillator strength *f* is expressed as $f_{a,b} = \frac{8\pi^2 m\nu}{he^2}\frac{\chi_L}{n}\frac{1}{g_a}S_{a,b}$ where *h* is the Planck's constant, *n* is the refractive index of host refraction, ν is the mean photon frequency, g_a is the degeneracy of the initial state *a* ($g_a = 2J_a + 1$), *m* and *e* are the electron mass and charge and χ_L is the local field correction. The local field correction occurs due to different polarizability between the host and the ion and can be expressed as the following for the electric dipole transitions $\chi_L = \left(\frac{n^2+2}{3}\right)^2$. For RE ions, the oscillator strength is typically on the order of $\sim 10^{-6}$ (it is ~1 for allowed transitions).

4.1.3. Broadening of emission / absorption bands

As the energy state lifetime is finite ($\triangle E \triangle t \geq \hbar$, Heisenberg uncertainty principle) and as the interaction between the RE ions and their environment is very specific, the emission / absorption band can be described by a **Lorentzian function**. The homogeneous broadening of the emission / absorption band, which is mainly due to the ion-phonon interaction dominant mechanism, varies with temperature T as follows: (1) for $T \gg T_{Debye}$ (10–20 K), Raman processes, which can be described as a two-phonon mechanism, are predominant, and the homogeneous linewidth varies as T^2. (2) for $T < 10\,K$, the dependence follows the T^α power law with $\alpha = 1$–2 in glasses as reported in [81]. This behavior is different from that of a crystal and is explained in the framework of the Two-Level State model [82]. Homogeneous linewidth is typically ten times larger in glasses than it is in crystals. (3) The inhomogeneous broadening is due to site-to-site variation of the crystal field modifying the Stark splitting (see H_{CF} splitting in Fig. 7) and also the optical transitions strength. The overall transitions can then be described using a Gaussian function. As opposed to the homogenous broadening, the inhomogeneous broadening does not depend on temperature. (4) Homogeneous and inhomogeneous broadenings have comparable values (about 10–100 cm^{-1}) at room temperature. The transitions line shape can then be described by a Voigt function, the convolution of a Gaussian and Lorentzian function.

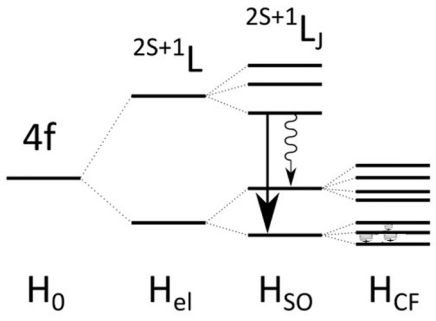

Fig. 7. Energy levels diagram of a RE ion in bulk material, the straight arrow shows radiative transition between $^{2S+1}L_J$ levels; the wavy arrows correspond to non-radiative transitions that may occur between $^{2S+1}L_J$ Stark levels.

4.1.4. Radiative and non-radiative lifetimes

Fluorescence and phosphorescence are two light re-emission mechanisms which differ by their emission lifetime values: fluorescence re-emission lifetime is shorter (ns or μs) whereas phosphorescence emission lifetime is longer (>ms). The fluorescence lifetime (τ) of a level depends on both the radiative (τ_r) and non-radiative (τ_{nr}) lifetimes as $\frac{1}{\tau} = \frac{1}{\tau_r} + \frac{1}{\tau_{nr}}$. More specifically, the τ_r radiative lifetime is expressed as $\frac{1}{\tau_r} = A_{a,b}$, where the Einstein $A_{a,b}$ coefficient accounts for the spontaneous transition rate from energy level a to energy level b, it relates to the oscillator strength $f_{a,b}$, $f_{a,b} = 4\pi\epsilon_0 \frac{mc^2}{8\pi^2 ne^2\nu^2} \frac{1}{\chi_L} A_{a,b}$. The τ_{nr} non-radiative lifetime component is due to the interaction of the RE with the vibration states of the host and occurs within the Stark levels where the energy differences between sub-levels are small. Stark level populations are thus mainly governed by Boltzmann statistics, with the non-radiative rate W_{nr} expressed as $\frac{1}{\tau_{nr}} = W_{nr} = W_0 exp(-\alpha(\Delta E) - 2E_p)$, where W_0 and α are characteristic constants of the host material, $\triangle E$ is the energy difference between the two levels where the transition occurs and E_p is the highest phonon energy. Both radiative and non-radiative lifetimes depend on macroscopic properties of the glass such as its refractive index and phonon energy. The phonon energy, which depends on the host material, impacts the radiative and non-radiative nature of the transition. For example, the transition from the $^3H_4$ level of Tm^{3+} is 98% non-radiative in silica, which exhibits a (maximum) phonon energy of ~1100 cm^{-1}. In a fluoride glass, this same transition is close to 100% radiative since fluorides typically possess phonon energies on the order of ~550 cm^{-1}.The variation in the radiative lifetime of the Eu^{3+} ion in Y_2O_3 nanocrystals, taken as an example, as a function of n is illustrated in Fig. 8 [83]. Fig. 8 clearly shows that, despite the Eu^{3+} ions are embedded in nanocrystals, the radiative lifetime increases with the decrease of the host refractive index.

For particles embedded in glass (material considered as heterogeneous), the effective medium approximation model introduces an effective dielectric permittivity ε_{eff} or effective refractive index, $n_{eff.}$ which is the average of individual dielectric permittivities. This approximation is valid only while the material is considered homogeneous at the optical wavelength scale. Typically, nanoparticles should be smaller than $\lambda/4$ (quasi-static approximation) and of sufficient number to consider the material as homogeneous [84]. A variety of models enable calculation of ε_{eff} *(or* n_{eff}*)* for specific composite geometries such as the Maxwell-Garnett geometry which can be used for small particles inclusion in a host material, and the Bruggeman geometry in which the material is seen as two interconnected phases (spinodal decomposition) with one phase containing the RE element. The effect of the local-field on the spontaneous emission rate *A,* or the radiative fluorescence lifetime τ_{loc} ($A = 1/\tau_{loc}$) of a luminescent ion is $\tau_{\mathrm{loc}} = \frac{1}{n_{\mathrm{eff}}} \left(\frac{3}{n_{\mathrm{eff}}^2 + 2} \right)^2 \tau_{\mathrm{vac}}$. where τ_{vac} is the radiative lifetime of the luminescent ion in vacuum, and n_{eff} is the effective refractive index. An example of the dependence of relaxation time between the two lowest $^5F_5$ sublevels of Ho^{3+} in LaF_3 nanocrystals embedded in a silicate host with the size of nanocrystal was reported in [85] (Fig. 9**a**). When particle size reaches 25 nm, the relaxation time is near that expected for the LaF_3 single crystal (Fig. 9**b**).

4.1.5. Energy transfer

When the concentration of RE ions is large, RE ion can interact with any other RE ions, or with any additional ion which has energy transfer resonant with its own transition. This ion-ion interaction occurs when the average distance between two ions is on the order of one nanometer, i.e., a concentration of about 10^{27} atoms/m^{-3} for a homogeneous distribution [86]. For the energy transfer to occur, a resonance between a pair of energy levels of a so-called donor ion and that of a so-called acceptor ion is required. There are three kinds of transfers, as illustrated in Fig. 10 in the case of atoms with two energy levels.

(1) ***Radiative resonant transfer*** can be defined as the emission of a photon by the donor ion, which is absorbed by the acceptor. The probability of radiative resonant energy transfer between the donor ion and the acceptor ion can be written as $P_{DA} = \frac{\sigma_A}{4\pi R^2 \tau_D} \int g_D(\nu) g_A(\nu) \delta\nu$ where τ_D is the lifetime of the donor ion, σ_A is the integrated absorption cross-section of the acceptor ion and the integral represent the spectral overlap between the emission spectrum of the donor ion and the absorption spectrum of the

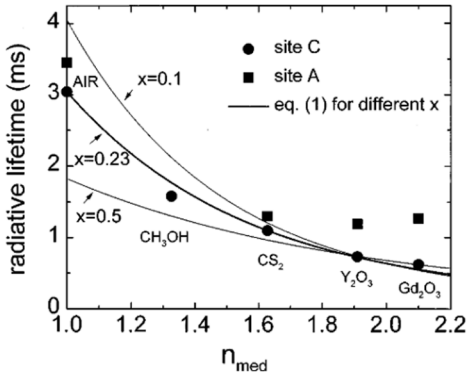

Fig. 8. The dependence of $^5D_0$ radiative lifetime for the Eu^{3+} ion in Y_2O_3 nanoparticles (C and A sites) on the refraction index (n_{med}) of media surrounding the particles at T = 295 K. Solid lines represent fits for nanocrystalline samples (Eu^{3+} in site C) with different filling factors (x). (Reproduced from Ref. [83] with permission from American Physical Society).

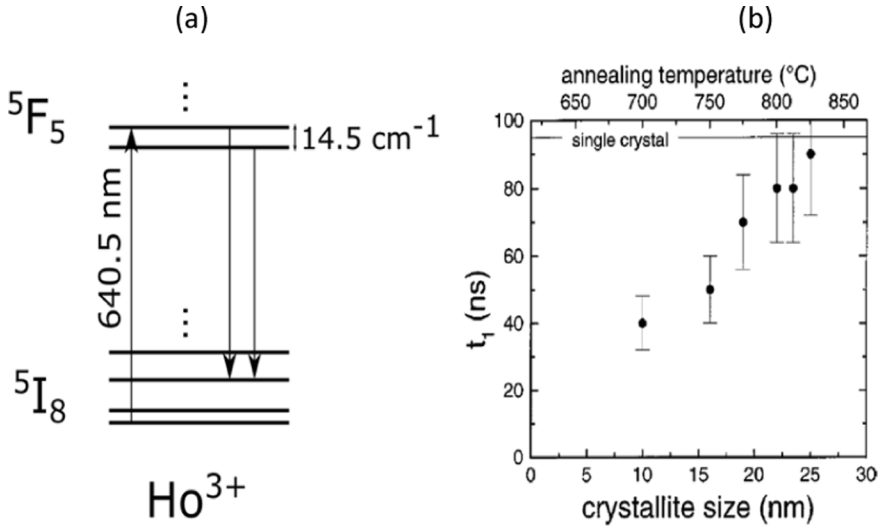

Fig. 9. (a) Energy level diagram of Ho^{3+} ions, with only first sublevels of $^5I_8$ and $^5F_5$ manifolds represented. (b) Relaxation time t_1 between the two lowest $^5F_5$ state sublevels of Ho^{3+}. Solid line: the relaxation time value for LaF_3 single crystal. (Reproduced from Ref. [85] with permission from American Physical Society).

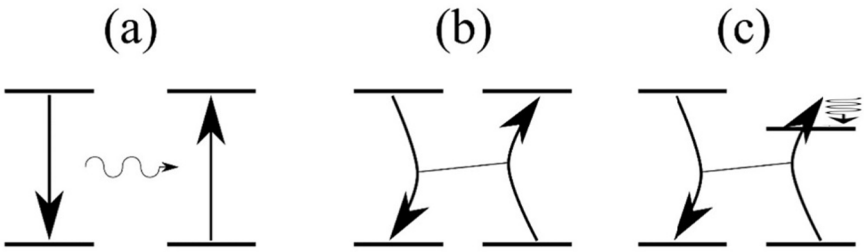

Fig. 10. Three main energy transfer mechanisms between RE ions: (a) radiative resonant, (b) non radiative resonant, (c) non-resonant non-radiative.

acceptor ion, assuming that $\int g_D(\nu)\delta\nu = 1$ and $\int g_A(\nu)\delta\nu = 1$. This type of transfer can take place over long distances and can lead to energy migration or radiation trapping which has the effect of increasing the lifetime of the donor ion.

(2) ***The non-radiative resonant transfer*** corresponds to the exchange of energy between the donor and acceptor ions without emission of a photon. The two ions are coupled by a Coulomb interaction of the Van der Walls type. This multipolar interaction can be expressed as $P_{DA} = \frac{(R_0/R)^s}{\tau_D}$ where s = 6, 8, 10 for dipole–dipole, dipole-quadrupole and quadrupole–quadrupole type electrical interactions, respectively, τ_D is the lifetime of the donor ion (without ion A), R_0 is the critical distance for which τ_D is halved with the presence of an A ion.

(3) ***The non-resonant non-radiative transfer*** corresponds to an exchange of energy with emission or absorption of several phonons to compensate for the non-resonance between the energy levels of the donor and acceptor ions.

If the donor ion has three energy levels separated by the same energy gap, the highest energy level can then be excited towards the intermediate level by transferring its energy to the acceptor ion. This mechanism is called cross-relaxation. This effect causes the luminescence extinction of the donor ion at high concentration and is manifested by a reduction in the luminescence lifetime of the level considered. The previous mechanism leads to a Stokes emission of the acceptor ion, i.e., to an energy emission lower than that of the high level of the donor ion. However, such an energy transfer can take place several times and lead to anti-Stokes emissions. This effect has been called Addition de Photons par Transfert d'Energie (APTE). Cooperative sensitization consists of the simultaneous de-excitation of two donor ions to excite an acceptor ion. Cooperative luminescence results from the same deexcitation of two donor ions simultaneously but to excite a virtual level as in the case of Yb^{3+} to yield a green emission.

4.2. Common applications of luminescent glasses

Lighting: Due to their ability to emit in the visible, RE ions have been useful for the development of lighting systems. Currently, lighting systems such as white-light LEDs (wLEDs) consist of a blue-emitting LED (InGaN) and a layer of $Y_3Al_5O_{12}:Ce^{3+}$ converting part

of the blue radiation into yellow, the combination of the two colors producing white [87]. However, such a combination emits a weak red emission which limits color-rendering. In addition, the phosphors are mixed in a resin whose thermal properties and chemical stability can have long-term disadvantages. Glasses doped with rare earth ions then present a very interesting alternative. White emission can be obtained by doping with one, two or three rare earths, involving either down-conversion or up-conversion processes [88]. The Dy^{3+} ion has been particularly well studied for white light emission because it emits blue and yellow-orange following an excitation around 450 nm [89]. The Eu^{2+} ion represents an alternative for single doped white light sources. By varying its concentration, its emission wavelength can vary from cyan to yellowish-green and thus provide white light when combined with a 385 nm UV LED or a 450 nm blue LED [90]. In the case of co-doping with two REs, the activator ion is used for its own emission and to excite another ion through energy transfer. For white light sources, the activator ion often is Dy^{3+} co-doped with Eu^{3+} or Tm^{3+}. Co-doping with Eu^{3+} makes it possible to add an emission in the red spectrum [91]. Tm^{3+} ion is incorporated to increase the blue emission intensity whereas the Dy^{3+} ion emits a strong intensity in the yellow [92]. Another activator ion of interest is Ce^{3+} which can be co-doped with Dy^{3+} [93], Sm^{3+} [94] or Tb^{3+} [95]. Triply-doped materials can selectively emit blue, green and red, and were studied as early as 1991 in a borate glass doped with Ce^{3+} (blue), Tb^{3+} (green) and Mn^{2+} (red) [96]. At that time, the interest was for low pressure mercury vapor lamps emitting at a wavelength of 254 nm. More recently, other rare earth ion pairs have been reported for wLEDs such as $Tm^{3+}/Tb^{3+}/Eu^{3+}$ in an aluminoborate glass [97], $Tm^{3+}/Tb^{3+}/Sm^{3+}$ in a phosphate glass [98], and $Ce^{3+}/Dy^{3+}/Eu^{3+}$ in a borosilicate glass [99]. The generation of white light can also be obtained by using a diode emitting at 980 nm [100] and exploiting up-conversion mechanisms. The Yb^{3+} ion is mainly used to absorb this irradiation and transfer its energy to other rare earth ions capable of emitting blue, green and red.

Laser glasses: The first glass laser, reported in 1961, was based on a Nd^{3+} doped barium silicate glass [18]. To be used as high-power laser amplifiers, the glass must exhibit low optical nonlinearity and a high threshold for optical damage [101]. For example, glasses within the P_2O_5-Al_2O_3-M_2O-MO system (M_2O = K_2O or a mixture of alkali oxides, MO = alkaline earth oxide) have been used for high-peak-power laser application, especially the commercial glasses LG-770 (58-62P_2O_5-6-10Al_2O_3-20-25K_2O-5-10MgO-0-2Nd_2O_3 Schott Glass Technologies) and LHG-8 (55-60P_2O_5-8-12Al_2O_3-13-17K_2O-10-15BaO-0-2Nd_2O_3, Hoya Corporation), which are used in installations such as the Laser MégaJoule (LMJ, France) and the National Ignition Facility (NIF, USA) [102].

Scintillator glass: Scintillators are materials that emit visible light when subjected to ionizing radiation such as alpha or beta particles, electrons, neutrons, x-rays or gamma-rays [103]. They are used in many fields such as high energy physics [104], medicine and health [105], or microscopy [106]. Initially, ionizing radiation of energy much higher than the bandgap of the material creates electrons in the conduction band (and holes in the valence band). Then, in the "thermalization" stage, these electrons interact with the other atoms of the host thereby losing energy, until they have an energy approximately the same as the bottom of the conduction band (and the holes thermalize to the top of the valence band). The electrons and holes can then recombine directly (intrinsic luminescence) or through a luminescent center, which is generally an impurity or dopant (extrinsic luminescence). Compared to the single crystals generally used, glasses can be prepared with low-cost and large-volume production with various shapes (e.g., rods, fibers, discs, etc.) while providing high optical transparency. Their chemical durability can also be an advantage over common crystalline scintillators. As an example, for neutron detection, a ^{6}Li aluminosilicate glass scintillator is preferred to a ^{6}LiI crystal because iodides are deliquescent [107]. On the other hand, glasses can contain a large number of defects (intrinsic or induced by the irradiation) constituting many traps for the electrons or holes, which can delay radiative recombination or degrade the luminescence yield. Trivalent cerium

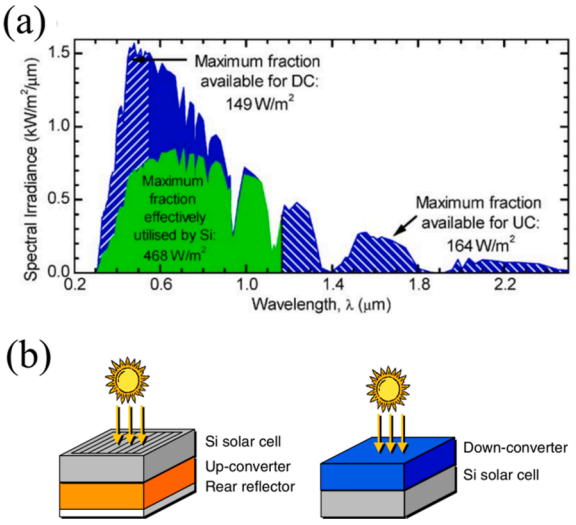

Fig. 11. (a) Regions of the solar spectrum that can be used in a solar cell trough Down-conversion (DC) and Up-conversion (UC) (blue with lines). The fraction absorbed by a thick solar silicon device is shown in green. (b) Examples of a solar cell with an UC layer placed at the rear (left) and a DC layer placed at the front (right). (Reproduced from Ref. [112] with permission from Elsevier). (For interpretation of the references to color in this figure legend, the reader is referred to the web version of this article.)

(Ce^{3+}) ion often is used as an emitting center because it has a visible emission suitable for commonly used detectors and exhibits a fluorescence lifetime of a few tens of ns (5d-4f transition), favoring a fast detector response for high frequency applications. Eu^{2+} ion is considered an alternative ion because its blue emission results from a 5d-4f transition whose lifetime is longer, on the order of a few microseconds, than that of Ce^{3+} [108]. To increase the emission yield, it has been proposed to co-dope with the Gd^{3+} ion in concentrations of the order of 20 mol% to promote the transfer of energy towards the emitting center [109].

Solar cell concentrators: In the context of sustainable development, renewable energy sources are very popular. This is particularly the case with solar energy using solar cells to convert the sunlight into electricity. Solar cells are made of semiconductor materials. One of the fundamental limitations to the conversion of solar radiation is based on the poor overlap between the solar spectrum and the energy bandgap of the semiconductor. In the case of c-Si, the bandgap energy is 1.1 eV. Thus, photons having a wavelength >1127 nm are not absorbed (Fig. 11**a**). Similarly, photons with an energy twice greater than the gap (2.2 eV or 560 nm) have sufficient energy to sufficiently excite electrons that thermalization mechanisms (loss of energy by interaction with other electrons) lead to heating. To increase the optical-to-electronic efficiency of photovoltaic (PV) cells, it has therefore been proposed to convert IR and UV photons into wavelengths that can be properly absorbed by the c-Si to generate electricity. From this point of view, the use of rare earth ions has proven to be particularly interesting due to the mechanisms of frequency conversion: up-conversion (converts IR photons to visible photons) and down-conversion (converts UV photons to visible photons) [110,111]. The rare-earth doped layer allowing the down-conversion is placed above (between the solar radiation and the c-Si) while the up-conversion layer is placed below, a reflective layer making it possible to return photons to c-Si film (Fig. 11**b).**

To promote energy transfer, an alternative approach consists of preparing glass-ceramics to enhance the spectroscopic performance of the rare earth ions via its insertion into the nanocrystalline phase. The use of rare earth doped glasses is less common for the up-conversion layer. The main limitation arises from the fact that up-conversion generally requires high powers. $NaYF_4:Er^{3+}$ was the first phosphor proposed to improve the yield of Si cells by up-conversion [113]. More recently, the Ho^{3+}/Yb^{3+} pair was studied in a fluoroindate glass [114]. An improvement in the generation of electron-hole pairs has been observed but using a 1000 sun solar concentrator.

Taggants: Due to their rich energy level diagrams, all rare-earth ions can be excited in the UV and emit their characteristics emission spectra with small emission linewidths, limiting potential overlap. Given the low cost of manufacture and the ease of synthesis, glasses doped with rare earth ions are of interest for the development of tags for the field of security, in particular as markers to fight against counterfeiting. Rare-earth ions of particular interest for taggants are Ce^{3+}, Tm^{3+}, Tb^{3+} and Dy^{3+}, which emit cyan, blue, green and red colors, respectively. For example, an assembly of different glasses in multi-layers made it possible to obtain a microbarcode [115]. RE-doped alkaline earth aluminosilicate glasses were stacked to form a preform, each layer of glass corresponding to a specific color through the appropriate RE doping. This preform was then drawn into fiber and cut to obtain microbarcodes of 20x100 μm. Each microbarcode is defined by the order of the colors (Fig. 12**a**).

Recently, an $Ho^{3+}/Tm^{3+}/Yb^{3+}$ doped tellurite glass has been studied [117]. A 973 nm wavelength laser excites the Yb^{3+} ions leading to excitation of the Tm^{3+} and Ho^{3+} ions by up-conversion and so to emission in the visible (blue and red for Tm^{3+}, green and red for Ho^{3+}). This up-conversion process, requiring 2- or 3-photons to promote step-wise excitation, depends very strongly on the excitation power. Thus, by keeping the same laser power, but displacing the glass, it is possible to vary the excitation density locally (by defocusing the laser beam) resulting in a modification of the color of the glass which is a feature of the glass composition (Fig. 12**b**).

Data storage devices: Modulation of the emission intensity of rare earth ions is the basis of optical data storage applications. One study looked at europium or dysprosium-doped tungsten phosphate glasses [118]. By irradiating these glasses with a 473 nm laser, a decrease in transmission was observed in the visible – NIR range. This is attributed to a change in valence of Sb and W ions according to the reactions $Sb^{3+} + hv \rightarrow Sb^{5+} + 2e^-$ and $W^{6+} + hv + e^- \rightarrow W^{5+}$, where hv is the photon energy. The photochromism of the glass is attributed to the generation of W^{5+}. Under excitation with an Xe lamp at 465 nm, the Eu^{3+} doped glass emits in the red with more or less intensity depending on the photochromic effect locally induced by the laser at 473 nm. It is thus possible to store information.

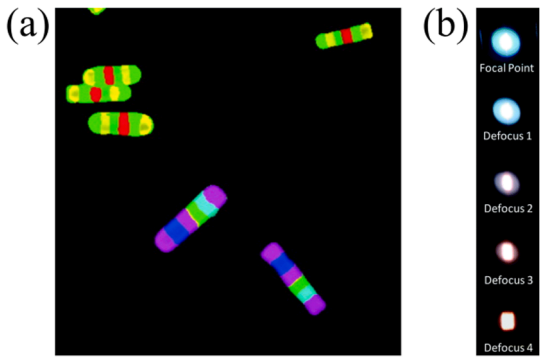

Fig. 12. (a) Images of the RE-doped microbarcodes under an UV excitation and observed with a 420-nm long pass filter (Reproduced from Ref. [115] with permission from National Academy of Sciences). (b) Image of the $Ho^{3+}/Tm^{3+}/Yb^{3+}$ doped tellurite glass excited by a NIR laser at different focal point (defocused positions are recorded by placing the samples at 2, 4, 6 and 8 cm intervals from the focal point of the laser beam) (Reproduced from Ref. [116] with permission from Royal Society of Chemistry).

Heating to 300 °C then resets the glass (Fig. 13).

4.3. Recent research trends and future directions in luminescent glasses

Effort worldwide has been focused, for the past few decades, on the development of glasses with enhanced spectroscopic properties. While silica is the most technologically important glass, its solubility for RE ions is low leading to the formation of highly doped clusters in the glass. A representative study on the local environment, distribution and clustering of Eu^{3+} behavior in silica glasses, as an example, can be found in [119]. These RE clusters form in silica glass due to the relative mismatch in size and valence between the RE and the Si as well as the rigidity of the silica network. Such clusters lead to the deterioration of the spectroscopic properties, most commonly concentration quenching. Indeed, the probability of an excited RE ions to reach a defect site is increased when clusters are formed due to the higher probability of energy transfer between two excited neighboring RE ions and/or energy migration between excited and non-excited ions. The maximum concentration of RE which can be incorporated in silica glass without forming clusters can be as low as 0.1 mol%. Thus, one of the goals has been to prevent RE clustering in silica glass. For example, the addition of Al_2O_3 and/or P_2O_5 in silica glass can be used to prevent the RE clustering [120]. A "solvation shell" around the RE is expected to form when adding Al or P [121]. As explained recently in [122], the presence of Al and P in the silica network can be used to increase the Yb^{3+} asymmetry degree and so the intensity of the emission at ~1 μm in silicate glasses. Multicomponent silicate and phosphate glasses are well-known glasses to accommodate high RE concentration (up to 10^{21} ions/cm^3) without luminescence quenching [123]. Alkali and alkaline-earth ions can be added into both glass types with changes in the RE emission linewidth due to such alkali and alkaline-earth additions, as reported for Tm^{3+} [124], Yb^{3+} [125] and Er^{3+} [126]. For example, Sun et al. reported a 57% enhancement in the absorption and emission cross-sections of Yb^{3+} when adding Li^+, Mg^{2+} or Ca^{2+} into silicate glasses due to changes in electronegativity and covalency [125]. In phosphate glasses, BaO can promote a more depolymerized network, resulting in better luminescence efficiency than when smaller dopants such as MgO and CaO were employed [127]. The crystal field can also be changed by doping with highly polarizable ions. For example, the addition of Pb^{2+} in a glass matrix creates Pb-O bonds and can result in an enhancement of the spectroscopic properties, such as that reported in lead silicate glass doped with Ho^{3+} [128] and with Er^{3+} [129]. Borate glass have also been studied with modifiers such as ZnO, Li_2O, and K_2O added in the network to increase mechanical strength by converting the planar BO_3 units into stable tetrahedral BO_4 units. Recently, a sodium lithium borate glass doped with 2 mol% of Er_2O_3 was reported to be promising for infrared laser and optical amplifier applications due to its high emission cross-section [130] (Fig. 14).

In the past several decades, interest in glasses with mid-infrared (MIR) emissions has increased. Thus, to develop efficient lasing glasses, the host should possess minimal absorption in the MIR region and low nonradiative decay rates so that radiative emission rates are high. Tellurite and germanate glasses are suitable candidates for MIR light sources due to their low phonon energy, relatively high refractive indices (promoting larger absorption and emission cross-sections) and extended transmittance further into the infrared. Since the first report on RE-doped tellurite glasses as potential optical amplifiers and fiber devices [131], a large number of tellurite and germanate glasses have been engineered, especially with high RE solubility, good chemical durability and thermal stability. The use of RE doped tellurite and germanate glasses to produce NIR and MIR luminescence has been reported in many studies [132,133], just to cite a few. Fluoride glasses also have attracted attention due to their low phonon energy and, more importantly, due to their transparency further into the MIR spectral range. High RE doping levels (up to 10 mol%) have been obtained in fluoride glasses. Most studies have focused on ZBLAN glasses (ZrF_4-BaF_2-LaF_3-AlF_3-NaF), including those doped with Er^{3+} or co-doped Er^{3+}/Pr^{3+} [134]. Recently, a fluoride glass in the ZrF_4-BaF_2-AlF_3-YF_3 system has been reported with a high erbium-doping concentration (up to 6 mol. %) and with minimum concentration quenching of the luminescence at 2.7 μm [135]. However, currently, fluorides still exhibit intrinsically low thermal and chemical stability limiting their uses. Consequently, glasses with mixed anions, such as oxyfluoride

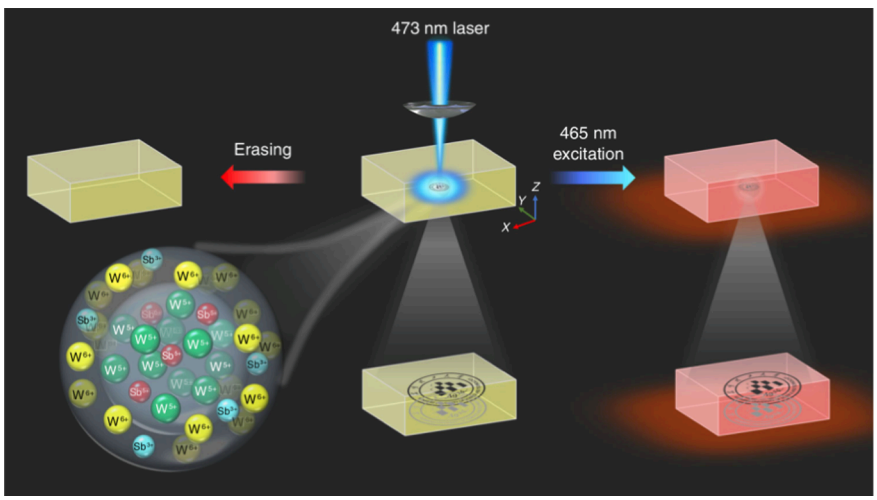

Fig. 13. Schematic of the writing, reading, and erasing of optical information. (Reproduced from Ref. [118] with permission from Optica).

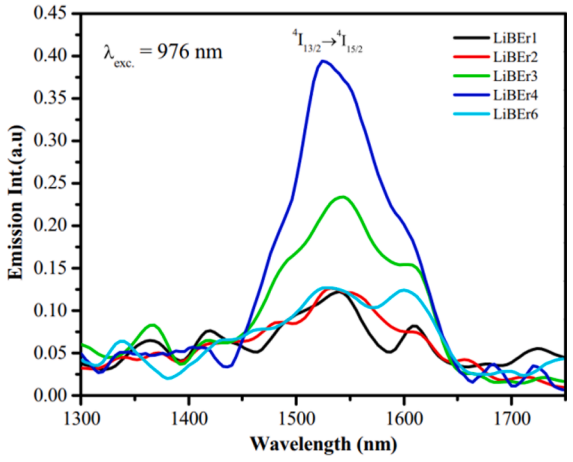

Fig. 14. Emission spectra of Er^{3+} doped glass with the composition: $(65 - x)B_2O_3 - 15Na_2O - 10PbO - 5ZnO - 5Li_2O - xEr_2O_3$ with × = 0.05, 0.1, 0.5, 1.0, 2.0 and 4.0 mol% (denoted as LiBEr, LiBEr1, LiBEr2, LiBEr3, LiBEr4, LiBEr5, and LiBEr6, respectively) (Reproduced from Ref. [130] with permission from Elsevier).

glasses, have prompted interest. Compared to the parent oxide glasses, oxyfluoride glasses often possess good transparency in the ultraviolet and infrared regions while also exhibiting reduced phonon energies. As opposed to fluoride glasses, the composition of oxyfluoride glasses can be more broadly tailored so that this family of glasses exhibit good thermal stability and chemical durability. Oxyfluorides have been obtained in different glass systems (silicate, tellurite, borate, phosphate, just to cite a few) [136]. For example, an increase in the intensity of the Er^{3+} up-conversion was reported due to the decrease of the phonon energy when replacing CaO by CaF_2 in a phosphate glass [137]. An increase in the fluorine content in gadolinium calcium phosphate oxyfluoride glass was also reported to increase the intensity of co-dopant Sm^{3+} emissions due to the reduction of phonon energies [138]. Recently, ErF_3 doped tellurite–gallium oxyfluoride glass was reported to be promising as IR laser gain material with large emission cross sections at 1.55 μm (6.32×10^{-21} cm^2) and 2.73 μm (9.68×10^{-21} cm^2) as well as a long fluorescence lifetime (6.84 ms at 1.55 μm and 262 μs at 2.73 μm) [139]. Another recently reported promising material for application at 1064 nm (Nd^{3+}) and 2020 nm (Ho^{3+}) is the oxyfluoride barium gallo-germanate glass [140]. The addition of fluorine into the glass allows for the preparation of glass with lower hydroxyl concentrations due to the reaction $OH^- + F^- \rightarrow HF + O^{2-}$ [141], so enhanced spectroscopic properties can be realized due to the reduction in OH, known to be a luminescence quencher [142]. ChGs have also been of great interest, especially for optical emissions beyond 4 μm as the non-radiative decay rates in the MIR are reduced in these glasses due to their low phonon energy. Even though ChGs have covalent bonds and rigid networks, generally limiting the addition of RE ions, ChGs in different multicomponent systems, such as As-S(Se), Ga-La(Sb)-S, Ga-Ga-S, Ge-Ga-As(Sb)-S(Se), have been successfully prepared with REs including Dy^{3+}, Tb^{3+}, Ho^{3+}, Pr^{3+}, Tm^{3+}, and Er^{3+} [143,144]. However, due to the low RE solubility in the ChGs in comparison to oxide glasses, ChGs exbibit poor fluorescence efficiency. Thus, effort has been focused on the development of ChGs with greater RE solubility so that they could exhibit larger emission cross-sections in addition to their high linear and nonlinear refractive index, low phonon energies, and extended transmission

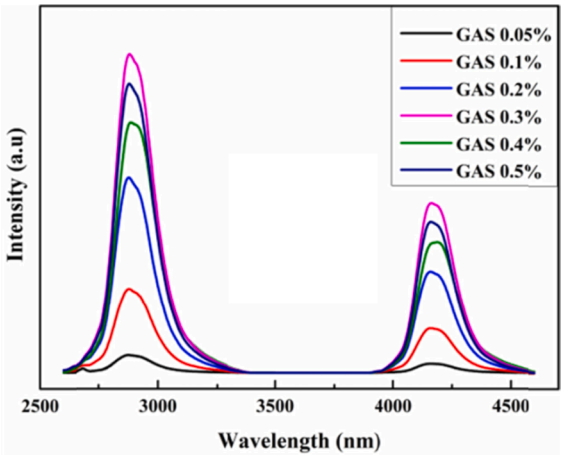

Fig. 15. Emission spectra of GAS glass with the $Ga_{0.8}As_{39.2}S_{60}$ composition doped with different amount of Dy^{3+} pumped at 1707 nm (Reproduced from Ref. [149] under the terms of the Open Access Publishing Agreement).

properties. The addition of modifier such as Ga was reported to increase the RE solubility due to the formation of edge-sharing [GaS_4] units that bond to the RE ions [145,146]. Maximum RE solubility, <300 ppm in the As_2S_3 glass, could be increased to 1000 ppm in the glasses within the Ge-As(Sb)-Ga-S(Se) systems [144]. Recently, Jiao et al. confirmed that Ga could also be used to enhance the IR quantum efficiency of Er^{3+} doped sulfide glasses [147]. Glasses in the Ga-Ge-Sb-S glass system exhibit NIR and MIR emissions when adding Nd^{3+} up to 7500 parts-per-million by weight (ppmw) [148]. Ga was also added in the As-S system and large RE solubility was reported in the $Ga_{0.8}As_{39.2}S_{60}$ glass as Dy^{3+} could be added up to 0.3 wt% in this glass without the formation of nanocrystallites [149]. This glass emits MIR photoluminescence at wavelengths beyond 4 μm (Fig. 15).

Strong green emission was observed from a ChG in the GeS_2-Ga_2S_3-KCl system after adding 0.1 mol% of Er^{3+} due to the gallium based units, such as [$Ga_2S_{6/2}$] and [$GaS_{3/2}Cl$]$^-$, surrounding the RE ions [150]. Glass with composition 64GeS_2-16Ga_2S_3-20CdI_2 (in mol%) was reported to also be a suitable candidate due to its thermal stability against crystallization and high refractive index (n_D = 2.34). This glass can incorporate up to 3 wt% of Dy^{3+} without deteriorating its transparency, and concentration quenching occurs when adding >0.6 wt% of Dy^{3+} [151]. Despite the large number of studies on glasses with MIR emissions, there are still challenges related to the development of mid-infrared lasers emitting beyond a wavelength of 4 μm. New glasses with lower phonon energies, wider infrared transmission windows, and higher RE solubility are needed for the development of new light sources with efficient mid-infrared light emission.

Another strategy used to enhance the spectroscopic properties of glass is the co-doping approach already noted briefly. Yb^{3+} ion is one of the most popular sensitizers due to its high absorption cross-section at a wavelength of 980 nm and the possibility of efficient energy transfer to other RE ions. Among the RE ions, the Er^{3+}/Yb^{3+} co-doping has been intensively investigated for enhancing up-conversion, NIR and MIR emissions of Er^{3+}, and energy transfer Yb^{3+} → Er^{3+} [152]. Yb^{3+} can also be used as a sensitizer for Tm^{3+} allowing the emission of UV / blue up-conversion emission under near-IR excitation due to the energy transfer Yb^{3+} → Tm^3 [153] as well as for Ho^{3+}, as illustrated in Fig. 16.

Mid-infrared emission at ~2.85 μm from a Yb^{3+} / Ho^{3+} co-doped fluoroaluminate glass was recently demonstrated [154]. The Ho^{3+} emission can also be enhanced by using Er^{3+} ions, rather than Yb^{3+}, due to its absorption at 980 nm and the small energy gap between the $^4I_{13/2}$ level of Er^{3+} and the $^5I_7$ level of Ho^{3+} (Fig. 17**a**). Such glasses are promising materials for application in the MIR range using 980 nm pumping (Fig. 17**b**) [155]. Ho^{3+} / Tm^{3+} and Ho^{3+} / Nd^{3+} co-doping have been also investigated for enhancement of emission at 2 μm and 3.9 μm under excitation at wavelengths of ~888 or 808 nm [156,157].

Park et al. tested Pr^{3+}, Ho^{3+}, Tb^{3+} and Tm^{3+} as potential sensitizers to enhance the emission of Dy^{3+} at 2.95 μm from $Ge_{30}Ga_5Sb_5Se_{60}$ (at%) chalcogenide glass and a significant enhancement of the emission was observed due to the transfer between Pr^{3+} and Dy^{3+} [158]. Triply-doped glasses have also prompted attention lately. For example, Nd^{3+}-Er^{3+}-Pr^{3+} triply-doped tellurite glass was successfully prepared and shown to emit over a very broad band, ranging from 760 to 1150 nm [159]. As discussed, co-doping of glass with multiple RE ions has been of interest for the development of new smart white lights to replace the established YAG:Ce^{3+} crystals, which deteriorate in the quality and intensity of the white light emission over time. Lodi et al. demonstrated that a calcium boroaluminate glass co-doped with Dy^{3+} and Eu^{3+} is promising materials that showed promise for obtaining white light [160]. White light emissions also were obtained by adding Tm^{3+}, Er^{3+} and Yb^{3+} in oxyfluoride tellurite glass [161].

Another approach to enhancing the spectroscopic properties of a glass is the use of noble metal nanoparticles which possess unique electronic and optical properties. The confinement of a large electric field around the nanoparticles occurs when the incident light interacts with the NP surface when the particle size is smaller than the wavelength of the light. The free electrons in the conduction band of the (nano)metal oscillate due to polarization by the electromagnetic field of the incident light. This oscillation leads to localized surface plasmon resonance (SPR) field and, therefore, to the strong absorption and scattering of light. Mie theory can be used to explain this process and can provide analytical solution to Maxwell's equations for (plasmonic) spheres with various diameters. The SPR band strongly depends not only on the size and shape of the nanoparticles but also on the dielectric constant of the surrounding medium. This surface plasmon resonance (SPR) field can be used to enhance the luminescence efficiency of the RE ions doped into the host glass when the luminescence frequency and / or the frequency of the excitation beam are close to the frequency of the SPR band of the NPs. However, since the position of the SPR band depends on the geometry of the nanoparticles, it is crucial to control the size and

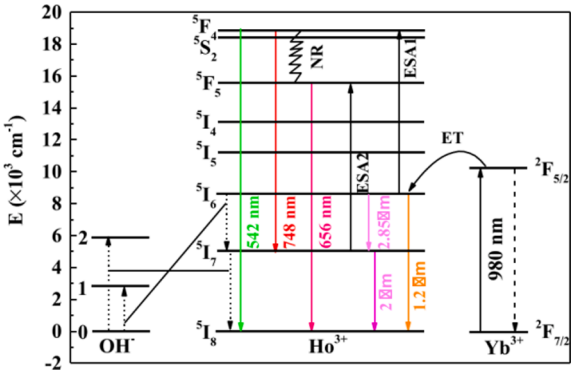

Fig. 16. Energy transfer process between Ho^{3+} and Yb^{3+} (Reproduced from Ref. [154] with permission from Elsevier).

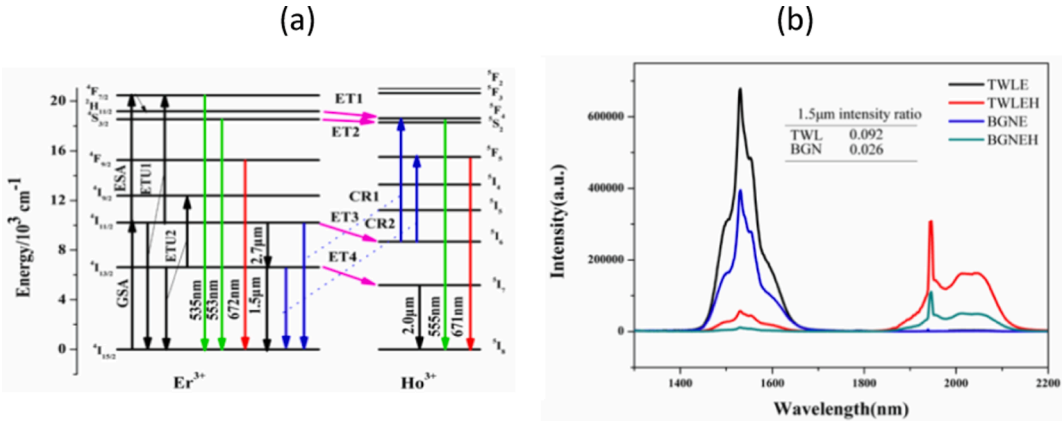

Fig. 17. (a) Energy level diagram of Er^{3+} and Ho^{3+} ions. (b) Emission spectra of glasses with the composition $54TeO_2 - 31WO_{1.5} - 15LaO_{1.5} - 2ErO_{1.5} - xHoO_{1.5}$ (x = 0, 2); $55BiO_{1.5} - 30GeO_2 - 15NaO_{0.5} - 2ErO_{1.5}$ - $xHoO_{1.5}$ (x = 0, 2) (labelled as TWLE, TWLEH, BGNE, and BGNEH, respectively) (λ_{exc} = 980 nm) (Reproduced from Ref. [155] under the terms of the Open Access Publishing Agreement).

shape of the NPs in the host to optimize the spectroscopic properties of the composite glass. As discussed by Pillonnet et al., the optimal coupling distance between the NPs and RE ions needs to be optimized as well. If the NPs and RE are too far apart, there would be no energy transfer whereas, if they are too close, there is a risk for back transfer energy to NPs [162]. Metal NPs usually are obtained by heat treating a glass prepared with a specific nucleating precursor. For example, AgCl, $AgNO_3$ or $AgSO_4$ can be used as the precursors for the Ag nanoparticles. The temperature of the heat treatment is above the glass transition temperature of the host glass so that the number of the NPs remains constant while maintaining a small size and size distribution of the NPs. The most investigated nanoparticles in glass matrix are silver (Ag) and gold (Au) nanoparticles. Enhancement of Eu^{3+} luminescence properties in the visible was first reported in the presence of small Ag particles in borosilicate glass in 1985 [163]. Similar enhancements in the Eu^{3+} emission were later observed from tellurite glass prepared with Ag NPs with an average size of 8 nm (Fig. 18**a**) [164]. The reduction of Ag^+ is suspected to occur during the tellurite glass melting leading to the formation of Ag^0 atoms, from which the Ag NPs can form and grow during a thermal treatment. Due to the energetic proximity of the Ag NPs SPR band and the Eu^{3+} emission wavelengths, energy transfer from the surface of the NPs to the Eu^{3+} leads to an enhancement of the Eu^{3+} spectroscopic properties (Fig. 18**b**). Similar enhancement of the Eu^{3+} emission can be obtained using Au nanoparticles as reported in germanate [164] and tellurite [165] glasses.

Additionally, Mechergui et al. combined fluorine and Ag_2CO_3, the latter a precursor to Ag nanoparticles, in a Sm^{3+} doped tellurite glass [167]. A thermal treatment at slightly above the glass transition temperature for up to 16 h was used in order to grow Ag NPs with a size of 20–40 nm, leading to broad absorption band due to SPR of Ag NPs. Also observed was an increase in intensity of the emissions related to the transition from the Sm^{3+} $^4G_{5/2}$ state to the $^6H_{5/2}$, $^6H_{7/2}$, $^6H_{9/2}$ and $^6H_{11/2}$ levels. Similar improvement in the luminescence efficiency in the visible and at 1.5 μm was reported from Er^{3+} doped glasses using both Ag [168] and Au NPs [169]. Er^{3+} doped ChGs

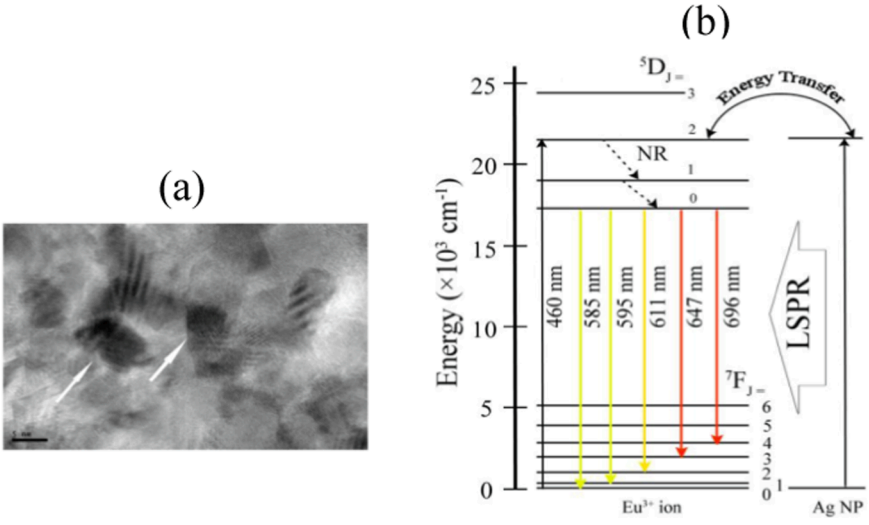

Fig. 18. (a) TEM images with arrows pointing to Ag NPs (scale is 5 nm). (b) Schematic partial energy level diagram of the Eu^{3+} ion in vicinity of a silver NP doped tellurite glass (Reproduced from Ref. [166] under the terms of the Open Access Publishing Agreement).

have been also prepared with Ag NPs, although fewer studies on NPs formation in ChGs can be found. A glass with the composition $Ga_{10}Ge_{25}S_{65}$ was reported to be a promising host. The Er^{3+}doped glass with the composition $Ga_{10}Ge_{25}S_{65}$ was heat treated at 370 °C for 10 h to grow Ag NPs resulting to significant enhancement of the Er^{3+} up-conversion as depicted in Fig. 19 [170].

Recently, Jia et al. investigated the effect of Ag NPs on the MIR emission properties of Er^{3+}-doped germanate glass and reported similar enhancement of the luminescence centered at 2.7 μm [171]. Ag NPs can also be used to increase the intensity of the emissions between 530 and 650 nm and in the NIR of Pr^{3+} doped tellurite glass [172]. Similar enhancement in the emission at 494 nm was reported from Pr^{3+} doped chalcogenide glass in the Ge-Ga-S system containing Ag NPs [173]. Enhancements to the spectroscopic properties of Tm^{3+} doped glasses can be also obtained using Ag NPs [174]. These are just few examples as the enhancement of the spectroscopic properties of active glasses using noble metal NPs have been intensively reported. Many of these studies related the enhancement of RE luminescence properties to the coherent coupling of photons to free electron oscillations occurring at the nanoparticles-glass interface (SPR) and to the intensified local field effect created by the NPs. Intensified local fields around the metal also are thought to enhance the emission [175]. Energy transfer to other silver species, such as silver ions, atoms, dimers, clusters, molecule-like non-plasmonic entities, to the RE ions also are suspected as means to improve the spectroscopic properties [176]. Wei et al. demonstrated that the excitation at 464 nm of Eu^{3+} doped oxyfluoride silicate glass led to the SPR effect of the Ag NPs whereas the energy transfer from very small molecule-like, nonplasmonic Ag particles to Eu^{3+} energy transfer is suspected to occur when under excitation at a wavelength of 350 nm. Under excitation at 270 nm, the enhancement in the Eu^{3+} luminescence is related to the energy transfer from isolated Ag^{+} to Eu^{3+} [177]. Quenching of the luminescence intensity can occur when the glass contains large NPs with high volume fraction leading to energy transfer from RE to the NPs [178]. Despite numerous studies on metal NPs in glasses, the mechanism for improved spectroscopic response due to the metal NPs is not fully understood and debate remains amongst the scientific community. In-depth exploration of the metal NPs growth rate in various glass compositions is necessary to further understand the formation and growth mechanism of metal NPs nanoparticles in host matrices.

Crystals are promising hosts for RE dopants as they possess most of the optical and thermomechanical properties required to produce high intensity lasers. However, one of their limitations is their size and their synthesis, which is usually more expensive and complex than melting glasses. Consequently, glass-ceramics (GCs) have been materials of interest. GCs were originally defined by Stookey in 1960 as "Glass-ceramics are made by first melting and forming special glasses containing nucleating agents and then causing controlled crystallization of the glass" [11]. As compared to parent glasses, GCs can be developed with improved mechanical and thermal properties. To be promising as a lasing material, the GC should be transparent with minimum light scattering, including Rayleigh scattering. To avoid Mie scattering, the GCs should contain small crystals (<15–30 nm) with narrow size distribution and with similar refractive index (n) than the glass host. The crystals should also be homogeneously distributed in the volume of the glass with no aggregation. The separation between the crystals should be comparable to their size. Finally, for the GCs to possess promising spectroscopic properties, the crystals should have specific crystalline phase and should contain the RE, the diffusion of which from the glass matrix to the crystals depends on the activation energy and diffusion coefficient of the RE. GCs are commonly obtained by heat treating a glass and, therefore, the heat treatment parameters such as temperatures and duration should be tailored in order to control the growth of the nuclei into crystals. The first transparent RE doped GC with enhanced up-conversion efficiency was reported in 1993 and was related to the precipitation of (Pb, Cd)F_2 crystalline phase after heat treating the Er^{3+}, Yb^{3+} co-doped aluminosilicate glass [152]. Since this work, efforts have focused on the development of new GCs. However, most of the studies have been focused on silicate GCs and one of the latest transparent silicate GC was reported with enhanced up-conversion emission and long fluorescent lifetime due to the precipitation of Er^{3+} doped KEr_3F_{10} nanocrystals with low phonon and with reduced Er^{3+}–Er^{3+} distances (Fig. 20**a** and **b**) [179].

Highly crystalline (>90%) GCs have been successfully obtained from fluoride glasses [180]. Surprisingly, a limited number of studies related to the development of transparent borate and phosphate GCs have been reported. Satyanarayana et al. investigated the crystallization mechanism of Pr^{3+} doped borate glasses in the PbO–Sb_2O_3–B_2O_3 system [181]. However, multiple crystals, such as $Pb_5Sb_2O_8$, $Pb_3(SbO_4)_2$, PbB_4O_7, β-$PrSbO_4$, Pr_3SbO_7, and $Pr_3Sb_5O_{12}$, were observed in the heat-treated glasses. Nonetheless, the thermal treatment was found to improve the luminescence efficiency. Transparent Dy^{3+} doped borate GCs were reported with blue emission band due to the precipitation of $PbWO_4$ microcrystals using appropriate thermal treatment (T = 450 °C for 10 h) [182]. Transparent

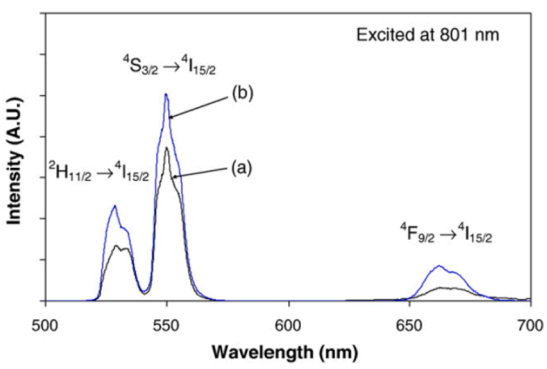

Fig. 19. Up-conversion spectra of Er^{3+} doped (black) and Er^{3+}/ Ag co-doped (blue) ChG (Reproduced from Ref. [170] with permission from Elsevier). (For interpretation of the references to color in this figure legend, the reader is referred to the web version of this article.)

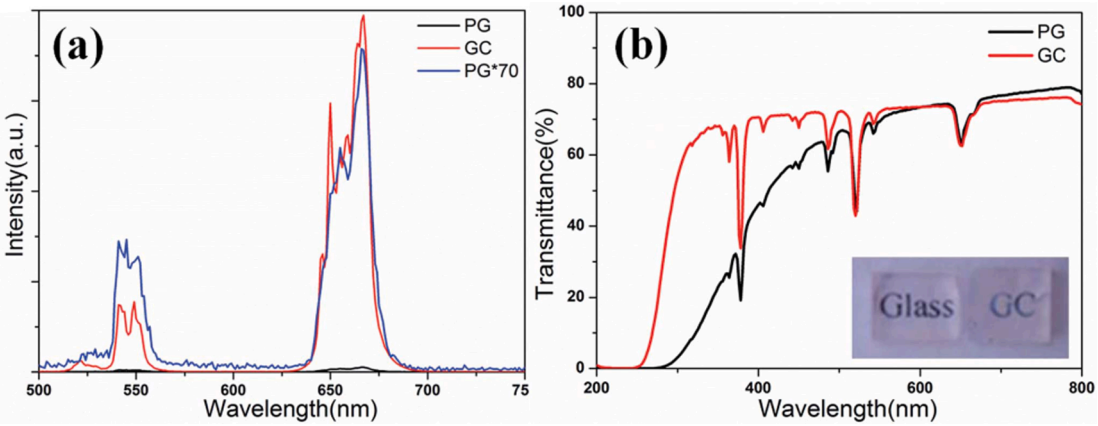

Fig. 20. (a) Up-conversion spectra of the glass in the SiO_2-KF-ZnF_2 system (PG)and the corresponding GC obtained by heat treating the glass at 625 °C for 10 h (λ_{exc} = 980 nm) (PG*70 shows that the up-conversion intensity of red emission of the GC is enhanced by >70 times compared to that of the PG). (b) Transmittance spectra of the glass and GC. Inset is the picture of the glass prior to and after heat treatment (Reproduced from Ref. [179] under the terms of the Open Access Publishing Agreement). (For interpretation of the references to color in this figure legend, the reader is referred to the web version of this article.)

oxyfluoride phosphate GCs exhibiting intense green and red up-conversion emissions due to the volume precipitation of CaF_2 crystals doped with Er^{3+} have been reported [183]. Transparent germanate and tellurite GCs have been also successfully prepared. For example, Kang et al. reported the preparation and characterization of transparent tellurite GCs with intense emission at 2.7 μm due to the presence of $PbTe_3O_7$ nanocrystals doped with Er^{3+} [184]. $K_2Nb_{14}O_{36}$ crystals with a size smaller than 20 nm were found to precipitate in germanate glass in the GeO_2-Nb_2O_5-K_2O system during heat treatment leading to an increase in the quantum efficiency [185]. However, luminescence quenching was observed when the crystallization step was too long, clearly demonstrating the challenge related to the preparation of GCs using thermal treatment. ChG GCs have been also studied. The heat treatment of glasses in the $(GeS_2)_x$-$(Ga_2S_3)_{1-x}$ system leads to the surface precipitation of GeS_2 crystals and volume precipitation of Ga_2S_3 crystals. Due to the presence of Er^{3+} at the surface of the Ga_2S_3 crystals, enhancement of the emission at 1.54 μm was reported after heat treatment of the $Ge_{20}Ga_{10}S_{70}$ glass [186]. Similar results were obtained after heat treating the glass with the composition 80$GeSe_2$-20Ga_2Se_3 (mol%) due to the formation of Ga_2Se_3 phase inside the glass matrix [187]. Glass-ceramics with a glass phase and the desired crystals have also been prepared using the "Frozen sorbet" (FS) method [188]. In this approach, the glass–ceramic results when the liquid–solid mixture is suitably quenched. Nakanishi et al. used this technique to prepare GC with $SrAl_2O_4$ crystals in which B^{3+} ions partially substitute for the Al^{3+} sites from the $SrOAl_2O_3B_2O_3$ glass as the precipitation of such crystals is extremely difficult to obtain in glass. To reduce Eu^{3+} into Eu^{2+}, a flow of 5% H_2 + 95% N_2 was used as was heated graphite powder. The GCs exhibit excellent long persistent phosphorescence properties. However, the main limitation of the FS method is the growth of the crystals using the elements of the glass which limits the preparation of glasses with similar crystals. The other challenge with the glass–ceramic method is the lack of general and precise empirical or theoretical model of the crystallization process for a glass of given chemical composition. There is a need for closed-loop approach; experiments, theory and simulations to advance the fundamental understanding of the nucleation and growth mechanisms of glasses in different glass system allowing one to predict the formation of transparent glass-ceramics from the glass composition and various properties. Therefore, another approach to fabricate glasses with embedded crystals is to introduce directly in

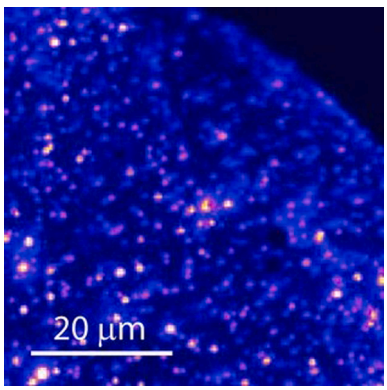

Fig. 21. Confocal image showing the color center fluorescence in the diamond nanocrystals in tellurite glass (Reproduced from Ref. [189] with permission from John Wiley and Sons).

the glass, crystals of specific phase, dopant and doping level, size and shape. As the RE ions are located in the crystals, the RE are not impacted by the glass host. For example, diamond nanocrystals were embedded in tellurite glass (see Fig. 21) [189].

As noted, the crystals are added in the glass melt prior to the quenching step. As explained in [190], the melting process needs to be controlled to limit the decomposition of the crystals in the glass during the glass preparation. The decomposition is associated with the diffusion of the elements from the crystals to the glass leading to changes in the site of the RE inside the crystals and, so, to changes in the spectroscopic properties of the crystals embedded in the glass. In the case of persistent luminescent phosphors, the decomposition is correlated to the oxidation of Eu^{2+} to Eu^{3+}, which decreases the persistent luminescence properties. The chemical stability of the crystals was found to be sensitive to the melting conditions and to the glass composition [190]. Nonetheless, using this approach, numerous glasses were prepared with persistent luminescent phosphors [191] as well as upconverter phosphate glasses, which were prepared by adding 5 wt% of $NaYF_4$:Er^{3+}, Yb^{3+} crystals in the glass melt [192]. These studies clearly show the promise of the direct doping technology for the development of the next generation of active glass-based materials.

Due to their optical properties and high compositional versatility, glasses also have been at the forefront of the biophotonic research. Biophotonics is a multidisciplinary field that combines photonic, material science, and biology. The use of light in healthcare has had tremendous impact on diagnoses (molecular diagnostics, point-of-care, diagnostic imaging) as well as on therapy and surgery [193–198]. The impact of a wide range of wavelengths on photosensitive molecules, proteins and cells also has been investigated. For example, UV light (100–400 nm) is known to modulate the immune response whereas UVB can activate the release of antimicrobial peptide as well as activate T-cells, B-cells and mast cells [196]. Multifunctional bioresorbable phosphate glass optical fibers have recently been used for theranostics. Such materials are innovative, as such fibers are not only promising for therapy and diagnosis but in addition the resorbability of the material may prevent the need for the removal of the fiber [199]. More recently, Lemiere et al. reported the first production of resorbable biophotonic fibers with green persistent luminescence [200]. Such materials are promising in view of guiding light in photoresponsive porous biomaterials. Furthermore, biophotonic scaffolds have been developed. Those materials are able to emit visible light under adequate excitation, where excitation depends on the rare earth used and the emission wavelength targeted [201]. By combining bioactive properties with luminescent properties into one glass, one can foresee the future development of integrated actuators in bioactive materials, able to favor tissue regeneration for example. Light can be used to selectively and spatiotemporally release active agents, such as growth factors or drugs. However, in such application, one must convert NIR light (deep penetration) into visible lights (efficient photocleavage of polymers). Fig. 22**a** presents selected photoactivated polymers which release nitric oxide (NO) when properly excited. However, the challenge lies in generating enough energy for the photocleavage. As shown in Fig. 22**b,** maximum tissue penetration is reached in the NIR. Therefore, there is a clear need for efficient conversion of NIR into visible light for the development of biomaterials able to release, on-demand, active agents.

5. Nonlinear glasses

Nonlinear optical (NLO) properties relate to changes in the polarizability of the material, in a nonlinear way, due to the electric field of the excitation light. Even if there have been earlier experiments, it is generally considered that the first observation of NLO behavior was that of second-harmonic generation in 1961, soon after the realization of the first laser in 1960 [18]. Glass, as an isotropic material, does not have intrinsic second order NLO property, which can be obtained only if the symmetry is broken. Some representative NLO materials, including mostly crystalline organic and inorganic materials, have been reviewed in [203]. This Section is focused on glass materials with the objective to bring additional details to already published review papers [204,205].

5.1. Principles

5.1.1. Basic considerations

The light is an electromagnetic wave consisting of electric and magnetic fields alternately oscillating at optical frequencies. When this electromagnetic wave encounters a dielectric solid, an electronic polarization is induced mainly by instantaneous displacements of electronic charges from their initial positions. When the applied electric field (*E*) is weak in intensity, the induced dielectric polari-

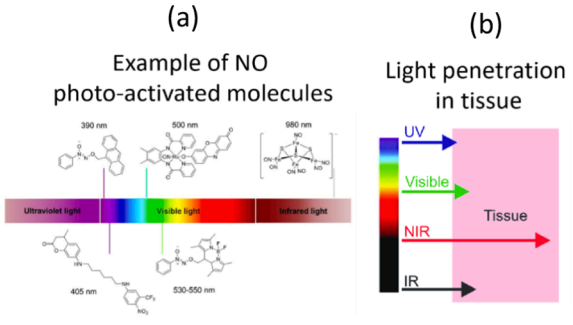

Fig. 22. (a) Molecules able to photo-release nitric oxide (Reproduced from Ref. [202] under the terms of the Open Access Publishing Agreement) and (b) light penetration in tissues as a function at various wavelength.

zation density (the electric dipole moment per unit volume; P) is linearly proportional to E, which can be expressed as $P = \varepsilon_0 \chi E$ where ε_0 and χ denote the vacuum permittivity and the linear susceptibility, respectively. In the presence of a strong optical field, e.g., the electromagnetic field of a tightly focused laser beam, the induced polarization is no longer linearly proportional to E, but starts to deviate from the situation of a charge poised to a harmonic potential, thus exhibiting a nonlinear behavior. To describe this event in a practical way, P is expressed as a power series of E normally up to the third order, such that $P = \varepsilon_0 \left(\chi^{(1)}E + \chi^{(2)}E^2 + \chi^{(3)}E^3\right)$. Here, $\chi^{(2)}$ and $\chi^{(3)}$ are the second-order and third-order NLO susceptibilities, respectively [206]. The first-order susceptibility ($\chi^{(1)}$) is related to linear refractive index (n_0) via $n_0^2 = 1 + \chi^{(1)}$ and is responsible for linear optical interactions such as refraction, absorption, dispersion and birefringence [207]. The second order susceptibility $\chi^{(2)}$ is nonzero if the material lacks inversion symmetry. Since glasses are isotropic at a length scale smaller than the wavelength of light, they lack second-order nonlinearities such as second harmonic generation (SHG), frequency mixing, and parametric generation. As such, breaking the inversion symmetry inherent in glass is required to exploit its second-order nonlinearity. The third-order susceptibility $\chi^{(3)}$ is dependent only on intensity (or irradiance) of the incident light. As a result, glass is quite competitive to crystals in terms of intrinsic compositional flexibility in optimizing its optical nonlinearity and cost-effectiveness in fabricating desired forms.

Nonlinear optical effects are classified qualitatively into two different categories, i.e., parametric and non-parametric processes. As with conventional linear refraction taking place as a parametric process in transparent, i.e., lossless, linear dielectric media, a parametric nonlinear process occurs without the involvement of real quantum states, i.e., non-resonant with any gaps between the energy levels, and, as a consequence, this process is in general more instantaneous than a non-parametric nonlinear process. A few examples of such parametric nonlinear processes are SHG and THG. Non-parametric nonlinear processes are associated with energy transfer between optical fields and quantum states, which normally take place less instantaneously. The imaginary part of $\chi^{(3)}$ is central to such effects as stimulated Raman scattering (SRS), stimulated Brillouin scattering (SBS), and two photon absorption (TPA). It is noteworthy that energy and momentum should be conserved for both parametric and non-parametric nonlinear processes. As such, the phase matching conditions expressed in terms of frequency and wavevector of interacting optical fields need to be satisfied for enhancement of a specific nonlinear optical event.

The real and imaginary parts of $\chi^{(3)}$ can be described in terms of nonlinear refractive index (n_2) and nonlinear absorption coefficient (β), respectively. In order to properly account for the intensity-dependent change of refractive index (n), it is convenient to adopt an equation $n = n_0 + n_2 I$, where I is intensity of the incident optical fields [208]. Likewise, the absorption coefficient (α) can be expanded to incorporate the intensity-dependent change of absorption in the form of $\alpha = \alpha_0 + \beta I$, where α_0 is the linear absorption coefficient [209]. As is the case of the linear refraction and absorption expressed as n_0 and α_0 being mutually interrelated via Kramers-Krönig relations, both the nonlinear optical constants (n_2 and β) are also connected through nonlinear Kramers-Krönig relations [207].

Exploitation of glass for use in practical applications where its optical nonlinearity plays a critical role is accomplished through compositional tailoring to optimize $\chi^{(3)}$ as well as transmission and thermal stability. Arguably the most well-known and simple equation is Miller's rule, given by $\chi^{(3)} = \left[\chi^{(1)}\right]^4 \times 10^{-10}$ (in esu unit). This is an empirical rule for correlating the linear and nonlinear susceptibilities applicable for the pursuit of nonresonant nonlinear materials. According to this rule, as shown in Fig. 23, high nonlinear refractive index is expected for glasses with high linear refractive index, which further implies that glasses composed of heavy elements tend to feature a high nonlinear refractive index. For example, Se-based ChGs have been experimentally verified to possess higher nonlinearity than S-based ChGs [209,210].

Boling's relation is also useful, which relates n_2 to both n_0 and Abbe number (ν) in the form of $\frac{n_2 \propto (n_0 - 1)}{\nu^4}$ [211]. Here, glasses with higher dispersion tend to be more optically nonlinear. It is worth noting that even though this relation contains only the two linear macroscopic parameters to estimate n_2, it works better for glasses with n_d values lower than ≤ 1.7, where n_d refers to refractive index measured at the sodium d-line ($\lambda = 589nm$), and wavelength dependence of the estimated n_2 is not revealed [207]. If the glass is an amorphous semiconductor, at least in terms of the magnitude of bandgap energy (E_g), the formulation by Sheik-Bahae et al. can be used

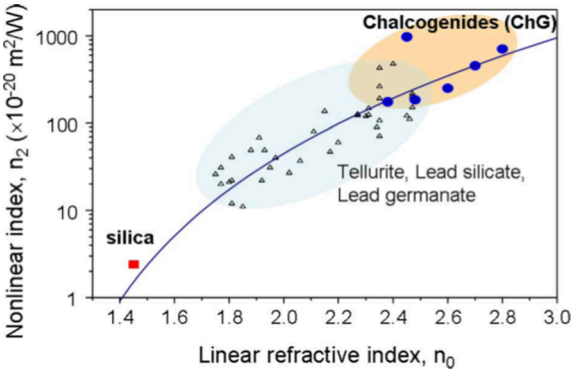

Fig. 23. Graphical representation of Miller's rule, denoted as the curved line, correlating nonlinear refractive index n_2 and linear refractive index n. Also plotted as symbols are the measured data for some highly nonlinear oxide and chalcogenide glasses. (Reproduced from Ref. [210] with permission from IEEE).

to correlate n_2 and E_g as in the forms of $n_2 \propto n_0^{-2} E_g^{-4}$ and $\beta \propto n_0^{-2} E_g^{-3}$, respectively [211]. Even though the Sheik-Bahae model does not account for tail states that usually occur in glasses, especially in ChGs, it can provide valuable implication as to optical nonlinearity of glass in which electronic absorptions are governed by transition between valence and conduction bands without involvement of molecular or atomic levels [211]. Here, both n_2 and β are strongly dependent on E_g rather than on n_0. Specifically, since n_0 of glasses normally varies from ~1.5 at the visible wavelengths (silicate glasses) to ~3.2 at the infrared wavelengths (telluride glasses), contributions of n_0 are relatively insignificant. This E_g dependence of optical nonlinearity of glass turns out to work properly for rough compositional assessment of nonlinear glasses for use at near-infrared wavelengths [207].

The net efficiency of nonlinear optical processes is determined not only by the nonlinear susceptibility of a given material but also by the phase matching conditions. Especially when the nonlinear events involve optical fields at dissimilar frequencies, the energy conservation is satisfied straightforwardly in most cases, but the momentum conservation expressed in terms of mismatches between the wavevectors of the involved optical fields, i.e., $\Delta k = 0$, brings about additional criteria for selecting a nonlinear optical material [212]. To extract an optimized energy conversion efficiency, the phase-matching condition with regard to $\Delta k = 0$ should be satisfied in many nonlinear optical processes. As the electromagnetic waves participating in the nonlinear optical events need to be described as linear wave propagation, the $\Delta k = 0$ condition is directly related to changes of refractive index against wavelength or polarization. As such, in the case of glasses, refractive index dispersion expressed in the form of Abbe number exerts a particular influence. Given that the phase matching condition utilizing adjustment of temperature- and/or polarization-dependent refractive indexes is not available, quasi-phase matching (QPM) can be exploited as a viable option. Normally, QPM is achieved either via inverting the sign of the nonlinear susceptibility after each coherence length or via allowing each coherence length of nonlinear interaction with the other sections remaining to get only linear propagation that rearranges the relative phases [213]. To meet the QPM conditions, material under investigation needs to possess the 2nd-order optical susceptibility, so that glass should undergo a poling process to create a nonzero $\chi^{(2)}$ value [213].

5.1.2. Third order nonlinearity in glass

In isotropic materials such as glass, second order NLO coefficients are zero if the centrosymmetry is not broken. In such cases, the dominant nonlinear parameter is the nonlinear refractive index, n_2, which is related to the third order susceptibility $\chi^{(3)}$ as $n_2 = \frac{3}{n_0 \varepsilon_0^2 c} \chi^{(3)}$, where n_0 is the linear refractive index and ε_0 vacuum permittivity, c the speed of light in vacuum. For almost all glasses, it has been found that the nonlinear susceptibility is closely related to the linear refractive index. A glass with high linear refractive index will also have high nonlinear refractive index, as shown in Fig. 23. Considering the complexity of the glass composition, some small deviation from the Miller's rule can be found for some glasses [214,215]. These results indicate that the linear and nonlinear refractive index are mostly determined by the same parameter, which is essentially the polarizability of the ions in the glass matrix. This is, of course, important for designing appropriate glass composition for different applications and spectral ranges.

5.1.3. Generation of second-order optical nonlinearity in glasses

Different techniques have been developed to generate effective second order NLO in glass by breaking the centrosymmetry of the isotropic glass structure. The illumination of glasses by two mutually coherent beams with fundamental and doubled frequencies leads to the formation of a long-lived reversible electrostatic polarization. This process is known as optical poling. During optical poling, glass changes its symmetry and the photoinduced second harmonic generation can be produced. This phenomenon has been investigated especially in silica-based oxide glasses and fibers [216,217], and, more recently, in tellurite glasses [218]. Efficient SHG has been obtained with commercial optical fibers using quite high pumping/poling power during several hours. In tellurite glasses, the maximum SHG was reached relatively rapidly, only after several minutes of poling, with a peak pumping power density in the range of GW/cm^2. A recent study has been reported to better understand the optical poling efficiency in multimode fibers [219].

A thermal poling process involves the application of a DC field to a heated glass with sufficient ionic mobility, and the cooling down to room temperature in order to "freeze" the internal electric field generated during the poling, which can be more or less permanent. This process has been applied to many different glasses and the poling mechanism has been carefully studied [220–225]. The obtained second order susceptibility is generated mainly on the surface layer near the anode due to the mobility of charge carriers. The nature and the composition of the glass as well as the poling conditions may affect greatly the poling efficiency.

5.1.4. Introduction of crystals in glasses

The introduction of crystals inside the glass matrix is another well-studied method for generating second order NLO properties. The idea is to benefit from the (potentially high) second order nonlinearity of crystals and the ease of glass fabrication and shaping. For example, tellurite glass-ceramics containing centrosymmetric $K_2Te_4O_9$ crystals showed clearly an effective second-order susceptibility of 1.3 pm/V at the wavelength of 532 nm, ten times that of quartz [226]. It was concluded that the SHG originated from the abrupt changes in optical susceptibility at the interfaces between the glass and the crystal, together with the higher-order nonlinear response. This result indicated that it is not mandatory to have non-centrosymmetric crystals inside the glass matrix to obtain significant second order nonlinearity. The main issue with the glass-ceramics for optical application is the management of scattering losses induced by crystals. The most important parameters to be optimized include the size, the quantity of the crystal as well as the refractive index difference between the crystals and the glass matrix. Tellurite glass–ceramic fibers have been investigated with demonstrated SHG and the propagation loss of the partially crystallized fiber was in the range of 0.15 dB/cm, comparable to that of a typical $LiNbO_3$ planar waveguide [227].

5.2. Common applications of nonlinear glasses

Brillouin and Raman amplifications: Brillouin scattering refers to the inelastic scattering of light from acoustic phonons of the material and is one of the third-order nonlinear optical phenomena, together with Raman scattering, that is associated with phonons [228]. Glass can act as gain medium in which the stimulated Brillouin scattering (SBS) results from the interaction of intense pump light with either externally injected seed light or Stokes-shifted light originating from spontaneous Brillouin scattering (SpBS). SBS from fiber or planar waveguides find many applications such as for optical phase conjugation, pulse compression, serial beam combination, and distributed sensors [229]. Unlike its potential adverse impact on fiber-based optical communication systems, SBS is quite efficient as a nonlinear amplification route that provides a large optical gain with pump power as low as several milliwatts [230]. Specifically, the optical gain in SBS can be used for amplification of weak optical signals at frequencies equal to Brillouin shift [231]. For example, Brillouin fiber amplifiers have applications in microwave photonics, radio-over-fiber technology, and fiber-optics sensing. From the viewpoint of the efficiency of acousto-optic devices that can be used for evaluating Brillouin gain medium, glass is considered less effective compared to crystalline materials, e.g., TeO_2 crystal, in terms of refractive index, photo-elastic constant, acoustic velocity [232]. However, the high degree of freedom of glass compositions and forms are attractive. A large Brillouin gain coefficient is desired not only to mitigate the pump power requirements but also to shorten the interaction length [233]. Listed in Table 4 are Brillouin gain coefficient, Brillouin linewidth, and Brillouin frequency shift of some representative glasses.

Raman scattering results from acoustic phonons interacting with the pump light, and both spontaneous and stimulated scattering can occur. When the light-induced molecular motions occur in a coherent fashion, stimulated Raman scattering (SRS) results, which implies that the vibrational modes oscillate in harmony resulting in a coherent polarization, and, therefore, the subsequent light emission is coherent [236]. SRS is one of the active applications of nonlinear optical glasses and is employed commercially as fiber Raman amplifiers or lasers. Given the compositional versatility of glass, the Raman (and Brillouin) properties, such as the scattering coefficient and Stokes shift, can be broadly tailored. A proper adjustment of pump wavelength allows SRS emission at a desired wavelength range, which enables the exploitation of fiber Raman amplifier in practical wavelength-division multiplexing optical communication systems [231]. Ge-doped single mode silica glass fibers are common in modern optical communications networks. Even though the typical single-mode fiber itself can serve as a distributed Raman gain element to amplify the transmission of optical signals [237], the Raman gain coefficient of the Ge-doped silica glass is relatively low compared to other multicomponent silicate glasses as well as ChGs. Listed in Table 5 are Raman gain coefficient, gain bandwidth, and Stokes shift of some representative optical glasses.

Since the optical (and acoustic) phonon spectrum is broader in glass than in crystals, Raman (and Brillouin) scattering from glasses features generally broader band. For example, the Raman gain spectrum of silica fiber extends over a frequency range up to 40 THz [237]. Optical amplification at any desired wavelengths is allowed, in principle, given that a proper pump source is available. This is a key advantage of SRS over narrower-band ion-doped amplifier glasses, e.g., Er- or Yb-doped glasses. Progress in low-loss ChG has improved performance now permitting lasing action in mid-infrared wavelengths [243,245]. A recent analysis on Raman characteristics of Ge-As-S glasses showed that Raman gain coefficient tends to decrease, but laser damage threshold becomes improved upon increase of Ge content [243].

All-optical switching: All-optical switching can result from the modulation of optical signals by a control optical beam, which arises from various third-order optical nonlinearities. A practical all-optical switch is normally composed of nonlinear optical materials in the form of photonic (or plasmonic) micro- or nano-structures [246,247]. The practicality of nonlinear optical materials for use as all-optical switching can be assessed in terms of power consumption, switching time, and switching efficiency [247]. Taking these parameters into consideration, highly nonlinear glasses are quite competitive for the construction of all-optical switching devices. As nonlinear switching media, glasses exhibit ultrafast response times, compatibility with existing fiber-drawing capabilities, and low optical losses. In particular, ChGs possess inherently high nonlinearities, compared to the oxide counterparts, and the introduction of micro/nanoscale structures to ChGs can further improve their all-optical switching performance. Summarized in Table 6 are representative parameters related to the third-order optical nonlinearity of different glasses. As the optical bandgap energies of the glasses listed in Table 6 are quite different from each other, the proper selection of operating wavelength is required, in addition to the parameters related to optical nonlinearity, in order to fully exploit the figure of merit (FOM) values.

Optical limiting: Optical limiting normally refers to a nonlinear optical phenomenon in which low-intensity light is allowed to transmit but high-intensity light is not. Optical limiting originates from various nonlinear optical phenomena such as nonlinear refraction, nonlinear absorption, and nonlinear scattering [263]. In addition to conventional applications, e.g., protection of eyes and sensitive detectors against intense radiation, optical limiting can also be applied to all-optical neuromorphic devices functioning as a proper ultrafast optical switching component [263]. If optical limiting behavior stems from nonlinear absorption of a given glass, an abrupt decrease in the transmission should occur at a given threshold intensity. Optical limiting can also be observed via nonlinear

Table 4
Brillouin scattering-related values of some representative glasses.

Composition (mol%)	SBS gain coefficient (cm/GW)	Brillouin linewidth (MHz)	Brillouin frequency shift (GHz)	Ref.
$74.5SiO_2$-$10.2B_2O_3$-$10.2Na_2O$-$5.1K_2O$	2.2	165.0	34.6	[234]
Silica	2.9	162.0	32.6	[234]
$10K_2O$-$90SiO_2$	3.1	208.0	21.8	[235]
$55.8ZrF_4$-$14.4BaF_2$-$5.8LaF_3$-$3.8AlF_3$-20.2NaF	360.8	96.0	18.8	[235]

Table 5
Raman scattering-related values of some representative glasses.

Composition (mol%)	Raman gain coefficient ($\times 10^{-13}$ m/W)	Raman frequency shift (THz)	Ref.
Silica	1.1	13.5	[238]
$85TeO_2$-$15WO_3$	30.0	21.4	[238]
$85TeO_2$-$10Nb_2O_5$-5MgO	21.0	22.0	[238]
$63TeO_2$-$27Tl_2O$-10PbO	38.0	21.3	[239]
$80TeO_2$-$10Bi_2O_3$-10BaO	38.8	22.3	[240]
$45TeO_2$-10ZnO-$5Na_2O$-$10Nb_2O_5$-$15WO_3$-$15P_2O_5$	49.3	20.3	[241]
$60TeO_2$-10ZnO-$5Na_2O$-$10Nb_2O_5$-$15MoO_3$	72.9	20.1	[241]
$30K_2O$-$30Nb_2O_5$-$40SiO_2$	27.5	19.9	[242]
$As_{40}S_{60}$	279	10.3	[243]
$Ge_7As_{32}S_{61}$	234	10.3	[243]
$Ge_{23}As_{12}S_{65}$	163	10.3	[244]
$Ge_{25}Ga_5S_{70}$	142	10.2	[244]
$Ge_{33}S_{67}$	131	10.3	[244]

Table 6
Third-order nonlinear optical properties of various glasses.

Composition (mol%)	n_0 (@1.55 μm)	n_2 (10^{-17} m^2/W)	$\frac{n_2}{n_2(\text{silica})}$	β (cm/GW)	$\chi^{(3)}$(10^{-12} esu)	FOM $n_2/\beta\lambda$	E_g (eV)	Ref.
$As_{40}S_{60}$	2.45	–	220	<0.030	3.5	>13.12	2.35	[248]
$As_{40}Se_{60}$	2.81	–	930	0.14	26.0	11.94	1.77	[249]
$As_{40}S_{40}Se_{20}$	2.55	–	300	0.06	–	9.03	2.10	[249]
$Ge_{15.12}Sb_{15.11}S_{69.77}$	2.44	4.17	–	22.0	931.1	0.12	2.45	[250]
$Ge_{12.5}Sb_{20}Se_{67.5}$	2.80	1.14	409	0.37	–	0.20	1.57	[251]
$Ge_{15}Sb_{15}Se_{70}$	2.69	1.0	358	0.35	–	2.0	1.62	[251]
$Ge_{17}Se_{83}$	2.33	–	–	–	2.6	–	2.65	[252]
$Ge_{14.45}In_{15}$ $Se_{70.55}$	2.37	–	–	–	3.1	–	2.57	[252]
$Ge_{15.38}As_{30.77}S_{53.85}$	–	–	130	< 0.01	–	> 21.0	2.53	[253]
$Ge_{20}As_{40}Se_{40}$	–	–	620	0.24	–	4.20	1.82	[253]
§$Ge_{31}Sb_9S_{60}$	2.35	0.26	87	<0.10	–	>2.50	1.80	[254]
§$Ga_{10}Sn_{20}Se_{70}$	2.65	–	2491	11.40	–	0.61	1.58	[254]
¶$Ge_{10}As_{20}Te_{70}$	3.66	4.96	–	3.34	–	0.50	0.74	[255]
¶$Ge_{20}Se_{10}Te_{70}$	3.37	2.24		2.23		0.33	0.84	[256]
†$Ge_{33}S_{67}$	2.47	2.75	–	<0.10	21.0	>17.74	2.75	[250]
†$Ge_{30}In_{10}S_{60}$	–	–	2297	17.40	–	0.40	1.97	[257]
†$Ge_{20}Sb_{10}Cd_{7.5}S_{62.5}$	2.40	0.32	–	1.08	–	3.70	2.15	[258]
†$Ge_{26.7}Ga_8S_{65.3}$	2.00	0.06	–	8.75	–	0.01	2.73	[259]
†$Ge_{28.3}Ga_{4.4}Cs_2I_2S_{63.3}$	2.16	0.31	–	1.45	2.8	0.27	2.58	[260]
†10CaO–$35Bi_2O_3$–$55B_2O_3$	–	–	–	0.03	–	–	–	[246]
†$70TeO_2$-$5Bi_2O_3$-25BaO	2.05	0.15	–	2.59	2.4	0.07	3.11	[260]
‡$60Bi_2O_3$-$25GeO_2$-$15TiO_2$	2.24	–	–	0.20	7.2	–	2.17	[261]
‡$60Bi_2O_3$-$20B_2O_3$-$20SiO_2$	2.04	–	–	–	9.3	–	–	[262]

§ measured at 1064 nm; ¶ measured at 3 μm; † measured at 800 nm; ‡measured at 633 nm.

refraction in the form of self-focusing or self-defocusing being responsible for the intensity-dependent transmittance. ChGs are considered as good candidates for optical limiting. For instance, $Ge_{28}Sb_{12}Se_{60}$ glass was demonstrated to exhibit a two-photon absorption coefficient of 3.5 cm/GW, promising for optical limiting applications at ~1 μm [264].

Low-nonlinearity glass: In glasses for high-power laser applications, optical nonlinearities are often parasitic instead of beneficial. The gain coefficient tends to increase in proportion to the linear refractive index by way of the local-field enhancement [265]. On the other hand, the nonlinear refractive index becomes more significant in its effects especially at high optical powers because the refractive index changes accompanied by changes of pump and/or laser intensity [266]. Silicate and phosphate glasses have been used as laser glasses; however, the relatively lower optical nonlinearity inherent in fluoride glasses is fascinating [267]. Combining the better damage threshold of oxide glasses and the lower optical nonlinearity of fluoride glasses can be a good compromise, and in this regard fluorosilicate and fluorophosphate glasses are readily available as practical laser glass [268]. Since the optical gain is determined not only by gain coefficient but also by loss coefficient, synthesis of impurity-free homogeneous glass is crucial for high-peak-power laser applications. In addition to the merits of fluoride glass brought by the reduced nonlinear refraction and nonlinear absorption, the relatively more extended transmission window of fluoride glasses is advantageous in achieving laser activity in mid-infrared wavelengths.

5.3. Recent research trends and future directions in nonlinear glasses

To further enhance the third-order nonlinearity, glass with relatively low nonlinearity can serve as host matrix for semiconductor nanocrystals (quantum dots; QDs) or metallic nanoparticles, which possess very large optical nonlinearities. It has been known that

glasses doped with QDs, e.g., CdS, CdSe, CdTe, PbS, and CuCl, are promising materials for resonant-type nonlinear optical devices with switching times in the picosecond range [269]. Here, the blueshift of the exciton absorption peaks depends on ratio of the QD radius to the exciton Bohr radius. When the excitons possess an effective Bohr radius significantly larger than the QD radius, 'electron-hole confinement' dominates. However, for the opposite situation, the 'exciton confinement' becomes dominant [270]. As a result, the effective exciton mass differs, which, in turn, affects the effective bandgap energy of the QDs as compared to the 'bulk' bandgap energy of the parent semiconductor. This quantum confinement effect normally manifests itself in blue-shifting the exciton resonances upon the increasing quantum confinement with decreasing QD size [271]. The changes both in position and magnitude of the exciton absorptions result in changes of refractive indexes, which can be quantitatively assessed using the Kramers-Krönig transformation. This approach allows a correlation between changes in absorption coefficient and the corresponding changes in refractive index to which the nonlinear refractive index is proportional. As such, the third-order nonlinearity of glass doped with QDs is further enhanced in the case of smaller size and larger volume fractions of QDs [271]. A variety of QD compositions have been introduced into glasses. However, the majority of these compositions are direct bandgap compound semiconductors as opposed to indirect bandgap elemental (unary) semiconductors. Enhancement of third-order nonlinearities that are induced by the embedded QDs is worth noting. Buso et al. prepared Na_2O-B_2O_3-SiO_2 glass doped with 1 wt% PbS QDs via a sol–gel route [272]. The presence of the PbS QDs with average diameter of 3.5 nm, far smaller than the Bohr radius of the 18 nm exciton in bulk PbS crystals [272], was confirmed using high-resolution transmission electron microscopy. Along with the typical blueshift of absorption peak due to the quantum confinement effect, the PbS QD containing glass featured nonlinear refractive index of 2.03×10^{-14} cm^2/GW and nonlinear absorption coefficient of 7.05×10^{-10} cm/GW, both of which were measured using Z-scan method. Du et al. synthesized ZnO-TeO_2-P_2O_5 glasses via conventional melt-quenching technique, and precipitated ZnTe QDs inside the glass matrix [273]. The $\chi^{(3)}$ values obtained using Z-scan technique reached up to $\sim 10^{-11}$ esu, which is roughly 100 times larger than that of silica glass, and 10 times larger than that of tellurite glass, without QDs [273]. The resulting $\chi^{(3)}$ was attributed to the presence of ZnTe QDs, the number of which tended to increase with increasing TeO_2 content in the range from 10 to 30 mol%. More recently, the nonlinear properties of glass doped with perovskite QDs was reported by Xu et al. [274]. Specifically, perovskite $CsPbBr_3$ QDs were precipitated in borosilicate ZnO-B_2O_3-SiO_2 glass through a typical melt-quenching-annealing approach. Together with a strong photoluminescence in the visible wavelengths, the prepared glasses exhibited nonlinear absorption coefficient of 1.85×10^{-12} m/W, which further revealed a cross-over from saturated absorption (SA) to reverse saturated absorption (RSA) by increase either in the pumping intensity or in the QD size.

In addition to semiconducting QDs-doped glasses, metallic nanoparticles (NPs)-doped glasses have been actively pursued as a means to enhance the effective third-order optical nonlinearity [275]. The third-order nonlinear susceptibility of metallic NPs embedded in glass is governed not only by the composition and size of the metallic NPs but also by the effective dielectric constant of the metallic NP-dispersed glass. Appearance of surface plasmon resonance (SPR) induced by the presence of metallic NPs is well-known [276]. SPR evidently observed from the metallic NPs-containing glass tends to enhance their $\chi^{(3)}$ values with picosecond temporal responses. Excitation of the free-electron gas at the surface of the metallic NPs induced by the incident electromagnetic field gives rise to collective oscillations of the free electrons, thus exploiting surface plasmons. If the size of the metallic NPs is significantly smaller than the wavelength of incident light, and the volume fraction of the spherical NPs is very small, then the absorption coefficient of the composite is maximized at the SPR frequency [277]. This corresponds to the collective electronic excitations at the metal/glass interface. The optical response of the metallic NPs-dispersed glass is determined either by the enhanced local electric field near the metallic NPs, i.e., dielectric confinement, or by quantum confinement. It was experimentally verified that the increased third-order nonlinearity of these glasses containing metallic NPs arose mostly from the local electric field enhancement in the vicinity of SPR wavelengths in which a peak $\chi^{(3)}$ value of $\sim 10^{-7}$ esu was observed [278]. A useful figure of merit for these types of nonlinear optical glasses is the $\chi^{(3)}/\alpha$ term. As such, an optimum operation wavelength may be chosen in consideration of the increase of $\chi^{(3)}$ compromised with the corresponding increase of α [278].

As one of the key recent studies associated with glass doped with metallic NPs, works on the formation and characterization of glass doped with bimetallic NPs deserve more attention. Not only optical nonlinearity but also magnetic (or magneto-optic) properties are known to be tailored by employing plasmonic-magnetic bimetallic NPs with compositions of Au-Ni [279], Cu-Ni [280], Au-Cu [281], and Ag-Ni [282] NPs, all being dispersed in silicate glasses. These types of bimetallic NPs contribute to tuning the surface plasmon absorption band, thus enhancing the magnetic-optical properties. A recent study reported that magneto-optic effect of plasmonic-magnetic NPs could be increased by an order of magnitude over the single metal component [283]. As stated, the lack of second-order nonlinearities in glass makes it an ideal host matrix for the bimetallic NPs [279]. For example, glass containing 42 nm-AuNi NPs exhibited large third-order nonlinear susceptibility of 8.14×10^{-11} esu and strong ferromagnetization [279].

A processing route for the preparation of glasses with novel metal and/or semiconductor NPs is worth noting [284]. Lin et al. proposed that Si, Ge, Bi, and Cu NPs can be formed in Na_2O-B_2O_3-SiO_2 glasses via melt-quenching followed by thermal treatment with metallic Al used as a reducing agent. The size of NPs was controlled by heat-treatment temperature and holding time. The fabricated NP/glass composites exhibited large third-order optical nonlinearities of up to 10^{-8} esu and response times of picoseconds.

Optical glasses for use in imaging applications require precisely defined linear refractive index and its dispersion over a suitable range of wavelengths. In this case, the optical nonlinearity can generally be ignored because the incoming optical fields are weak in intensity. It is well-known that a variety of glasses are required to minimize optical aberrations. In the visible spectral range, there are many glass compositions commercially available, represented over a wide range of the Abbe diagram [9]. However, as the performance of image sensors operating in the visible range is rapidly improving, and at the same time as the camera module needs to be more compact for compatibility with mobile devices [285], packaging the optical aberration-free lens assembly into a compact-size camera module becomes more critical. In this regard, glass lenses are replacing polymeric lenses that have been applied for

miniaturized lens assemblies. The most versatile optical glasses for imaging applications require high refractive index and low dispersion, enabling a more compact lens with an increased optical power. Moreover, fabrication process of lenses based on direct machining or precision molding is facilitated because the surface curvature is relieved for refractive lens. In addition, the advent of urban air mobility (UAM) as well as self-driving vehicles should require conspicuously more visible cameras in addition to thermal cameras operating at the long-wavelength infrared (LWIR; 8–12 μm) range. For these applications, in the civilian sectors, processing cost for lens assembly can be mitigated by employing the precision glass molding (PGM), and therefore recent studies are focused on search for moldable glasses [286]. This moldability issue tends to make compositional optimization more complex because PGM process often relies on hard molds such as diamond-like-carbon coated tungsten carbide (WC). Compositional searches for optical glasses for visible imaging uses have been largely performed empirically. However, recent studies utilizing machine learning (ML) are worth mentioning. To develop compositions with tailored Abbe number (ν_d) and refractive index, Zaki et al. elaborated ML models to predict the composition-dependent variations of ν_d and n_d through identifying the contribution of each input constituent towards target prediction [287]. That work verified that glass formers such as SiO_2, B_2O_3, and P_2O_5, and intermediates, such as TiO_2, PbO, and Bi_2O_3, played a significant role in controlling the optical properties. As presented in Fig. 24, an Abbe diagram was created using ML models that allows for the accelerated discovery of new glasses for optical properties.

Cassar et al. sought to correlate the glass transition temperature (T_g) and refractive index (n_d) utilizing a dataset exceeding 40,000 compositions with >37 different chemical elements [288] and employed data-driven predictive neural network models with a genetic algorithm. Glass compositions featuring $n_d > 1.7$ and $T_g < 500$ °C were screened, and two groups of glasses, significantly different from the compositions in the datasets, were explored to demonstrate the usefulness of ML-guided design of optical glasses for use as visible imaging components.

Glasses for LWIR imaging applications, remain relatively unexplored in terms of the compositional diversity required for widening the LWIR Abbe diagram. This should be carried out to keep-up with the rapidly advancing LWIR image sensors, e.g., uncooled microbolometers [289]. Because the candidate glasses should be transparent to a wavelength of at least 12 μm, Se-based chalcogenide glasses have been commercialized mostly in the compositional systems of binary As-Se and ternary Ge-(As, Sb)-Se [290]. For further enhancement of the LWIR glasses, several issues need to be resolved: (1) glass with higher refractive index and less dispersion is in demand, and in this regard a new glass with refractive index at 10 μm (n_{10}) and LWIR Abbe number (ν_{10}) >3.2 and 200, respectively. (2) As noted, the commercialized glasses to date contain As and/or Sb, which are generally considered toxic (though debate on the toxicity of Sb is not resolved yet), so glasses without these elements may be preferred. (3) Ge is costliest among the known constituents (at least 8 times more expensive than the others), which becomes an obstacle to overcome for use in the civilian applications. Therefore, glasses containing no Ge or less Ge would be more competitive. (4) Moldability of the LWIR-imaging glasses should be settled for cost effectiveness of mass production.

Unlike the case of the visible imaging glasses, the refractive index dispersion of LWIR imaging glasses tends to be more sensitive to the IR transmission edge, which results from multiphonon absorption [291]. Therefore, multiphonon absorption, which depends on the vibrational modes present in a given glass, can affect both the IR optical cutoff and the LWIR Abbe number. Fig. 25 presents a typical LWIR Abbe diagram incorporating sulfide, selenide, and telluride glasses as well as mixed-chalcogen glasses. It is worth mentioning that most of the glasses presented in Fig. 25 are already commercially available or will be for use as LWIR lenses. Sulfide glasses tend to feature lower n_{10} values and at the same time lower ν_{10} values than the other ChGs. This is understandable in that sulfur atom is the lightest and lowest in atomic polarizability among the chalcogen S, Se, and Te atoms. This reasoning can also be applied in understanding the behaviors of telluride glasses. Mixed-chalcogen ChGs such as Ge-Sb-S-Se and Ge-Ga-Se-Te glasses would be able to bridge the n_{10} and ν_{10} gaps in the LWIR Abbe diagram that are situated between single-chalcogen sulfide, selenide, and telluride glasses.

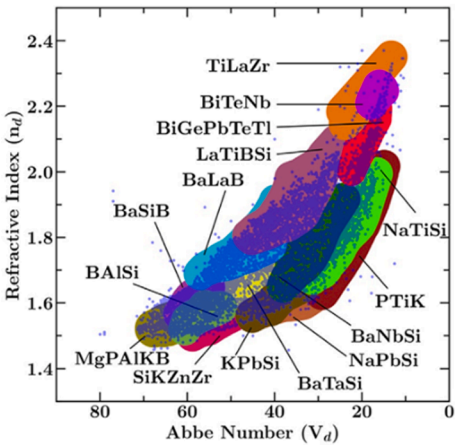

Fig. 24. An Abbe diagram for the visible wavelengths generated using the machine learning models. Points represent the experimental data, and the colored regions indicate the range of properties achievable using respective glass compositions (Reproduced from Ref. [287] with permission from American Ceramic Society).

For use in imaging applications, the moldability of optical glasses is a topic that requires deeper attention for more cost-effective solutions. A multi-cavity molding technique in which at least 4 preforms are simultaneously subject to the PGM process is available, and, further, wafer-level molding techniques are being developed for production of small-size lenses. Moldability issues tend to make the compositional design more complicated. For example, to ensure the service time of a mold, the molding temperature needs to be as low as possible. However, a lower molding temperature needs to consider the thermal stability of the given glass.

Grafting optical metastructures (metasurfaces in many cases) into nonlinear optical glass is anticipated as a viable option to further enhance the nonlinearity performance of glass. In addition to the well-known application of glass-based metalenses, some recent studies concerning metastructured nonlinear glasses show considerable promise. It is noteworthy that ChGs are treated as a proper medium in most cases because of their strong optical nonlinearity and relative ease of deformability for introducing metastructure. As a recent example, the surface of As_2S_3 glass film was metastructured by Xu et al. [292] in such a way that the transmitted light could be reshaped into a beam carrying a well-defined orbital angular momentum (OAM), depending on the intensity of the input light. The strong Kerr effect inherent in the ChG film enabled this reconfigurability, and the use of a resonant design of the metasurface pattern yielded a larger index change as compared to an unpatterned film. Gupta et al. [293] employed ChG metasurfaces to demonstrate experimentally and theoretically that significant SHG can be obtained within the Se-based ChG metasurfaces. A ChG film deposited by evaporation onto nanoimprinted Si master was dewetted to adjust the SHG of the all-dielectric metasurfaces. The measured second harmonic conversion efficiency was larger than a comparable plasmonic metasurfaces or silicon-based structures. Frantz et al. noticed that precise tuning of the resonance frequency is challenging in metastructure fabrication [294]. To resolve this challenge, they exploited the temperature dependence of the refractive index of As_2Se_3 glass. A large refractive index change of approximately 0.1 in the evaporated As_2Se_3 films was responsible for the thermal tuning of ChG-based metastructure. This thermal tuning was exemplified by a metastructure in which a 10-nm shift of the resonance wavelength was shown, thus broadening the feasibility of ChG-based metastructures. Gao et al. experimentally demonstrated a near-infrared to ultraviolet frequency conversion in an As_2S_3-based metasurface [295]. It was evidenced that ChG can also be used to generate THG in the UV frequencies despite the presence of strong material absorption in the UV range. A photonic metasurface consisting of As_2S_3 glass nanowires featured THG intensity to be about 5.5 times larger than that from the reference 300-nm-thick As_2S_3 thin film. Phase locking mechanism between the near-infrared pump and the inhomogeneous portion of the third harmonic signal was proposed to be responsible for generation of the intense THG in the previously unexploited spectral range for ChGs.

As for the future, nonlinear optical materials are playing increasingly important roles in modern photonics for light conversion, amplification, guiding, switching and many more. Nonlinear crystals are still the preferred materials for optical engineers and scientists. However, glasses have numerous advantages in terms of ease of fabrication and shaping, making complex devices possible, which are necessary for practical applications. Different glass families will have different transmission window and very different optical nonlinearity. Glasses with low nonlinearity, such as silica glass, will be able to withstand high pumping power, while glasses having high nonlinear refractive index, such as chalcogenide glasses, only need a short interaction length. Compromise or selection should be performed for each application. The unique capability of glass enabling easy incorporation of other foreign particles inside as well as relatively facile structuring its surface or interior makes lower nonlinearity glass also attractive, in addition to inherently highly NLO glass. Glass intrinsically does not have second order optical nonlinearity because of the isotropic structure. Different techniques have been investigated during the last two or three decades to efficiently break the centrosymmetry of glass. These investigations are among the current research topics on nonlinear optical glasses.

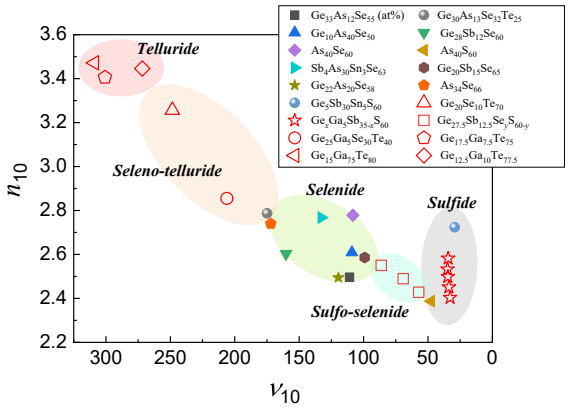

Fig. 25. LWIR Abbe diagram composed of ChGs. Note that the infrared-side transmission edges of most of the ChGs are located at >12 μm. The solid symbols indicate ChGs commercially available for use as thermal imaging lenses, whereas the open symbols denote ChG compositions that are potentially applicable as molded lenses.

Table 7
Main point defects in different glass systems.

Defects		Wavelength of the band maximum (position of the band given in eV)	References
Silicate system			
HC	Hole center	200 (6.2)	[298]
Si-EC	Trapped electrons.	220 (5.6), 245 (5) and 305 (4.1)	
H_I and H_{II}	Trapped holes on one or two nonbridging oxygens on the same SiO_4 tetrahedron	440 (2.8) and 660 (1.9)	
Ozone		258 (4.8)	[299]
Phosphate system			
POHC	Phosphorus oxygen hole center with an unpaired electron shared by two nonbridging oxygen atoms bonded to the same phosphorus	540, 430, 325 (2.30, 2.88, 3.81)	[300]
PO_3^{2-} (phosphoryl)	Defects characterized by an unpaired electron localized on the central P atom generally called phosphorus-oxygen	210 (5.9)	
PO_4^{4-} (phosphoranyl)	electron centers (POECs)	240 (5.17)	
PO_2^{2-} (phosphinyl)		265 (4.68)	
OHC	Oxygen hole centers	290 (4.27)	
Tellurite glass			
Te-NBOHC	Central Te atom linked to three bridging oxygens and one oxygen being a non-bridging one with positive charge indicating a trapped hole	–	[301]
$TeEC/V_O$	Electron and hole trapped in an oxygen vacancy, respectively, while the Te is connected to three oxygen	–	[302]
TeOHC:	Hole trapped in the bridging oxygen	–	[303]
Germanate system			
$(GLPC)^+$	Germanium atom linked to two oxygens and a lone pair of electrons	225 (5.5)	[304]
GEC	Germanium electron trapped center with a fully coordinated Ge atom with an extra electron trapped at the center.	261 (4.75) and 315 (3.9)	
Ge E′	Neutral color center defect where a Ge is linked to three oxygens and the fourth link is replaced by a lone pair of electrons.	197 (6.3)	[305]
Ge-NBOHC	Germanium-related non-bridging oxygen hole center with a central Ge atom linked to four oxygens	375 (3.3)	[306]
$GeO_3^{\cdot}$	Ge linked to three oxygens, and a residual positive charge	–	[307]
Borate system			
B-OHC	Hole trapping on a nonbridging oxygen between 3 or 4 coordinated borons.	360 (3.4) and 500 (2.7)	[298]
B-EC’	Trapped electrons.	240 (5.2) and 280 (4.4)	

6. Photochromic/photosensitive glasses

Photochromic glasses change color temporarily when exposed to light whereas photosensitive glasses change color as a result of radiation treatment. Work on this topic in oxide glasses began in the 1940s. Since the extensive work from Stookey, who investigated the impact of radiation treatment on the optical properties of glasses in various glass systems in the 1950s [296], the investigation of glass-light interaction has been ongoing worldwide ever since. This section reviews such evolution over the past 6 decades, highlighting some of the key findings in both oxide and non-oxide glass materials.

6.1. Principles

One of the first studies examining post-irradiation color changes focused on understanding the impact of glass composition on the optical properties after solar radiation being reported already in the 1950s [297]. To understand their photo-response, glasses have been subjected to different radiation sources ranging from ionizing sources (e.g., alpha, beta, gamma and x-rays) to non-ionizing sources (e.g., radio waves, microwaves, infrared, (visible) light and ultraviolet). The radiation treatment can lead to the formation of internal defects, often referred to as color centers with specific properties, or to structural rearrangements that lead to a permanent or reversible shift in the glass' band edge energy/wavelength. Table 7 lists the most common defects reported in some oxide glasses.

Dopants to retard or eliminate the formation or stability of defects are often added to the glass to compensate and stabilize the charge species created. These additives are called sensitizers and are usually (for negative charge defects) multivalent species which can combine with the charged species to neutralize it. A review of material performance and solarization effects for various oxides is contained in [308]. For further information about photo-response of oxide glasses in various systems, readers are referred to these different reviews [309–311].

Photoinduced effect in chalcogenide glasses has been studied for >40 years as these glasses are known to be photosensitive to band-gap radiation. Here, the photo-response is typically governed by the chalcogen atoms [312] and their lone pairs of electrons. The absorption of the light near the band gap leads to structural rearrangement leading to changes in some properties of the glass such as refractive index and density, as well as other electronic properties where charged species can influence response. The first model of the photo-response of chalcogenide glasses was reported in 1977 [313]. In this model, the absorption of a photon is thought to produce an electron-hole pair generating a bonding state (exciton), the recombination of which occurs by recombination to the fundamental state or by the creation of a metastable pair $D^{+}D^{-}$. Since then, different models have been developed to understand the photo-response of chalcogenide glasses. For some models, the radiation treatment is expected to break and rearrange bonds while in other models it modifies the coordination spheres leading to the formation of residual charge and defects. The different models on photo-induced processes in chalcogenide are summarized in [314]. The photo-response of the As_2S_3 glass has been intensively investigated. Upon illumination (in the bandgap and with a visible/NIR cw/pulsed laser), the structure of this glass becomes more disordered with a larger distribution of bond distances and angles. The irradiation also leads to the creation of As-As and S-S bonds at the expense of As-S bonds in glasses in the As-S system, whereas heteropolar Ge-Se bonds were found to form from the less stable Ge-Ge/Se-Se bonds in $Ge_xAs_{45-x}Se_{55}$ glasses upon radiation treatment [315].

Compaction is usually observed after irradiating glasses with rather open three-dimensional structure such as silica-based and gallium–lanthanum–sulfide glasses whereas expansion is seen in glasses with more dense structure such as As_2S_3 and fluoride glasses [316]. For example, the volume expansion observed after irradiating germanate glass was correlated to the diffusion of the chalcogen atoms, especially S, into the irradiated spot [316].

The changes in the glass induced by the irradiation are often reversible. For some glasses with lower glass transition temperatures, the glass can be returned to its initial state at room temperature over sufficient time (via sub-T_g relaxation impacting optical and physical or mechanical properties) or using a heat treatment at elevated temperatures or an optical illumination [317]. Such mechanisms for a wide range of non-oxide materials have been reviewed in [318].

All the studies on glass-light interaction clearly show that investigating the glass photo-response is extremely difficult and complex. This is because the photo-response varies with glass composition and with the concentration of impurities. Additionally, the glass can exhibit different photo-response depending on the radiation source and parameters. For example, the pre-existing defects in phosphate glasses can be converted into color centers using gamma radiation while the irradiation with an excimer laser can be used to free electrons through multiphoton ionization and hole defect centers [319]. Similar studies have been carried out in non-oxide glasses where their use in planar photonics and potential use in space applications, warrants an understanding of their response to a range of radiation types. These efforts are ongoing but a report on the comparison of time resolved, radiation response of bulk and films of As_2Se_3 to gamma irradiation defines some of the challenges of making such measurements due to the rapid bond-healing that can occur in the low T_g glass network [320].

Although it is a difficult task, it is still crucial to understand the glass-light interaction as the formation of color centers can impact the spectroscopic properties of luminescent glass. Indeed, the color centers are thought to play a crucial role in the photodarkening (PD) process, known to yield a decrease in the performance of the fiber during operation due to the progressive increase in the optical power losses associated with the appearance of a broadband absorption, the intensity of which increases with working time. The first observation of the PD effect was reported in thulium (Tm^{3+}) doped silica optical fibers in 1988 [321] and, almost 10 years later, in Yb^{3+} doped fiber [322]. Although PD in Yb^{3+} doped fibers has been intensively studied, there are still some debates about its mechanism. For example, PD has been related to the creation of color centers and so to changes in the refractive index of the glass [323]. According to Ref. [324], the irradiation leads to the formation of defects in silica glass such as trapped electron centers (TEC), trapped hole centers (THC), and Si-E' centers, which increase the absorption loss. These color centers were found to absorb the pump

leading to an increase in the temperature of the fiber and consequently to mode instabilities damaging the beam quality of the fiber lasers [325]. Others suggested that PD could be due to the partial change of valence of Yb^{3+} ions to $Yb^{2+}$and also due to the hole-related color centers from trapping the charge carriers [326] although the presence of Yb^{2+} has never been clearly verified. Another suggestion for the origin of PD is related to two photons together with phonons from Yb^{3+} ions, which lead to electron transfer between non-binding oxygen atoms [327]. PD is also thought to be related to a non-radiative energy transfer from Yb^{3+} ions to the color defects [326]. The PD mechanism of the photodarkening in Pr^{3+} doped glass was recently published [328] and the addition of Pr^{3+} ions in silicate glasses was reported to promote the formation of TEC while limiting the formation of THC during radiation due to its higher ability to trap a hole center than Si^{4+} and B^{3+} ions. The amount of Pr^{3+} ions is also expected to decrease during lasing due to the potential reaction $Pr^{3+} + h^{+} \leftrightarrow (Pr^{3+})^{+}$ leading to the decrease in the lasing properties. Similar phenomenon is expected to occur in Yb^{3+} doped fiber. For more information, the readers are referred to a recent review on the recent advances in the PD mechanism in active glasses [329].

Extrinsic defects can also be formed upon irradiation. They can originate from the dopants, such as multivalent transition metal elements, as they can easily change their oxidation states during the radiation treatment leading to new absorption bands. For example, Co^{2+}, Mn^{2+}, and Fe^{2+} photo-oxidize to the trivalent state replacing partially the intrinsic hole center defects [330].

Glasses have been also prepared with noble metal ions which can be reduced using radiation treatment due to the formation of defects such as electron and hole traps. These metal ions can grow into metal nanoparticles with specific surface plasmon resonance (SPR) properties changing the color of the glass. The SPR band can be tailored from visible to NIR, depending on the composition of the nanoparticles and on their size, size distribution, shape, and their concentration [330]. This nanoparticles growth phenomenon has been mainly reported in Ag and Au containing glass. For example, a Ag_2O containing phosphate glass was reported to emit at 500 and 620 nm after gamma irradiation due to the electron trapping Ag^0 forming Ag^{2+} species and Ag_3^{2+} emitting centers [331]:

$$Ag^{+} + e^{-} \rightarrow Ag^{0} \quad (1)$$

$$Ag^{+} + Ag^{0} \rightarrow Ag_2^{+} \quad (2)$$

$$Ag_2^{+} + Ag^{+} \rightarrow Ag_3^{2+} \quad (3)$$

Ag_m^{x+} clusters with different m/x ratio are also suspected to form depending on the dose of the radiation source.

Electrons can also be produced by using other photosensitive elements that act as electron donors. For example, Ce^{3+} can interact with the light leading to the formation of Ce^{4+} with the release of an electron.

Using the same principle, glasses have been prepared with electron donors and acceptors but also with halogen ions which can participate in the formation of the crystalline phases. These glasses are known as photo-thermo-refractive (PTR) glasses. The glasses can be locally colored using radiation and thermal treatments. The radiation treatment first leads to the photo-ionization of Ce^{3+} to $Ce^{4+}$and one electron and so Ag^0. A thermal treatment is then used to grow the metal nanoparticles which act as nucleation centers, around which halide crystals such as NaF crystals grow when performing an additional thermal treatment at higher temperature. For more details, a review on the photo-thermal mechanism and crystallization of PTR glass was recently published [332].

Photosensitive agents have also been used to engineer glasses to become dark when exposed to light while reverting to their initial color state after removing the radiation source. This kind of glasses is known as photochromic glasses. The change in the glass coloration is due to the precipitation of noble metal nanocrystals in the bulk with specific absorption properties based on their composition and size. This particularity is due to the presence of crystallites in the glass. These crystallites can be cuprous chloride or silver chloride or bromide. When the glass is impinged by the light with sufficient energy, there is an electron transfer from Cl^- to Ag^+ resulting in a change to Cl and Ag as:

$$Cl^{-} + h\nu \rightarrow Cl + e^{-} \quad (4)$$

$$e^{-} + Ag^{+} \rightarrow Ag \quad (5)$$

The electron is trapped when it reaches a silver atom that is not equivalent to those on interior lattice sites, attracting then more electrons and silver ions until the formation of colloids of silver on the surface of the crystallite. Fading can occur upon removing the light source due to diffusion of the electrons (or holes) leading to a recombination when an electron crosses the surface enclosing the holes. A thermal treatment can also be used to fade the glass due to a diffusion process.

The specific glass composition has a significant impact on the photochromic properties. Glasses can be prepared with different rates of darkening and fading, different sensitivity spectra to the radiation and different optical densities in the darkened state. To increase the darkening and fading rates, sensitizers can be added, such as cerium and europium, although fatigue was reported overtime when adding them in the glass [333]. Other sensitizers such as arsenic, antimony, tin, and copper, for example, can be used.

6.2. *Common applications of photochromic/photosensitive glasses*

3D optical data storage: Silver and tungsten emerge as the most promising candidates, for 3D optical data storage. While ionic silver is of interest due to its high sensitivity to light and its facility to reduce towards the formation of clusters and/or nanoparticles with distinct luminescent properties, tungsten is the focus of studies concerning the redox of W^{6+} ions, which leads to color centers formation and drastic changes in the optical properties. In both cases, chemistry, physics and engineering must work in synergy to achieve the high density of data per cubic inch, necessary to overcome the increased demand for storage information. The interaction

of femtosecond lasers with photochromic silver-based glasses has been the center of intensive efforts to manipulate structures in 2 and 3D. Besides 3D optical storage, many applications are at the cutting edge for photonic devices, including more efficient Bragg gratings and diffractive optical elements. Direct laser writing (DLW) using femtosecond lasers in silver based glasses has been shown to be very promising for 3D optical storage and the patterning has achieved dimensions below the diffraction limit (~100 nm) making possible the storage of hundreds of petabits in reduced dimensions [334]. Depending on the writing conditions, the data storage can be reversible or permanent. However, some drawbacks must be overcome as several factors, such as stability with time, as well as writing and reading speeds, must be established although the mechanisms involved in the photochromic effect are quite comprehended. Active waveguides are other interesting devices to be obtained using silver based photochromic materials. The sizes of the clusters are responsible to tunning the emission of light in the visible range, and in several cases can generate white light as already proposed and stablished in the literature [335]. The production of special waveguides emitting white light will be achieved by the control of power and repetition rate of the laser to tailor the response of the waveguide. The threshold between producing the guide and, at the same time, inducing the controlled photoreduction of silver is very important from technological point of view. Also, depending on the glass composition of the matrix, the color of the glass can follow the reduction and while low refractive index glasses (~1.5) present the SPR in the range from 415 to 450 nm conferring light yellow color to the matrix, other glasses with refractive index higher than 1.8 exhibit SPR bands from 500 up to 600 nm leading to deep red or brown colors.

Holographic optical elements: Photo-thermal refractive (PTR) glasses are already a reality and well stablished devices for the visible and near infrared regions, with applications as volume Bragg gratings, Bragg reflectors, super-narrow band filters, waveguides, laser beam combiners, distributed feedback lasers, among others [332]. Effort has been concentrated on the preparation of holographic optical elements. For example, the substitution of bromide by chlorine in alumino-silicates glasses was reported to decrease the size of the crystals precipitating after a thermal treatment, reducing the scattering in the blue range of the electromagnetic spectra for applications in the higher visible energy range [336]. A recent review of PTR glasses and other photo-induced crystallization materials for gradient refractive index applications that discuss mechanisms and materials for refractive and diffractive optical applications, can be found in [337]. While the visible-NIR spectral range is covered by the aluminum–silicate PTR glasses, another potential spectral range emerges and is related to the tailoring of the transmission window towards the middle infrared, as far as 6 μm, by using heavy metal oxides or heavy metal oxyfluoride based glasses. The challenge here will be to develop new glasses, as stable as the well-known PTR glasses, prepared with chemical elements which can be sensitized by visible light (such as silver) and latter be selectively crystallized by a controlled thermal treatment. Among the most promising candidates, we can highlight germanates and gallates based glasses. Extending the transmission window to such region is pertinent once new sensors for detecting pollutants and greenhouse gases are emerging rapidly, but up to now, functionality in this region is only covered by chalcogenide glasses [338].

5D data storage: Recently, a 5D data storage material has been proposed by P. Kazansky and collaborators using fused silica and the formation of nanogratings by irradiation with femtosecond lasers [339]. Access the 4th and 5th dimensions is based on the use of different wavelengths associated to changes in the polarization states. With this approach, the possibility of encoding 10 Tb in a small spot size of 100 nm was demonstrated through the technology called super-resolution photoinduction inhibition nanolithography (SPIN), which breaks the optical diffraction barrier, reaching sizes as low as 9 nm (Fig. 26).

Such technologies have been demonstrated using fused silica. Another important feature stems from the fact that its lifetime is estimated to 319 million years, making it the most long-lived data storage structure known. Since 3D data storage in tungsten based photochromic was proposed by Poirier et al. in 2006 [340], the challenge has been to obtain more reliable and trustable materials along the time. Recently, researchers have demonstrated that the addition of rare earths together with tungsten increases both resolution and readability and consequently the resolution of the data storage transforming such glasses into alternatives technologies for 3D data storage. Tungsten phosphate [117] and tungsten borates [341] reversible photochromic glasses seem to fulfill partially some of the prerequisites necessary to encode data inside the glass using visible and femtosecond laser sources, respectively. In both cases, the authors added RE ions in combination to tungsten to increase the readability of the encoded data using luminescence processes

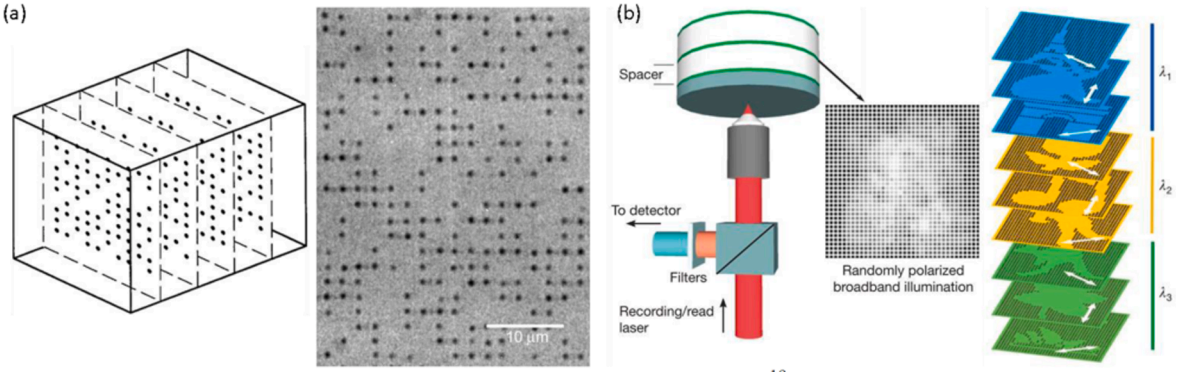

Fig. 26. (a) Binary 3D data pattern stored in fused silica by femtosecond laser. (b) Multiplexed 5D optical memory using gold nanorods. The patterns were fabricated using different wavelengths and polarization states as 4th and 5th dimensions (Reproduced from Ref. [339] under the terms of the Open Access Publishing Agreement).

improving the quality of the material. In the borate system, silver was added to the other two components, allowing the uses of the femtosecond lasers and increasing the fidelity and resolution of the reading data. Even if significant advances are achieved in new 3D data storage media in tungsten-based glasses, it is clear that improvements to achieve long time stability and high resolution of both writing and erasing processes must be demonstrated to pave the way towards the market.

6.3. *Recent research trends and future directions in photochromic / photosensitive glasses*

Recent global efforts have focused on the development of glasses with tailored photo-response, which is achieved by modifying the glass composition. For example, when developing high-power laser fibers, it is crucial to develop glasses with suppressed photo-induced phenomena, such as PD, which is one major factor limiting their output. One of the approaches to develop photo-resistant glasses is to optimize their glass composition. As noted, a potential origin of photodarkening in Yb^{3+} doped silica fiber is the Yb clusters, which can be reduced by adding Al_2O_3 or P_2O_5 in the glass [342]. Indeed, the addition of Al_2O_3 or P_2O_5 in the silica glass leads

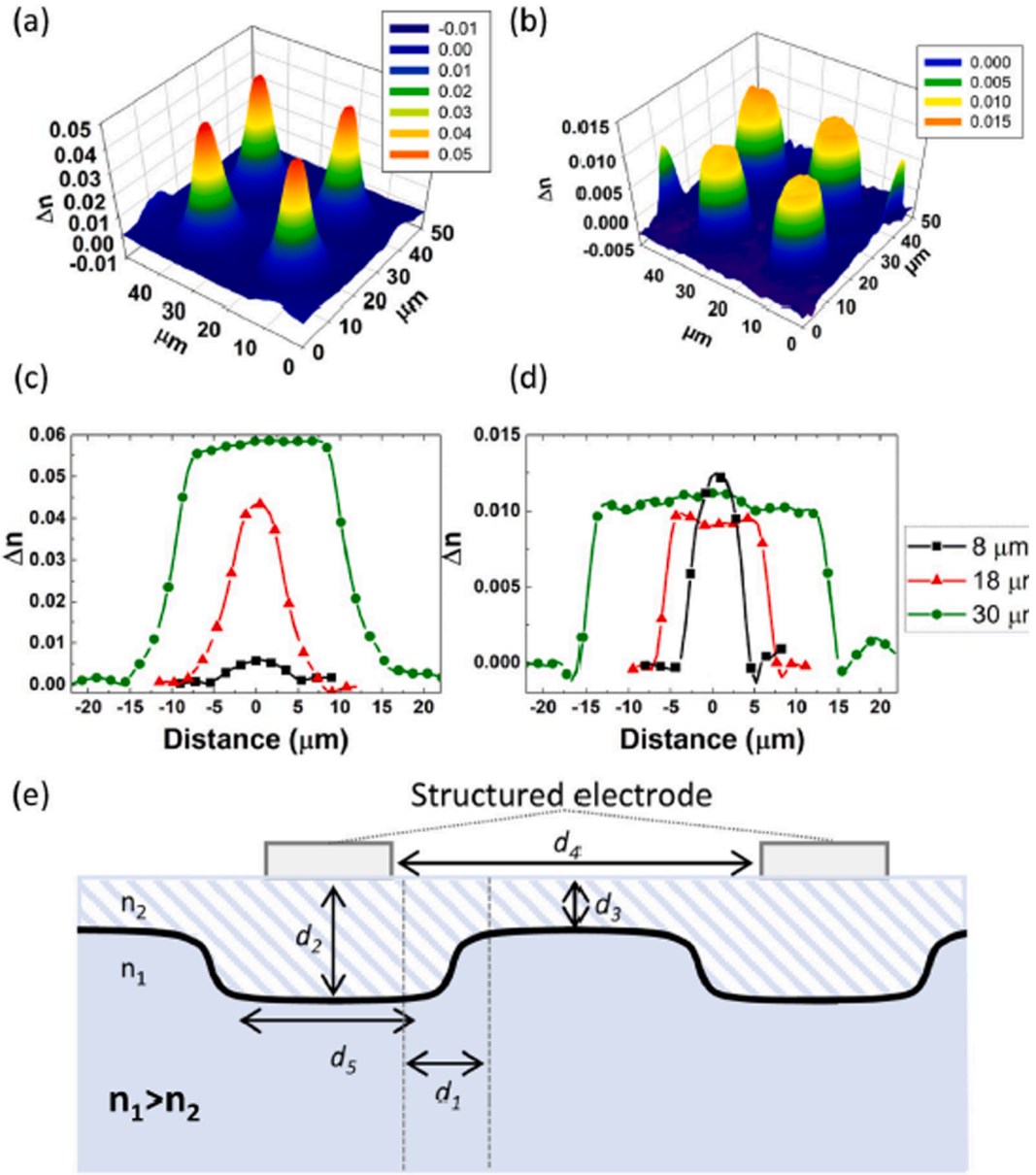

Fig. 27. Phasics map at λ = 750 μm of 18 μm spots imprinted on a chalcogenide (a) and soda lime glass (b) subjected to identical poling voltages; Δn profiles measured across circles 8, 18 and 30 μm wide on a chalcogenide (c) and soda lime glass (d); principle parameters controlling the gradient of index geometry in the glass after thermal poling (**e**). (Reproduced from Ref. [355] under the terms of the Open Access Publishing Agreement).

to the formation of non-bridging oxygen increasing the Yb-Yb distance and thus avoiding Yb^{3+} clusters in the glass [343]. According to Deschamps et al. [344] P_2O_5 doping allows a better dissolution of the Yb^{3+} clusters leading to lower level of PD than Al_2O_3 doping due to the shift of the charge transfer band to higher energy. Jetschke et al. demonstrated that PD could be suppressed by adding the same concentration of P_2O_5 and Al_2O_3 in the Yb^{3+} doped silica glass [345]. Reduction in PD was also reported after adding Tm^{3+} or Er^{3+} ions to act as a de-excitation channels [346]. Engholm et al. demonstrated suppression of the photodarkening in Yb^{3+} doped glass by co-doping the silica glass with Ce^{3+}, which can inhibit the formation of defects [347]. Indeed, the holes centers formed while pumping the fiber are trapped by Ce^{3+} leading to the formation of Ce^{4+} though the reaction $Ce^{3+} + h^{+} \rightarrow Ce^{4+}$. Ce^{4+} can then capture the electron center leading to the formation of Ce^{3+} through the reaction $Ce^{4+} + e^{-} \rightarrow Ce^{3+}$. Ce^{3+} was found to have similar role in Pr^{3+} doped fiber. As mentioned also in the previous section, PD has been also related to the defects present in the silica network, especially the non-bridging oxygen hole centers (NBOHC) and the aluminum oxygen hole centers (AlOHCs). The addition of H_2 during the glass processing was reported to be useful to reduce these defects as the H_2 molecules can easily diffuse in the glass and react with NBOHC. Following the reaction: $Si–O \cdot O–Si + H_2 \rightarrow 2Si–OH$, H_2 allows the formation of –OH bond while releasing the electrons bound with the hole-related defects [348]. Recently, deuterium loading was also reported to be more efficient to suppress PD in Tm^{3+} doped fiber than H_2 loading due to the reaction of deuterium with peroxide defects forming ─OD bonds ($Si–O \cdot O–Si + D_2 \rightarrow 2Si – O\text{-}D$) [349]. Effort has been also focused on reducing the photo-induced phenomena in other glasses. For example, elements, such as Nb_2O_5 or Sb_2O_3, were reported to inhibit the formation of defects in oxide glasses [350]. The electrons released during the radiation treatment of phosphate glass can be captured by Nb^{5+} ions or Sb^{4+} ions avoiding then the formation of defects such as POECs and POHC in large amounts. Similar reduction in the number of defect-forming during the radiation treatment was observed after adding PbO, or V_2O_5, in phosphate glasses or TiO_2 in silicate glasses [351].

Although efforts have focused on developing chalcogenide glasses with increased photosensitivity, less effort has been focused on the development of photo-stable chalcogenide glasses. These glasses can have restricted applications due to their photo-response, which impacts their optical properties. For example, Cu or Pb can be added to tighten the network increasing the photo-resistance of chalcogenide glasses in As-S, As-Se and Ge-S system which is associated with the disappearance of the changes in the structure upon irradiation [352]. Very few studies have been focused on optimizing the chalcogenide glass composition to increase their photo-resistance. Chalcogenide glass with the $Ge_{10}As_{35}Se_{55}$ composition was reported as the first ChG glass with negligible photosensitivity [353] which was related to the mean coordination number (MCN), defined as the sum of the products of the individual abundance times the valency of the constituent atoms). Su et al. demonstrated that glasses in the Ge–As–Se system with low and high MCN, meaning with floppy and stressed-rigid phases, respectively, have large photosensitivity whereas the glasses with a MCN between 2.45 and 2.5 are the most photo-stable glasses [354].

Recently, efforts to engineer glass networks to accommodate such structural changes to enhance long term stability have gained ground. As an example, thermal-electric induced rearrangement has been demonstrated in alkali-doped Ge-Sb-S glasses designed for thermal-electric poling for gradient index (GRIN) optics. In these studies, demonstrated in both oxide and this chalcogenide glass system, long-lived (>4yrs) post-poled refractive index changes were demonstrated when the glass network was designed specifically with excess non-bridging anion sites, that allowed the physical accommodation of the diffusing Na^{+} ion, preventing its post-poled relaxation over time [355]. Such a ‘lock and key’ mechanism can be employed if its use does not adversely impact other desirable optical properties. Fig. 27 illustrates the resulting refractive index profiles possible related to the gradient in alkali content achieved

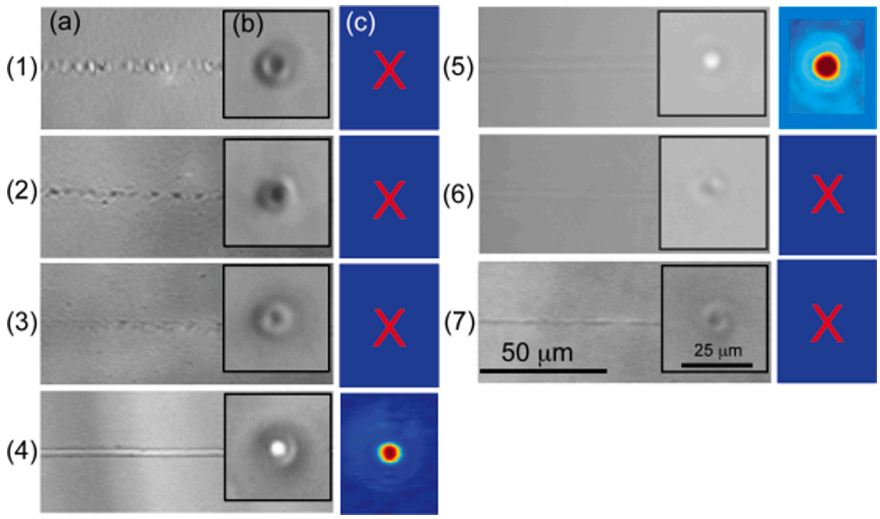

Fig. 28. (a) Images of the modification along the waveguide direction, (b) Transmission images of the modification cross-section and (c) 660 nm transmission near field images of (1) $30.0ZnO\text{-}10.0Al_2O_3\text{-}60.0P_2O_5$; (2) $50.0ZnO\text{-}50.0P_2O_5$; (3) $55.0ZnO\text{-}45.0P_2O_5$; 4) $60.0ZnO\text{-}40.0P_2O_5$; (5) $0.7Er_2O_3\text{-}1.3Yb_2O_3\text{-}56.0ZnO\text{-}42.0P_2O_5$; (6) $0.7Er_2O_3\text{-}1.3Yb_2O_3\text{-}58.8ZnO\text{-}39.2P_2O_5$ and (7) $65.0ZnO\text{-}35.0P_2O_5$ glasses (Reproduced from Ref. [359] under the terms of the Open Access Publishing Agreement).

with a patterned electrode. Variation of the structured electrode shape (circles, squares, gratings) can lead to realization of a range of optical functions in both oxide and non-oxide glasses (micro-lens arrays, gratings, structured high χ^2 media (i.e., for use as splitters in planar photonics [223]), local variation in surface chemical reactivity), if the post-poled network structure can be stabilized.

Photo-sensitive glasses have been also of great interest for the various applications described in the previous sections. One of the main goals is thus to develop glasses with increased photo-sensitivity useful for light activated patterning. For example, optical waveguides were successfully inscribed in fused silica and germanate using different radiation sources, even using femtosecond infrared signal pulses at 1.5 μm [356]. Recently, waveguides with losses as low as 0.2 dB/cm were successfully obtained from Yb^{3+} doped lead-germanate glass with laser slope efficiency of ~28%, the highest reported in such glass [357]. Waveguides have been also written in glass in the TeO_2-Na_2O system, one of the first waveguides being reported in 2014 [358]. It is the migration of the Te atoms towards the irradiated areas which increases the refractive index whereas the Na atoms travels to the tellurium deficient zone leading to a region with low refractive index. Phosphate glasses usually exhibit a reduction in the refractive index upon irradiation with fs laser. Fletcher et al. demonstrated that ZnO could be added in phosphate glasses in order to successfully write waveguides in which light can be confined due to an increase in the refractive index after irradiation (Fig. 28) [359].

Elements such as Ge, B, Pb, Bi, Sn, Ce^{3+}, Eu^{3+} can be added into the (silica, germanate, phosphate) glasses to increase their photosensitivity as, for example, shown in [360]. The photosensitivity can also be tailored by changing the atmosphere used during the glass preparation. For example, a larger increase in the refractive index was obtained by melting a Bi containing silicate glass in nitrogen atmosphere and was related to the incorporation of N in the glass structure [361].

Recently, a novel type of positive refractive index modification following irradiation with femtosecond laser pulses was reported from phosphate glasses [362]. Silver was added in the phosphate glass so that silver clusters Ag_m^{x+} are formed at the periphery of the interaction voxel during the laser writing allowing the inscription of the waveguides as illustrated in Fig. 29 **a** and **b.**

Using similar technologies, lasers were used to write 3D patterning at the sub-micrometer scale in zinc phosphate glass as shown in Fig. 30**a and b** [363].

Electron-beam irradiation, for example, also has been demonstrated as a promising and alternative radiation source to form the Ag nanoparticles. This approach may allow for the fabrication of nanoplasmonic devices as it allows the precipitation of Ag nanocrystals in high concentration at the subsurface of the PTR glass [364].

Chalcogenide glasses are highly photo-sensitive especially to visible light exposure. The ability to write waveguides into chalcogenide has been also demonstrated for years. Recently, 3D structures in As_2S_3 glass were obtained by combining laser writing and chemical etching which is used to etch selectively the unexposed glass [365]. Glass patterning can also be obtained by locally precipitating crystals using radiation treatment. In this process, the laser powers and translation speeds should be optimized to control the nucleation and growth of the crystals. Numerous studies on the localized precipitation of crystals in oxide glasses can be found in the literature. For example, laser was used to structure phosphate glasses with lines of $KSm(PO_3)_4$ crystals [366] and also nonlinear optical crystals lines such as β-BaB_2O_4 crystals with c-axis orientation along to the laser scanning direction, $LiNbO_3$ crystals and $Li_2Si_2O_5$ crystals [367], $Ba_2TiGe_2O_8$ crystals [368], and even active crystals such as Er^{3+}-doped CaF_2 [369]. However, contrary to the oxide glasses, very little in this topic has been done on chalcogenide glasses due to different challenges related to the formation of crystals in chalcogenide glasses as discussed in [370]. Nonetheless, using direct laser writing, single SbSI crystals were found to grow in chalcogenide glasses [371].

Lasers have also been used to pattern photo-thermo-refractive glasses. The two commercially available PTR glasses are Foturan (Schott, Germany) and PEG3 (Hoya, Japan). These lithium silicate glasses are prepared with cerium and silver which act as photosensitive agents as discussed in the previous section. As explained earlier, the UV irradiation leads to the photoionization of Ce^{3+} ions with trapping the photoelectrons by the Ag^+ ions which grow into silver nanoparticles during the subsequent thermal treatment. These Ag nanoparticles act a nucleation agent for the growth of NaF-AgBr phases. Effort has been focused on the development of transparent PTR, implying the control of the process so that the nanocrystals are small (20–40 nm). Studies demonstrated that it is the UV dosages that controls the number of nucleation centers whereas the size of the nanocrystals and their volume fraction are controlled by the heat treatment parameters [372]. For the past decades, effort has been focused on developing new PTR glasses with lasing properties. Aseev

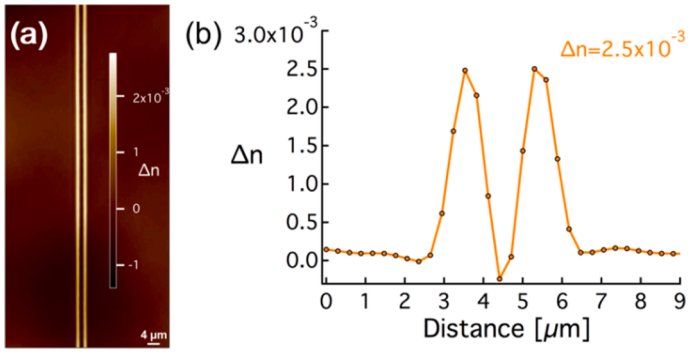

Fig. 29. (a) Top view of the waveguide under illumination at around 550 nm and (b) refractive index profile. (Reproduced from Ref. [362] under the terms of the Open Access Publishing Agreement).

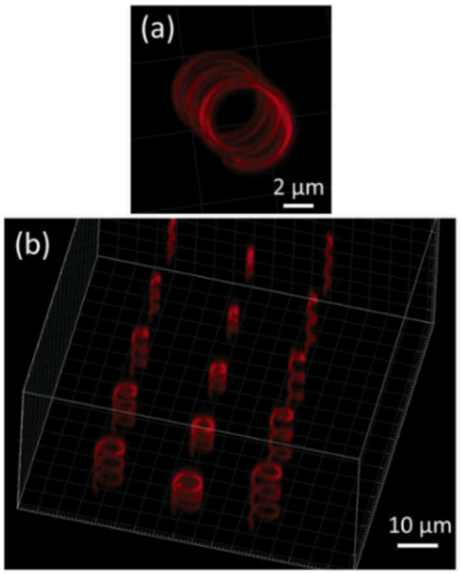

Fig. 30. (a) Single and (b) array of helicoidal patterns with different dimensions. (Reproduced from Ref. [363] with permission from John Wiley and Sons).

et al. were the first to report PTR glass co-doped with Er^{3+} and Yb^{3+} with similar laser characteristics than the commercially active phosphate glasses [373]. Few years later, Nd^{3+} doped PTR glass was reported with a wide bandwidth laser action at 1053.9–1063.3 nm [374]. As the PTR glass contain sodium, waveguides can be developed using ion exchange technology. This process occurs at low temperature and the refractive index increases due to the replacement of Na^+ by Ag^+ which leads to changes in various properties of the glass surface layer such as the thermal, structural and optical properties for example. Sgibnev et al. were the first to report ion exchange process in PTR [375] and few years later, planar waveguides with low losses were demonstrated by exchanging Na^+ by Ag^+, K^+, Rb^+ or Cs^+ [376].

Although research and development of new photo-sensitive / photo-resistant glasses have been extremely active for decades, fewer studies have been conducted to develop novel photochromic glasses. Tungsten based glasses are, by far, the most studied since being first reported in 1978 [377]. The expansion of the studies into other materials emerged in the beginning of this century with the works of Poirier et al. [378]. They systematically explored the redox effect in tungsten-based phosphate glasses with respect to different wavelengths of irradiation and demonstrated, for the first time, the possibility to store data in 1, 2 or 3D arrangements using different sources of light. The photochromic effect in that case was demonstrated to be reversible by thermal treatment in moderate temperatures. Since then, several papers have explored the color changes and fundamental aspects related to this property of tungsten containing glasses [378,379]. Broader fundamental studies about new photochromic glasses containing tungsten have led to the combination of many chemical elements, and a review about such glass systems can be found in [380]. The special characteristics of all these chemical elements arises from the possibility to change their oxidation state under the correct energy of irradiation. During the glass synthesis the tungsten atoms are intended to be stabilized in their highest oxidation states, W^{6+}. From transition metal chemistry, it is well known that the color of compounds can be manipulated from changes in the crystal field splitting around the metal when d electrons are available to promote electronic transitions. Thus, since electrons are present into d orbitals, internal d-d electronic transitions are expected, and most of them have their maximum absorption in the visible range. To induce the reduction of W^{6+} cations towards electronic configurations, such as W^{5+} or W^{4+}, selected chemical elements, such as Sb^{3+} Ce^{3+}, and Sn^{2+}, need to be added to the glass batches to act as electrons donors, as shown by Stookey [381]. Tungsten oxide or sodium tungstate can be used as raw materials. However, they lead to different electronic configurations into the glass matrices; while WO_3 presents WO_6 octahedral units, it is encountered as tetrahedral WO_4 units in Na_2WO_4. Structural differences apart, both present d^0 W^{6+} ions while the reduced ion W^{5+} has d^1 configuration. In the reduced ion, d-d transitions are allowed and are manifested by a large absorption band in the visible range, usually, conferring blue color to the glass. As the WO_6 octahedral can be influenced by the ligand field, the chemical composition of the matrix may also induce changes in the tonality of the blue.

While a wide range of advances have been made, there remain multiple challenges and questions that still require further study. Specifically, how can photo-induced property modification be achieved at will to tailor properties through secondary phase formation or alternative strategies? Can this be carried out with minimal influence on spectral loss and or induced nonlinearities that are often undesirable? What is the long-lived stability of such modifications to allow them to be reversible or irreversible, as desired? Is it possible to exploit such changes to enable new functionality in a glass, regardless of its form (bulk, film or fiber)? Many questions still remain about the mechanism for the index change under light and for photodarkening. Further improvement in the reduction of the propagation loss is needed when writing waveguide by optimizing not only the quality of the glass but also the laser parameters used to inscribe the waveguide. The answers to these questions will enable further advances to enable the use of glass in future component and

device designs, that are not yet envisioned.

7. Magneto-optical glasses

This section highlights recent developments in magneto optical (MO) glasses. Magneto-optic effects relate to changes in the polarization state of light, usually polarization rotation, as it passes through an optical medium in the presence of a magnetic field [269]. Such effects were first observed by Faraday in the middle of the 19th century [382].

7.1. Principle

Magneto-optical (MO) effects, especially in glasses, manifest in two general methodologies: transmission of light through an MO glass or reflection from its surface. The first transmission is more commonly called "Faraday rotation," or the "Faraday effect," while the second one is the called Kerr magneto-optic effect [383]. In both MO cases, the effects are related to changes in the polarization state of light. The mathematical development belying such effects will not be explored here. The interested reader can find the theory in recent reviews and books [269,384,385].

In glasses and glass-ceramics, the Faraday effect is the more explored of the two cases. The Faraday effect can be described by $\theta_F = V.l.B$, where, θ_F is the rotation angle of the polarized light beam transmitted through a medium in the presence of a magnetic flux density B. V is the Verdet constant, which depends on the properties of the material, particularly its chemical composition and magnetic moment, and l is the propagation length of the light through the material in the presence of the magnetic field. For devices making use of this property, such as optical isolators, optical modulators, magnetic and electric field sensors, etc., it is important to obtain high values of θ_F since the sensitivity of the device will be proportional to its magnitude. In this sense, the aim of the researchers is to obtain materials with high Verdet constants.

Inorganic materials, including glasses, can be classified into four main families according to their interactions with a magnetic field: Ferromagnetic, ferrimagnetic, paramagnetic, and diamagnetic. The two first families present the highest values of V, which can range from 10^3 to 10^6 times higher than those observed for diamagnetic and paramagnetic materials. Despite that, ferrimagnetic and ferromagnetic materials are not commonly used in MO devices intended for use in the visible to near infrared spectral region, because they also exhibit high optical absorption levels in the spectral ranges of use. The figure of merit (FOM) defining the utility of a MO material is $FOM = \frac{\theta_F}{A_{db}}$, where A_{db} is the absorption coefficient at a given wavelength, in decibel.

The difference between diamagnetic and paramagnetic systems arises from the presence or absence of unpaired electrons and, consequently, of magnetic moments. Glasses containing filled orbitals are diamagnetic and present no magnetic moments, whereas those containing unpaired electrons are paramagnetic, where the unpaired electrons can be aligned in the presence of an external magnetic field. As described above, the Verdet constant depends on the magnetic moment exhibited by the glass and, as an example, silicate glasses usually exhibit values between 4 and 27 $rad{\cdot}T^{-1}{\cdot}m^{-1}$ [385] while Tb^{3+} containing glasses can reach >100 $rad{\cdot}T^{-1}{\cdot}m^{-1}$ (both measured at a wavelength of 633 nm) [386]. The appearance of such effects in diamagnetic glasses originates from its high refractive index associated with large polarizable atoms, such as Pb^{2+}, Bi^{3+}, La^{3+}, etc. [269].

The number of paramagnetic ions and, consequently, the magnitude of the magnetic moment that can be induced, will dictate how large the magnetic flux density needs to be to yield the necessary rotation for a given material and interaction length. Transition metals, such as Mn, Fe, Co, Ni and their related oxides are classic ferromagnet species when doped into crystalline phases. On the other hand, the presence of these ions in glasses make them only fair paramagnetic materials. From the viewpoint of chemical synthesis, the way to increase the magnetic moment in paramagnetic glasses is by adding rare earth ions, since these elements possess unfilled inner electronic shells. It is possible to calculate the magnetic moment and, thus predict the intensity of the magnetic moment by $\mu_{eff} = g_J\sqrt{J(J+1)}\mu_B$, where, μ_B is the Bohr magneton and g_J may be calculated from the equation $g_J = \frac{3}{2} + \frac{S(S+1)-L(L-1)}{2J(J+1)}$, where L and S are the total orbital molecular momentum and total spin angular momentum, respectively and J is the total angular momentum.

Table 8 summarizes magnetic moments calculated or observed experimentally for selected transition metal and rare earth ions. The experimental values for the transition metals are slightly lower than those calculated because electrons in the outer shell of transition metals are influenced to a greater extent by neighbor ions leading to crystal field splitting and subsequent quenching the orbital molecular momentum.

For practical purposes, considering only applications for glasses, the following aspects must be considered to obtain higher θ_F values.

Table 8
Magnetic moments, calculated and obtained experimentally, for selected paramagnetic ions [387].

Element	*Term*	$m_{eff}/(m_B)$ *calc*	$m_{exp}/(m_B)$ exp
Fe^{2+}	$^5D_4$	6.7	5.3
Mn^{2+}	$^6S_{5/2}$	5.92	5.9
Ce^{3+}	$^2F_{5/2}$	2.54	2.4
Tb^{3+}	$^7F_6$	9.72	9.5
Dy^{3+}	$^6H_{15/2}$	10.65	10.4

***(1) Refractive index of the matrix*:** Several studies have shown that glasses with higher refractive indices exhibit larger Verdet constants, even for diamagnetic materials. Accordingly, heavy metal oxide glasses, based on borogermanates, have been shown to be best [388] due to their high refractive index associated with the heavy metal ion concentrations. The relationship between the Verdet constant and the polarizability of the entities present in the glass compositions can be better understand by means of the equation $V = \frac{-3\alpha^2 I}{4r^6}$, where α is the polarizability (in m^3), I is the ionization energy of the atom, and r is the distance between atoms.

***(2) The concentration of the paramagnetic ions*:** As stated, the number of paramagnetic ions contributes to an increase in the MO property of glasses. For practical purposes, terbium has been shown to be one of the best candidates to MO devices due to possessing the highest magnetic moment per ion and a wide transparency range that extends from ~500 to 1600 nm. However, the solubility of Tb^{3+} or any transition metals or rare earths, is relatively limited [389–391].

(3) The application wavelength: Many devices are idealized to be used at 633 nm or in the near infrared region, such as at 1550 nm for telecom applications. However, the Verdet constant is higher in the vicinity of the absorption line, increasing from the visible towards the UV region. The relationship of V as a function of the wavelength is explained by the Van Vleck-Hebb theory and can be expressed as $V^{-1} = \frac{g\mu_B ch}{4\pi^2 \chi C_t}\left(1 - \frac{\lambda^2}{\lambda_t^2}\right)$, where, g is the Landé g-factor, c is the velocity of light, h is the Plank constant, χ is the magnetic susceptibility, C_t is the probability of effective transition, and λ_t is the wavelength of the effective transition.

7.2. Typical applications of magneto-optical glasses

Magneto optical glasses are mainly used in non-reciprocal telecommunication devices including Faraday rotators, circulators, or isolators and for magnetic and electric field sensors.

Faraday rotators, circulators, or isolators: MO glasses prevent back reflection of light into lasers or optical amplifiers and reduce signal instability and noise. MO glasses are crucial elements to use in high-power controlled laser fusion experiments, for example, where amplified light is directed against a small target as there is a risk that laser materials or optical components are hit by light back reflected by the target, so they need to be protected against such a possibility, by an optical isolator. For these applications, temperature insensitivity over a broad temperature range is required. Thus, diamagnetic glasses are commonly chosen as their temperature dependence is much less than that of paramagnetic materials.

MO glasses are used as optical components to allow the light to travel in only one direction (Fig. 31).

The plane of polarization of the linearly polarized laser light is rotated 45° by a magneto-optical glass placed in a magnetic field. If the same laser light is reflected back through this same path, its plane of polarization is rotated a further 45° when it passes through the MO glass becoming perpendicular to the polarization of the incident light,

Magnetic and electric field sensors: these sensors are typically made of fiber coil rotating around an electric power cable. The polarization state of the light propagating in the coiled fiber is rotated due to the Faraday effect generated by the current passing through the cable, and emitted from the fiber. The light is divided into two orthogonally polarized beams and the rotation of the polarization angle is converted into intensities of light. Such sensors based on optical fiber present significant advantages compared to typical electrical sensors. For instance, they show no interference with electromagnetic radiation. Consequently, they can be used in hostile environments where typical sensors would fail [392]. The magneto-optical sensors can also be envisaged to monitor very low magnetic fields. For example, the magnetic field of the Earth is in a scale of micro-Tesla, while changes in the magnetic field in the vicinity of a volcano produced by an imminent eruption can be in the range of few nano-Tesla. Still less intense than such fields, there is a range called biomagnetic signals, produced by human organs, such as heart and muscles which can extend from few nano-Tesla to femto-Tesla.

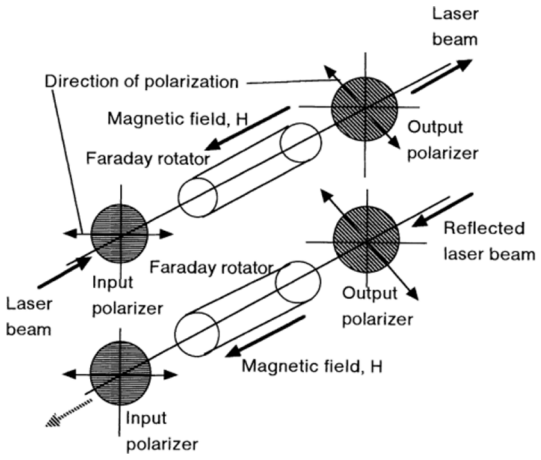

Fig. 31. Principle of optical isolator using Faraday effect [269].

7.3. Recent research trends and future directions in magneto-optical glasses

Among the most promising compositions for magneto-optical glasses are borates [393], aluminosilicates and borogermanates [388,390], borosilicates [394], gallogermanate [395], phosphates [269], and fluorophosphates [396]. The development of new glasses exhibiting enhanced magneto-optical properties is largely focused on fundamental properties [397]. Some glasses already exhibit Verdet constants in excess of the standard TGG crystals (-134 rad·T^{-1}·m^{-1} at a wavelength of 633 nm) and can be as high as −300 rad·T^{-1}·m^{-1} [398] for special synthesis conditions and −234 rad·T^{-1}·m^{-1} using aerodynamic levitation techniques [399]. For more conventional techniques, such as melt-quenching Verdet constants range are on the order of −172 rad·T^{-1}·m^{-1} for a borogermanate-phosphate glass containing both Tb_2O_3 and Ho_2O_3 [400] and −162 rad·T^{-1}·m^{-1} for a borogermanate-silicate glass combining Tb_2O_3 and Dy_2O_3 [401]. The highest value reported was −184 rad·T^{-1}·m^{-1} [402]. However, Ho^{3+} has several visible absorptions that may limit applicability. Further increases in Verdet constants without compromising the thermal stability may require non-conventional glass fabrication methods, such as levitation processing [399].

Transparent glass-ceramics exhibiting magneto-optical properties are not so common in the literature and only few works having been reported [403–405]. Recently demonstrated are glass-ceramics based on rare earth gallium garnets in complex glass compositions, preserving the transparency in the visible range [406]. As observed for crystalline materials or thin films, magnetic nanoparticles can be used for magneto-optical applications due to their very high Verdet constants when doped into glasses. As an example, ferromagnetic nanoparticles of different compositions, including oxides or metals, were incorporated in calcium phosphate glasses [407–409]. As phosphate glasses are quite known to be very good media to dissolve both oxides and metallic nanoparticles, the ferromagnetic nanoparticles must be protected before been incorporated into the glasses as in [409]. The monodispersed $Fe_{3-\delta}O_4$ nanoparticles shown in Fig. 32**a** were first covered with a SiO_2 shell (Fig. 32**b**) then mixed with calcium phosphate coacervates prior to the melting. The transmission window of the phosphate glass was not compromised either by the presence of transition metals, such as Fe or Co, nor by scattering, due to the small size of the particles. (Fig. 32**c**). Using this fabrication technique, both the core and shell of the nanoparticles are preserved after melting (Fig. 32**d** and **e**).

Such process to fabricate hybrids can be employed for a series of different nanoparticles and can take advantage of the very high Verdet constants of crystalline phases, such as bismuth yttrium iron garnet, $BiYFe_5O_{12}$. The Verdet constant of these magnetic phases can be employed beyond those available from the paramagnetic glasses, which can be drawn into optical fibers to take advantage of length.

Current sensors based on glass optical fibers are commercially available, but the high doping required for increased Verdet constants makes single mode operation difficult. Bragg gratings written in the core of the fibers and the construction of complex interferometers systems are alternatives to increase the sensitivity of silica-based fibers [410]. The next generation of magneto-optical fibers should include the properties described above along the high sensitivity of heavy metal oxide glasses comprising the paramagnetic ions. In Fig. 33 are shown the preform of a MO borogermanate glass containing high content of Tb^{3+} (a) and the fiber obtained from it (b). In Fig. 33**c** is shown the Verdet constant measured for the fiber as a function of the wavelength [386]. The Verdet constant measured at 1550 nm is about 9.5 rad·T^{-1}·m^{-1}, what is 16 times higher that of the silica multimode fibers at the same wavelength.

Future exploration includes the development of novel stable glass compositions with higher contents of rare earths and of hybrid photonic crystal fibers containing magnetic fluid infiltrated nanoholes [411]. Ferromagnetic nanoparticles solutions, which are

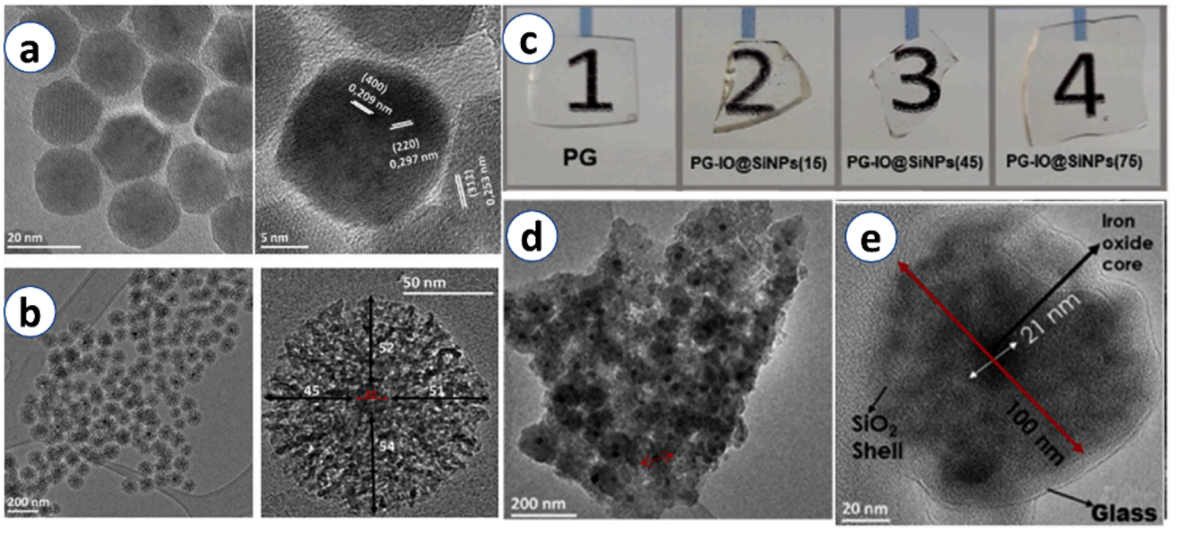

Fig. 32. (a) TEM micrographs of $Fe_{3-\delta}O_4$ nanoparticles, NP, (b) TEM micrographs of $Fe_{3-\delta}O_4$@SiO_2 core–shell NP, (c) Pictures of the pristine phosphate glass (PG) and the samples containing iron oxide (IO) melted for 15, 45 and 75 min, (d and e) TEM micrographs of sample PG-IO@SiNP (15) in different scales. (Reproduced from Ref. [409] with permission from Elsevier).

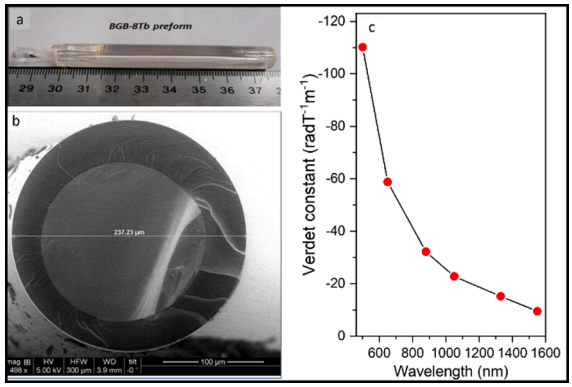

Fig. 33. (a) Preform of a magneto-optical borogermanate glass, (b) Optical fiber obtained after pulling and (c) the Verdet constant measured for the fiber, as a function of the wavelength (Reproduced from Ref. [386] with permission from Springer Nature).

commercially available, are injected into the holes of a silica based photonic crystal fiber. The obtained hybrid material can be used to detect magnetic fields as low as 2 mT with a fast response of 0.1 s using an infrared laser source (976 nm). The interesting approach here is that the fluid can be changed to achieve more sensitive devices, while the drawback is the fact that such solutions usually present absorptions in the visible region. The photonic crystal fibers have also limited transmission ranges.

Magneto optical fibers used as optical isolators in applications for high power laser systems actuate to eliminate damaging back-reflections from different parts into the system. However, high power lasers induce thermal changes in the material causing several distortions of the optical properties, such as birefringence and nonuniform temperature distribution which leads to changes in the Verdet constant and decreases the performance of the device. Despite paramagnetic glasses be the most used materials for magneto-optical devices, they are more susceptible to changes of temperature than diamagnetic glasses, thus the development of high Verdet diamagnetic fibers is interesting for such application, especially in the blue and UV-regions. Heavy metal oxide glasses, based in highly polarizable chemical elements, fulfill the requirements needed for this proposal, but for the best of our knowledge, few works have proposed the use of such glasses and for this reason the interest in research in this field has increased in the last years [412].

8. Optical glass waveguides

Glass waveguides serve a wide array of critical modern technologies since they confine and guide light around sharp bends on, for example, optoelectronic chips, and over long distances without distortions and with very low loss of intensity such as with optical fiber.

8.1. Principle of light propagation

Most modern applications, further discussed below, employ the physical phenomenon called “total internal reflection” to confine and propagate light. Total internal reflection was first used to explain rainbows as early as 1300 BCE and more quantitatively and systematically studied three centuries later. Popularization of total internal reflection was done by Colladon and Babinet in the 1840s and by Tyndall in the 1850s [413-415]. Total internal reflection relies on exceeding the validity range of Snell’s Law when light is incident upon a material whose refractive index is higher than that from which it is coming above a critical angle. In such cases, the light is reflected at the interface, rather than refracted, and suitably cladding the higher index material with a lower index periphery leads to confinement. The more complete wave-optic description is based on Maxwell’s electromagnetic equations bounded by the constitutive equations for the materials comprising the waveguide and its geometry (e.g., planar or cylindrical). The solutions to Maxwell’s equation under the material and geometric constraints of the waveguide represent the propagating modes, which have been well established for a variety of forms [416–420].

While studies on plastics (organic glasses) dates at least to the 1940s [421,422], the development of inorganic glass waveguides dates to the seminal work of Kapany in the 1950s [423,424]. The 1960s represent a truly foundational period of optical glass waveguide development with the realization that appropriately purified glasses could carry light at optical frequencies with sufficiently low loss as to make light-based communications feasible [20]. For the impact of this work, Kao received the 2009 Nobel Prize in Physics for “groundbreaking achievements concerning the transmission of light in fibers for optical communication.” Concurrent with these innovations in glass optical fibers were important developments and applications in planar glass integrated optics [425]. The history of optical glass waveguides is dominated by silica and silicates, given their superior properties to other glass systems at wavelengths of greatest practical interest. However, as are discussed elsewhere in this Review, other oxides and non-oxides play important specialty roles, such as for bioactive light-guiding fibers, infrared fiber lasers, etc [426].

While total internal reflection is the most used phenomenon for waveguides, there are numerous other ways to confining and guiding light. For example, building off “artificial dielectrics” from the 1950s developed for millimeter and microwaves [e.g., 427,428], and following the work of Purcell [429] in the 1940s to control spontaneous emissions, Yablonovitch [430] and John [431] separately but contemporaneously created the field of “photonic crystals,” which are engineered periodicities on the order of the

wavelength of light that create bands of allowed and forbidden energies and polarizations to propagate, not unlike Bragg diffraction of x-ray by atomic crystals, but for optical wavelengths and applications. Another novel route to waveguiding stems from the work of Anderson, for which he shared the 1977 Nobel Prize in Physics for work associated with the absence of diffusion in random structures [432]. Such "Anderson localization" was first realized in a glass optical fiber in 2012 [433], and subsequently shown to enable high fidelity image transmission.

8.2. Optical glass waveguide fabrication

Structures that confine and guide light are called waveguides. This Section reviews the broad range of fiber and planar waveguide fabrication approaches and importance considerations of each.

8.2.1. Preform and fiber fabrication processes

The emergence of new uses of optical fibers has always benefited from the development of new manufacturing processes capable of meeting requirements such as mass production, low cost, specifications relating to transparency, doping with luminescent ions, etc. The main manufacturing processes currently used are presented in this section.

– Rod-in-tube and Molten core (powder-in-tube, melt-in-tube): In the rod-in-tube process, a core glass rod is inserted into the cladding glass tube to create the preform. The compositions of the two glasses, as for all the processes, must satisfy two characteristics: (i) the refractive index of the core glass must be higher than that of the surrounding cladding (assuming total internal reflection as the guidance mechanism) and (ii) the thermo-mechanical properties of the core rod and cladding tube glasses must be sufficiently close to co-process via fiber drawing. The core glass typically is obtained by fusion methods (i.e., melting of powders) while the cladding tube is obtained by casting the glass in a rotating furnace. The quality of the surface of the glasses must be optimal to limit imperfections at the core/clad interface, which would yield high optical losses. The "Powder-in-Tube" process, now called the molten core method (MCM) [434], is an alternative to the "Rod-in-Tube" process in which powders are inserted into the cladding tube instead of the glass rod. The powders are required to melt at a temperature below where the cladding glass tube, sealed at the bottom, draws into fiber. The drawing parameters must be chosen to eliminate any trapped air bubbles that might occur from incomplete fining of the melted powder core during the draw.

– Double crucible: two crucibles, surrounded by heating elements, are placed concentrically, and are fed with glass powders, cullet, or rods. Heating of the crucibles melts the glasses which then flow through a nozzle located at the crucible bottom and directly forms the fiber. The core / clad ratio is determined primarily by the crucible geometry. To prevent any oxidation or hydration of the molten glasses, an inert gas is used as ambient atmosphere.

– Chemical vapor deposition: The two processes described above are based on manufacturing glass fiber via melting processes, which entails risks of contamination by impurities. To overcome this potential problem, new processes were developed in the 1970s based on the synthesis of silica by chemical means in the vapor phase. This process had been developed within the Corning company in the early 1940s [435]. This process is based on the oxidation reaction $SiCl_4$(liquid) + O_2(gas) → SiO_2(solid) + $2Cl_2$(gas), making it possible to obtain SiO_2 powders of very high purity benefiting on the one hand to the very high purity of $SiCl_4$ and on the other hand to its very high vapor pressure compared to possible contaminants such as Fe (main impurity present in fused silica and impacting the transparency of the glass). The three CVD-derived methods represented in the Fig. 34 are now described.

– *Outside vapor deposition:* a mixture of reagents (e.g., $SiCl_4$ and O_2) is delivered in gaseous form to an oxygen-hydrogen burner. Within the flame, oxidation and hydrolysis reactions (e.g., $SiCl_4 + 2H_2O \rightarrow SiO_2 + 4HCl$) occur forming the silica soot. The soot, with a particle diameter of ~100 nm, is deposited on a rotating cylindrical mandrel ("bait rod"; Fig. 34**a**). The preform is obtained by translating the target and by using multiple layer-by-layer depositions. The precursors are usually chlorides ($SiCl_4$, $GeCl_4$, $AlCl_3$) or chelates (for rare-earth ions). The porous preform is then removed from the bait to be heated (~1500 °C) to consolidate the soot. To reduce the presence of hydroxyl groups (and avoid the detrimental absorption band around 1.38 μm), a flow of chlorine is used.

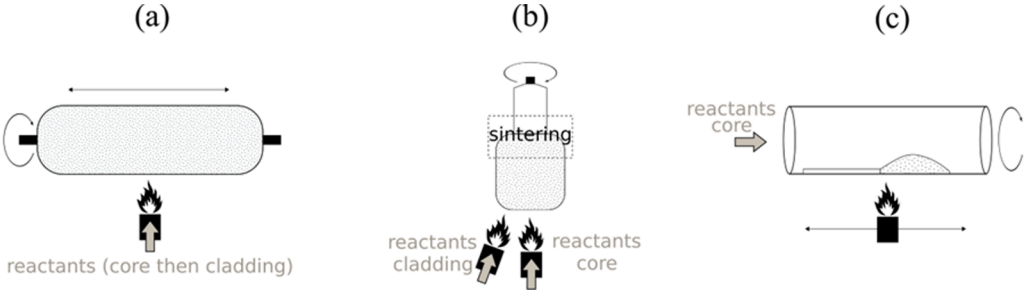

Fig. 34. Schematic diagrams of the (a) outside vapor deposition (OVD), (b) vapor axial deposition (VAD) and (c) Modified Chemical Vapor Deposition (MCVD) methods. Dashed areas correspond to soot. Reactants can be $SiCl_4$, $GeCl_4$, O_2, etc. Upper part of the VAD method and layer on the left of the burner in the MCVD method correspond to consolidated soot (i.e., glass bulk or layer).

The preform is then introduced into a vertical furnace (~2000 °C) to be collapsed (closing of the central hole due to the mandrel) and then drawn into fiber.

– *Vapor axial deposition*: compared to the OVD, the core and the cladding of the preform are created at the same time, along the longitudinal axis of the preform. Two torches are used, one to deposit the core, the other for the cladding; see Fig. 34**b**. The soot is delivered onto a rotating silica rod, the translation of which allows vertical formation of the preform. Like OVD, the torches are supplied with gaseous reactants such as chlorides. On the other hand, VAD makes it possible to obtain a preform without a central hole. Once the soot has been deposited, the preform passes through a furnace placed in line above to consolidate the soot and to obtain a clear glass preform.
– *Modified chemical vapor deposition:* the MCVD process leads to preforms of smaller sizes: typical diameter of the order of one cm for a length of less than one meter. MCVD is best employed for the fabrication of specialty silica-based fibers, such as those used for fiber lasers and amplifiers. Compared to OVD and VAD, MCVD relies on the successive deposition of vitreous layers inside a silica tube (Fig. 34**c**). Precursors, such as chlorides, are delivered inside the silica tube with oxygen as a carrier gas. Through the heat of an oxygen-hydrogen torch, located under and traversing along the silica tube, the precursors oxidize to form the soot, which is deposited by thermophoresis inside the rotating tube. Only a few ions (those mentioned before as well as fluorine and boron) can be added per gaseous phase. All other components, such as rare earth ions or aluminum, are added via the "solution-doping" method [436]. During this step, the deposited layer is left porous and is soaked in an alcoholic or hydrous solution in which the dopant chloride salts (e.g., $ErCl_3$, $AlCl_3$, etc.) are dissolved.

– Stack and draw: The "stack-and-draw" process is used to obtain microstructured and photonic crystal fibers. The guiding of the light in the core is ensured by the refractive index difference between the cladding which contains a certain proportion of air holes and the "solid" glass core (microstructured fibers) or the periodic (hence "crystalline") arrangement of the holes in the cladding around the core forming a photonic crystal structure, which acts like a mirror because only certain wavelengths can propagate. In a typical process, silica capillaries are periodically stacked inside a larger cladding tube, with thin glass rods to fill the interstitial holes. The thickness of the tubes determines the air filling fraction. This first preform is drawn to form a cane (larger diameter "fiber" which usually is not very flexible). Several canes are usually assembled and redrawn together to form the final fiber with the desired hole dimensions. The drawing is usually carried out at a lower temperature than conventional fibers, and pressure is applied inside the air holes to control their sizes and shapes. Other processes have been developed to prepare microstructured fibers such as direct drilling of glass [437]. Another process consists of casting a chalcogenide glass in a circular silica mold containing silica capillaries whose arrangement will determine that of the holes in the preform [438].

The next step then consists of fabricating the optical fiber by thermal drawing of this glass preform. The preform is placed in a furnace (resistive or induction) located at the top of the drawing tower. The temperature of the oven must be higher than the Littleton temperature (or softening temperature) which corresponds to the temperature at which the preform flows under its own weight; it corresponds to a viscosity of about $10^{6.6}$ Pa·s. The fiber is coated with one or two layers of photopolymerized resin by an ultraviolet

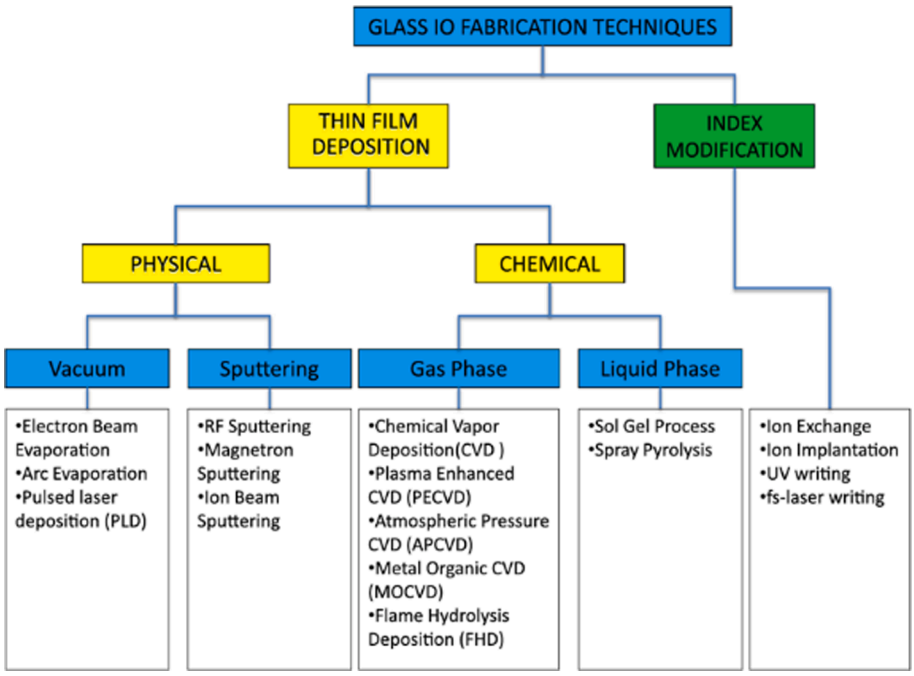

Fig. 35. Summary of major fabrication techniques adopted for the manufacturing of glass optical waveguides and glass integrated optical components. (Reproduced from [439] under the terms of the Open Access Publishing Agreement).

(UV) lamp. The first layer (acrylate-type coating) minimizes micro-bending stresses while the second coating has a higher mechanical modulus to ensure higher physical protection. At the bottom of the tower, the fiber passes through a capstan, which pulls the fiber and allows the diameter of the fiber to be controlled. The drawing of a fiber corresponds to managing several interconnected parameters such as the temperature, the drawing tension, the diameter, the speed of descent of the preform and the drawing speed.

8.2.2. *Planar waveguide fabrication*

Fig. 35 provides a summary overview of the various fabrication processes of glass optical waveguides. A brief description of the most relevant techniques follows in this sub-section in an order corresponding to the classification shown in the Figure, from left to right.

– Pulsed laser deposition (PLD): The structural modification process of glassy materials using pulsed laser deposition may be classified into two phenomenologically different plasma-assisted processes**:** (a) deposition of ablated materials [440,441], and (b) surface modification by utilizing the energy of plasma generated via the interaction of short-pulsed laser with the target material. In the surface modification process, the energy of the plasma promotes the implantation of ions present in the ablated plasma plume [442], leading to a change in the superficial refractive index. The emergence of high-quality phase-controlled femto-second (10–100 fs, 1 fs $= 10^{-15}$s) pulsed Ti-sapphire and Yb^{3+}-doped crystal lasers have opened opportunities for such sources to precisely ablate low-dimensional (few nm) to 100 s nm thick films. The effect of the repetition rate of a pulsed laser source on interaction with the target materials may be understood better using the Planck's law, in which the energy (E, J) of a laser cavity may be explained by the Planck's equation $E = n(h\vartheta)$. Here the $(h\vartheta)$ term defines the packet energy of photons and n is the number of photon packets. Thus, in a high repetition rate cavity when (n) is large, the total energy of the laser cavity, E, is distributed amongst the n packets, making each packet small. Conversely, in a slow repetition rate laser cavity, each packet carries more energy. For ablation of the target material, the following equations are essential in ascertaining the ablation rate and efficiency, which may be understood by referring to a schematic of the laser translation process in Fig. 36 [443].

The important process parameters of dimensionless ablation profile (AP), ablation rate (AR, mm^3s^{-1}), and ablation efficiency (AE, mm^3J^{-1}) are expressed in Eqs. (6)–(8), in which the terms on the left- and right-hand sides are shown in the schematic diagram in Fig. 36 [443].

$$\frac{2(x_i - x_o)^2}{\omega_o^2} + \frac{(z_i - z_o)^2}{D_p} = ln\left(\frac{F_p}{F_{th}}\right) = ln\left(\frac{E_p}{E_{th}}\right) \tag{6}$$

$$AR = A_{area} \bullet \nu = D_p \bullet \nu \bullet A_w \left[ln\left(\frac{F_p}{F_{th}}\right) - \frac{A_w^2}{6\omega_o^2}\right] \tag{7}$$

$$AE = \frac{AR}{P} = \frac{D_p \bullet \nu \bullet A_w}{P}\left[ln\left(\frac{F_p}{F_{th}}\right) - \frac{A_w^2}{6\omega_o^2}\right] \tag{8}$$

Control of 1–100 MHz repetition rate lasers has created opportunities for the controlled deposition of ablated materials at nano and sub-nanometer scales over centimeter surface areas for device engineering [444,445]. Another unique difference between low (kHz) and high (MHz-GHz) repetition rate lasers used for ablation is manifested by the energy imparted per second by the photon packets into the target material, which then generates a unique ablated volume of matter, characterized by the color of plasma. The length and color of ablated plasma plume also depends on the electronic absorption edge of the target material and incident photon energy and wavelength [446–448]. The plasma plume is generated by the incident energy of a pulse laser, as shown in Fig. 37**a** and **b,** and depends on the laser fluence. Only above a threshold fluence, when the incident laser energy exceeds the energy for breaking the chemical bonds, the ionization process generates electrons and ions in the plasma from the surface of target materials. Since the excited state

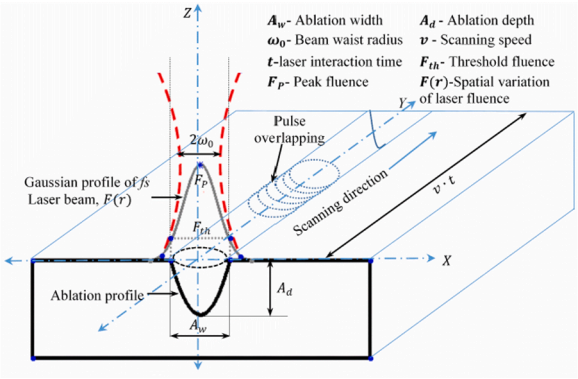

Fig. 36. A schematic representation of pulsed laser ablation with process parameters defined in the inset of the figure. The laser fluence (F) is a parameter defined by the pulse energy (E_p) divided by the waist area of a Gaussian beam with diameter $2\omega_o$ in mm (Reproduced from Ref. [443] under the terms of the Open Access Publishing Agreement).

ions and electrons in plasma are above the chemical bond energy of the target material, the ions and electrons recombine and new chemical bonds form spontaneously in a sub-picosecond time scale. This recombination of excited states generates a high kinetic energy plume travelling towards a cold substrate [449,450]. The plume material then condenses and deposits onto a cold substrate by forming a thin film.

Four essential parameters for controlling the optical quality of the deposited thin films of glassy and crystalline materials are (a) laser wavelength, fluence and repetition rate, (b) deposition chamber pressure and gas composition, (c) substrate temperature, and (d) distance between the target and substrate (Fig. 37**a**). The importance of parametric control during PLD is extensively discussed for thin film deposition of optical materials in a recently published review [451]. The pulsed laser deposited thin films may vary in phase and composition, depending on the materials used for ablation. In general, a congruent glass composition maintains its stoichiometry and congruency after deposition, which may not be the case when dealing with the incongruent compositions (i.e., where a phase does not melt or vaporize by maintaining it stoichiometric composition). Any departure from congruency may lead to deviation in composition between the target material and the substrate. Since 1965 [452,453], when pulsed laser source was used for thin-film deposition, several authors have reported thin glassy films with active RE-ions which were deposited using pulsed laser on inorganic substrates [447–450,454–456]. The selected target materials were suitably doped silicate, chalcogenides, fluoride, germanate [457,458], and tellurite-based glasses. Besides selenium and arsenic based chalcogenide glasses, the oxide-chalcogenide composites have been deposited using PLD [459]. More recently gallium lanthanum sulphide oxide-based glasses have also been used for pulsed laser ablation for engineering optical quality films [460]. Using PLD, the lead-germanate family of glassy films were investigated by controlling the oxygen partial pressure in the deposition chamber [461,462]. The spectroscopic properties of lithium-aluminum-phosphate based glassy films doped with Er^{3+}, Pr^{3+}, and Nd^{3+}-ions were investigated for device applications [463]. PLD of ZBLAN fluoride glass films with Er^{3+} ion doping was formed using ArF-excimer laser, followed by the fs-pulsed laser machining for resonant cavity engineering using the 980 nm diode laser as a pump source [464]. Using 193 nm laser, the thin films of Er^{3+}-Ce^{3+}-ion doped phosphate modified tellurite glass film was deposited on Q-dot GaAs pump waveguide for signal amplification in the 1530 nm range. More than 2.0 dB/cm of internal gain was recorded in the integrated waveguide structure for first time. The waveguide engineering demonstrated the future of photonic device integration strategy [465]. Glass-polymer superlattice structure was fabricated using sequential pulsed laser deposition of two materials on a silica substrate for waveguide inscription using an 800 nm Ti-sapphire laser. The laser-machined waveguide demonstrated strong evidence of photoluminescence for amplification and lasing device engineering [466].

– Sputtering deposition: The physics and technology of sputtering is quite complex [467–469] but generally employs positively charged, highly accelerated ions to eject particles - mainly, atomic clusters or neutral atoms - from a target made of the material to be deposited. The ejected particles impinge on and adhere to a substrate thus creating a dense film, which slowly grows with time. The structure of the simplest sputtering systems is constituted of a vacuum chamber, including a cathode (on which the target is placed) and an anode (with the substrate) usually electrically grounded; a low-pressure inert gas (usually argon) is then introduced, so that an applied voltage creates a glow discharge plasma where the target ejected particles are accelerated. For metal targets it is sufficient to apply a direct current voltage, but the sputtering of an insulating material (such as a glass) requires an RF discharge (usually at 13.56 MHz frequency) to avoid the accumulation of negative electron charges onto the target. To achieve higher sputtering rates, a magnetron configuration may be used, with permanent magnets placed below the cathode: the magnetic field coupled with the sputtering source traps the electrons close to the target surface, decreasing their mean free path in the plasma. Consequently, more ions are generated by impact with the electrons close to the target and a higher flux of particles is accelerated toward the substrate [469]. Sputtering is a relatively slow process, with deposition rates of the order of a few nm/hr per watt of RF electric power applied to the electrodes, but the film quality is very high. In typical working conditions, the pressure of the sputtering gas is on the order of 10^{-2} mbar, and the electric power is in the range of 200–300 W. Composition and refractive index of sputtered films vary as a function of the power level and/or the gas pressure at which the deposition is made. When sputtering oxide glasses, there may be a loss of oxygen caused by the dissociation of glass during the collisions of ions onto the target. This problem may be overcome by introducing oxygen

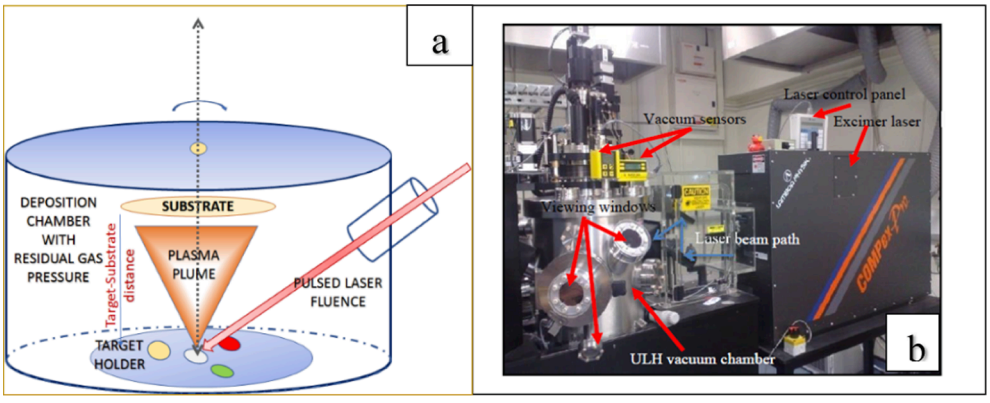

Fig. 37. (a) A schematic representation of PLD operation with process parameters needed for control of the quality of deposited thin films. (b) Photograph of the pulsed laser deposition chamber with excimer lasers on the right.

into the plasma (reactive sputtering) and/or applying a small potential to the anode (bias sputtering). A thermal annealing process may also be necessary to reduce optical absorption of the deposited layer. Annealing has the effect of oxidizing the sputtered material and homogenizing the thin film.

– Chemical vapor deposition (CVD) and CVD-derived processes: in the field of glasses, the CVD method has found its main application for the production of the high-purity preforms of optical fibers, as described in earlier, but it can also be employed to create glass thin films. As an example, to produce thin oxide glass layers with SiO_2-B_2O_3-GeO_2 composition reactive gases, such as $SiCl_4$, BBr_3, and $GeCl_4$ being fed into a vacuum chamber along with oxygen as the carrier gas. Homogeneous chemical reactions occur in the vapor phase before striking the substrate, where they condensate, whereas the gaseous by-products of the reaction are transported out of the reaction chamber. Typically, the process occurs at temperatures higher than 1200 °C with the vitrification of the soot (small glass particles formed by the vapor phase reactions) occurring at a temperature around 1700 °C, producing a highly homogeneous film suitable for waveguiding. A lower-index cladding may also be deposited on top of the guiding layer by repeating the process, but with a lower flowing rate of $GeCl_4$, for example. The waveguides produced by this technique may exhibit propagation loss lower than 0.1 dB/cm at a wavelength of 632.8 nm (and lower at a wavelength of 1.55 mm). The CVD process is the base of several other fabrication techniques used to manufacture high-quality, low-loss glass film waveguides and integrated optical devices: they include Flame Hydrolysis Deposition (FHD) [470,471] plasma enhanced CVD (PECVD) [472], and atmospheric pressure CVD (APCVD) [473]. Among these techniques, FHD is the most economical for the deposition of SiO_2 films, using the hydrolysis of $SiCl_4$ in a high temperature H_2-O_2 flame. Disadvantages of FHD are represented by the need of a precise control of deposition and stoichiometry and of an additional process of densification to transform the porous soot into a dense SiO_2 film [471]. An example of application of PECVD, a technique that in some cases permits energetic reactions at temperatures as low as 100 °C, is the fabrication of low-loss silica and silica-germanate waveguides [474]. An interesting application of the hot-wall CVD process under atmospheric pressure (APCVD) was reported by Huang et al., who deposited germanium sulphide glass thin films on CaF_2 and Schott N-PSK58 glass substrates [475]. Their channel waveguides produced by mask photolithography and argon ion-beam etching exhibited propagation losses of 2.1 $\pm$ 0.3 dB/cm at a wavelength of 632.8 nm.

– Sol-gel deposition: Sol-gel is a versatile, highly adaptable, and low-cost approach to fabricate, study, and apply innovative planar photonic structures (see also Section 3.3). The possibility of starting from molecular precursors and elementary building blocks permits one to tailor structures at the molecular level and to create new materials with enhanced optical properties. Of specific interest for the study of important physical effects as well as for application in light management are confined structures on the nano-micro scale as photonic crystal and planar waveguides. Activation by luminescent species and, in particular, by rare earth ions allows for the use of integrated optics in sensing, biomedical diagnostic, telecommunication, lightning, and photon management.

Sol gel-derived optical waveguides and planar light-wave circuits are a well consolidated research area. In this context a significant role is played by the binary systems such as silica-hafnia or silica-tin oxide, where the two components determine the final optical, spectroscopic, and structural properties of the fabricated systems. The first requirement to obtain effective waveguiding structures is to optimize the sol–gel fabrication protocol and in particular the composition and the kinetics. Two chemical reactions are at the base of sol–gel approach, namely hydrolysis and polycondensation of molecular inorganic (metal–organic) precursors in typically alcoholic solutions. Besides simplicity, sol–gel synthesis allows many benefits for films fabrication, such as precise stoichiometry control of precursor solutions, tailored microstructure, easy composition control, possibility to incorporate various functional groups and luminescent species, lower annealing temperatures than melting glass processes, simple experimental equipment. This makes sol–gel method very popular in nanomaterials preparation by spinning, dip-coating or impregnation techniques [53]. However, the sol–gel approach deserves specific attention in the planar waveguide fabrication processes because of weak bonding, low wear-resistance, and difficulties in porosity control. The thickness of sol–gel coating is also crucial to avoid cracks in the film. The presence of organic compounds in thick layers often leads to failure during thermal treatment process. Moreover, the success of sol–gel approach for waveguide application strongly depends on the substrate, and the thermal expansion coefficient must be accurately considered. Focusing attention on the waveguide systems, three aspects should be considered: (i) the role of high refractive index material concentration on the structural and optical properties of the optical film, (ii) the role of dopant content (for active films) on the luminescence quantum yield, and (iii) the deposition parameters. The most effective technique to fabricate optical waveguide is dip-coating on vitreous SiO_2 or on silica-on-silicon substrates [476]. The starting solution, commonly obtained by mixing tetraethylorthosilicate (TEOS), ethanol, deionized water and hydrochloric acid as a catalyst, is pre-hydrolyzed. When a luminescent species is added, attention is paid to obtain the suitable molar concentration and avoid physical and chemical clustering. Using this type of solution, waveguides are prepared using a well-defined dipping rate. The dipping-annealing cycle is very crucial for the final optical properties, including propagation losses. Finally, the waveguides are further annealed, and duration and temperature of the process may be different for each desired waveguide. This thermal process should assure as much elimination of residual OH groups as possible without nano-scale cracking of the films.

– Ion diffusion: In addition to thin film deposition, another effective route for the fabrication of optical waveguides requires a spatially selective change of the refractive index (RI), so to create a higher RI (core) layer capable of confining the light. Two major classes of ion diffusion processes are usually considered for glass waveguides, namely, ones that are low-energy (e.g., ion exchange) and others at high-energy (e.g., ion implantation). A third route employs direct laser writing technologies, by exploiting either the photorefractivity of the glass (UV writing) [439] or the physical–chemical structural changes induced by high power density ultrafast laser pulses (fs writing), discussed in previous subsections.

- *Ion exchange (IE)* is based on the substitution of an ion already present in the glass (usually Na^+) with another ion (e.g., Ag^+, K^+, Li^+) supplied from an external source (usually a salt melt). When substituting Na^+ ions with K^+ ions, which have considerably larger ionic radius, a compressive stress is generated, and this phenomenon was exploited for the strengthening of glass surface (also sometimes called ion stuffing or chemical strengthening). The suitability of IE technology to produce optical waveguides in glass has been recognized since the early 1970 s, and both purely thermal and electric field assisted diffusion have been widely exploited. Some excellent review papers are available, and the reader is referred to them for an overview of the different processes, models, and fabricated devices [477–479].
- *Ion implantation*. In this process, a beam of atoms is ionized, accelerated to kinetic energies up to several MeV, and made to impinge on a material. The implanted ions lose their energy by electronic and nuclear damage. The physics of the process is quite complex and for more details we can refer the interested reader to one of the many books on the subject [480]. When considering dielectric materials, implantation is always producing a change in RI, but the sign (increase or decrease of RI) depends on the process and the material. In most cases, the damage occurs at the end of the ion track inside the substrate, producing a volume expansion with consequent decrease of physical density and refractive index. An optical barrier is thus created, that permits the confinement of light in a narrow layer between the substrate's surface and the barrier. Usually, this confinement is rather weak, allowing the so-called tunneling effect, with leakage of energy of the propagating beam. The two types of confining structure of ion implanted glass waveguides are thus labeled as "barrier" and "well + barrier." The penetration depth profile of the vacancies produced by the ion beam is generally calculated with the Stopping and Range of Ions in Matter (SRIM) code; it matches quite well the experimental results [481]. A review of ion-implanted waveguides in glass was published by Liu, et al. [482].

8.2.3. Glass optical microcavities

As already mentioned, the confinement of light may be achieved not only in conventional planar waveguides, usually consisting of a three-layer structure (the substrate, the guiding film, and the upper medium), but also in circular-symmetry structures that support the so-called whispering gallery mode (WGM) propagation of the electromagnetic field. Spherical optical microcavities are the most well known guiding structure of this type.

Nowadays, the concept of optical cavity is usually immediately associated with that of laser, since a resonant structure is essential part of any laser, allowing an extended interaction length between the active medium and the optical field, and therefore the buildup of the optical power. But the long light circulation may also be exploited to enhance the sensitivity of measurements, and indeed the first, and simplest, linear optical cavity, made by two parallel mirrors, was invented by Fabry and Pérot in 1899 [483] and has been used as a high-finesse interferometer in uncountable spectroscopic applications.

The development of photonics has forced the downscaling of optical cavities to micro- and nano-meter sizes, for application as very narrow-line micro(nano)lasers and as very sensitive micro(nano)sensors. Thus, new geometries have emerged, such as 3D whispering gallery modes (WGM) resonators and 1D or 2D photonic crystal microcavities, but glasses continue to play a fundamental role also in this scientific game.

The observation by Lord Rayleigh in early 1900s of a curious acoustic phenomenon, described in his paper entitled *The Problem of the Whispering Gallery* [484], eventually led to the development of a new class of optical guided-wave devices, called Whispering-Gallery Mode (WGM) resonators [485]. WGMs are typically associated with circular-symmetry structures, where light is confined along the surface due to total internal reflection; examples of such structures, that find diverse applications, from quantum photonics to biosensing, are microspheres, microbubbles, microbottles, microcylinders, microtubes, microtoroids, microdisks, and microrings. Typical radius varies in the range from 15 to 200 μm.

Glass microspheres constitute the simplest and one of the most effective WGM resonators [486], capable of exhibiting a very-high quality factor, Q or, put another way, a very narrow resonance linewidth $d\nu$, their relationships being $Q = \nu/d\nu = 2\pi N_{eff}/\alpha\lambda$, where ν is the operational frequency, λ the corresponding wavelength, N_{eff} the effective refractive index, and α the loss coefficient, which includes

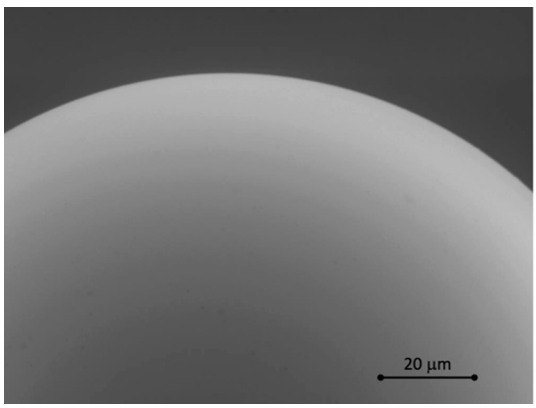

Fig. 38. Electron micrograph, magnified 1900 times, of a portion of the surface of a microsphere fabricated by melting the tip of a telecom single-mode optical fiber. No surface defects can be seen.

both the absorption of the microsphere material and the light scattering at its surface.

The quest for a material with very low absorption coefficient has led to a very effective and simple result, namely exploiting the ultra-pure silica glass used for the core of optical fibers. Thus, using a single-mode standard telecommunications fiber and melting its distal end allows one to directly fabricate microspheres with very high Q. In fact, heating the tip of the fiber till to its softening produces, thanks to the surface tension, an almost perfect microsphere (roundness of equatorial circle > 0.99) with a surface almost fully free from any defect, as testified by the scanning electron microscope (SEM) image in Fig. 38.

The most common and effective method to produce single silica glass microspheres makes use of the arc discharge generated between the two metal electrodes in a commercial fiber splicer. By varying the number of arc shots, it is also possible to control the size of the microsphere [487]. Values of Q as high as 10^7–10^8 are routinely achieved, with record values close to the theoretical limit of 10^{11} [488]. Such ultra-high-quality factors permit extremely narrow resonant linewidth, long decay time and a high energy density, characteristics that, in turn, may be exploited in cavity-QED experimentation, detection and sensing, frequency stabilization, and optical filtering functions. The availability of commercial fibers based on As_2S_3 chalcogenide glass (ChG) has also made possible the easy fabrication of high-index microspheres with size in the range 80–380 mm, all with $Q \sim 10^6$, suitable for mid-IR applications [489].

Different fabrication methods must be used when other glass compositions or multiple microspheres are wanted. For example, finely-ground glass may be poured in a vertical cylindrical structure heated by a plasma torch. The glass grains are melted during the fall, and microspheres of different sizes (corresponding to the size distributions of the grains) are collected at the bottom of the tube. Sol-gel chemistry may also be used to produce many microspheres (down to nanospheres) with the advantage of material's very high purity and of the easy tailoring of the glass composition.

The integration of microspheres in complex integrated photonic circuits is made difficult by their 3D geometry. An interesting approach to a commercial fabrication of spherical microresonator arrays is to create silica structures on a silicon wafer that can then be molten into spherical form, the simplest choice being to fabricate silicon posts topped with silica blocks; a controlled heating of the wafer induces the silica blocks to develop spheroidal curvature while remaining attached to the silicon posts [490]. Fig. 39 provide SEM images of a microdisk resonator with a radius of 45 μm fabricated in a 300 nm thick GeSbSe film waveguide, thermally evaporated from GeSbSe glass powder and cladded by a 30 nm thick SiO_2 film deposited by magnetron sputtering.

The geometry was defined by electron-beam lithography followed by plasma dry etching. The refractive index of the ChG film was ~2.8 at a wavelength of 1550 nm, and a loaded Q factor of $\sim 5 \times 10^5$ was measured [491].

Characterization of a WGM microresonator is usually performed by analyzing the light transmitted along an optical fiber which acts as coupler of the light from a tunable laser diode into the resonator; see Fig. 40. When coupling occurs, the intensity of the transmitted light presents a well-defined dip at the resonance frequency; the measurement of the central frequency and of the linewidth permits to calculate the Q of the resonator. The resonance frequency depends on the radius and the refractive index of the resonator; thus, any environmental change induces a frequency shift, as sketched in Fig. 40.

The extreme sensitivity of the resonator frequency to variations in the environment makes the WGM microspheres very useful for sensing [492-495]. Examples include temperature sensing (silica and compound glass microspheres have exhibited maximum sensitivity of few pm/K and top resolution equal to a fraction of mK [492]), pressure sensing (luminescent oxyfluoride glass microspheres achieved groundbreaking levels of relative sensitivity and limit of detection [493]), and outstanding achievements in biosensing [494], which include the detection of a single virus of influenza A [495]. An interesting solution to the problem of a robust and efficient coupling structure, which is particularly critical for a microlaser, was proposed recently: an erbium-doped microsphere, with 30–50 μm typical diameter, is placed in an open microcavity produced in a standard single-mode optical fiber by fs-laser machining and fusing slicing technique, in such a way that the microsphere is in contact with the core of the fiber [496]. Even if still challenging, this approach proves that there is much room for further innovations in the fabrication, processing and photonic applications of glass microspheres.

8.3. *Recent research trends and future directions in optical waveguides*

8.3.1. *Optical fiber waveguides*

The advent of different fiber architectures (core-cladding, microstructured fiber, photonic crystal fiber, etc.), different glasses

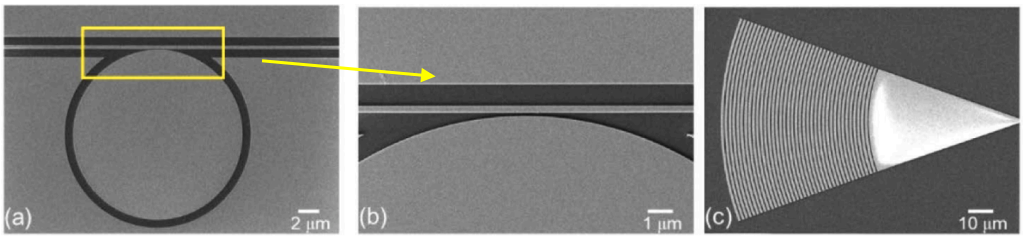

Fig. 39. (a) SEM image of a ChG microdisk resonator, with 45 μm diameter is 45, coupled to an access waveguide. (b) Magnified view of the waveguide-resonator coupling region. (c) SEM image of the TE mode grating used to couple light to the waveguide from an external fiber. (Reproduced from Ref. [491] under the terms of the Open Access Publishing Agreement).

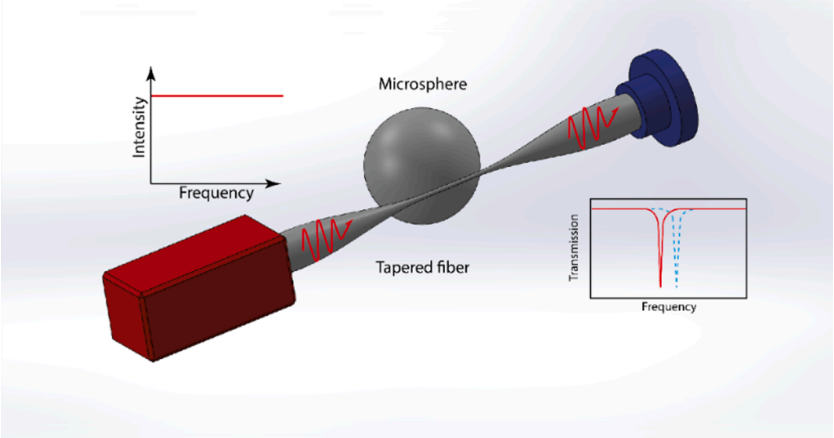

Fig. 40. Simplified outline of the characterization of a microsphere resonator. Light from a tunable laser diode is launched into an optical fiber: coupling of light into the resonator occurs in the tapered section of the fiber. The light intensity detected at the end of the fiber shows a dip corresponding to the coupling; this resonance frequency shifts when the resonator senses a change in the environment.

(silica, fluoride, chalcogenide, phosphate, germanate, etc.) and different processes have been the basis for the development of many useful applications over the last fifty years, such as high-power fiber lasers, fiber amplifiers, and fiber sensor, to name just a few. The remainder of this Section illustrates these most significant developments with a few examples.

Ultra low loss fibers: Improving the transparency of optical fibers has always been a leitmotiv through the continual improvement of materials and the development of optimized manufacturing processes. In 1966, when Kao and Hockham [415] set the transparency goal of 20 dB/km (1% of light transmitted after 1 km) as the critical threshold for optical fibers to be of interest for telecommunications, they had no idea that in about ten years this threshold will be pulverized to reach an attenuation of 0.2 dB/km (1% of light transmitted after 100 km), courtesy of the emergence of CVD processes described in Section 8.2. These low loss fibers were obtained by successively eliminating the presence of impurities, such as iron and, then, hydroxyl radicals. At a wavelength of 1550 nm, the point of minimum spectral attenuation, the optical losses are mostly related to Rayleigh scattering caused by density and composition fluctuations in the Ge-doped silica core. This density variation can be characterized by measuring the fictive temperature, T_f, which corresponds to the temperature at which the structure of the glass is the same as that of the supercooled liquid. This fictive temperature therefore depends on the variation in viscosity as a function of the cooling rate. Reducing the drawing temperature, the drawing speed, or the addition of annealing during the draw process, thus make it possible to reduce the quenching rate and, therefore, to reduce T_f. A significant improvement in T_f was also obtained by modifying the core composition. For example, a 110 K decrease in T_f was obtained in a fiber with a silica core (slightly F-doped) surrounded by an F-doped cladding, resulting in an attenuation of 0.14 dB/km [497]. If this improvement may seem limited compared to the gain achieved in the 1970s, this research is motivated by the improvement made to long-distance submarine transmission. Indeed, with an optical loss of 0.2 dB/km, an optical amplifier (EDFA) must be placed every 80 km. A transatlantic link therefore requires a hundred repeaters. An attenuation of 0.14 dB/km would reduce the number of repeaters by 7%, which would have a significant impact on the reliability, cost and power consumption of a submarine link. Up to now, the low-loss fibers were mainly driven by the solid-core silica-based fiber. However, recent progress in the hollow core fiber fabrication allows to reach a highly competitive 0.174 dB/km in the C-band and 0.22 dB/km in the O-band, better than conventional silica fiber [498]. Moreover, as light is propagating in the air, such fibers would allow a lower latency data transmission by 30% [499]. Another alternative would be glass fluoride. Indeed, although fluoride fibers are theoretically ten times more transparent than silica-based fibers, in practice they remain ten times less transparent. However, the recent drawing of fluoride fiber (ZBLAN) in micro-gravity made it possible to achieve a transparency very close to that expected theoretically, i.e., 0.01 dB/km at 2 μm [500]. The production of such fibers over very long lengths could therefore have the potential to ensure a transatlantic link with only a few repeaters.

Nanoparticles in optical fibers: Nanoparticles in optical fibers were initially introduced to obtain novel luminescence properties of rare earth ions or transition metals ions. By encapsulating the luminescent ions within the nanoparticles, it is possible to combine the luminescence properties dependent on the characteristics of the nanoparticles (composition, structure) while keeping a silica-based fiber and its advantages (e.g., low cost, reliability, numerous manufacturing processes, etc.). However, the presence of nanoparticles in the core of the optical fiber imposes a strong constraint: Rayleigh or Mie light scattering impacting the transparency of optical fibers. Indeed, the title of the first article discussing this new generation of optical fiber speaks for itself: “Are low-loss glass–ceramic optical waveguides possible?” [501]. As the targeted applications for such fibers do not concern telecom fibers but instead are directed towards fiber-based lasers and sensors, the ultra-low attenuation constraint (as discussed in the previous section) can be relaxed. From then on, it had been identified that the nanoparticles had to satisfy certain characteristics including a size of ~15 nm and a low refractive index difference between the nanoparticles and the glass host. To grow crystalline nanoparticles, the most widely used process consists of applying a heat treatment to the fiber by analogy with glass–ceramic processes. The control of the temperature ramp makes it possible to control the nucleation and the growth (i.e., the radius) of the nanoparticles. However, this post heat treatment can bring disadvantages since it requires handling the fiber (remove the coating before heating step then recoating it,

limited fiber length, potential mechanical embrittlement).

Amorphous nanoparticles were obtained directly by drawing a prepared MCVD preform [502]. During solution doping step, ions such as alkaline earths ions (e.g., Mg, Ca) or La^{3+} are introduced and initiate particle formation via phase separation mechanisms. The in-depth study of these fibers has yielded very original results. It was first demonstrated that the composition of amorphous phase-separated particles varies according to their sizes with an enrichment in Mg [503]. It follows that the smallest particles (with a composition very close to that of silica) are of little interest with respect to the modifications of the luminescence properties. A compromise must therefore be found for the size: small to minimize optical losses, large to obtain a composition modification of interest for the luminescence properties. The study of these fibers has shown that the particles elongate or even fragment during drawing [504]. An engineering of the characteristics (size and shape) of the nanoparticles is therefore possible by controlling the drawing parameters (temperature, drawing speed); see Fig. 41**a.** This could be assimilated to a "top-down" process as mother particles in the preform can lead to small daughter particles in the fiber. Very recently, optical scattering induced by nanoparticles has been used to develop new fiber sensors based on the analysis of the backscattered light using Optical Backscatter Reflectometry or the comparison between transmitted and reflected intensity of light [505]. Such sensors can be applied to measure in real time temperatures, biochemical environments, mechanical stresses then 3D deformation measurements, see Fig. 41**b** and **c**, and detection of ionizing radiation.

Semiconductor core optical fiber: Another topic that has received considerable recent attention is the development of glass-clad optical fibers with crystalline semiconductor cores [506]. Such fibers marry the benefits of light guidance in optical fiber with the infrared, terahertz, and nonlinear excellence of semiconductor materials. Glass-clad semiconductors were first fabricated using a high-pressure chemical vapor deposition (HP-CVD) method [507] but, today, are made globally using the molten core method (MCM) described above. A summary of these two primary approaches can be found in Refs. [508–510]. Materially, both amorphous and crystalline semiconductor core fibers can be made using HP-CVD whereas the MCM can only yield crystalline cores. As used here, "crystalline" refers to the local structure of the semiconductor. In all cases, over sufficient fiber axial position, the cores are poly-crystalline as small perturbations in growth (HP-CVD) or solidification (MCM) lead to new crystalline grains forming.

These two processes have been employed to yield a remarkably broad range of glass-clad semiconductor core phases including: silicon (amorphous, crystalline, and hydrogen-doped [511–513]), germanium (amorphous and crystalline [514,515]), silicon–germanium alloys [516–518], indium antimonide [519], gallium antimonide [520], zinc selenide [521,522], gallium arsenide [523], to name just a few. The underlying materials science and phase equilibria for fiber core phases of interest to optics, opto-electronics, and thermoelectrics was recently reviewed [524]. The advent and subsequent optimization of post-fiber fabrication laser annealing and recrystallization treatments has led to marked reductions in loss, improvements in linear and nonlinear performance, tapering to single mode core sizes, and the formation of controlled in-fiber compositional gradients and microstructures [525–532]. Over the past 10 years, semiconductor core fibers have evolved from more exploratory research efforts through fiber optimization and, now, to devices of interest to a range of applications. These include photoconductive fiber antennae [533], passive and Kerr nonlinear microresonators and switches [534,535], light sources based on nonlinear processes (e.g., Raman, supercontinuum generation, FWM and parametric gain [536–541]), in-fiber radial junction and microwire solar cells [542,543], low-loss nanospike fiber couplers to telecom fiber [544], fiber Bragg gratings strain and temperature sensors [545], THz transmission and modulation [546,547], and frequency combs [548].

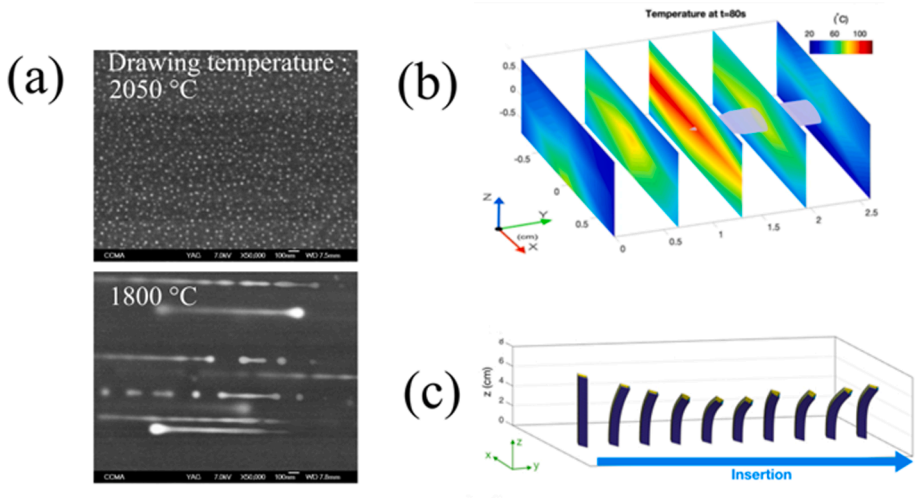

Fig. 41. (a) SEM images of the longitudinal cross-sections of fibers containing La-silicate nanoparticles (white features in images) drawn at two temperatures from the same preform. (b,c) Examples of applications using backscattering properties of optical fibers containing nanoparticles: (b) 3D temperature mapping, (c) evolution of a needle bending during an epidural insertion (Reproduced from Ref. [505] with permission from The Optical Society].

3D printing of preforms: The additive manufacturing or 3D printing technology has attracted a lot of attention over the last decade thanks to its opportunity for fast prototyping and manufacturing of customizable structures. This technology was first used for polymeric, metallic, and ceramic materials, before only recently gaining momentum for glass. In 2017, a team at Karlsruhe Institute of Technology (KIT) developed a stereolithography process [549]. High spatial resolution (~10 μm) was obtained thanks to the mixing of glass nanoparticles (SiO_2) and photocurable monomers (mainly hydroxyethylmethacrylate (HEMA) monomers) with a refractive index close to that of glass, limiting light scattering issue which could be detrimental for spatial resolution. In this process, UV irradiation leads to the formation of a polymerized composite, which gives a fused silica glass after debinding (600 °C) and sintering (1300 °C) stages to remove all the organic parts and to collapse the porosity. This process makes it possible to overcome the problems of high temperature necessary to lower the viscosity of the silica to make it flow as in the Fused Deposition Modeling (FDM) process. The customization possibilities offered by 3D printing techniques open new perspectives for the manufacture of optical fibers. The first achievement dates from 2015 and was obtained by the group of John Canning [550]. A microstructured polymer preform was prepared using the FDM process. This same group prepared the first preform based on silica glass in 2019 using the Digital Light Processing (DLP) process (Fig. 42) [551]. This preform was then drawn into optical fiber using the classic drawing process but at a slightly lower temperature (1855 °C) to remove air, water, and residual polymer gradually. The optical loss of this first 3D fiber is high (~5.5 dB/m at 1550 nm) but there is room for improvement to reduce this attenuation, in particular by improving the optical quality of the preform via the sintering step to eliminate the residual porosity or waveguide structure defects (core geometry for example). The selective laser sintering process (SLS) was used to prepare preforms with more complex geometries such as photonic crystal fiber and antiresonant fibers; see Fig. 42**b** and **c** [552]. These processes open the door to new perspectives, in particular for the production of new geometries (e.g., non-circular fiber, non-symmetrical geometries, concentration gradient, etc.) that are difficult to achieve using standard processes.

While there is no doubt that the development of future optical fiber devices (lasers, amplifiers, sensors, etc.) will be based on the processes and trends described in the previous sections [553], the next few years will see too an increase in the coupling between optical fibers and Artificial Intelligence (AI) methods in at least two aspects. A first aspect will concern the management of information generated by optical fibers, to control telecommunications networks [554], to analyze the light propagation [555], or to manage data from sensors [556], to name a few examples. A second aspect will concern fiber design assistance (material, geometry, etc.) [557,558]. Exotic geometries designed by the AI methods will take advantage of the recent advent of 3D printing techniques for glass. It paves the way for brand new class of fibers. In the context of global warming, it is important to consider optical fiber and sustainability.

8.3.2. Planar waveguides

There are numerous challenges before achieving real breakthroughs in glass planar photonics; the quest for new compositions (and corresponding technologies) to ensure all the desired features and to develop novel material platforms for different photonic applications and the continuous advances in high-performance telecommunications and data transfer services, including the practical application of the Internet of Things technology,which lead to a growing demand of photonic circuits characterized by low loss, high integration density and high tunability.

Glass-ceramic waveguides: For waveguide application, it is important that the glass–ceramic must have good transparency, which implies means low optical scattering and absorption. As explained well in Quandt et al. [559] and also mentioned previously, a low scattering level in a glass–ceramic can be obtained in two ways: (i) both crystalline phases and glass matrix have closely matched refractive index and microcrystals are characterized by low birefringence, and (ii) the crystallite size is much smaller than the wavelength of light. All the effective systems fulfil this second requirement, being constituted by materials with different refractive index and appropriately sized.

There are two main processes that are employed to fabricate transparent glass-ceramics active planar waveguides by sol–gel. One is a “bottom-up” procedure consisting of separately preparing the nanocrystals and them imbedding them in the matrix. The drawback is that when the nanocrystals are imbedded in the host the thermal treatment, necessary to consolidate the structure, can modify the nanocrystal composition and, under some conditions, induce their melting, as observed also in the case of glass–ceramic fiber drawing. One of the first examples of successful bottom-up approach is the fabrication of hybrid organic–inorganic waveguides reported by Ribeiro et al. [560], who reported on waveguides obtained by doping 3-glycidoxipropil) trimethoxisilane (GPTS) with 4 nm hafnia nanocrystals. A transparent colloidal sol was prepared by refluxing for 2 h an ethanolic hafnium oxychloride solution. A second solution was prepared diluting GPTS with butanol in a volume ratio 1:0.5 and prehydrolyzed with HCl. After vigorous stirring overnight at room temperature the sol containing hafnium nanocrystals was added. In 2007, Jestin et al. [561] reported on the fabrication of Er^{3+} doped SiO_2-HfO_2 glass-ceramics by a “top-down” approach, simply adding a further heat treatment at 1000 °C for 30 min to nucleate HfO_2 nanocrystals inside the previously deposited amorphous waveguide. The result was promising for integrated optics application. Based on the single exponential decay profiles obtained for the compositions with 20% and 30% HfO_2, doped with 0.3% Er^{3+}, one can assume a complete embedding of rare earth ions in the crystalline phase. The most common method for transparent glass-ceramics waveguides is the consolidated top-down procedure allowing to optimize the thermal protocol to nucleate the nanocrystals as well as the composition. Very effective results have been obtained with this technique as reported in Refs. [562–564]. The fabricated SnO_2 – based glass–ceramic systems exhibit low losses, high luminescence quantum yield and photorefractivity. However, the targeted objective of that work was to combine greater functionality into the same platform. SiO_2-based glass-ceramics waveguides have recently demonstrated to be an excellent system for this aim. In fact, some recent papers have clearly demonstrated that photonic glass-ceramics activated by SnO_2 nanocrystals exhibit two strategic and powerful characteristics: (a) high luminescence quantum yield, thanks to the role of the nanocrystals as luminescence sensitizing and (b) important change in the refractive index due to the tin dioxide photorefractivity [565,566]. Zur et al., too, demonstrated the important role of tin dioxide nanocrystals as luminescence sensitizers

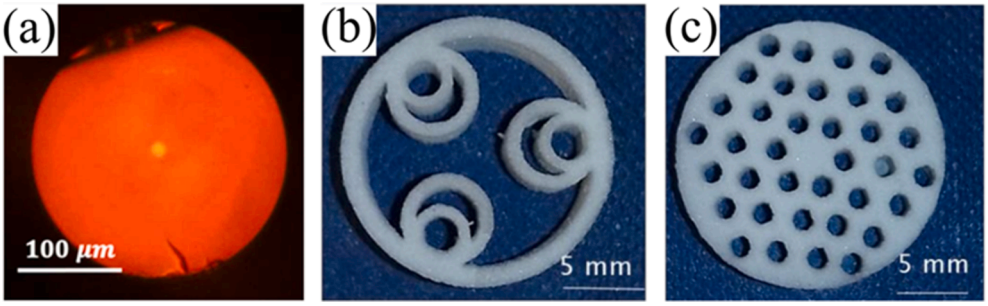

Fig. 42. (a) Cross-section of a 3D printed multimode fiber (Reproduced from Ref. [551] with permission from Optica) (b) Antiresonant fiber preform and (c) photonic crystal fiber preform prepared by SLS (Reproduced from Ref. [552] with permission from SPIE).

[567].

The role of SnO_2 nanocrystals is evident in Fig. 43, which shows the excitation spectrum of a Er^{3+}-activated silica-tin dioxide glass-ceramics waveguide, monitored by the 1530 nm Er^{3+} emission. A more intense emission from the Er^{3+} metastable state $^4I_{13/2}$ is achieved by indirect pumping, i.e., by excitation at the SnO_2 bandgap. A much lower emission intensity of Er^{3+} at 1.5 μm is obtained when the sample is irradiated under the direct excitation. Further, the emission spectra of Er^{3+} under two excitation schemes, (i) UV SnO_2 bandgap excitation and (ii) direct excitation to the Er^{3+} $^2H_{11/2}$ level, are shown. Under the indirect UV excitation ($\lambda_{ex} = 306$ nm) into the SnO_2 bandgap, the $^4I_{13/2} \rightarrow {}^4I_{15/2}$ emission spectrum exhibits Stark splitting and narrow peaks which puts in evidence the Er^{3+} ions location in crystalline environment. On the contrary, the $^4I_{13/2} \rightarrow {}^4I_{15/2}$ photoluminescence spectra obtained by directly exciting the $^2H_{11/2}$ level of the Er^{3+} ions exhibit a broad band typical of the Er^{3+} ions embedded in the glass matrix [565].

The photorefractivity of SiO_2-SnO_2:Er^{3+} glass–ceramic planar waveguides was clearly demonstrated in Ref. [565]. Under UV irradiation at 248 nm, a fast photorefractive response was achieved, leading to a negative effective refractive index change in the order of 10^{-3}. Fig. 44 shows the effective refractive index change of the fundamental 1550 nm TE_0 mode of the $70SiO_2$-$30SnO_2$:$0.5Er^{3+}$ planar waveguide as a function of the cumulative irradiation dose.

Fig. 45 shows a grating formed with 5 μm pitch raster pattern over 4 × 4 mm^2 on a $70SiO_2$-$30SnO_2$:$0.5Er^{3+}$ planar waveguide, fabricated by a CW frequency doubled argon laser ($\lambda = 244$ nm). Moreover, a comparison with the gratings fabrication on hydrogen loaded germanium doped silica glasses [565] shows that the energy density, required to achieve a similar change in the refractive index, is one order of magnitude greater than for the SnO_2-based glass–ceramic waveguides [568]. It is evident that this material system paves the way to the fabrication of sol–gel based photonic devices where the direct UV writing overcomes the drawbacks related to the reactive ion etching method as well as to the micromachining technique. SiO_2-SnO_2 glass-ceramics activated by rare-earth ions appear to be a promising system for constructing active optical integrated components.

As exhaustively discussed in the Special Issue of Elsevier's journal *Optical Materials* entitled "Flexible Photonics: a multidisciplinary tool enabling sustainable development" [569], the objective of this topic, as already achieved for electronics, is the integration of passive and active photonic devices on flexible substrates for a broad spectrum of application ranging from optical interconnection to sensors for civil infrastructure and environments, to coherent and uncoherent light sources and functionalized coatings for integration on biological tissue. Flexible planar integrated photonic structures, such as gratings, channel waveguides but also solar cells and protective coatings, offer unique performance characteristics compared to their rigid classical counterparts. In a recent paper, for example, Tran et al. [570] report on rare-earth doped SnO_2 photoluminescent thin films deposited by sol–gel technology on ultrathin glass (AS 87-eco Schott) flexible substrates. The main significant outcomes of this work can be summarized as follows: (a) a reliable sol–gel fabrication protocol for coating flexible glass substrate is developed, (b) the films are not damaged after several bending circles.

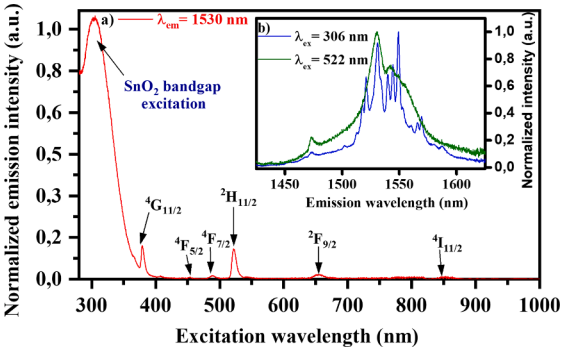

Fig. 43. (a) Excitation spectrum monitored at emission $\lambda_{em} = 1530$ nm of Er^{3+} and (b) emission spectra under two excitation schemes: (i) UV SnO_2 bandgap excitation at 306 nm and (ii) direct excitation to an Er^{3+} electronic state $^2H_{11/2}$ at 522 nm using Edinburgh FLS980 spectrofluorometer of the $70SiO_2$-$30SnO_2$:$0.5Er^{3+}$ planar waveguide. (Reproduced from [565] with permission from Elsevier).

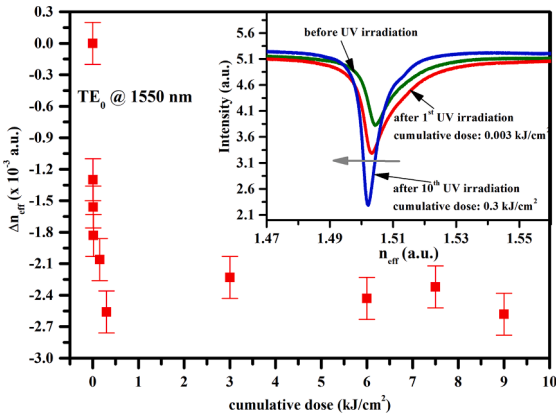

Fig. 44. Effective refractive index changes on 1550 nm TE_0 mode supported by the $70SiO_2$-$30SnO_2$:$0.5Er^{3+}$ planar waveguide as a function of cumulative dose. The inset image is the shift to the lower index values of the 1550 nm TE_0 mode after the two UV cumulative doses: 0.003 kJ/cm^2 (the 1st UV irradiation) and 0.3 kJ/cm^2 (the 10th UV irradiation). (Reproduced from [565] under the terms of the Open Access Publishing Agreement).

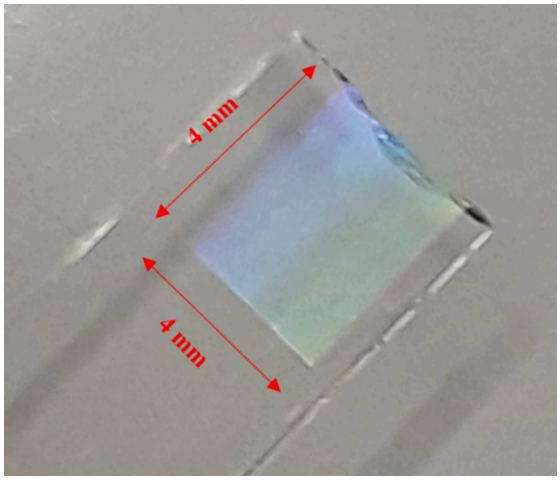

Fig. 45. Optical gratings fabricated by a CW frequency doubled argon laser $\lambda = 244$ nm with a writing fluence of 1.0 kJ/cm^2 on a 4x4 mm^2 area of the $70SiO_2$-$30SnO_2$:$0.5Er^{3+}$ glass–ceramic planar waveguide. One can see the colors due to the interference patterns scattering from the gratings based on the Bragg law. (Reproduced from [565] under the terms of the Open Access Publishing Agreement).

Bending test was performed using a homemade 3-point bending setup with span (ΔL) set at 30 mm shown in Fig. 46.

Based on these recent results, an important increase in sol–gel photonic research is expected to successfully lead to innovative fabrication protocols where photorefractivity, luminescence enhancement and mechanical flexibility can be exploited.

Integration density of on-chip glasses: Efforts have been directed towards a deeper study of femtosecond laser direct writing (FLDW) processes, which offers the capability of 3D structuring inside transparent glasses with a limited effect on the propagation losses. Recent reviews present active and passive devices fs-written in both glass and crystal materials [571,572]. Fig. 47 summarizes the processing items of the waveguide fabrication by ultrafast laser direct writing (ULDW), the key parameters, and examples of application areas [564]. Whereas many results in the literature refer to phosphate glasses, a very recent paper focuses on direct writing of channel waveguides in Er^{3+} aluminosilicate glass and reports a minimum propagation loss of about 1.51 dB/cm at a wavelength of 1.5 μm, claiming great potential to create active gain devices for application in integrated photonics and all-optical communication [573].

Direct fs-laser writing of channel waveguides has also been very important for chalcogenide glasses, to avoid the waveguide walls' scattering losses resulting from the chemical or physical etching process. Recent investigations aimed at exploring the laser-induced damage thresholds of $Ga_{0.8}As_{29.2}Sb_{10}S_{60}$ glasses with various doping levels of Tm^{3+} rare earth ions and the effects of such a damage on the glass' luminescence properties [574]. Tm^{3+} doping considerably decreased the laser-induced damage, from about 3400 to 1900 mJ/cm^2, when the Tm^{3+} concentration was increased from 0 to 5000 ppm by weight (ppmw). Moreover, despite the existence of a damage, the luminescence properties were barely affected. In-glass optical elements offer many advantages for prototype stability and lifetime, but also in terms of complexity and variety of possible applications, due to the flexible 3D design. Chalcogenide glasses, in

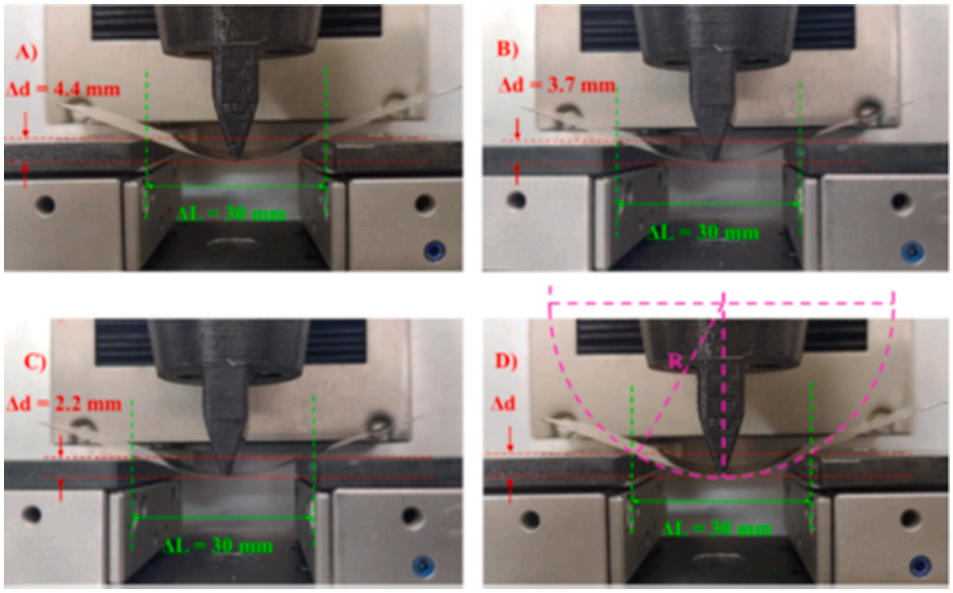

Fig. 46. Maximum deflection during the bending test for: (a) untreated ultrathin AS 87 eco Schott glass; (b) ultrathin AS 87 eco Schott glass heat-treated at 500 °C for 4 h; (c) ultrathin AS 87 eco Schott glass coated with SnO_2:Yb^{3+} (1.67 mol%) sol gel film and heat-treated at 500 °C for 4 h; and (d) the representation of the approximate determination of the radius of curvature for bent samples. (Reproduced from Ref. [570] with permission from Elsevier).

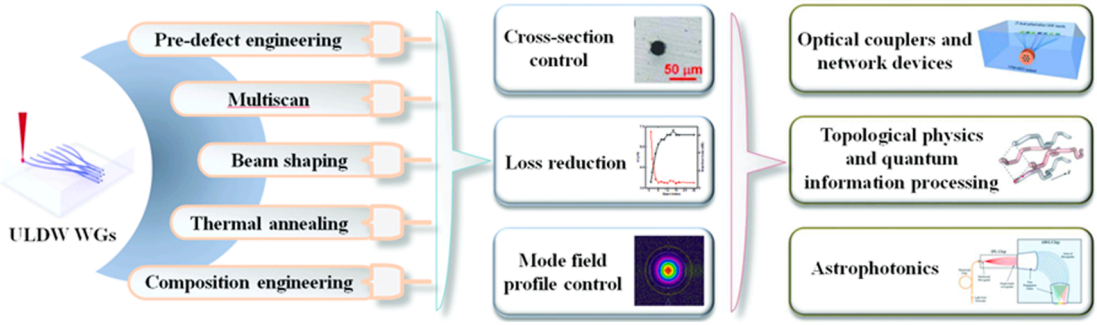

Fig. 47. Overview of the key mechanisms for reducing losses of waveguides produced by ultrafast laser direct writing (ULDW) in glass substrates. A few application areas are also indicated. (Reproduced from Ref. [564] under the terms of the Open Access Publishing Agreement).

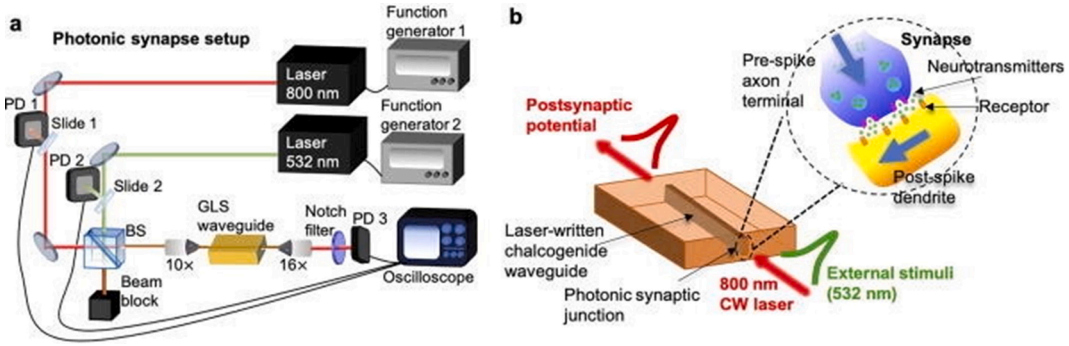

Fig. 48. (a) Experimental setup used to emulate a biologic synapse in a waveguide written in gallium lanthanum sulfide (GLS) glass by fs-laser. (b) The entrance volume of the waveguide, which can photodarken, corresponds to the photonic synapse junction, whereas the waveguide, which transmits the signal, represents the photonic axon. (Reproduced from Ref. [576] with permission from American Institute of Physics).

particular, offer high-index contrast and operation in infrared and mid-infrared wavelength range, with relevant applications in sensing and imaging. D'Amico et al. showed efficient signal extraction from the transported light for large-mode-area light transport and extraction in sulfur-based chalcogenide mid-infrared glasses [575]. As an example, that work demonstrated a near-IR saturable absorber 3D concept based on ultrafast laser-fabricated coupled waveguide arrays, suitable for IR ultrashort laser pulses at a low, kilowatt threshold. Another noteworthy example of application of fs-laser writing technology in chalcogenide glass is represented by the implementation of optical waveguides that can work as all-optical neuromorphic units: the results prove the potential for large-scale single-step fabrication of fully integrated photonic chips based on cognitive principles [576]. Fig. 48 shows the experimental arrangement used to emulate in the chip the function of the biological synapse. By using proper modulation rate and intensity, this system constitutes a proof of concept that optical waveguides may well mimic the excitatory and inhibitory spiking activities typical of biologic neuronal systems [576].

Recently, an increasing interest has been addressed to the fs-laser writing of optical waveguides in silver-containing glasses [335,362,577–579]. It is well known that the presence of silver in glass may confer enhanced functionalities, making the material suitable for the fabrication of photosensitive layers, ion selective electrodes, ion conductors and anti-reflecting coatings, not to mention its application among bioactive glasses. A train of fs-laser pulses in Ag-doped phosphate glasses allows both local second- and third-harmonic generations (SHG and THG) [579] and that Ag multimers in Tb–Yb co-doped SiO_2-ZrO_2-Na_2O films can provide an efficient optical sensitizing effect for rare earth ions, leading to a broadband enhanced excitation, with a great potential technological impact on the development of light emitting devices and solar cells [580].

Referring to the refractive index change Δn created by fs-laser pulses, such change is usually classified into three distinct types (Types 1, 2, or 3), depending on the laser parameters used: Type 1 corresponds to a smooth change in the refractive index (and is therefore generally preferred for the direct writing of waveguides and photonic components), Type 2 refers to the generation of negative Δn and noticeable birefringence, and Type 3 can be attributed to voids. Ag-containing glasses (and, particularly, a silver containing zinc phosphate glass) can exhibit a new type of refractive index change, namely type A (where A stays for Argentum). As reported in [362], Type A requires much lower laser fluence compared to other Δn change types and is due to the formation of fluorescent silver clusters distributed around the laser-glass interaction voxel and that act as an extrinsic agent. Fig. 49 schematically presents the irradiation process and the morphology of the resulting structure.

As detailed in Ref. [362], to proof the suitability of the new material/irradiation technique for the development of integrated optical circuits, 7-mm long single-mode waveguides were inscribed, with an overall propagation loss of 1.2 dB/cm at a wavelength of 630 nm, this value being the upper bound, estimated considering the simulated mismatch, Fresnel losses of 0.43 dB (n = 1.59) and the measured insertion losses of the waveguide. Fig. 50**a-d** present the scheme of a 50:50 beam splitter, its photoluminescence profile, and the intensity profiles of the output modes. The waveguides were written using a 9 TW/cm^2 fluence and a 60 μm/s translation speed.

Another important advance was recently achieved by Tsimvrakidis et al., who used an $AgPO_3$ silver metaphosphate glasses and demonstrated the capability of laser writing buried waveguides as well as erasing and re-writing them by means of a single femtosecond laser source [578]. This non-ablative phenomenon relies on the local relaxation of the glass network caused by the heat deposited upon pulsed laser irradiation. Before that work, the possibility of erasing a fs-written structure had already been demonstrated but only by using thermal annealing, and often with some limitations; for instance, Hughes et al. fs-laser wrote waveguides in Ni-doped Li_2O–Ga_2O_3–SiO_2 glass and glass–ceramic (GC), which could be erased when the glass is annealed to form a GC. However, once the GC is formed, the waveguides could not be erased any more by annealing [581]. On the contrary, according to the new findings, photonic applications can be envisaged which involve infinite cycles of write/erase/re-write processes without the need of intermediate thermal annealing steps. Fig. 51 shows a write/erase/re-write cycle with the photographic and electron micrographs of the waveguides.

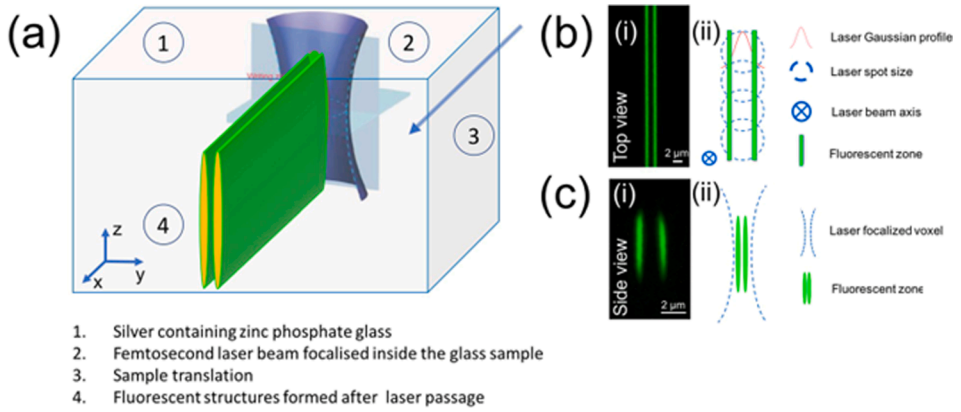

Fig. 49. (a) Schematic presentation of the morphology of the structures following translation perpendicular to laser beam propagation inside silver-containing zinc phosphate glasses. Fluorescence confocal images of the (b.i) top view, and (c.i) side view. Schematic presentation of the writing process with (b.ii) top view and (c.ii) side view. (Reproduced from Ref. [362] under the terms of the Open Access Publishing Agreement).

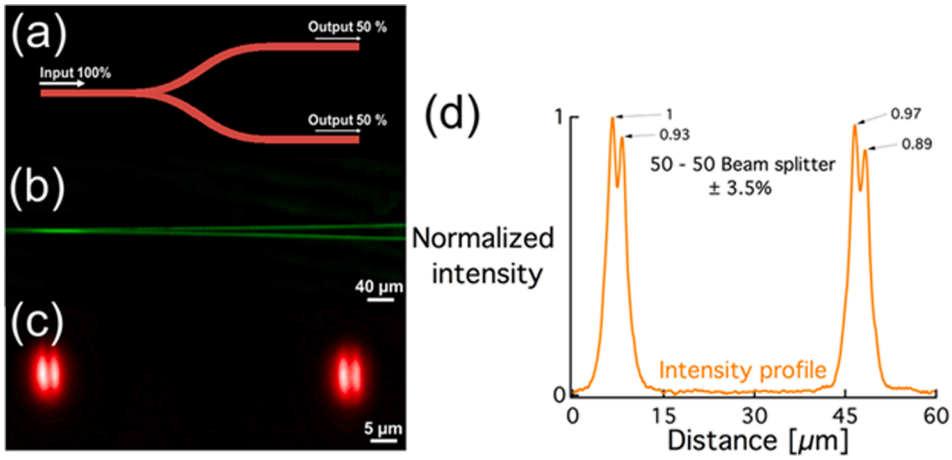

Fig. 50. (a) Schematic presentation of a 50–50 beam splitter (top view), (b) fluorescent image (top view) of the written 50–50 beam splitter under 488 nm excitation and emission in the visible range, (c) output modes of the beam splitter, and (d) normalized intensity profile of the output modes. (Reproduced from Ref. [362] under the terms of the Open Access Publishing Agreement).

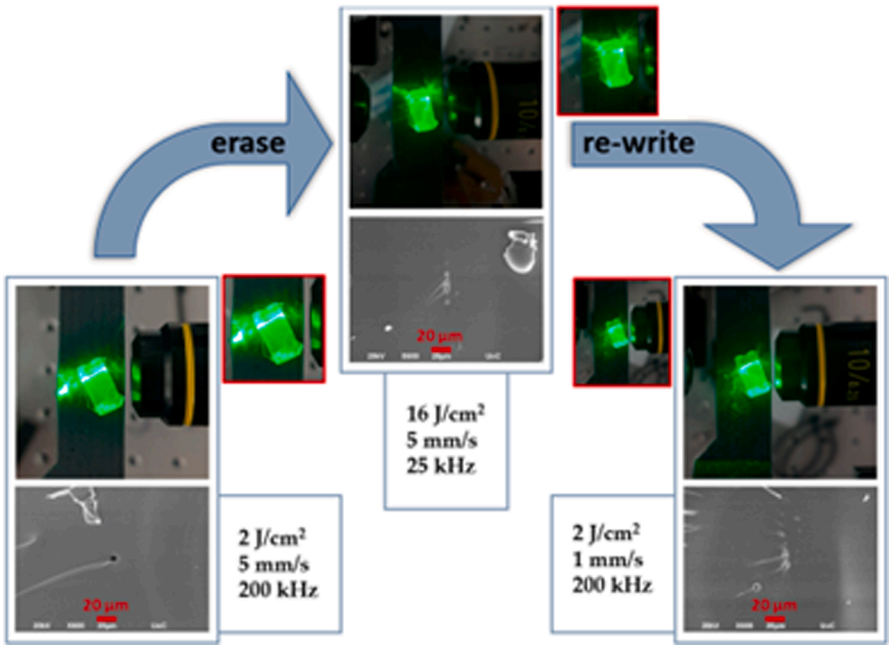

Fig. 51. Photographic images (and corresponding cross-section SEM images) of the waveguiding effect of laser-inscribed lines. The process parameters for initial fabrication (left), erasing (middle) and re-writing are indicated. All the images correspond to a same glass spot. (Reproduced from Ref. [578] under the terms of the Open Access Publishing Agreement).

Among photonic applications, two areas remain of great importance where glass, too, may play an important role: optical amplification and lasing (for telecommunications and sensing), and nonlinear optics (NLO, for wavelength conversion, all-optical switching, etc.). A material suitable for both the application areas would be extremely attractive, and new host structures based on heavy metals have been thoroughly investigated [582,583]. Novel inorganic NLO materials are being explored, which include fluorooxoborates and fluorophosphates for deep-UV region, various oxide-based metal compounds for UV and Vis–NIR bands, and metal chalcogenides and metal halides for mid-IR region. A review of applications of heavy metal oxides and their compositional glasses, together with their applications in optoelectronics and biomedicine, has been the subject of a recently published book [584]. When channel waveguide fabrication in these materials is concerned, some problems may arise during the etching process used to define the waveguide sidewalls, due to metals' presence. An interesting solution to overcome the problem has been suggested, which adopts a pedestal waveguide structure [585]. As represented in Fig. 52**a,** the pedestal is first defined by reactive ion etching on the lower cladding layer, which may be thermally grown SiO_2 on top of a Si wafer. After mask removal, the core layer (e.g., silicon oxide,

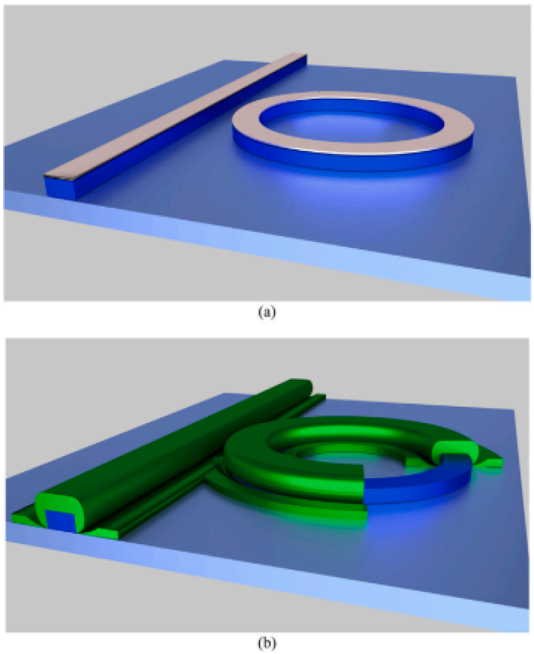

Fig. 52. Fabrication of a pedestal waveguide. (a) Etching of the lower cladding (blue). (b) Deposition of the core material (green). In the (b) image some parts of the film that composes the core were removed for clarity. (Reproduced from Ref. [586] with permission from Elsevier). (For interpretation of the references to color in this figure legend, the reader is referred to the web version of this article.)

aluminum nitride, tellurite or germanate glass) is deposited (Fig. 52**b**). As an example of application, in Yb^{3+}/Er^{3+} co-doped TeO_2–WO_3–Bi_2O_3 pedestal waveguides 20 μm wide, a gain of 3.7 dB/cm was achieved at a wavelength of 1530 nm, under 980 nm excitation [586].

As to the future prospects for integration of waveguide integrated circuits using ultrafast laser processing, the laser-induced structural changes on the glass surface are dependent on the incident average pulse energy (or power) and pulse duration [441,442,453]. Typically, for materials ablation, the average pulse energy is larger than that required for refractive index modification on surface or subsurface of a glass. The dynamics of ablation induced machining of transparent materials involves the following steps occurring in three different temporal regimes: carrier excitation; (i) carrier excitation via multiphoton absorption (in sub-pico $<$ 10-100sps), (ii) avalanche ionization (100sps to sub ns), thermalization during relaxation (iii) carrier-carrier scattering in sub pico second, (iv) carrier-phonon scattering during recombination, and thermal relaxation leading to structural changes (v) shock-wave emission, (vi) thermal diffusion, and finally (vii) condensation or cooling leading to a metastable structure [585]. The incident laser cuts simultaneously the layers of materials [466], which is not feasible in the standard wet and dry etching processes. For laser machining, the control of beam polarization and spot size are the two most important parameters for achieving good surface and edge finish.

The waveguide inscription or writing by modifying the sub-surface refractive index in the glass requires average pulse energies in the 10 s–100 μJ, so that the structural changes are highly localized by controlling the polarized beam diameter. In this process, the control of beam polarization also plays an important role because of the coupling of the electric field in laser with electrostatic field in materials. Depending on the type of glassy materials used, the apparent change in the refractive index may arise via a combination of relaxation: expansion-compression because the shock-wave generation and localized thermal event and rapid relaxation induces a confined density segregation. In certain glasses in which the photo-sensitive ions are present, the irradiation with femto-second pulsed lasers may also induce photo-darkening, leaving permanent color centers which might be useful in writing Bragg or long-period gratings in a waveguide and magneto-optic memory applications [587–589].

9. Conclusions and further musings on future opportunities

Each section above provided specific topical insights into current and future opportunities for advancements in glass optical materials. More generally, as true now as it has been over a hundred years, a deeper understanding of the interconnections between glass composition, processing, structure, and properties across all the states application spaces is critical. It also is worth noting that the marriage of glass and light will only grow stronger with time as photonics continues to impact every corner of modern life.

A few cross-cutting topics for future exploration and development include: (1) the use of machine learning and artificial intelligence to help predict passive and active optical properties of glasses in all forms (bulk, films, fiber, etc.), particularly as relates to (i) luminescent and nonlinear optical properties, (ii) empirical or theoretical predictions of crystallization process for any given glass composition, that will enable consideration of novel composite materials that enhance and expand the capabilities of glass or glass

-ceramic media, and (iii) glasses with higher refractive index and less dispersion; (2) glass process research that permits reduced cost, environmental impact, and scaling of more exotic glasses for high performance applications, e.g., infrared optics and sources, plasmonic and nanocrystalline glass-ceramics, etc.; (3) pushing the transmission limits of glass, both spectrally (e.g., deeper into the UV and further into the IR) and with respect to loss (e.g., lower-than-silica attenuation across broad spectral ranges); (4) compositions and fabrication methods that permit nonlinearities that are markedly higher or lower than currently available, including second-order phenomena; (5) novel approaches to create microstructures inside glass forms, (6) hybrid integration with semiconductors, crystals, and organic materials to realize novel and complex functions such as optical computing, sensing, monitoring, and data processing, and (7) a more complete understanding of photosensitivity and photo-induced properties in order to make greater use of such glasses.

Declaration of Competing Interest

The authors declare that they have no known competing financial interests or personal relationships that could have appeared to influence the work reported in this paper.

Data availability

Data will be made available on request.

Acknowledgment

YGC acknowledges support of Basic Science Research Program through the National Research Foundation of Korea (NRF) funded by the Ministry of Science and ICT (No. 2020M3D1A2101797), and the Institute of Information & Communications Technology Planning & Evaluation (IITP) grant funded by the Ministry of Science and ICT (No. 2021-0-00019; Research on Optical Learning Technology for AI). MN acknowledges the São Paulo Research Foundation – FAPESP (grants n° 2013/07793-6) for financial support. KR acknowledges the support of the UCF Board of Trustee Endowed Chair program. JM acknowledges Academy of Finland (Academy projects 331924 and 328079) as well the Jane and Aatos Erkko foundation for financial support. JB acknowledges the J. E. Sirrine Foundation. LP acknowledges the Academy of Finland (Flagship Programme, Photonics Research and Innovation (PREIN-320165) and Academy Projects (326418, 316483 and 328078)), the Magnus Ehrnrooth Foundation, and the Pirkanmaa Regional Fund.

References

[1] Chopinet ME. Springer handbook of glass. In: Musgraves JD, Hu J, Calvez L, editors. Springer handbook; chapt 1: The history of glass, Springer Nature. Switzerland AG; 2019.
[2] Haase G, Arnold D, Pohl HJ. 'Glas in englisher art aus der dresdener hütte zur chemisch analytischen untersuchung von dresdener gläsen', In Annales du 10e Congrès de l'Association Internationale pour l'Histoire du Verre: Madrid-Segovie 1985. Amsterdam: AIHV; 1987. p. 481–96.
[3] Charleston RJ. English glass and the glass used in England, circa 400–1940.London. Allen & Unwin; 1984.
[4] Dalton J. A new system of chemical philosophy, part 1 (Manchester and London: S. Russell [for R. Bickerstaff], 1808), 157, 189.
[5] Zachariasen WH. The atomic arrangement in glass. J Am Chem Soc 1932;54:3841–51.
[6] Rasmussen SC. How glass changed the world: the history and chemistryof glass from antiquity to the 13th century. New York: Springer; 2012. 85 p. ISBN: 978-3642281822.
[7] Kurkjian CR, Prindle WR. Perspectives on the history of glass composition. J Am Ceram Soc 1998;81:795–813.
[8] Busch E. Report on the requirements of the Rathenow optical industry 1883. In: Ernst Abbe, editor. Gesammelte Abhandlungen. Georg Olms, vol. IV; 1989.
[9] Hartmann P, Jedamzik R, Reichel S, Schreder B. Optical glass and glass ceramic historical aspects and recent developments: a Schott view. Appl Opt 2010;49:D157.
[10] Kappler D, Steiner J. SCHOTT 1884–2009 Vom Glaslabor zum Technologiekonzern. SCHOTT AG; 2009. p. 1884–2009.
[11] Stookey SD. Method of making ceramics and products thereof, US Patent 2,920,971; 1960.
[12] Shultz-Sellack C. Diathermansie einer Reihe von Stoffen für Wärme sehr geringer Brechbarkeit. Ann Phys 1870;139:182.
[13] Frerichs R. New optical glasses transparent in the infra-red up to 12μm. Phys Rev 1950;78:643.
[14] Ovshinsky SR. Reversible electrical switching phenomena in disordered structures. Phys Rev Lett 1968;21:1450.
[15] Borisova ZU. Glassy semiconductors. New York: Plenum Press; 1981. 7.
[16] Lucas J. Review of fluoride glasses. J Mater Sci 1989;24:1–13.
[17] Adam J. Fluoride glass research in france. J Fluorine Chem 2001;107:265–70.
[18] Snitzer E. Optical maser action of Nd^{3+} in a barium crown glass. Phys Rev Lett 1961;7:444–6.
[19] Koester C, Snitzer E. Amplification in a fiber laser. Appl Opt 1964;3:1182–6.
[20] Kao KC, Hockham GA. Dielectric-fibre surface waveguides for optical frequencies. Proc IEE 1966;113(7):1151–8.
[21] Kapron F, Keck D, Maurer R. Radiation losses in glass optical waveguides. Appl Phys Lett 1970;17:423–5.
[22] Miya T, Terunuma Y, Hosaka T, Miyashita T. Ultimate low-loss single-mode fibre at 1.55 μm. Electron Lett 1979;15:106–8.
[23] Ballato J, Dragic P. Glass: the carrier of light – a brief history of optical fiber. Int J Appl Glass Sci 2016;7(4):413–22.
[24] Robinson AL. Chalcogenide glasses: a decade of dissension and progress. Science 1977;197:1068–70.
[25] Mauro J, Zanotto ED. Two centuries of glass research: historical trends, current status, and grand challenges for the future. Int J Appl Glass Sci 2014;5(3):313–27.
[26] Jacobs M. Review of how glass changed the world: the history and chemistry of glass from antiquity to the 13th century. J Chem Educ 2015;92:406–7.
[27] Ediger MD, Angell CA, Nagel SR. Supercooled liquids and glasses. J Phys Chem Solids 1996;100:13200–12.
[28] Abou Neel EA, Knowles JC. In: Cellular response to biomaterials Chapter 7: Biocompatibility and other properties of phosphate-based glasses for medical applications, Woodhead Publishing Series in Biomaterials; 2009. p. 156–82.
[29] Rivier N. Combinatorics in glass. Math Comput Model 1997;26:255–67.
[30] Dietzel A, Wickert H. The Degree of Glass Formation in the System Na_2O - SiO_2. Glass Sci Technol: Int J Germ Soc Glass Technol (DGG) 1956;29:1.
[31] Turnbull D. Under what conditions can a glass be formed? Contemp Phys 1969;10:473–88.
[32] Uhlmann DR. Kinetics of glass formation and devitrification behavior, J Phys Colloq 1982; 43: C9-175-C9-190.
[33] Avrami MJ. Grand partition functions and so-called thermodynamic probability. J Chem Phys 1939;7:103.

[34] Avrami MJ. Kinetics of phase change. II Transformation-time relations for random distribution of nuclei. J Chem Phys 1940;8:212.
[35] Avrami MJ. Granulation, phase change and microstructure kinetics of phase change III. J Chem Phys 1941;9:177.
[36] Kelton KF, Greer AL. Pergamon materials series, Chapter 1 - Introduction, vol. 15. Pergamon; 2010. p. 1–15.
[37] Christian JW. The theory of metals and alloys. Oxford: Pergamon Press; 1965.
[38] Shelby JE. Introduction to glass science, 2nd ed. RS.C; 2005.
[39] Kelton KF. Transient nucleation in glasses. Mater Sci Eng B 1995;32:145.
[40] Pye LD, Stevens HJ, Lacourse WC. Introduction to glass science. Proceedings of a tutorial symposium held at the State University of New York. Alfred, NY: College of Ceramics at Alfred University; 1970.
[41] Kirkpatrick RJ. Kinetics of crystallization of igneous rocks. Washington, D.C.: Mineralogical Society of America; 1981. p. 321–98.
[42] Zanotto ED. Glass crystallization research — a 36-year retrospective. Part I, Fundamental studies. Int J Appl Glass Sci 2013;4:105–16.
[43] James PJ. Kinetics of crystal nucleation in silicate glasses. J Non-Cryst Solids 1985;73:517–40.
[44] Müller R, Zanotto ED, Fokin VM. Surface crystallization of silicate glasses: nucleation sites and kinetics. J Non-Cryst Solids 2000;274:208–31.
[45] Massera J, Remond J, Musgraves J, Davis MJ, Misture S, Petit L, et al. Nucleation and growth behavior of glasses in the TeO_2–Bi_2O_3–ZnO glass system. J Non-Cryst Solids 2010;356:2947–55.
[46] Dimesso L, Gnappi G, Montenero A, Fabeni P, Pazzi GP. The crystallization behaviour of bismuth germanate glasses. J Mater Sci 1991;26:4215–9.
[47] Pradel A. Glass to Crystal: Chapter 21: Nucleation, crystallisation and phase separation in chalcogenide glasses.
[48] Altounian Z, Guo-Hua T, Strom-Olsen JO. Crystallization characteristics of Cu-Zr metallic glasses from $Cu_{70}Zr_{30}$ to $Cu_{25}Zr_{75}$. J Appl Phys 1982;53:4755.
[49] Ohja N, Szczodra A, Boetti NG, Massera J, Petit L. Nucleation and growth behavior of Er^{3+} doped oxyfluorophosphate glasses. RSC Adv 2020;10:25703–16.
[50] Meneghetti M, Caillaud C, Chahal R, Galdo E, Brilland L, Adam JL, et al. Purification of Ge-As-Se ternary glasses for the development of high quality microstructured optical fibers. J Non Cryst Solids 2019;503–504:84–8.
[51] Ledemi Y, El Amraoui M, Messaddeq Y. Transmission enhancement in chalco-halide glasses for multiband applications. Opt Mater Express 2014;4:1725.
[52] Massera J, Haldeman A, Jackson J, Rivero-Baleine C, Petit L, Richardson K. Processing of tellurite-based glass with low OH content. J Am Ceram Soc 2011;94:71–7.
[53] Hench LL, West JK. The sol-gel process. Chem Rev 1990;90:33–72.
[54] Kajihara K. Review article recent advances in sol–gel synthesis of monolithic silica and silica-based glasses. J Asian Ceram Soc 2013;1:21–133.
[55] Roy R. Gel route to homogeneous glass preparation. J Amer Ceram Soc 1969;52:344.
[56] Lepry WC, Nazhat SN. A review of phosphate and borate sol-gel glasses for biomedical applications. Adv NanoBiomed Res 2021;1:2000055.
[57] Dejneka M, Riman RE, Snitzer E. Sol–gel synthesis of high-quality heavy-metal fluoride glasses. J Am Ceram Soc 1993;76:3147.
[58] Saad M, Poulain M. Fluoride glass synthesis by sol–gel process. Am Ceram Soc Bull 1995;74:66.
[59] Melling PJ. Alternative methods of preparing chalcogenide glasses. Am Ceram Soc Bull 1984;63:1427.
[60] Yong-Taeg O, Fujino S, Morinaga K. Fabrication of transparent silica glass by powder sintering. Sci Technol Adv Mater 2002;3:297–301.
[61] McGill D, Ghozi-Bouvrande JB, Kang M, Dolhen M, Delaizir G, Chenu S, et al. Hot-pressing of tellurite glass with a sacrificial pressure-transmitting medium. J Non-Cryst Sols 2020;528:119713.
[62] Bertrand A, Carreaud J, Delaizir G, Duclere JR, Colas M, Cornette J, et al. A comprehensive study of the carbon contamination in tellurite glasses and glass-ceramics sintered by spark plasma sintering (SPS). J Am Ceram Soc 2014;97:163–72.
[63] Cui S, Boussard-Pledel C, Calvez L, Rojas F, Chen K, Ning H, et al. Comprehensive study of tellurium based glass ceramics for thermoelectric application. Adv Appl Ceram 2015; 114: S42–S47.
[64] Babu S, Balda R, Fernandez J, Sedano M, Gorni G, Cabral AA, et al. $KLaF_4$:Nd^{3+}doped transparent glass-ceramics processed by spark plasma sintering. J Non-Cryst Solids 2022;578:121289.
[65] Calvez L. Chalcogenide glasses and glass-ceramics: Transparent materials in the infrared for dual applications. Comptes Rend Physi, Acad Sci 2017;18:314–22.
[66] Singarapu B, Galusek D, Duran A, Jesús Pascual M. Review: glass-ceramics processed by Spark Plasma Sintering (SPS) for optical applications. Appl Sci 2020;10:2791.
[67] Angell CA. Relaxation in liquids, polymers and plastic crystals — strong/fragile patterns and problems. J Non-Cryst Solids 1991;131–133:13–31.
[68] Aggarwal ID, Sanghera JS. development and applications of chalcogenide glass optical Fibers at NRL. J Optoelectron Adv Mater 2002;4:665–78.
[69] Barney ER, Abdel-Monei NS, Towey JJ, Titman J, McCarthy JE, Bookey HT, et al. Correlating structure with nonlinear optical properties in $xA_{s40}Se_{60}$ - (1–x) $As_{40}S_{60}$ glasses. Phys Chem Chem Phys 2015;17:6314–27.
[70] Fleming JW, Wood DL. Refractive index dispersion and related properties in fluorine doped silica. Appl Opt 1983;22:3102–4.
[71] Yadav AV, Singh P. A review of the structures of oxide glasses by Raman spectroscopy. RSC Adv 2015;5:67583.
[72] Kamitsos EI. Infrared spectroscopy of glasses. In: Book: modern glass characterization; 2015. p. 32–73.
[73] Youngman R. NMR spectroscopy in glass science: a review of the elements. Mater 2018;11:476.
[74] Mackenzie JD. Structures and properties of ormosils. J Sol-Gel Sci Technol 1994;2:81–6.
[75] Rogers E, Dorenbos P, Van der Kolk E. Systematics in the optical and electronic properties of the binary lanthanide halide, chalcogenide and pnictide compounds: an overview. New J Phys 2011;13(9):093038.
[76] Liu G, Jacquier B, editors. Spectroscopic properties of rare earths in optical materials. Springer Science & Business Media; 2006.
[77] Gschneidner KA, Bunzli JC, Pecharsky VK, editors. Handbook on the physics and chemistry of rare earths. Elsevier; 2005.
[78] Jacobsohn LG, Toncelli A, Sprinkle KB, Kucera CJ, Ballato J. Spectral engineering of LaF_3: Ce^{3+} nanoparticles: the role of Ce^{3+} in surface sites. J Appl Phys 2012;111(7):074315.
[79] You S, Li S, Jia Y, Xie RJ. Interstitial site engineering for creating unusual red emission in $La_3Si_6N_{11}$: Ce^{3+}. Chem Mater 2020;32(8):3631–40.
[80] Dodson CM, Zia R. Magnetic dipole and electric quadrupole transitions in the trivalent lanthanide series: Calculated emission rates and oscillator strengths. Phys Rev B 2012;86(12):125102.
[81] Schmidt T, Macfarlane RM, Völker S. Persistent and transient spectral hole burning in Pr^{3+}-and Eu^{3+}-doped silicate glasses. Phys Rev B 1994;50(21):15707.
[82] Lyo SK. Anomalous optical homogeneous linewidths in glasses. Phys Rev Lett 1982;48(10):688.
[83] Meltzer RS, Feofilov SP, Tissue B, Yuan HB. Dependence of fluorescence lifetimes of Y_2O_3: Eu^{3+} nanoparticles on the surrounding medium. Phys Rev B 1999;60(20):R14012.
[84] Egan WG, Aspnes DE. Finite-wavelength effects in composite media. Phys Rev B 1982;26(10):5313.
[85] Meltzer RS, Yen WM, Zheng H, Feofilov SP, Dejneka MJ. Relaxation between closely spaced electronic levels of rare-earth ions doped in nanocrystals embedded in glass. Phys Rev B 2002;66:224202.
[86] Auzel F, Goldner P. Towards rare-earth clustering control in doped glasses. Opt Mat 2001;16(1–2):93–103.
[87] Nishiura S, Tanabe S, Fujioka K, Fujimoto Y. Properties of transparent Ce:YAG ceramic phosphors for white LED. Opt Mat 2011;33:688–91.
[88] Erol E, Vahedigharehchopogh N, Kıbrıslı O, Ersundu MC, Ersundu AE. Recent progress in lanthanide-doped luminescent glasses for solid-state lighting applications—a review. J Phys: Condens Matter 2021;33:483001.
[89] Pawar PP, Munishwar SR, Gautam S, Gedam RS. Physical, thermal, structural and optical properties of Dy^{3+} doped lithium alumino-borate glasses for bright W-LED. J Lumin 2017;183:79–88.
[90] Zhang X, Wang J, Huang L, Pan F, Chen Y, Lei B, et al. Tunable luminescent properties and concentration-dependent, site-preferable distribution of Eu^{2+} ions in silicate glass for white LEDs applications. ACS Appl Mater Interfaces 2015;7:10044–54.
[91] An J, Zhang S, Liu R, Hu G, Zhang Z, Qiu Y, et al. Luminescent properties of Dy3+/Eu3+ doped fluorescent glass for white LED based on oxyfluoride matrix, J Rare Earths 2021; 39: 36–2.
[92] Lakshminarayana G, Yang H, Qiu J. White light emission from Tm^{3+}/Dy^{3+} co-doped oxyfluoride germanate glasses under UV light excitation. J Solid State Chem 2009;182:669–76.

[93] Caldiño U, Lira A, Meza-Rocha AN, Pasquini E, Pelli S, Speghini A, et al. White light generation in Dy^{3+}-and Ce^{3+}/Dy^{3+}-doped zinc–sodium–aluminosilicate glasses. J Lumin 2015;167:327–32.
[94] Vijayalakshmi L, Naveen Kumar K, Hwang P. Dazzling cool white light emission from Ce^{3+}/Sm^{3+} activated LBZ glasses for W-LED applications. Ceram Int 2018;44:21083–90.
[95] Wei R, Zhang H, Li F, Guo H. Blue-white-green tunable luminescence of Ce^{3+}, Tb^{3+} Co-doped sodium silicate glasses for white LEDs. J Am Ceram Soc 2012;95:34–6.
[96] Zhang JC, Parent C, le Flem G, Hagenmuller P. White light emitting glasses. J Solid State Chem 1991;93:17–29.
[97] Zhao CJ, Cai JL, Li RY, Tie SL, Wan X, Shen JY. White light emission from $Eu^{3+}/Tb^{3+}/Tm^{3+}$ triply-doped aluminoborate glass excited by UV light. J Non-Cryst Solids 2012;358:604–8.
[98] Zhong H, Chen G, Yao L, Wang J, Yang Y, Zhang R. The white light emission properties of $Tm^{3+}/Tb^{3+}/Sm^{3+}$ triply doped SrO–ZnO–P_2O_5 glass. J Non-Cryst Solids 2015;427:10–5.
[99] An J, Zhang Z, Qiu Y, Yuan FZ, Zhou Y, Zeng F. Luminescence properties of borosilicate glass doped with $Ce^{3+}/Dy^{3+}/Eu^{3+}$ under ultraviolet excitation for white LED. J Non-Cryst Solids 2019;503–504:208–13.
[100] Gong H, Yang D, Zhao X, Yun Bun Pun E, Lin H. Upconversion color tunability and white light generation in $Tm^{3+}/Ho^{3+}/Yb^{3+}$ doped aluminum germanate glasses. Opt Mat 2010;32:554–9.
[101] Weber MJ. Science and technology of laser glass. J Non-Cryst Solids 1990;123:208–22.
[102] Campbell JH, Suratwala TI, Thorsness CB, Hayden JS, Thorne AJ, Cimino JM, et al. Continuous melting of phosphate laser glasses. J Non-Cryst Solids 2000;263&264:342–57.
[103] Weber MJ. Inorganic scintillators: today and tomorrow. J Lumin 2002;100:35–45.
[104] Mao R, Zhang L, Zhu RY. Optical and scintillation properties of inorganic scintillators in high energy physics. IEEE Trans Nucl Sci 2008;55:2425–31.
[105] van Eijk CWE. Inorganic scintillators in medical imaging. Phys Med Biol 2002;47:R85.
[106] Zuidema W, Kruit P. Transmission imaging on a scintillator in a scanning electron microscope. Ultramicroscopy 2020;218:113055.
[107] Oshima Y, Yasumune T, Masuda T, Maehata K, Ishibashi K, Umeno T. Temperature dependence of li-glass scintillator response to neutrons. Prog Nucl Energy 2011;1:296–9.
[108] Chewpraditkul W, Chen D, Yu B, Zhang Q, Shen Y, Nikl M, et al. Luminescence and scintillation of Eu^{2+}-doped high silica glass. Phys Status Solidi Rapid Res Lett 2011;5(1):40–2.
[109] Nikl M, Nitsch K, Mihokova E, Solovieva N, Mares JA, Fabeni P, et al. Efficient radioluminescence of the Ce^{3+}-doped Na–Gd phosphate glasses. Appl Phys Lett 2000;77:2159.
[110] Ghazy A, Safdar M, Lastusaari M, Savin H, Karppinen M. Advances in upconversion enhanced solar cell performance. Sol Energy Mater Sol Cells 2021;230:111234.
[111] Day J, Senthilarasu S, Mallick TK. Improving spectral modification for applications in solar cells: a review. Renew Energy 2019;132:186–205.
[112] Richards BS. Enhancing the performance of silicon solar cells via the application of passive luminescence conversion layers. Sol Energy Mater Sol Cells 2006;90:2329–37.
[113] Shalav A, Richards BS, Trupkel T, Corkish RP, Game KW, Gude HU, Green MA. The application of up-converting phosphors for increased solar cell conversion efficiencies. In: 3rd world conference on phorovoltoic energy conversion, May 11–18. 2003 Osaka. Japan.
[114] Lahoz F, Perez-Rodrıguez C, Hernandez SE, Martın IR, Lavın V, Rodrıguez-Mendoza UR. Upconversion mechanisms in rare-earth doped glasses to improve the efficiency of silicon solar cells. Sol Energy Mater Sol Cells 2011;95:1671–7.
[115] Dejneka MJ, Streltsov A, Pal S, Frutos AG, Powell CL, Yost K, et al. Rare earth-doped glass microbarcodes. PNAS 2003;100(2):389–93.
[116] Vahedigharehchopogh N, Kıbrıslı O, Erol E, Ersundu MC, Ersundu AE. A straightforward approach for high-end anti-counterfeiting applications based on NIR laser-driven lanthanide doped luminescent glasses. J Mater Chem C 2021;9:2037.
[117] Hu Z, Huang X, Yang Z, Qiu J, Song Z, Zhang J, et al. Reversible 3D optical data storage and information encryption in photo-modulated transparent glass medium. Light Sci Appl 2021;10:140.
[118] Downing E, Hesselink L, Ralston J, Macfarlane R. A three-color, solid-state, three-dimensional display. Nature 1996;273:1185–9.
[119] Kokou L, Du J. Rare earth ion clustering behavior in europium doped silicate glasses: simulation size and glass structure effect. J Non-Cryst Solids 2012;358:3408–17.
[120] Likhachev ME, Bubnov MM, Zotov KV, Medvedkov OI, Lipatov DS, Yashkov MV, et al. Erbium-doped aluminophosphosilicate optical fibres. Quant Electron 2010;40:633–8.
[121] Saitoh A, Matsuishi S, Se-Weon C, Nishii J, Oto M, Hirano M, et al. Elucidation of codoping effects on the solubility enhancement of Er^{3+} in SiO_2 glass: Striking difference between Al and P codoping. J Phys Chem B 2006;110(15):7617–20.
[122] Glorieux B, Salminen T, Massera J, Lastusaari M, Petit L. Better understanding of the role of SiO_2, P_2O_5 and Al_2O_3 on the spectroscopic properties of Yb^{3+} doped silica sol-gel glasses. J Non-Cryst Solids 2018;482:46–51.
[123] Izumitani TS. Optical glass. New York: American Institute of Physics; 1986. p. 162–72.
[124] Xin W, Fan S, Li K, Lei Z, Wang S, Hu L. Compositional dependence of the 1.8 μm emission properties of Tm^{3+} ions in silicate glass. J Appl Phys 2012;112:103521.
[125] Sun Y, Wang X, Liao M, Hu L, Wang T. Compositional dependence of Stark splitting and spectroscopic properties in Yb^{3+}-doped lead silicate glasses. J Non Cryst Solids 2020;532:119890.
[126] Shen X, Chen S, Sun Y, Wang X, Wei W, Hu L. Investigation of Er^{3+}-doped phosphate glass for L^{+} band optical amplification. IEEE Photon J 2021;13:2200506.
[127] Rao PR, G. Krishna M, Brik MG, Gandhi Y, Veeraiah N. Fluorescence features of Sm^{3+} ions in Na_2SO_4–MO–P_2O_5 glass system—Influence of modifier oxide, J Lumin 2011; 131: 212–217.
[128] Liu X, Huang F, Gao S, Wang X, Hu L, Chen D. Compositional investigation of 2 μm luminescence of Ho^{3+}-doped lead silicate glass. Mater Res Bull 2015;71:11–5.
[129] Capobianco IA, Prevost G, Proulx PP, Kabro P, Bettinelli M. Upconversion properties of Er^{3+} doped lead silicate glasses. Opt Mater 1996;6:175–84.
[130] Rajagukguk J. Fitrilawati, Sinaga B, Kaewkhao J, Structural and spectroscopic properties of Er^{3+} doped sodium lithium borate glasses. Spectrochim Acta A Mol Biomol Spectrosc 2019;223:117342.
[131] Wang JS, Vogel EM, Snitzer E. Tellurite glass: a new candidate for fiber devices. Opt Mater 1994;3:187–203.
[132] Ma Y, Guo Y, Huang F, Hu L, Zhang J. Spectroscopic properties in Er^{3+} doped zinc- and tungsten-modified tellurite glasses for 2.7μm laser materials. J Lumin 2014;147:372–7.
[133] Wei T, Tian Y, Chen F, Cai M, Zhang J, Jing X, et al. Mid-infrared fluorescence, energy transfer process and rate equation analysis in Er^{3+} doped germanate glass. Sci Rep 2014;4:6060.
[134] Zhu X, Jain R. Compact 2 W wavelength-tunable Er:ZBLAN mid-infrared fiber laser. Opt Lett 2007;32:2381–3.
[135] Huang F, Guo Y, Ma Y, Zhang L, Zhang J. Highly Er^{3+}-doped ZrF_4-based fluoride glasses for 2.7 μm laser materials. Appl Opt 2013;52(7):1399.
[136] Lin L, Ren G, Chen M, Liu Y. The behavior of Er^{3+} dopants during crystallization in oxyfluoride silicate glass ceramics. J Alloys Comp 2009;486:261.
[137] Nommeots-Nomm A, Boetti NG, Salminen T, Massera J, Hokka M, Petit L. Luminescence of Er^{3+} doped oxyfluoride phosphate glasses and glass-ceramics. J Alloys Compd 2018;751:224–30.
[138] Meejitpaisan P, Insiripong A, Kedkaew C, Kim HJ, Kaewkhao J. Radioluminescence and optical studies of gadolinium calcium phosphate oxyfluoride glasses doped with Sm^{3+}. Radiat Phys Chem 2017;137:62–7.
[139] Wan R, Wang P, Li S, Ma Y, Zhang G. Spectroscopic properties of ErF_3 doped tellurite–gallium oxyfluoride glass for ~3 μm laser materials. J Appl Phys 2021;129:153105.

[140] Pisarska J, Sołtys M, Górny A, Kochanowicz M, Zmojda J, Dorosz J, et al. Rare earth-doped barium gallo-germanate glasses and their near-infrared luminescence properties. Spectrochim Acta A Mol Biomol Spectrosc 2018;201:362–6.
[141] Nazabal V, Todokori S, Nukui A, Matsumoto T, Suehara S, Hondo T, et al. Oxyfluoride tellurite glasses doped by erbium: thermal analysis, structural organization and spectral properties. J Non-Cryst Solids 2003;325:85–102.
[142] Yan Y, Faber AJ, de Waal H. Luminescence quenching by OH groups in highly Er-doped phosphate glasses. J Non-Cryst Solids 1995;181:283–90.
[143] Heo J. Optical characteristics of rare-earth-doped sulphide glasses. J Mater Sci Lett 1995;14(14):1014–6.
[144] Iovu MS, Shutov SD, Andriesh AM, Kamitsos EI, Varsamis CPE, Furniss D, et al. Spectroscopic studies of bulk As_2S_3 glasses and amorphous films doped with Dy, Sm and Mn. J Optoelectron Adv Mater 2001;3(2):443–54.
[145] Ivanova ZG, Koughia K, Aneva Z, Tonchev D, Vassilev VS, Kasap SO. Photoluminescence of Er^{3+} ions in $(GeS_2)_{80}(Ga_2S_3)_{20}$ glasses. J Optoelectron Adv Mater 2005;7:349–52.
[146] Wei K, Machewirth DP, Wenzel J, Snitzer E, Sigel GH. Spectroscopy of Dy^{3+} in Ge–Ga–S glass and its suitability for 1.3 μm fiber-optical amplifier applications. Opt Lett 1994;19:904–6.
[147] Jiao Q. Li Ge, Li L, Lin C, Wang G, Liu Z, Dai S, Xu T, Zhang Q, Effect of gallium environment on infrared emission in Er^{3+}-doped gallium– antimony– sulfur glasses. Sci Rep 2017;7:41168.
[148] Chahal R, Starecki F, Doualan JL, Němec P, Trapananti A, Prestipino C, et al. Nd^{3+}:Ga-Ge-Sb-S glasses and fibers for luminescence in mid-IR: synthesis, structural characterization and rare earth spectroscopy. Opt Mater Express 2018;8(6):1650.
[149] Cui J, Xiao X, Xu Y, Cui X, Chen M, Guo J, et al. Mid-infrared emissions of Dy^{3+} doped Ga-As-S chalcogenide glasses and fibers and their potential for a 4.2 μm fiber laser. Opt Mater Express 2018;8(8):2089.
[150] Jihong Z, Haizheng T, Xiujian Z. Upconversion luminescence properties of Er^{3+} doped GeS_2-Ga_2S_3-KCl chalcohalide glasses. Rare Met 2011;30(1):18.
[151] Wang Z, Guo H, Xiao X, Xu Y, Cui X, Lu M, et al. Synthesis and spectroscopy of high concentration dysprosium doped GeS_2-Ga_2S_3-CdI_2 chalcohalide glasses and fiber fabrication. J Alloys Compd 2017;692:1010–7.
[152] Wang Y, Ohwaki J. New transparent vitroceramics codoped with Er^{3+} and Yb^{3+} for efficient frequency upconversion. Appl Phys Lett 1993;63:3268.
[153] Méndez-Ramos J, Velázquez JJ, Yanes AC, Del-Castillo J, Rodriguez VD. Up-conversion in nanostructured Yb^{3+}-Tm^{3+} co-doped sol-gel derived SiO_2-LaF_3 transparent glass-ceramics. Phys Status Solidi Appl Mater Sci 2008;205(2):330–4.
[154] Zhou B, Wei T, Cai M, Tian Y, Zhou J, Deng D, et al. Analysis on energy transfer process of Ho^{3+} doped fluoroaluminate glass sensitized by Yb^{3+} for mid-infrared 2.85 μm emission. J Quant Spectrosc Radiat Transf 2014;149:41–50.
[155] Zhao G, Jin W, Fang Y, He Y, Li Y, Liu Y, et al. Comparative study of 2.7 μm emission of Ho^{3+} desensitized Er^{3+} in tellurite and bismuth glass. Opt Mater Express 2017;7(4):1147.
[156] Wang R, Zhao H, Zhang M, Zhang J, Jia S, Zhang J, et al. Enhancement mechanisms of Tm^{3+}-codoping on 2 μm emission in Ho^{3+} doped fluoroindate glasses under 888 nm laser excitation. Ceram Int 2020;46:6973–7.
[157] Wang R, Zhang J, Zhao H, Wang X, Jia S, Guo H, et al. 3.9 μm emission and energy transfer in ultra-low OH^-, Ho^{3+}/Nd^{3+} co-doped fluoroindate glasses. J Lumin 2020;225:117363.
[158] Park BJ, Seo HS, Ahn JT, Choi YG, Heo J, Chung WJ. Dy^{3+} doped Ge-Ga-Sb-Se glasses and optical fibers for the mid-IR gain media. J Ceram Soc JAPAN 2008;116(1358):1087–91.
[159] Hou GN, Zhang CM, Fu WB, Li GS, Xia JN, Yu XR, et al. Improvement of ultra-broadband near-infrared emission at around 1.0 μm in Nd^{3+}-Er^{3+}-Pr^{3+} tri- doped tellurite glasses. J Non-Cryst Solids 2021;553:120511.
[160] Lodi TA, Sandrini M, Medina AN, Barboza MJ, Pedrochi F, Steimacher A. Dy: Eu doped CaBAl glasses for white light applications. Opt Mater 2018;76:231–6.
[161] Ming C, Song F, Ren X, An L, Qin Y. $Tm^{3+}/Er^{3+}/Yb^{3+}$ tri-doped TeO_2–PbF_2–AlF_3 glass for white-light-emitting diode. Opt Commun 2013;304:80–2.
[162] Pillonnet A, Berthelot A, Pereira A, Benamara O, Derom S, Colas des Francs G, et al. Coupling distance between Eu^{3+} emitters and Ag nanoparticles. Appl Phys Lett 2012;100(15):153115.
[163] Malta OL, Santa-Cruz PA, De Sa GF, Auzel F. Fluorescence enhancement induced by the presence of small silver particles in Eu^{3+} doped materials. J Lumin 1985;33:261–72.
[164] Kassab LRP, da Silva DG, de Almeida R, de Araújo CB. Photoluminescence enhancement by gold nanoparticles in Eu^{3+} doped GeO_2–Bi_2O_3 glasses. Appl Phys Lett 2009;94:101912.
[165] de Almeida R, da Silva DM, Kassab LRP, de Araujo CB. Eu^{3+} luminescence in tellurite glasses with gold nanostructures. Opt Commun 2008;281:108–12.
[166] Dousti MR, Amjad RJ. Luminescence enhancement in Eu(III)-doped tellurite glass embedded silver nanoparticles. J Nanostruct 2013;3:435–41.
[167] Mechergui I, Fares H, Mohamed SA, Nalin M, Elhouichet H. Coupling between surface plasmon resonance and Sm^{3+} ions induced enhancement of luminescence properties in fluoro-tellurite glasses. J Lumin 2017;190:518–24.
[168] Soltani I, Hraiech S, Horchani-Naifer K, Elhouichet H, Férid M. Effect of silver nanoparticles on spectroscopic properties of Er^{3+} doped phosphate glass. Opt Mater 2015;46:454–60.
[169] Awang A, Ghoshal SK, Sahar MR, Dousti MR, Amjad RJ, Nawaz F. Enhanced spectroscopic properties and Judd-Ofelt parameters of Er-doped tellurite glass: effect of gold nanoparticles. Curr Appl Phys 2013;13:1813–8.
[170] Pan Z, Ueda A, Aga Jr R, Burger A, Mu R, Morgan SH. Spectroscopic studies of Er^{3+} doped Ge-Ga-S glass containing silver nanoparticles. J Non-Cryst Solids 2010;356:1097–101.
[171] Jia X, Xia M, Xu Y, Yang L, Zhang Y, Li M, et al. Silver nanoparticle enhanced 2.7 μm luminescence in Er^{3+}-doped bismuth germanate glasses. Opt Mater Express 2018;8(6):1625.
[172] Cheng P, Zhou Y, Zhou M, Su X, Zhou Z, Yang G. Enhanced broadband near-infrared luminescence from Pr^{3+}-doped tellurite glass with silver nanoparticles. Opti Mater 2017;73:102–10.
[173] Rai VK, de Araújo CB, Ledemi Y, Bureau B, Poulain M, Zhang XH, et al. Frequency upconversion in a Pr^{3+} doped chalcogenide glass containing silver nanoparticles. J Appl Phys 2008;103:103526.
[174] Xu W, Chen D, Yan Q, Ren J, Chen G. Silver metal enhanced photoluminescence of Tm^{3+} doped GeS_2–Ga_2S_3–CsCl glasses. J Non-Cryst Solids 2012;358:3065–8.
[175] Qi Y, Zhou Y, Wu L, Yang F, Peng S, Zheng S, et al. Silver nanoparticles enhanced 1.53mm band fluorescence of Er^{3+}/Yb^{3+} codoped tellurite glasses. J Lumin 2014;153:401–7.
[176] Jimenez JA. Influence of Ag Nanoparticles on the Luminescence dynamics of Dy^{3+} ions in glass: the "plasmonic Diluent" effect. Phys Chem Chem Phys 2013;15:17587–94.
[177] Wei RF, Li JJ, Gao JY, Guo H. Enhancement of Eu^{3+} Luminescence by Ag Species (Ag NPs, ML-Ag, Ag^+) in Oxyfluoride Glasses. J Am Ceram Soc 2012;95(11):3380–2.
[178] Jimenez JA, Sendova M. In situ isothermal monitoring of the enhancement and quenching of Sm^{3+} photoluminescence in Ag Co-Doped glass. Solid State Commun 2012;152:1786–90.
[179] Xia Z, Huang H, Chen Z, Fang Z, Qiu J. Enhanced up-conversion luminescence in transparent glass-ceramic containing KEr_3F_{10}:Er^{3+} nanocrystals and its application in temperature detection. RSC Adv 2019;9:10999.
[180] Jewell JM, Friedele EJ, Aggarwal ID. Transparent heavy metal fluoride glass-ceramic. J Non-Cryst Solids 1995;188:285.
[181] Satyanarayana T, Brik MG, Venkatramaiah N, Kityk IV, Plucinski KJ, Ravikumar V, et al. Influence of crystallization on the luminescence characteristics of Pr^{3+} ions in PbO–Sb_2O_3–B_2O_3 glass system. J Am Ceram Soc 2010;93(7):2004–11.
[182] Pisarska J, Czopek I, Lisiecki R, Ryba-Romanowski W, Goryczka T, Pisarski WA. $PbWO_4$ formation during controlled crystallization of lead borate glasses. Ceram Int 2013;39:9151–6.
[183] Szczodra A, Mardoukhi A, Hokka M, Boetti NG, Petit L. Fluorine losses in Er^{3+} oxyfluoride phosphate glasses and glass-ceramics. J Alloys Compd 2019;797:797–803.
[184] Kang SL, Chen DD, Pan QW, Qiu JR, Dong GP. 2.7 μm emission in Er^{3+}-doped transparent tellurite glass ceramics. Opt Mater Express 2016;6(6):1861.

[185] Marcondes LM, Rodrigues L, da Cunha CR, Gonçalves RR, de Camargo ASS, Cassanjes FC, et al. Rare-earth ion doped niobium germanate glasses and glass-ceramics for optical device applications. J Lumin 2019;213:224–34.
[186] Yang Z, Wang R, Chen Y, Li Q, Shen X, Xu T. Enhancement of luminescence in Er^{3+} doped $Ge_{20}Ga_{10}S_{70}$ glass-ceramics. Opt Mater 2020;100:109677.
[187] Hubert M, Calvez L, Zhang X, Lucas P. Enhanced luminescence in Er^{3+}-doped chalcogenide glass-ceramics based on selenium. Opt Mater 2013;35(12):2527–30.
[188] Nakanishi T, Katayama Y, Ueda J, Honma T, Tanabe S, Komatsu T. Fabrication of Eu:$SrAl_2O_4$ -based glass ceramics using Frozen sorbet method. J Ceram Soc JAPAN 2011;119(7):609–15.
[189] Henderson MR, Gibson BC, Ebendorff-Heidepriem H, Kuan K, Afshar VS, Orwa JO, et al. Diamond in tellurite glass: a new medium for quantum information. Adv Mater 2011;23:2806–10.
[190] Ojha N, Nguyen H, Laihinen T, Salminen T, Lastusaari M, Petit L. Decomposition of persistent luminescent microparticles in corrosive phosphate glass melt. Corros Sci 2018;135:207–14.
[191] Ojha N, Laihinen T, Salminen T, Lastusaari M, Petit L. Influence of the phosphate glass melt on the corrosion of functional particles occurring during the preparation of glass-ceramics. Ceram Int 2018;44:11807–11.
[192] Nguyen H, Tuomisto M, Oksa J, Salminen T, Lastusaari M, Petit L. Upconversion in low rare-earth concentrated phosphate glasses using direct $NaYF_4$: Er^{3+}, Yb^{3+} particles doping. Scr Mater 2017;139:130–3.
[193] Evans JR, Michelessi M, Virgili G. Laser photocoagulation for proliferative diabetic retinopathy. Cochrane Database Syst Rev. 2014;2014:CD011234.
[194] Goldman L. Surgery by laser for malignant melanoma. J Dermatol Surg Oncol 1979;5:141–4.
[195] Amzayyb M, van den Bos RR, Kodach VM. Martiin de Bruin D, Niisten T, Martino Neumann HA, van Gemert MJC, Carbonized blood deposited on fibres during 810, 940 and 1,470 nm endovenous laser ablation: thickness and absorption by optical coherence tomography. Lasers Med Sci 2010;25:439–47.
[196] Gläser R, Navid F, Schuller W, Jantschitsch C, Harder J, Schröder JM, et al. UV-B radiation induces the expression of antimicrobial peptides in human keratinocytes in vitro and in vivo. J Allergy Clin Immunol 2009;123:1117–23.
[197] Woodgate P, Jardine LA. Neonatal jaundice: phototherapy. BMJ. Clin Evid 2015;2015:0319.
[198] Dai T, Gupta A, Huang YY, Yin R, Murray CK, Vrahas MS, et al. Blue light rescues mice from potentially fatal Pseudomonas aeruginosa burn infection: efficacy, safety, and mechanism of action. Antimicrob Agents Chemother 2013;57:1238–45.
[199] Milanese D, Gallichi-Nottiani D, Pugliese D, Boetti NG, Janner D. Multifunctional bioresorbable phosphate glass optical fibers for theranostics. In: Caspani L, Tauke-Pedretti A, Leo F, Yang B, editors. OSA advanced photonics congress (AP) (IPR, NP, NOMA, Networks, PVLED, PSC, SPPCom, SOF), OSA Technical Digest (Optica Publishing Group, 2020), paper SoM4H.1; 2020.
[200] Lemiere A, Szczodra A, Vuori S, Bondizor B, Hawkins TW, Ballato J, et al. Bioactive phosphate glass-based fiber with green persistent luminescence. Mater Res Bull 2022;153:111899.
[201] Roldan Del Cerro P, Teittinen H, Norrbo I, Lastusaari M, Massera J, Petit L. Novel borosilicate bioactive scaffolds with persistent luminescence. Biomed Glasses 2020;6:1–9.
[202] Rong F, Tang Y, Wang T, Feng T, Song J, Li P, et al. Nitric oxide-releasing polymeric materials for antimicrobial applications: a review. Antioxidants 2019;8:556.
[203] Xu J, Boyd RW, Fischer GL. Nonlinear optical materials. Ref Modul Mater Sci Mater Eng 2016:1–10.
[204] Yamane M, Asahara Y. Nonlinear optical glass. Cambridge: Cambridge University Press; 2009.
[205] Dussauze M, Cardinal T. Nonlinear optical properties of glass, In book: Springer handbook of glass; 2019. p. 157–89.
[206] Nalwa HS. Organometallic materials for nonlinear optics. Appl Organomet Chem 1991;5:349–77.
[207] Tanaka K. Optical nonlinearity in photonic glasses. J Mater Sci: Mater Electron 2005;16:633–43.
[208] Coso RD, Solis J. Relation between nonlinear refractive index and third-order susceptibility in absorbing media. J Opt Soc Am B 2004;21:640–4.
[209] Ogusu K, Yamasaki J, Maeda S, Kitao M, Minakata M. Linear and nonlinear optical properties of Ag–As–Se chalcogenide glasses for all-optical switching. Opt Lett 2004;29:265–7.
[210] Pelusi MD, Ta'eed VG, Fu L, Magi E, Lamont MRE, Madden S, Choi DY, Bulla DAP, Luther-Davies B, Eggleton BJ. Application of highly-nonlinear chalcogenide glass devices tailored for high-speed all-optical signal processing. IEEE J Sel Top Quantum Electron 2008;14:529–39.
[211] Tanaka K. Nonlinear optics in glasses: how can we analyze? J Phys Chem Solids 2007;68:896–900.
[212] Zhu SN, Zhu YY, Ming NB. Quasi-phase-matched third-harmonic generation in a quasi-periodic optical superlattice. Science 1997;278:843–6.
[213] Fejer MM, Magel GA, Jundt DH, Byer RL. Quasi-phase-matched second harmonic generation: tuning and tolerances. IEEE J Quantum Electron 1992;28:2631–54.
[214] Monro TM, Ebendorff-Heidepriem H. Progress in microstructured optical fibers. Annu Rev Mater Res 2006;36:467–95.
[215] Nasu H, Uchigaki T, Kamiya K. Nonresonant-type third-order nonlinearity of (PbO, Nb_2O_5)-TiO_2-TeO_2 glass measured by third-harmonic generation. Jpn J Appl Phys 1992;31:3899–900.
[216] Balakirev MK, Kityk IV, Smirnov VA, Vostrikova LI, Ebothe J. Anisotropy of the optical poling of glass. Phys Rev A 2003;67:023806.
[217] Osterberg U, Margulis W. Dye laser pumped by Nd:YAG laser pulses frequency doubled in a glass optical fiber. Opt Lett 1986;11:516–8.
[218] Soulis M, Duclère JR, Hayakawa T, Couderc V, Dutreilh-Colas M, Thomas P. Second harmonic generation induced by optical poling in new TeO_2–Tl_2O–ZnO glasses. Mater Res Bull 2010;45:551–7.
[219] Jonard M, Colas M, Leventoux Y, Mansuryan T, Cornette J, Tonello A, et al. Towards a new understanding of optical poling efficiency in multimode fibers. Proc SPIE 2022;12143:21.
[220] Thamboon P, Krol DM. Second-order optical nonlinearities in thermally poled phosphate glasses. J Appl Phys 2003;93:32–7.
[221] Kazansky PG, Russel PSJ. Thermally poled glass: frozen-in electric field or oriented dipoles? Opt Commun 1994;110:611–4.
[222] Poirier G, Dussauze M, Rodriguez V, Adamietz F, Karam L, Cardinal T, et al. Second harmonic generation in sodium tantalum germanate glasses by thermal poling. J Phys Chem C 2019;123:26528–35.
[223] Karam L, Adamietz F, Rodriguez V, Bondu F, Lepicard A, Cardinal T, et al. The effect of the sodium content on the structure and the optical properties of thermally poled sodium and niobium borophosphate glasses. J Appl Phys 2020;128:043106.
[224] Quiquempois Y, Godbout N, Lacroix S. Model of charge migration during thermal poling in silica glasses: Evidence of a voltage threshold for the onset of a second-order nonlinearity. Phys Rev A 2002;65:043816.
[225] Guignard M, Nazabal V, Smektala F, Zeghlache H, Kudlinski A, Quiquempois Y, et al. High second-order nonlinear susceptibility induced in chalcogenide glasses by thermal poling. Opt Exp 2006;14:1524–32.
[226] Hart RT, Ok KM, Halasyamani PS, Zwanziger JW. Powder second-harmonic generation study of $(K_2O)_{15}(Nb_2O_5)_{15}(TeO_2)_{70}$ glass ceramic. Appl Phys Lett 2004;85:938–9.
[227] Iafuchi A, Fujiwara T, Benino Y, Komatsu T. Optical characteristics of nanocrystallized glass fiber with second-order optical nonlinearity. J Ceram Soc Jpn 2009;117:143–6.
[228] Kobyakov A, Sauer M, Chowdhury D. Stimulated Brillouin scattering in optical fibers. Adv Opt Photonics 2010;75:1–59.
[229] Garmire E. Stimulated Brillouin review: Invented 50 years ago and applied today. Int J Opt 2018;2018:1–17.
[230] Gökhan FS, Götas H, Sörger VJ. Analytical approach of Brillouin amplification over threshold. Appl Opt 2018;57:607–11.
[231] Singh SP, Gangwar R, Singh N. Nonlinear scattering effects in optical fibers. Prog Electromagn Res 2007;74:379–405.
[232] Deroh M, Beugnot JC, Hammani K, Finot C, Fatome J, Smektala F, et al. Comparative analysis of stimulated Brillouin scattering at 2 μm in various infrared glass-based optical fibers. J Opt Soc Am B 2020;37:3792–800.
[233] Abedin KS. Stimulated Brillouin scattering in single-mode tellurite glass fiber. Opt Exp 2006;14:11766–72.
[234] Bai Z, Yuan H, Liu Z, Xu P, Gao Q, Williams RJ, et al. Stimulated Brillouin scattering materials, experimental design and applications: a review. Opt Mater 2018;75:626–45.

[235] Hwa LG, Schroeder J, Zhao XS. Intrinsic Brillouin linewidths and stimulated Brillouin gain coefficients in glasses studied by inelastic light scattering. J Opt Soc Am B 1989;6:833–9.
[236] Prince RC, Frontiera RR, Potma EO. Stimulated Raman scattering: from bulk to nano. Chem Rev 2017;117:5070–94.
[237] Sirleto L, Ferrara MA. Fiber amplifiers and fiber lasers based on stimulated Raman scattering: a review. Micromachines 2020;11:247–67.
[238] Stegeman R, Jankovic L, Kim H, Rivero C, Stegman G, Richardson K, et al. Tellurite glasses with peak absolute Raman gain coefficients up to 30 times that of fused silica. Opt Lett 2003;28:1126–8.
[239] Stegeman R, Rivero C, Stegman G, Richardson K, Delfyett P. Raman gain measurements in bulk glass samples. J Opt Soc Am B 2005;22:1861–7.
[240] Jackson J, Smith C, Massera J, Baleine CR, Bungay C, Petit L. Estimation of peak Raman gain coefficients for barium-bismuth-tellurite glasses from spontaneous Raman cross-section experiments. Opt Exp 2009;17:9071–9.
[241] Yuan J, Yang Q, Chen DD, Qian Q, Shen SX, Zhang QY, et al. Compositional effect of WO_3, MoO_3, and P_2O_5 on Raman spectroscopy of tellurite glass for broadband and high gain Raman amplifier. J Appl Phys 2012;111:103511–6.
[242] Pernice P, Sirleto L, Vergara A, Aronne A, Gagliardi M, Fanelli E, et al. Large Raman gain in a stable nanocomposite based on niobiosilicate glass. J Phys Chem C 2011;35:17314–9.
[243] Zhang Y, Xu Y, You C, Xu D, Tang J, Zhang P, et al. Raman gain and femtosecond laser induced damage of Ge-As-S chalcogenide glasses. Opt Exp 2017;25:8886–95.
[244] Kohoutek T, Yan X, Shiosaka TW, Yannopoulos SN, Chirssanthopoulos A, Suzuki T, et al. Enhanced Raman gain of Ge-Ga-Sb-S chalcogenide glass for highly nonlinear microstructured optical fibers. J Opt Soc Am B 2011;28:2284–90.
[245] Shiryaev VS, Sukhanov MV, Velmuzhov AP, Karaksina EV, Kotereva TV, Snopatin QE, et al. Preparation of high purity Sm^{3+}-doped Ga-Ge-As-Se glass and low-loss fiber. J Lumin 2022;242:118552–60.
[246] Li Q, Yuan X, Jiang X, Wang J, Liu Y, Zhang L. Femtosecond-scale all-optical switching in oxyfluorogallate glass induced by nonlinear multiphoton absorption. RSC Adv 2021;11:32446–53.
[247] Chai Z, Hu X, Wang F, Niu X, Xie J, Gong Q. Ultrafast all-optical switching. Adv Opt Mater 2017;5:1600665.
[248] Nasu H, Matsuika J, Kamiya K. Second- and third- order optical non-linearity of homogeneous glasses. J Non-Cryst Solids 1994;178:23–30.
[249] Harbold JM, Ilday FÖ, Wise FW, Sanghera JS, Nguyen VQ, Shaw LB, et al. Highly nonlinear As–S–Se glasses for all-optical switching. Opt Lett 2002;27:119.
[250] Li Z, Wang K, Zhang J, Chen F, Lin C, Dai S, et al. Study on correlation between network structure and third-order optical nonlinearity of chalcogenide glasses within a Ge-Sb-S ternary system. J Non-Cryst Solids 2022;588:121628.
[251] Wang T, Gai X, Wei W, Wang R, Yang Z, Shen X, et al. Systematic Z-scan measurements of the third order nonlinearity of chalcogenide glasses. Opt Mater Express 2014;4:1011–22.
[252] Prasad A, Saxena AK. Non-linear optical analysis of $(Ge_{0.17}Se_{0.83})_{100-x}$ In_x chalcogenide glassy systems, IOSR. J Appl Phys 2019;11:29.
[253] Harbold JM, Ilday FÖ, Wise FW, Aitken BG. Highly nonlinear Ge-As-Se and Ge-As-S-Se glasses for all-optical switching. IEEE Photon Technol Lett 2002;14:822.
[254] Milam D. Review and assessment of measured values of the nonlinear refractive-index coefficient of fused silica. Appl Opt 1998;37:546–50.
[255] Li Q, Wang R, Xu F, Wang X, Yang Z, Gai X. Third-order nonlinear optical properties of Ge-As-Te chalcogenide glasses in mid-infrared. Opt Mater Express 2020;10:1413.
[256] Yang Z, Hu H, Li Q, Zhang Z, Niu L, Wu J, et al. Third-order optical nonlinearity in Ge-Se-Te chalcogenide glasses. Opt Mat 2021;117:111208.
[257] Yang Y, Ba O, Dai S, Chen F, Boudebs G. Large third-order optical nonlinearity of non-stoichiometric chalcogenide glasses within Ge-In-S ternary system. J Non-Cryst Solids 2021;554:120581.
[258] Lu X, Li J, Yang, Zhang R, Zhang Y, Ren J, et al. Third-order optical nonlinearity properties of $CdCl_2$-modifed Ge–Sb–S chalcogenide glasses. J Non-Cryst Solids 2020;528:119757.
[259] Ren J, Li B, Wagner T, Zeng H, Chen G. Third-order optical nonlinearities of silver doped and/or silver-halide modified Ge–Ga–S glasses. Opt Mat 2014;36:911.
[260] Xu T, Chen F, Dai S, Shen X, Wang X, Nie Q, et al. Glass formation and third -order optical nonlinear properties within TeO_2-Bi_2O_3-BaO Pseudo-ternary system. J Non-Cryst Solids 2011;357:2219–22.
[261] Chen F, Song B, Lin C, Dai S, Cheng J, Heo J. Glass formation and third-order optical nonlinear characteristics of bismuthate glasses within Bi_2O_3- GeO_2- TiO_2 pseudo-ternary system. Mater Chem Phys 2012;135:73.
[262] Hasegawa T, Nagashima T, Sugimoto N. Z-scan study of third-order optical nonlinearities in bismuth-based glasses. Opt Commun 2005;250:411–5.
[263] Tintu R, Nampoori VPN, Radhakrishnan P. Nonlinear optical studies on nanocolloidal Ga–Sb–Ge–Se chalcogenide glass. Appl Phys Lett 2010;108:073525.
[264] Krogstad MR, Ahn S, Park W, Gopinath JT. Nonlinear characterization of $Ge_{28}Sb_{12}Se_{60}$ bulk and waveguide devices. Opt Exp 2015;23:7870–8.
[265] Choi YG. Enhancing fluorescence emission properties of Dy^{3+} doped in chalcogenide glass via very small compositional modifications. J Lumin 2009;129:620–3.
[266] Campbell JH, Hayden JS, Marker A. High-power solid-state lasers: a laser glass perspective. Int J Appl Glass Sci 2011;2(1):3–29.
[267] Dragic PD, Cavillon M, Ballato J. Materials for optical fiber lasers: a review. Appl Phys Rev 2018;5(4):041301.
[268] Cavillon M, Kucera C, Hawkins T, Dawson J, Dragic PD, Ballato J. A unified materials approach to mitigating optical nonlinearities in optical fiber. III. Canonical examples and materials road map. Int J Appl Glass Sci 2018;9(4):447–70.
[269] Yamane M, Asahara Y. Glasses for photonics. Cambridge: Cambridge University Press; 2000.
[270] Reisfeld R. Nanosized semiconductor particles in glasses prepared by the sol-gel method: their optical properties and potential uses. J Alloys Compd 2002;341:56–61.
[271] Babu KS, Vijayan C, Devanathan R. Strong quantum confinement effects in polymer-based PbS nanostructures prepared by ion-exchange method. Mater Lett 2004;58:1223–6.
[272] Buso D, Falcaro P, Costacurta S, Guglielmi M, Martucci A, Innocenzi P, et al. PbS-doped mesostructured silica films with high optical nonlinearity. Chem Mater 2005;17:4965–70.
[273] Du X, Zhang L, Dong G, Sharafudeen K, Wen J, Chen D, et al. Coloration and nonlinear optical properties of ZnTe quantum dots in ZnO-TeO_2-P_2O_5 glasses. J Am Ceram Soc 2013;97:185–8.
[274] Xu Z, Chen T, Zhang D, Zheng G, Wu J, Yan J, et al. Linear and nonlinear optical characteristics of $CsPbBr_3$ perovskite quantum dots-doped borosilicate glasses. J Eur Ceram Soc 2021;41:729–34.
[275] Kim K, Husakou A, Herrmann J. Linear and nonlinear optical characteristics of composites containing metal nanoparticles with different sizes and shapes. Opt Exp 2010;18:7488–96.
[276] David FE. Nonlinear optical materials. Science 1991;253:281–7.
[277] Sheik-Bahae M, Said AA, Wei TH, Hagan DJ, Van Stryland EW. Sensitive measurement of optical nonlinearities using a single beam. IEEE J Quant Electron 1990;26:760–9.
[278] Uchida K, Kaneko S, Omi S, Hata C, Tanji H, Asahara Y, et al. Optical nonlinearities of a high concentration of small metal particles dispersed in glass: copper and silver particles. J Opt Soc Am B 1994;11:1236–43.
[279] Chen Q, Li Z, Miao B. Giant Faraday rotation, magnetic and nonlinearity of diamagnetic glass tailored by plasmonic-magnetic bimetallic Au-Ni NPs. J Alloys Compd 2022;900:163536.
[280] D'Acapito F, Battaglin G, Cattaruzza E, Gonella F, Maurizio C, Mazzoldi P, et al. Cu-Ni alloy nanocluster formation by ion implantation in silicate glasses: structure and optical properties. Eur Phys J D 2000;10:123–9.
[281] Zhang Y, Jin Y, He M, Zhou L, Xu T, Yuan R, et al. Optical properties of bimetallic Au-Cu nanocrystals embedded in glass. Mater Res Bull 2018;98:94–102.
[282] Yamada T, Takano A, Sugita K, Iwase A, Maekawa M, Kawasuso A, et al. Effect of dual implantation with Ag and Ni ions on the optical absorption of silica glass. Trans Mater Res Soc Jpn 2020;45:127–30.
[283] Gabbani A, Petrucci G, Pineidera F. Magneto-optical methods for magnetoplasmonics in noble metal nanostructures. J Appl Phys 2021;129:211101.

[284] Lin G, Luo F, Pan H, Smedskjaer MM, Teng Y, Chen D, et al. Universal preparation of novel metal and semiconductor nanoparticle–glass composites with excellent nonlinear optical properties. J Phys Chem C 2011;115:24598–604.
[285] Lu MC. Advancement of chip stacking architectures and interconnect technologies for image sensors. J Electron Packag 2022;144:020801.
[286] Liu Y, Xing Y, Yang C, Li C, Xue C. Simulation of heat transfer in the progress of precision glass molding with a finite element method for chalcogenide glass. Appl Opt 2019;58:7311–8.
[287] Zaki M, Venugopal V, Bhatto R, Bishnoi S, Singh SK, Allu AR, et al. Interpreting the optical properties of oxide glasses with machine learning and shapely additive explanations. J Am Ceram Soc 2021;105:4046–57.
[288] Cassar DR, Santos GG, Zanotto ED. Designing optical glasses by machine learning coupled with a genetic algorithm. Ceram Int 2021;47:10555–64.
[289] Lee JH, Kim H, Choi YG. Compositional screening of chalcogenide glass for use as molded lens: an exemplary case of ternary Ge-Sb-Se glass. J Asian Ceram Soc 2020;8:971–83.
[290] Singh PK, Dwivedi DK. Chalcogenide glass: fabrication techniques, properties and applications. Ferroelectrics 2017;520:256–73.
[291] Lee JH, Choi JH, Yi JH, Lee WH, Lee ES, Choi YG. Unravelling interrelations between chemical composition and refractive index dispersion of infrared-transmitting chalcogenide glasses. Sci Rep 2018;8:15482.
[292] Xu Y, Sun J, Frantz J, Shalaev MI, Walasik W, Pandey A, et al. Nonlinear metasurface for structured light with tunable orbital angular momentum. Appl Sci 2019;9:958.
[293] Gupta TD, Monier LM, Butet J, Yang KY, Leber A, Dong C, et al. Second harmonic generation in glass-based metasurfaces using tailored surface lattice resonances. Nanophotonics 2021;10:3465–75.
[294] Frantz JA, Bekele RY, Clabeau A, Myers JD, Nguyen V, Litchinitser N, et al. Thermally tuned resonances in chalcogenide glass dielectric metasurfaces. Proc SPIE 2020;11287:1128701.
[295] Gao J, Vincenti MA, Frantz J, Clabeau A, Qiao X, Feng L, et al. Near-infrared to ultra-violet frequency conversion in chalcogenide metasurfaces. Nat Commun 2021;12:5833.
[296] Stookey SD. Photosensitive Glass. Ind Eng Chem 1949;41:856–61.
[297] White JF, Silverman WB. Some studies on the solarization of glass. J Am Ceram Soc 1950;33:252.
[298] Ehrt D, Ebeling P. Radiation defects in borosilicate glasses. *Glass* Technol 2003;44(2):46.
[299] Kajihara K, Skuja L, Hosono H. Diffusion and reactions of photoinduced interstitial oxygen atoms in amorphous SiO_2 impregnated with 18O-labeled interstitial oxygen molecules. J Phys Chem C 2014;118:4282.
[300] Möncke D. Photo-ionization of 3d-ions in fluoride-phosphate glasses. Int J Appl Glass Sci 2015;6:249–67.
[301] Giehl JM, Pontuschka WM, Barbosa LC, Ludwig ZMCC. EPR of γ-induced paramagnetic centers in tellurite glasses. J Non Cryst Solids 2010;356:1762–7.
[302] Watterich A, Bartram RH, Gilliam OR, Kappers LA, Edwards GJ, Földvari I, et al. ESR identification of radiation-induced oxygen vacancy centers in paratellurite. Phys Rev B 1985;32:2533–7.
[303] Prohaska JD, Li J, Wang JS, Bartram RH. Electron spin resonance observations of excimer-laser-induced paramagnetic centers in tellurite glasses. Appl Phys Lett 1995;67:1841–3.
[304] Janer CL, Carballar A, Navarro L, Galo JL, Rubio RM. Photosensitivity color-center model for Ge-doped silica preforms. IEEE Photonics J 2013;5:6100511.
[305] Nishii J, Fukumi K, Yamanaka H, Kawamura KI, Hosono H. KawazoeH, Photochemical reactions in GeO_2-SiO_2 glasses induced by ultraviolet irradiation: comparison between Hg lamp and excimer laser. Phys Rev B 1995;52:1661–5.
[306] Chen X, Heng X, Tang G, Zhu T, Sun M, Shan X, et al. Gamma radiation induced darkening in barium gallo-germanate glass. Opt Exp 2016;24:9149.
[307] Padlyak BV, Jungner H, Fabisiak K, Dubelt SP. Radiation-induced defects in glasses and ceramics of the CaO-Ga_2O_3-GeO_2 system. Rev Adv Mater Sci 2006;12:97–105.
[308] Campbell JH, Rainer F. Optical glasses for high-peak-power laser applications. In: Proc SPIE 1761, damage to space optics, and properties and characteristics of optical glass; 1993.
[309] Girard S, Alessia A, Richard N, Martin-Samos L, De Michele V, Giacomazzi L, et al. Overview of radiation induced point defects in silica-based optical fibers. Rev Phys 2019;4:100032.
[310] Hongisto M, Veber A, Cardinal T, Danto S, Jubera V, Petit L. Review: radiation-induced defects/effects in germanate and tellurite glasses. Materials 2020;13:3846.
[311] Petit L. Radiation effects on phosphate glasses: a mini-review. Int J Appl Glass Sci 2020;11:511–21.
[312] Tanaka K. Photoinduced phenomena in glassy chalcogenides under hydrostatic pressure. J Non-Cryst Solids 1983;59&60:925.
[313] Street RA. Non-radiative recombination in chalcogenide glasses. Solid State Commun 1977;24:363–5.
[314] Petit L, Carlie N, Anderson T, Choi J, Richardson M, Richardson KC. Invited progress on the photoresponse of chalcogenide glasses and films to near-infrared femtosecond laser irradiation: a review. IEEE J Sel Top Quantum Electron 2008;14(5):1323–34.
[315] Zoubir A, Richardson M, Rivero C, Schulte A, Lopez C, Richardson K, et al. Direct femtosecond laser writing of waveguides in As_2S_3 thin films. Opt Lett 2004;29(7):748–50.
[316] Messaddeq SH, Li MS, Lezal D, Ribeiro SJL, Messaddeq Y. Above bandgap induced photoexpansion and photobleaching in Ga–Ge–S based glasses. J Non-Cryst Solids 2001;284:282–7.
[317] Morrell B, Okada G, Vahedi S, Koughia C, Edgar A, Varoy C, et al. Optically erasable samarium-doped fluorophosphate glasses for high-dose measurements in microbeam radiation therapy. J Appl Phys 2014;115(6):063107.
[318] Musgraves JD, Richardson K, Jain H. Laser-induced structural modification, its mechanisms, and applications in glassy optical materials. Opt Mater Express 2011;1(5):921–35.
[319] Ehrt D, Ebeling P, Natura U. UV transmission and radiation-induced defects in phosphate and fluoride-phosphate glasses. J Non-Cryst Solids 2000;263&264:240–50.
[320] Novak S, Singh V, Monmeyran C, Ingram A, Han Z, Borodinov N, et al. Positron annihilation lifetime spectroscopy (PALS) of gamma irradiated As_2Se_3 films used in MIR integrated photonics. J Non-Cryst Solids 2016;434:29–34.
[321] Millar CA, Mallinson SR, Ainslie BJ, Craig SP. Photochromic behavior of thulium-doped silica optical fibers. Electron Lett 1988;24:590–1.
[322] Paschotta R, Nilsson J, Barber PR, Caplen JE, Tropper AC, Hanna DC. Lifetime quenching in Yb-doped fibres. Opt Commun 1997;36:375–8.
[323] Jetschke S, Unger S, Roepke U, Kirchhof J. Photodarkening in Yb doped fibers: experimental evidence of equilibrium states depending on the pump power. Opt Exp 2007;15:14838–43.
[324] Mackey JH, Smith HL, Halperin A. Optical studies in x-irradiated high purity sodium silicate glasses. J Phys Chem Solids 1966;27(11):1759–72.
[325] Ponsoda JJMi, Söderlund MJ, Koplow JP, Koponen JJ, Honkanen S. Photodarkening-induced increase of fiber temperature. Appl Opt 2010;49:4139–43.
[326] Jetschke S, Schwuchow A, Unger S, Leich M, Jäger M, Kirchhof J. Deactivation of Yb^{3+} ions due to photodarkening. Opt Mater Exp 2013;3(4):452.
[327] Mattsson KE. Photo darkening of rare earth doped silica. Opt Exp 2011;19(21):19797–812.
[328] Sun Y, Ma J, Shao C, Wang X, Yu F, Liao M, et al. Photodarkening mechanisms of Pr^{3+} singly doped and Pr^{3+}/Ce^{3+} co-doped silicate glasses and fibers. J Am Ceram Soc 2022;105:3291–302.
[329] Sun T, Su X, Zhang Y, Zhang H, Zheng Y. Review progress and summary of photodarkening in rare earth doped fiber. Appl Sci 2021;11:10386.
[330] Stalmashonak A, Seifert G, Graener H. Spectral range extension of laser-induced dichroism in composite glass with silver nanoparticles. J Opt A: Pure Appl Opt 2009;11:065001.
[331] Dmitryuk A, Parmzina S, Perminov A, Solov'eva N, Timofeev N. The influence of glass composition on the properties of silver-doped radiophotoluminescent phosphate glasses. J Non-Cryst Solids 1996;202(1-2):173-177.
[332] Lumeau J, Zanotto ED. A review of the photo-thermal mechanism and crystallization of photo-thermo-refractive (PTR) glass. Int Mater Rev 2017;62(6):348–66.
[333] Armistead WH, Stookey SD. Photochromic silicate glasses sensitized by silver halides. Science 1964;144:150–4.

[334] Gan Z, Cao Y, Evans RA, Gu M. Three dimensional deep sub-diffraction optical beam lithography with 9 nm feature size. Nat Commun 2013;4:2061.
[335] Fares H, Santos SNC, Santos MC, Franco DF, Souza AE, Manzani D, et al. Highly luminescent silver nanocluster-doped fluorophosphate glasses for microfabrication of 3D waveguides. RSC Adv 2017;7:55935.
[336] Nasser K, Ivanov S, Kharisova R, Ignatiev A, Nikonorov N. A novel photo-thermo-refractive glass with chlorine instead of bromine for holographic application. Ceram Int 2022;48:26750–7.
[337] Shirshnev P, Kang M, Divliansky I, Richardson K, Glebov L. Engineered refractive and diffractive optical composites via photo-thermal processes. Opt Mater Express 2022;12(9):3429–48.
[338] Nazabal V, Adam JL. Infrared luminescence of chalcogenide glasses doped with rare earth ions and their potential applications. Opt Mater X 2022;15:100168.
[339] Zhang J, Čerkauskaitė A, Drevinskas R, Patel MA, Beresna M, Kazansky PG. Eternal 5D data storage by ultrafast laser writing in glass. Proc SPIE 2016;9736:9736oU-1.
[340] Poirier G, Nalin M, Cescato L, Messaddeq Y, Ribeiro S. Bulk photochromism in a tungstate-phosphate glass: a new optical memory material? J Chem Phys 2006;125:161101.
[341] Xiao D, Huang X, Cun Y, Hu Z, Xu Z, Bai X, et al. Large reversible upconversion luminescence modification and 3D optical information storage in femtosecond laser irradiation-subjected photochromic glass. Sci China Mater 2022;65(6):1586–93.
[342] Arai K, Namikawa H, Kumata K, Honda T, Ishii Y, Handa TJ. Aluminum or phosphorus co-doping effects on the fluorescence and structural properties of neodymium-doped silica glass. Appl Phys 1986;59:3430–6.
[343] Peretti R, Jurdyc AM, Jacquier B, Blanc W, Dussardier B. Spectroscopic signature of phosphate crystallization in erbium-doped optical fibre preforms. Opt Mater 2011;33:835–8.
[344] Deschamps T, Ollier N, Vezin H, Gonnet C. Clusters dissolution of Yb^{3+} in codoped SiO_2-Al_2O_3-P_2O_5 glass fiber and its relevance to photodarkening. J Chem Phys 2012;136:014503.
[345] Jetschke S, Unger S, Schwuchow A, Leich M, Kirchhof J. Efficient Yb laser fibers with low photodarkening by optimization of the core composition. Opt Exp 2008;16:15540.
[346] Jetschke S, Leich M, Unger S, Schwuchow A, Kirchhof J. Influence of Tm- or Er-codoping on the photodarkening kinetics in Yb fibers. Opt Exp 2011;19:14473–8.
[347] Engholm M, Jelger P, Laurell F, Norin L. Improved photodarkening resistivity in ytterbium-doped fiber lasers by cerium codoping. Opt Lett 2009;34:1285–7.
[348] Vitiello M, Lopez N, Illas F, Pacchioni G. H_2 cracking at SiO_2 defect centers. J Phys Chem A 2000;104:4674–84.
[349] Xing YB, Liu YZ, Zhao N, Cao RT, Wang YB, Yang Y, et al. Radical passive bleaching of Tm-doped silica fiber with deuterium. Opt Lett 2018;43:1075–8.
[350] Heng X, Qian Q, Chen X, Liu L, Zhao X, Chen D, et al. Reduced radiation damage in a multicomponent phosphate glass by Nb^{5+} or Sb^{3+} doping. Opt Mater Exp 2015;5:2272–80.
[351] Fayad AM, Ouis MA, ElBatal FH, ElBatal HA. Shielding behavior of gamma-irradiated MoO_3 or WO_3-doped lead phosphate glasses assessed by optical and FT infrared absorption spectral measurements. Silicon 2018;10:1873–79.
[352] Masuda A, Yonezawa Y, Morimoto A, Kumeda M, Shimizu T. Influence of Pb incorporation on light-induced phenomena in amorphous $Ge_{100-x-y}Pb_xS_y$ thin films. J Non-Cryst Solids 1997;217:121.
[353] Yang G, Jain H, Ganjoo A, Zhao D, Xu Y, Zeng H, et al. A photo-stable chalcogenide glass. Opt Exp 2008;16(14):10565–71.
[354] Su X, Wang R, Luther-Davies B, Wang L. The dependence of photosensitivity on composition for thin films of $Ge_xAs_ySe_{1-x-y}$ chalcogenide glasses. Appl Phys A 2013;113:575–81.
[355] Lepicard A, Bondu F, Kang M, Sisken L, Yadav A, Adamietz F, et al. Long-lived monolithic micro-optics for multispectral GRIN applications Sci. Rep 2018;8:7388.
[356] Saliminia A, Vallee R, Chin SL. Waveguide writing in silica glass with femtosecond pulses from an optical parametric amplifier at 1.5 μm. Opt Commun 2005;256:422–7.
[357] Khalid M, Chen GC, Ebendorff-Heidepreim H, Lancaster DG. Femtosecond laser induced low propagation loss waveguides in a lead-germanate glass for efficient lasing in near to mid-IR. Sci Rep 2021;11:10742.
[358] Fernandez TT, Hernandez M, Sotillo B, Eaton SM, Jose G, Osellame R, et al. Role of ion migrations in ultrafast laser written tellurite glass waveguides. Opt Exp 2014;22:15298.
[359] Fletcher LB, Witcher JJ, Troy N, Reis ST, Brow RK, Krol DM. Direct femtosecond laser waveguide writing inside zinc phosphate glass. Opt Exp 2011;19:7929–36.
[360] Potter Jr BG, Simmons-Potter K, Dunbar TD. Thermal stability of photosensitive Bragg gratings in sputter-deposited germanosilicate glass. J Non-Cryst Solids 2000;277:114.
[361] Yang Z, Zhang Q, Jiang Z. Photo-induced refractive index change of bismuth-based silicate glass. J Phys D: Appl Phys 2005;38:1461–3.
[362] Abou Khalil A, Bérubé JP, Danto S, Desmoulin JC, Cardinal T, Petit Y, et al. Direct laser writing of a new type of waveguides in silver containing glasses. Sci Rep 2017;7:11124.
[363] Marquestaut N, Petit Y, Royon A, Mounaix P, Cardinal T, Canioni L. Three-dimensional silver nanoparticle formation using femtosecond laser irradiation in phosphate glasses: analogy with photography. Adv Funct Mater 2014;24(37):5824–32.
[364] Podsvirov OA, Ignatiev AI, Nashchekin AV, Nikonorov NV, Sidorov AI, Tsekhomsky VA, et al. Modification of Ag containing photo-thermo-refractive glasses induced by electron-beam irradiation. Nucl Instrum Methods Phys Res B 2010;268(19):3103–6.
[365] Wong S, Deubel M, Pérez-Willard F, John S, Ozin GA, Wegener M, et al. Direct laser writing of three-dimensional photonic crystals with a complete photonic bandgap in chalcogenide glasses. Adv Mater 2006;18(3):265–9.
[366] Saito M, Honma T, Benino Y, Fujiwara T, Komatsu T. Formation of nonlinear optical $KSm(PO_3)_4$ crystals in phosphate glassesby YAG laser irradiation. Solid State Sci 2004;6(9):1013–8.
[367] Honma T. Laser-induced crystal growth of nonlinear optical crystal on glass surfaceJ. Ceram Soc JAPAN 2010;118(2):71–6.
[368] Dai Y, Ma H, Lu B, Yu B, Zhu B, Qiu J. Femtosecond laser-induced oriented precipitation of $Ba_2TiGe_2O_8$ crystals in glass. Opt Exp 2008;16(6):3912–7.
[369] Liu Y, Zhu B, Dai Y, Qiao X, Se Ye, Teng Y, Guo Q, et al. Femtosecond laser writing of Er^{3+}-doped CaF_2 crystalline patterns in glass. Opt Lett 2009;34(21):3433–5.
[370] Savytskii D, Knorr B, Dierolf V, Jain H. Challenges of CW laser-induced crystallization in a chalcogenide glass. Opt Mater Exp 2013;3(8):1026.
[371] Gupta P, Stone A, Woodward N, Dierolf V, Jain H. Laser fabrication of semiconducting ferroelectric single crystal SbSI features on chalcohalide glass. Opt Mater Exp 2011;1(4):652–7.
[372] Lumeau J, Glebova L, Glebov LB. Influence of UV-exposure on the crystallization and optical properties of photo-thermo-refractive glass. J Non-Cryst Solids 2008;354(2–9):425–30.
[373] Aseev VA, Nikonorov NV. Spectroluminescence properties of photothermorefractive nanoglass-ceramics doped with ytterbium and erbium ions. J Opt Technol 2008;75(10):676–81.
[374] Sato Y, Taira T, Smirnov V, Glebova L, Glebov L. Continuous-wave diode-pumped laser action of Nd^{3+}-doped photo-thermo-refractive glass. Opt Lett 2011;36(12):2257–9.
[375] Sgibnev YM, Ignatiev AI, Nikonorov NV, Efimov AM, Postnikov ES. Effects of silver ion exchange and subsequent treatments on the UV-VIS spectra of silicate glasses. I. Undoped, CeO_2-doped, and (CeO_2 + Sb_2O_3)-codoped photo-thermo-refractive matrix glasses. J Non-Crystal Solids 2013;378:213–26.
[376] Sgibnev YM, Nikonorov NV, Vasilev VN, Ignatiev AI. Optical gradient waveguides in photo-thermo-refractive glass formed by ion exchange method. J Light Technol 2015;33(17):3730.
[377] Braunstein R. Photochromic and electrochromic properties of tungstate glasses. Solid State Commun 1978;28:839–42.
[378] Poirier Nalin GM, Messaddeq Y, Ribeiro SJL. Photochromic properties of tungstate-based glasses. Sol State Ion 2007; 178: 871–5.
[379] Nalin M, Poirier G, Ribeiro SJL, Messaddeq Y, Cescato L. Glasses in the $SbPO_4$– WO_3 system. J Non Cryst Sol 2007;353:1592–7.

[380] Ataalla M, Afify AS, Hassan M, Adballah M, Milanova M, Aboul-Enein HY, et al. Tungsten-based glasses for photochromic, electrochromic, gas sensors and related applications: a review. J Non-Crystal Solids 2018;491:43–54.
[381] Stookey SD. Coloration of glass by gold, silver and copper. J Am Ceram Soc 1949;32:246.
[382] Faraday M. On the magnetization of light and the illumination of magnetic lines of force. Phil Trans Royal Soc 1846;136:1–20.
[383] Parker MR. The Kerr magneto-optic effect (1876–1976). Physica B+ C 1977;86:1171–6.
[384] Haider T. A review of magneto-optic effects and its application. Int. J Electromag Appl 2017;7:17–24.
[385] Trémolet de Lacheisserie E, Gignoux D, Schlenker M, Magnetism. NY: Springer; 2015.
[386] Franco DF, Ledemi Y, Correr W, Morency S, Afonso CRM, Messaddeq SH, et al. Magneto-optical borogermanate glasses and fibers containing Tb^{3+}. Sci Rep 2021;11:9906.
[387] Carlin RL. Magneto-Chemistry, Springer-Verlag, 1st ed. 1986.
[388] Gao G, Winterstein-Beckmann A, Surzhenko O, Dubs C, Dellith J, Schmidt MA, et al. Faraday rotation and photoluminescence in heavily Tb^{3+}-doped GeO_2-B_2O_3-Al_2O_3-Ga_2O_3 glasses for fiber-integrated magneto-optics Sci. Rep 2015;5:1–6.
[389] Starobor AV, Zheleznov DS, Palashov OV, Savinkov VI, Sigaev NV. Borogermanate glasses for faraday isolators at high average power. Opt Comm 2016;258:176–9.
[390] Franco DF, Fernandes RG, Felix JF, Mastelaro VR, Eckert H, Afonso CRM, et al. Fundamental studies of magneto-optical borogermanate glasses and derived optical fibers containing Tb^{3+}. J Mat Res and Tech 2021;11:312–27.
[391] Fernandes RG, Franco DF, Mastearo VR, Cardinal T, Toulemonde O, Nalin M. Thermal and structural modification in transparent and magnetic germanoborate glasses induced by Gd_2O_3. Ceram Int 2020;46:22079–89.
[392] Garcia-Souto JA, Lamela-Rivera H. High resolution (<1nm) interferometric fiber-optic sensor of vibrations in high-power transformers. Opt Exp 2006;14(21):9679–86.
[393] Tanaka K, Hirao K, Soga N. Large Verdet Constant of $30Tb_2O_3{\cdot}70B_2O_3$. Glass Jpn J Appl Phys 1995;34:4825.
[394] Yin H, Gao Y, Gong Y, Buchanan R, Song J, Li M. Wavelength dependence of Tb^{3+} doped magneto-optical glass Verdet constant. Cer Intern 2018;44:10929–33.
[395] Zaiter R, Dussauze M, Nalin M, Fargin E, Adamietz F, Danto S, et al. Thermal and structural modification in transparent and magnetic gallogermanate glasses induced by Gd_2O_3. J Alloys Comp 2022;912:165181.
[396] Qiu J, Tanaka K, Sugimoto N, Hirao K. Faraday effect in Tb^{3+}-containing borate fluoride and fluorophosphate glasses. J Non-Cryst Sol 1997;213:93–8.
[397] Suzuki F, Fujita N, Sato F. Proc SPIE 2019;10914:1091412.
[398] Akamatsu H, Fujita K, Murai S, Takaka K. Ferromagnetic Eu^{2+} based oxide glasses with reentrant spin glass behavior. Phys Rev B 2010;81:014423.
[399] Suzuki F, Sato F, Oshita H, Yao S, Nakatsuka Y, Tanaka K. Large Faraday effect of borate glasses with high Tb^{3+} content prepared by containerless processing. Opt Mat 2018;76:174–7.
[400] Lin H, Zhou L, Liu B, Li N, He J, Zhang T, et al. Research on the magneto-optical properties of Tb^{3+}-Ho^{3+} co-doped GeO_2-B_2O_3-P_2O_5-ZnO (GBPZ) Faraday glass. J Non-Cryst Sol 2022;587:121589.
[401] Lin H, Liu B, Li N, He J, Zhou L, Zhang T, et al. Research on the physical and optical properties of Dy^{3+} doped 30 mol % Tb_2O_3-B_2O_3-GeO_2-PbO- SiO_2 magneto-optical glass with high Verdet constant. J Phys Chem Sol 2022;166:110682.
[402] Hayakawa T, Nogami M, Nishi N, Sawanobori N. Faraday rotation effect of highly Tb_2O_3/Dy_2O_3 concentrated B_2O_3-Ga_2O_3-SiO_2-P_2O_5 glasses. Chem Mat 2002;14:3223–5.
[403] Lin H, Jia H, Zhou L, Li N, Liu B, He J, et al. Magneto-optical and fluorescence properties of Tb^{3+} doped glass-ceramics containing $AlPO_4$. J Non-Cryst Sol 2022;579:121377.
[404] Sandu V, Cimpoiasu E, Kuncser A, Nicolescu MS. Magnetic properties of glass-ceramics obtained by crystallization of iron-rich borosilicate glasses. J Adv Cer 2017;6:251–61.
[405] Chen Q. WO_3 concentration-dependent magneto-optical properties of Faraday rotating glass and glass-ceramics. J Non-Cryst Sol 2019;522:119584.
[406] Souza AE, Antonio SG, Ribeiro SJL, Franco DF, Galeani G, Cardinal T, et al. Heavy metal oxide glass-ceramics containing luminescent gallium- garnets single crystals for photonic applications. J Alloys Comp 2021;864:158804.
[407] Orives JR, Viali WR, Santagneli SH, Afonso CRM, Carvalho MH, de Oliveira AJA, et al. Phosphate glasses via coacervation route containing $CdFe_2O_4$ nanoparticles: structural, optical and magnetic characterization. Dalton Transac 2018;47:5771.
[408] Orives JR, Viali WR, Destro FB, Silva SW, Ribeiro SJL, Nalin M. Embedding CoPt magnetic nanoparticles within a phosphate glass matrix. J of Alloys Comp 2020;848:156576.
[409] Orives JR, Pichon BP, Mertz D, Sartori K, Begin-Colin S, Viali WR, et al. Phosphate glasses containing monodisperse $Fe_{3-\delta}O_4$@SiO_2 stellate nanopartciles obtained by melt-quenching process. Cer Intern 2020;46:12120–7.
[410] Masuno A. Functionalities in unconventional oxide glasses prepared using a levitation technique. J Cer Soc Jap 2022;130:563–74.
[411] Asad S, Mishra SK, Rezaei G, Izquierdo R, Ung B. Rapid and sensitive magnetic field sensor based on photonic crystal fiber with magnetic fluid infiltrated nanoholes. Sci Rep 2022;12:9672.
[412] Silva RM, Martins H, Nascimento I, Baptista JM, Ribeiro AL, Santos JL, et al. Optical current sensors for high power systems: a review. Appl Sci 2012;2:602–28.
[413] Colladon D. On the reflections of a ray of light inside a parabolic liquid stream. Compt Rend 1842;15:800.
[414] Babinet J. Note on the transmission of light by sinuous canals. Compt Rend 1842;15:802.
[415] Tyndall J. On some phenomena connected with the motion of liquids. Proc Royal Inst Great Britain 1854;1:446–8.
[416] Snyder AW, Love JD. Optical waveguide theory. New York: Chapman & Hall and Methuen Inc; 1984.
[417] Marcuse D. Theory of dielectric optical waveguides. New York: Academic Press; 1974.
[418] Snitzer E. Cylindrical dielectric waveguide modes. J Opt Soc Am 1961;51(5):491–8.
[419] Goldberg DA, Laslett LJ, Rimmer RA. Modes of elliptical waveguides: a correction. IEEE Trans Microwave Theory Tech 1990;38(11):1603–8.
[420] Ermert H. Guiding and radiation characteristics of planar waveguides. IEE J Microwave Opt Acoust 1979;3(2):59–62.
[421] Chandler CH. An investigation of dielectric rod as waveguide. J Appl Phys 1949;20(12):1188–92.
[422] Elsasser WM. Attenuation in a dielectric circular rod. J Appl Phys 1949;20(12):1193–6.
[423] Hopkins HH, Kapany NS. A flexible fibrescope, using static scanning. Nature 1954;173(4392):39–41.
[424] Singh KP. In memory of Narinder Singh Kapany. Nature Photon 2021;15:403–4.
[425] Miller SE. Integrated optics: an introduction. Bell Sys Tech J 1969;48(7):2059–69.
[426] Tao G, Ebendorff-Heidepriem H, Stolyarov AM, Danto S, Badding JV, Fink Y, et al. Infrared fibers. Adv Opt Photon 2015;7(2):379–458.
[427] Brown J, Jackson W. The properties of artificial dielectrics at centimetre wavelengths. Proc IEE-Part B 1955;102(1):11–6.
[428] Sharpless WM. Artificial dielectrics for microwaves. Proc IRE 1951;39(11):1389–93.
[429] Purcell EM. Spontaneous emission probabilities at radio frequencies. Phys Rev 1946;69:681.
[430] Yablonovitch E. Inhibited spontaneous emission in solid-state physics and electronics. Phys Rev Lett 1987;58(20):2059.
[431] John S. Strong localization of photons in certain disordered dielectric superlattices. Phys Rev Lett 1987;58(23):2486.
[432] Anderson PW. Absence of diffusion in certain random lattices. Phys Rev 1958;109(5):1492–505.
[433] Karbasi S, Hawkins T, Ballato J, Koch KW, Mafi A. Transverse Anderson localization in a disordered glass optical fiber. Opt Mater Exp 2012;2(11):1496–503.
[434] Ballato J, Peacock AC. Perspective: Molten core optical fiber fabrication—a route to new materials and applications. APL Photon 2018;3(12):120903.
[435] Hyde F. Inventor; Corning inc., assignee. Method of making a transparent article of silica. US patent US2272342A. 1942. 5 pages.
[436] Townsend JE, Poole SB, Payne D. Solution-doping technique for fabrication of rare-earth-doped optical fibres. Electron Lett 1987;7(23):329–31.
[437] El-Amraoui M, Gadret G, Jules JC, Fatome J, Fortier C, Désévédavy F, et al. Microstructured chalcogenide optical fibers from As_2S_3 glass: towards new IR broadband sources. Opt Exp 2010;18(25):26655–65.

[438] Coulombier Q, Brilland L, Houizot P, Chartier T, N'Guyen TN, Smektala F, et al. Casting method for producing low-loss chalcogenide microstructured optical fibers. Opt Exp 2010;18(9):9107–12.
[439] Righini GC, Chiappini A. Glass optical waveguides: a review of fabrication techniques. Opt Eng 2014;53:071819.
[440] Smith HM, Turner AF. Vacuum deposited thin films using a ruby laser. Appl Opt 1965;4(1):147–8.
[441] Lowndes DH, Geohegan DB, Puretzky AA, Norton DP, Rouleau CM. Synthesis of novel thin-film materials by pulsed laser deposition. Science 1996;273(5277):898–903.
[442] Chandrappan J, Murray M, Kakkar T, Petrik P, Agocs E, Zolnai Z, et al. Target dependent femtosecond laser plasma implantation dynamics in enabling silica for high density erbium doping. Sci Rep 2015;5(1):14037.
[443] Loganathan S, Santhanakrishnan S, Bathe R, Arunachalam M. Prediction of femtosecond laser ablation profile on human teeth. Lasers in Med Sci 2019;34(4):693–701.
[444] Resta V, Caricato AP, Loiudice A, Rizzo A, Gigli G, Taurino A, et al. Pulsed laser deposition of a dense and uniform Au nanoparticles layer for surface plasmon enhanced efficiency hybrid solar cells. J Nanoparticle Res 2013;15(11):2017.
[445] Afonso CN, Gonzalo J, Serna R, De Sande JC, Ricolleau C, Grigis C, et al. Vacuum versus gas environment for the synthesis of nanocomposite films by pulsed-laser deposition. Appl Phys A. 1999;69(1):S201–S207.
[446] Cesaria M, Mazzeo M, Quarta G, Aziz MR, Nobile C, Carallo S, et al. Pulsed laser deposition of $CsPbBr_3$ films: impact of the composition of the target and mass distribution in the plasma plume. Nanomaterials 2021;11(12):3210.
[447] Martino M, Caricato AP, Fernandez M, Leggieri G, Jha A, Ferrari M, et al. Pulsed laser deposition of active waveguides. Thin Solid Films 2003;433(1–2):39–44.
[448] Dikovska AO, Atanasov PA, De Castro MJ, Perea A, Gonzalo J, Afonso CN, et al. Optically active Er^{3+}–Yb^{3+} codoped Y_2O_3 films produced by pulsed laser deposition. Thin Solid Films 2006;500(1–2):336–40.
[449] Caricato AP, Fernández M, Ferrari M, Leggieri G, Martino M, Mattarelli M, et al. Er^{3+}-doped tellurite waveguides deposited by excimer laser ablation. Mater Sci Eng B 2003;105(1–3):65–9.
[450] Gonzalo J, Afonso CN, Perriere J. Influence of laser energy density on the plasma expansion dynamics and film stoichiometry during laser ablation of BiSrCaCuO. J Appl Phys 1996;79(10):8042–6.
[451] Jha A, Irannejad M. Inorganic glasses for pulsed-laser based waveguide engineering for integrated optics. In: Chakrabortry P, editor. Encyclopedia of materials: electronics. Elsevier. ISBN 9780128197356 (in Press).
[452] Miller SE. Integrated optics: an introduction. Bell Syst Tech J 1969;48:2059–69.
[453] Goell JE, Standley RD. Sputtered glass waveguide for integrated optical circuits. Bell Syst Tech J 1969;48:3445–8.
[454] Irannejad M, Jose G, Jha A, Steenson DP. A parametric study of Er^{3+}-ions doped Phospho-tellurite glass thin films by pulsed laser deposition. Opt Mater 2010;33(2):215–9.
[455] Irannejad M, Jose G, Steenson P, Jha A. Enhancement in optical and microstructure properties of Er^{3+}-doped phospho-tellurite glass thin films. Opt Mater 2012;34(8):1272–6.
[456] Eason R. Pulsed laser deposition of thin films: applications-led growth of functional materials. John Wiley & Sons. Inc.; 2007. p. 36–41.
[457] Balda R, Sanz O, Gonzalo JA, de Castro MJ, Perea A, Fernandez-Navarro JM, et al. Active Er^{3+}-doped lead-niobium-germanate planar waveguides produced by pulsed laser deposition. In: Rare-earth-doped materials and devices VII 2003 Jun 17, vol. 4990. SPIE. p. 30–7.
[458] Tsigara A, Velli L, Giannoudakos A, Varsamis CP, Kompitsas M, Vainos NA, et al. Pulsed laser deposited lead-germanate glass systems. Appl Phys A 2004;79(4):1319–21.
[459] Němec P, Charrier J, Cathelinaud M, Allix M, Adam JL, Zhang S, et al. Pulsed laser deposited amorphous chalcogenide and alumino-silicate thin films and their multilayered structures for photonic applications. Thin Solid Films 2013;539:226–32.
[460] Pompilian OG, Dascalu G, Mihaila I, Gurlui S, Olivier M, Nemec P, et al. Pulsed laser deposition of rare-earth-doped gallium lanthanum sulphide chalcogenide glass thin films. Appl Phys A 2014;117(1):197–205.
[461] Darby MS, Simpson RE, May-Smith TC, Hewak DW, Eason RW. Influence of deposition parameters on composition and refractive index of femtosecond and nanosecond pulsed laser deposited gallium lanthanum oxysulphide. J Non-crystal Sol 2008;354(40–41):4582–8.
[462] Dussauze M, Giannoudakos A, Velli L, Varsamis CP, Kompitsas M, Kamitsos EI. Structure and optical properties of amorphous lead-germanate films developed by pulsed-laser deposition. J Chem Phys 2007;127(3):034704.
[463] Epurescu G, Vlad A, Bodea MA, Vasiliu C, Dumitrescu O, Niciu H, et al. Pulsed-laser deposition of smooth thin films of Er, Pr and Nd doped glasses. Appl Surface Sci 2009;255(10):5295–8.
[464] Gottmann J, Moiseev L, Vasilief I, Wortmann D. Manufacturing of Er: ZBLAN ridge waveguides by pulsed laser deposition and ultrafast laser micromachining for green integrated lasers. Mater Sci Eng B 2008;146(1–3):245–51.
[465] Irannejad M, Pasha M, Jose G, Steenson P, Fernandez TT, Jha A, et al. Active glass waveguide amplifier on GaAs by UV-pulsed laser deposition and femtosecond laser inscription. Laser Phy Lett 2012;9(5):329.
[466] Zhao Z. Pulsed laser deposition and characterisation of rare earth doped glass-polymer optical materials. University of Leeds; 2012.
[467] Betz G, Wehner GK. Sputtering of multicomponent materials. In: Behrish R, editor. Sputtering by particle bombardment II. Berlin (DE): Springer; 1983. p. 11–90.
[468] Wasa K, Kitabatake M, Adachi H. Thin films materials technology: sputtering of compound materials. New York (US): Springer, William Andrew Inc Publishing; 2012.
[469] Gudmundsson JT. Physics and technology of magnetron sputtering discharges. Plasma Sources Sci Technol 2020;29:113001.
[470] Kawachi M, Yasu M, Edahiro T. Fabrication of SiO_2-TiO_2 glass planar optical waveguides by flame hydrolysis deposition. Electron Lett 1983;19:583–4.
[471] Bange JP, Patil LS, Gautam DK. Growth and characterization of SiO_2 films deposited by Flame Hydrolysis Deposition. Progr Electrom Res M 2008;3:165–75.
[472] Lin X, Ma X, He JJ. Void-filling and loss reduction in PECVD silica waveguide devices using boron-germanium codoped upper cladding. IEEE Phot Techn Lett 2010;22:1491–3.
[473] Saito T, Hanada T, Kitamura N, Kitamura M. Photosensitivity in silica-based waveguides deposited by atmospheric pressure chemical vapor deposition. Appl Opt 1998;37:2242–4.
[474] Ay F, Aydinlia A, Agan S. Low-loss as-grown germanosilicate layers for optical waveguides. Appl Phys Lett 2003;83:4743–5.
[475] Huang CC, Hewak DW, Badding JV. Deposition and characterization of germanium sulphide glass planar waveguides. Opt Exp 2004;12:2501–6.
[476] Brinker CJ, Frye GC, Hurd AJ, Ashley CS. Fundamentals of sol-gel dip coating. Thin Solid Films 1991;201:97–108.
[477] Tervonen A, West BR, Honkanen S. Ion-exchanged glass waveguide technology: a review. Opt Eng 2011;50:071107.
[478] Berneschi S, Righini GC, Pelli S. Towards a glass new world: the role of ion-exchange in modern technology. Appl Sci 2021;11:4610.
[479] Righini GC, Liñares J. Active and quantum integrated photonic elements by ion exchange in glass. Appl Sci 2021;11:5222.
[480] Townsend PD, Chandler PJ, Zhang L. Optical Effects of Ion Implantation. Cambridge: Cambridge University Press; 1994.
[481] Bányász, I, Berneschi, S Bettinelli, M, M. Brenci, Fried M, Khanh NQ, et al. MeV energy N^+-implanted planar optical waveguides in Er-doped tungsten-tellurite glass operating at 1.55 μm. IEEE Photon J 2012; 4: 721–7.
[482] Liu CX, Peng B, Wei W, Li WN, Guo HT, Cheng S. Ion implanted glass waveguides: a review. Phys Internat 2013;4:1–12.
[483] Fabry C, Pérot A. Théorie et applications d'une nouvelle méthode de spectroscopie interférentielle. Ann de Chim et de Phys 1899;16:115–144.
[484] Rayleigh L. The problem of the whispering gallery. Phil Mag 1910;20:1001–4.
[485] Cai L, Pan J, Zhao Y, Wang J, Xiao S. Whispering Gallery Mode optical microresonators: structures and sensing applicationsl. Phys Status Solidi A 2020;217:1900825.
[486] Chiasera A, Dumeige Y, Féron P, Ferrari M, Jestin Y, Nunzi Conti G, et al. Spherical whispering-gallery-mode microresonators. Laser Photon Rev 2010;4:457–82.
[487] Brenci M, Calzolai R, Cosi F, Nunzi Conti G, Pelli S, Righini GC. Microspherical resonators for biophotonic sensors. Proc SPIE 2006;6158:61580S.

[488] Gorodetsky ML, Savchenkov AA, Ilchenko VS. Ultimate Q of optical microsphere resonators. Opt Lett 1996;21:453–5.
[489] Andrianov AV, Marisova MP, Anashkina EA. Thermo-optical sensitivity of whispering gallery modes in As_2S_3 chalcogenide glass microresonators. Sensors 2022;22:4636.
[490] Laine J-P. Design and applications of optical microsphere resonators. Dissertation for the degree of Doctor of Science in Technology, Helsinki University of Technology; 2003.
[491] Zhang R, Yang Z, Zhao M, Xu P, Zhang W, Kang Z, et al. High quality, high index-contrast chalcogenide microdisk resonators. Opt Exp 2021;29:17775–83.
[492] Yu J, Lewis E, Brambilla G, Wang P. Temperature sensing performance of microsphere resonators. Sensors 2018;18:2515.
[493] Soler-Carracedo K, Estévez-Alonso P, Martin IR, Rios S. Improving the sensitivity of WGM pressure sensors with oxyfluoride glass microspheres. J Lumin 2021;238:118249.
[494] Righini GC, Soria S. Biosensing by WGM microspherical resonators Sensors 2016;16:905.
[495] Vollmer F, Arnold S, Keng D. Single virus detection from the reactive shift of a whispering-gallery mode. PNAS 2008;105:20701–4.
[496] Yang J, Wang DN, Li X. An Erbium-doped whispering-gallery-mode microlaser for sensing. J Lightwave Techn 2021;39:5177–82.
[497] Tamura Y, Sakuma H, Morita K, Suzuki M, Yamamoto Y, Shimada K, et al. The first 0.14-dB/km loss optical fiber and its impact on submarine transmission. J Light Technol 2018;36(1):44–9.
[498] Jasion GT, Sakr H, Hayes JR, Sandoghchi SR, Hooper L, Fokoua EN, et al. Bradley TD. 0.174 dB/km hollow core double nested antiresonant nodeless fiber (DNANF). In: 2022 optical fiber communications conference and exhibition (OFC). IEEE; 2022. p. 1–3.
[499] Hong Y, Bottrill KR, Bradley TD, Sakr H, Jasion GT, Harrington K, et al. Low-latency WDM intensity-modulation and direct-detection transmission over >100 km distances in a hollow core fiber. Laser Photon Rev 2021;15(9):2100102.
[500] Cozmuta I, Rasky DJ. Exotic optical fibers and glasses: innovative material processing opportunities in earth's orbit. New Space 2017;5(3):121–40.
[501] Tick PA. Are low-loss glass–ceramic optical waveguides possible? Opt Lett 1998;23(24):1904–5.
[502] Blanc W, Mauroy V, Nguyen L, Shivakiran Bhaktha BN, Sebbah P, Pal BP, et al. Fabrication of rare earth-doped transparent glass ceramic optical fibers by modified chemical vapor deposition. J Am Ceram Soc 2011 Aug;94(8):2315–8.
[503] Blanc W, Martin I, Francois-Saint-Cyr H, Bidault X, Chaussedent S, Hombourger C, et al. Compositional changes at the early stages of nanoparticles growth in glasses. J Phys Chem C 2019;123(47):29008–14.
[504] Vermillac M, Lupi JF, Peters F, Cabie M, Vennegues P, Kucera C, et al. Fiber-draw-induced elongation and break-up of particles inside the core of a silica-based optical fiber. J Am Ceram Soc 2017;100(5):1814–9.
[505] Blanc W, Lu Z, Robine T, Pigeonneau F, Molardi C, Tosi D. Nanoparticles in optical fiber, issue and opportunity of light scattering. Opt Mat Exp 2022;12(7):2635–52.
[506] Ballato J, Gibson UJ. Core opportunities for future optical fibers. J Phys Photonics 2021;3(4):041001.
[507] Sazio PJ, Amezcua-Correa A, Finlayson CE, Hayes JR, Scheidemantel TJ, Baril NF, et al. Microstructured optical fibers as high-pressure microfluidic reactors. Science 2006;311(5767):1583–6.
[508] Peacock AC, Sparks JR, Healy N. Semiconductor optical fibres: progress and opportunities. Laser & Photon Rev 2014;8(1):53–72.
[509] Peacock AC, Gibson UJ, Ballato J. Silicon optical fibres–past, present, and future. Adv Phys X 2016;1(1):114–27.
[510] Healy N, Gibson U, Peacock AC. A review of materials engineering in silicon-based optical fibres. Semicon Sci Technol 2018;33(2):023001.
[511] Won DJ, Ramirez MO, Kang H, Gopalan V, Baril NF, Calkins J, et al. All-optical modulation of laser light in amorphous silicon-filled microstructured optical fibers. Appl Phys Lett 2007;91(16):161112.
[512] Mehta P, Healy N, Day TD, Badding JV, Peacock AC. Ultrafast wavelength conversion via cross-phase modulation in hydrogenated amorphous silicon optical fibers. Opt Exp 2012;20(24):26110–6.
[513] Ballato J, Hawkins T, Foy P, Stolen R, Kokuoz B, Ellison M, et al. Silicon optical fiber. Opt Exp 2008;16(23):18675–83.
[514] Mehta P, Krishnamurthi M, Healy N, Baril NF, Sparks JR, Sazio PJ, et al. Mid-infrared transmission properties of amorphous germanium optical fibers. Appl Phys Lett 2010;97(7):071117.
[515] Ballato J, Hawkins T, Foy P, Yazgan-Kokuoz B, Stolen R, McMillen C, et al. Glass-clad single-crystal germanium optical fiber. Opt Exp 2009;17(10):8029–35.
[516] Coucheron DA, Fokine M, Patil N, Breiby DW, Buset OT, Healy N, et al. Laser recrystallization and inscription of compositional microstructures in crystalline SiGe-core fibres. Nature Comm 2016;7(1):13265.
[517] Wu W, Balci M, Song S, Liu C, Fokine M, Laurell F, et al. CO_2 laser annealed SiGe core optical fibers with radial Ge concentration gradients. Opt Mater Express 2020;10(4):926–36.
[518] Wu W, Balci MH, Mühlberger K, Fokine M, Laurell F, Hawkins T, et al. Ge-capped SiGe core optical fibers. Opt Mater Express 2019;9(11):4301–6.
[519] Ballato J, Hawkins T, Foy P, McMillen C, Burka L, Reppert J, et al. Binary III-V semiconductor core optical fiber. Opt Exp 2010;18(5):4972–9.
[520] Scott BL, Pickrell GR. Fabrication of GaSb optical fibers. Process Proper Adv Ceram Compos V: Ceram Trans 2013;1(240):65.
[521] Sparks JR, He R, Healy N, Krishnamurthi M, Peacock AC, Sazio PJ, et al. Zinc selenide optical fibers. Adv Mater 2011;23(14):1647–51.
[522] Hendrickson AT, Aro SC, Sparks JR, Coco MG, Krug JP, Mathewson CJ, et al. Post-processing ZnSe optical fibers with a micro-chemical vapor transport technique. Opt Mater Express 2020;10(12):3125–36.
[523] Zaengle T, Gibson UJ, Hawkins TW, McMillen C, Ghimire B, Rao AM, et al. A novel route to fibers with incongruent and volatile crystalline semiconductor cores: GaAs. ACS Photon 2022;9(3):1058–64.
[524] Gibson UJ, Wei L, Ballato J. Semiconductor core fibres: materials science in a bottle. Nat Comm 2021;12(1):3990.
[525] Morris S, McMillen C, Hawkins T, Foy P, Stolen R, Ballato J, et al. The influence of core geometry on the crystallography of silicon optical fiber. J Crystal Growth 2012;352(1):53–8.
[526] Morris S, Hawkins T, Foy P, Hudson J, Zhu L, Stolen R, et al. On loss in silicon core optical fibers. Opt Mater Express 2012;2(11):1511–9.
[527] McMillen C, Brambilla G, Morris S, Hawkins T, Foy P, Broderick N, et al. On crystallographic orientation in crystal core optical fibers II: Effects of tapering. Opt Mater 2012;35(2):93–6.
[528] Healy N, Fokine M, Franz Y, Hawkins T, Jones M, Ballato J, et al. CO_2 laser-induced directional recrystallization to produce single crystal silicon-core optical fibers with low loss. Adv Opt Mater 2016;4(7):1004–8.
[529] Song S, Lønsethagen K, Laurell F, Hawkins TW, Ballato J, Fokine M, et al. Laser restructuring and photoluminescence of glass-clad GaSb/Si-core optical fibres. Nat Comm 2019;10(1):1790.
[530] Fokine M, Theodosiou A, Song S, Hawkins T, Ballato J, Kalli K, et al. Laser structuring, stress modification and Bragg grating inscription in silicon-core glass fibers. Opt Mater Express 2017;7(5):1589–97.
[531] Franz Y, Runge AF, Ren H, Healy N, Ignatyev K, Jones M, et al. Material properties of tapered crystalline silicon core fibers. Opt Mater Express 2017;7(6):2055–61.
[532] Song S, Laurell F, Meehan B, Hawkins TW, Ballato J, Gibson UJ. Localised structuring of metal-semiconductor cores in silica clad fibres using laser-driven thermal gradients. Nat Comm 2022;13(1):2680.
[533] Davis R, Rice R, Ballato A, Hawkins T, Foy P, Ballato J. Toward a photoconducting semiconductor RF optical fiber antenna array. Appl Opt 2010;49(27):5163–8.
[534] Wang P, Lee T, Ding M, Dhar A, Hawkins T, Foy P, et al. Germanium microsphere high-Q resonator. Opt Lett 2012;37(4):728–30.
[535] Suhailin FH, Healy N, Franz Y, Sumetsky M, Ballato J, Dibbs AN, et al. Kerr nonlinear switching in a hybrid silica-silicon microspherical resonator. Opt Exp 2015;23(13):17263–8.
[536] Shen L, Ren H, Huang M, Wu D, Peacock AC. A review of nonlinear applications in silicon optical fibers from telecom wavelengths into the mid-infrared spectral region. Opt Comm 2020;463:125437.
[537] Ren H, Shen L, Wu D, Aktas O, Hawkins T, Ballato J, et al. Nonlinear optical properties of polycrystalline silicon core fibers from telecom wavelengths into the mid-infrared spectral region. Opt Mater Express 2019;9(3):1271–9.

[538] Wang P, Charlton O'Mahony C, Lee T, Ismaeel R, Hawkins T, Semenova Y, et al. Mid-infrared Raman sources using spontaneous Raman scattering in germanium core optical fibers. Appl Phys Lett 2013;102(1):011111.
[539] Peacock AC, Campling J, Runge AF, Ren H, Shen L, Aktas O, et al. Wavelength conversion and supercontinuum generation in silicon optical fibers. IEEE J Sel Top Quant Electron 2017;24(3):5100309.
[540] Wu D, Shen L, Ren H, Campling J, Hawkins TW, Ballato J, et al. Net optical parametric gain in a submicron silicon core fiber pumped in the telecom band. APL Photon 2019;4(8):086102.
[541] Sun S, Huang M, Wu D, Shen L, Ren H, Hawkins TW, et al. Raman enhanced four-wave mixing in silicon core fibers. Opt Lett 2022;47(7):1626–9.
[542] Martinsen FA, Smeltzer BK, Nord M, Hawkins T, Ballato J, Gibson UJ. Silicon-core glass fibres as microwire radial-junction solar cells. Sci Rep 2014;4(1):1–7.
[543] Martinsen FA, Ballato J, Hawkins T, Gibson UJ. Bulk fabrication and properties of solar grade silicon microwires. APL Mater 2014;2(11):116108.
[544] Huang M, Ren H, Aktas O, Shen L, Wang J, Hawkins TW, et al. Fiber integrated wavelength converter based on a silicon core fiber with a nano-spike coupler. IEEE Photon Technol Lett 2019;31(19):1561–4.
[545] Theodosiou A, Fokine M, Hawkins T, Ballato J, Gibson UJ, Kalli K. Characterisation of silicon fibre Bragg grating in near-infrared band for strain and temperature sensing. Electron Lett 2018;54(24):1393–5.
[546] Sørgård T, Song S, Vullum PE, Kores C, Mølster KM, Laurell F, et al. Broadband infrared and THz transmitting silicon core optical fiber. Opt Mater Exp 2020;10(10):2491–9.
[547] Sørgård T, Hawkins T, Ballato J, Österberg UL, Gibson UJ. All-optical high-speed modulation of THz transmission through silicon core optical fibers. Opt Exp 2021;29(3):3543–52.
[548] Sohanpal R, Ren H, Shen L, Deakin C, Heidt AM, Hawkins TW, et al. All-fibre heterogeneously-integrated frequency comb generation using silicon core fibre. Nat Comm 2022;13(1):3992.
[549] Kotz F, Arnold K, Bauer W, Schild D, Keller N, Sachsenheimer K, et al. Three-dimensional printing of transparent fused silica glass. Nature 2017;544(7650):337–9.
[550] Cook K, Canning J, Leon-Saval S, Reid Z, Hossain MA, Comatti JE, et al. Air-structured optical fiber drawn from a 3D-printed preform. Opt Lett 2015;40(17):3966–9.
[551] Chu Y, Fu X, Luo Y, Canning J, Tian Y, Cook K, et al. Silica optical fiber drawn from 3D printed preforms. Opt Lett 2019;44(21):5358–61.
[552] Rosales AL, Velázquez MM, Zhao X, Sahu JK. Optical fibers fabricated from 3D printed silica preforms 2020;vol. 11271:93–9.
[553] Ballato J, Dragic PD. Glass: The carrier of light—Part II—A brief look into the future of optical fiber. Int J Appl Glass Sci 2021;12(1):3–24.
[554] Mata J, de Miguel I, Duran RJ, Merayo N, Singh SK, Jukan A, et al. Artificial intelligence (AI) methods in optical networks: a comprehensive survey. Opt Switch Netw 2018;28:43–57.
[555] Närhi M, Salmela L, Toivonen J, Billet C, Dudley JM, Genty G. Machine learning analysis of extreme events in optical fibre modulation instability. Nat Comm 2018;9(1):4923.
[556] Peng Z, Jian J, Wen H, Gribok A, Wang M, Liu H, et al. Distributed fiber sensor and machine learning data analytics for pipeline protection against extrinsic intrusions and intrinsic corrosions. Opt Exp 2020;28(19):27277–92.
[557] Wetzstein G, Ozcan A, Gigan S, Fan S, Englund D, Soljačić M, et al. Inference in artificial intelligence with deep optics and photonics. Nature 2020;588(7836):39–47.
[558] Mu X, Ferreira FM, Ottino A, Zervas G. Design optimization of uncoupled six-core fibers in standard cladding diameter using artificial intelligence. In: Optical fiber communication conference 2021 (pp. Th1A-34). Optica Publishing Group.
[559] Quandt A, Ferrari M, Righini GC. Advancement of glass-ceramic materials for photonic applications. In: Mishra AK, editor. Sol-gel based nanoceramic materials: preparation, properties and applications. Cham (CH): Springer International Publishing AG; 2017. p. 133–55.
[560] Ribeiro SJL, Messaddeq Y, Gonçalves RR, Ferrari M, Montagna M, Aegerter MA. Low optical loss planar waveguides prepared by an organic-inorganic hybrid system. Appl Phys Lett 2000;77:3502–4.
[561] Jestin Y, Armellini C, Chiappini A, Chiasera A, Ferrari M, Goyes C, et al. Erbium activated HfO_2-based glass-ceramics waveguides for photonics. J Non-Cryst Solids 2007;353:494–7.
[562] de Pablos-Martin A, Ferrari M, Pascual MJ, Righini GC. Glass-ceramics: a class of nanostructured materials for photonics. Rivista del Nuovo Cimento 2015;38:311–69.
[563] Zur L, Tran LTN, Massella D, Vaccari A, Chiappini A, Chiasera A, et al. SiO_2-SnO_2 and SiO_2-HfO_2 transparent glass ceramics activated by rare earth ions. Proc SPIE 2019;10914:1091411.
[564] Tran TNL, Zur L, Chiasera A, Chiappini A, Blanc W, Bollani M, et al. Rare-earth-doped glasses and glass-ceramics for integrated optics. In: Righini GC, Ferrari M, editors. Chapter 5 in integrated optics, Modeling material platforms and fabrication techniques, Vol. 1. London (UK): The Institution of Engineering and Technology (IET); 2021.
[565] Tran TNL, Berneschi S, Trono C, Nunzi Conti G, Zur L, Armellini C, et al. SiO_2-SnO_2:Er^{3+} planar waveguides: Highly photorefractive glass-ceramics. Opt Mat X 2020;7:00056-1/6.
[566] Tran TNL, Armellini C, Varas S, Carpentiero A, Chiappini A, Głuchowski P, et al. Assessment of SnO_2-nanocrystal-based luminescent glass-ceramic waveguides for integrated photonics. Ceram Intl 2021;47:5534–41.
[567] Zur L, Tran TNL, Meneghetti M, Tran VT, Lukowiak A, Chiasera A, et al. Tin-dioxide nanocrystals as Er^{3+} luminescence sensitizers: formation of glass-ceramics thin films and their characterization. Opt Mat 2017;63:95–100.
[568] Sima C, Gates JC, Rogers HL, Mennea PL, Holmes C, Zervas MN, et al. Ultra-wide detuning planar Bragg grating fabrication technique based on direct UV grating writing with electro-optic phase modulation. Opt Exp 2013;21:5747–54.
[569] https://www.sciencedirect.com/journal/optical-materials/special-issue/10LJ4J18H61.
[570] Tran TNL, Szczurek A, Varas S, Armellini C, Scotognella F, Chiasera A, et al. Rare-earth activated SnO_2 photoluminescent thin films on flexible glass: synthesis, deposition and characterization. Opt Mat 2022;124:111978-1/7.
[571] Tan D, Wang Z, Xu B, Qiu J. Photonic circuits written by femtosecond laser in glass: improved fabrication and recent progress in photonic devices. Adv Photon 2021;3:024002-1-23.
[572] Cai C, Wang J. Femtosecond laser-fabricated photonic chips for optical communications: a review. Micromachines 2022;13:630 (1–26).
[573] Bai J, Long XW, Wang WQ, Xie P, Zhao W. Direct Writing of channel optical waveguides in Er^{3+}-doped aluminosilicate glass by low repetition rate femtosecond laser. ACS Appl Electron Mater 2022;4:3107–14.
[574] Liu L, Chen F, Cui J, Xiao X, Xu Y, Hou C, et al. The mutual influence between rare earth element doping and femtosecond laser-induced effects in Ga-As-Sb-S chalcogenide glass. Ceram Intl 2021;47:6388–96.
[575] D'Amico C, Martin G, Troles J, Cheng G, Stoian R. Multiscale laser written photonic structures in bulk chalcogenide glasses for infrared light transport and extraction. Photonics 2021;8(6):211.
[576] Ramos M, Bharadwaj V, Sotillo B, Gholipour B, Giakoumaki AN, Eaton SM, et al. Photonic implementation of artificial synapses in ultrafast laser inscribed waveguides in chalcogenide glass. Appl Phys Lett 2021;119:031104.
[577] Shakhgildyan G, Lipatiev A, Fedotov S, Vetchinnikov M, Lotarev S, Sigaev V. Microstructure and optical properties of tracks with precipitated silver nanoparticles and clusters inscribed by the laser irradiation in phosphate glass. Ceram Intl 2021;47:14320–9.
[578] Tsimvrakidis K, Konidakis I, Stratakis E. Laser-induced erasable and re-writable waveguides within silver phosphate glasses. Materials 2022;15:2983 (1–11).
[579] Smetanina EO, Chimier B, Petit Y, Royon A, Cardinal T, Canioni L, et al. Laser writing of nonlinear optical properties in silver-doped phosphate glass. Opt Lett 2017;42:1688–91.
[580] Enrichi F, Cattaruzza E, Riello P, Righini GC, Vomiero A. Ag-sensitized Tb^{3+}/Yb^{3+} codoped silica-zirconia glasses and glass-ceramics: systematic and detailed investigation of the broadband energy-transfer and downconversion processes. Ceram Intl 2021;47:17939–49.

[581] Hughes MA, Homewood KP, Curry RJ, Ohishi Y, Suzuki T. Waveguides in Ni-doped glass and glass–ceramic written with a 1 kHz femtosecond laser. Opt Mater 2014;36:1604–8.
[582] Rajesh D, Dousti MR, Amjad RJ, de Camargo ASS. Enhancement of down- and upconversion intensities in Er^{3+}/Yb^{3+} co-doped oxyfluoro tellurite glasses induced by Ag species and nanoparticles. J Lumin 2017;192:250–5.
[583] Kaur P, Kaur P, Alzahrani JS, Al-Buriahi MS, Alrowaili ZA, Singh T. Optical and spectroscopic behavior of Eu^{3+} doped heavy metal phosphate glasses. Ceram Intl 2022;48:19424–33.
[584] Mahalakshmi S, Mayandi J, Sagadevan S, Vajeeston P, Venkatachalapathy V. Heavy metal oxide glasses and their optoelectronic applications (infrared transmission, luminescence, nonlinear optical susceptibilities, etc.). In: Sagadevan S, Podder J, Mohammad F, editors. Metal oxides for optoelectronics and optics-based medical applications. Amsterdam (NL): Elsevier; 2022. p. 205–40.
[585] Gattass R, Mazur E. Femtosecond laser micromachining in transparent materials. Nat Photon 2008;2:219–25.
[586] Carvalho DO, Kassab LRP, Del Cacho VD, da Silva DM, Alayo MI. A review on pedestal waveguides for low loss optical guiding, optical amplifiers and nonlinear optics applications. J Lumin 2018;203:135–44.
[587] Liu Q, Johnston BF, et al. A parametric study of laser induced-effects in terbium-doped borosilicate glasses: prospects for compact magneto-optic devices. Opt Mater Exp 2013;3(12):2096–111.
[588] Efimov OM, Glebov LB, et al. Waveguide writing in chalcogenide glasses by a train of femtosecond laser pulses. Opt Mater 2001;17(3):379–86.
[589] Davis KM, Miura K, Sugimoto N, Hirao K. Writing waveguides in glass with a femtosecond laser. Opt Lett 1996;21:1729–31.